MONTAN UNIVERSITÄT
WWW.UNILEOBEN.AC.AT

PhD Thesis

Multiscale Modelling and Simulation of Flow Behavior of Polymer/Layered Silicate Nanocomposites Under Shear Flow

Written by

Ali Gooneie

KUNSTSTOFF TECHNIK LEOBEN
KUNSTSTOFFVERARBEITUNG

Supervisor: Univ.-Prof. Dr. Clemens Holzer

Leoben, February 2017

Affidavit

I declare in lieu of oath, that I wrote this thesis and performed the associated research myself, using only literature cited in this volume.

Leoben, 8.2.2017
Date

Signature

Acknowledgements

Firstly, I would like to express my sincere gratitude to my advisor Prof. Clemens Holzer for the continuous support of my PhD study and related research, for his patience, and motivation. His guidance helped me in all the time of research and writing of this thesis.

My sincere thanks also goes to Dipl.-Ing. Stephan Schuschnigg who provided me an opportunity to join his team, and who gave me access to the laboratory and research facilities. Without his precious support it would not be possible to conduct this research.

I would like to thank my parents, Nahid and Houshang, for their devoted support of all my dreams in my entire life, as a kid, as a teenager, and as a young ambitious man. Last but not least, the spiritual support of my lovely wife, Sayna, always motivated me to pursue my goals, not only in my PhD research, but also in my life. For this, I would like to dedicate my PhD thesis to Nahid, Houshang, and Sayna.

Ali Gooneie,

Leoben, 03.02.2017

Kurzfassung

Polymer-Nanoverbundwerkstoffe (engl. Polymer nanocomposites (PNCs)) weisen ausgezeichnete Eigenschaften auf, aufgrund von Phänomenen, die bei unterschiedlichen Längen- und Zeitskalen auftreten. Die Weiterentwicklung dieser Materialien beruht auf einem umfassenden Verständnis der Grundlagen ihrer Struktur und ihres Verhaltens. Daher kann ihre inhärente multiskalen Natur nur durch eine Multiskalen-Analyse reflektiert werden, die für jegliche Mechanismen gelten. Die grundlegenden Konzepte der Multiskalen-Simulationen von polymeren Materialien und die dazugehörigen Forschungsaussichten werden in dieser Doktorarbeit ausführlich behandelt. Es wird gezeigt, dass es trotz aller Bemühungen bisher nicht gelungen ist, eine übergreifende Struktur von der Abbildung der Mikrostrukturen bis hin zu makroskopischen Modellen zu bilden.

In dieser Dissertation wurde ein, für die Lösung dieses Problems, theoretisches Framework entwickelt, basierend auf gut berechneten mesoskopischen dissipativen Partikeldynamik-Modellen (DPD-Modellen) als eine Lösungsmethode. Zuerst wurde die dynamische Konformationsveränderung von linearen Polymerketten als Reaktion auf die Ausbildung einer stationären Scherströmung untersucht. Im nächsten Schritt wurden die Orientierungsmuster von anisometrischen Schichtsilikatteilchen unter verschiedenen Scherströmungen charakterisiert. Dabei wurde der Einfluss der Wechselwirkungen zwischen Schichtsilikaten und Polymerketten auf den Orientierungsprozess genauer betrachtet und analysiert. Zum Schluss wurden diese Forschungsergebnisse für die Entwicklung von DPD-Modelle integriert, um ein Hochskalierungsverfahren für die mesoskopischen Orientierungsmuster zum makroskopischen Fließen zu entwickeln. Dieses Hochskalierungsverfahren wurde erfolgreich anhand von aus der Literatur bekannten Standard-Orientierungsmodellen überprüft. Bei dieser Herangehensweise werden die Verläufe des Orientierungsprozesses von schwach wechselwirkenden Schichtsilikaten als eine Funktion der eingesetzten Scherdehnung anstelle der Zeit angenommen, basierend auf Experimenten mit nicht-brownschen Materialien, die belastungsabhängiges anstatt zeitabhängiges strukturelles Wachstum vorschlagen. Ausgehend von der Vorstellung, dass die Orientierungskinetik einfach die Änderungsrate in Bezug auf die Dehnung anstelle der Zeit ist, wurde die angewandte Dehnung ausgewählt, um die Orientierungsparameter auf eine grössere Skala durch eine einfache Kombination von affinen und nichtaffinen Deformationen zu übertragen. Diese Kombination wurde in ihrer einfachsten Form als zufälliges Mischen von DPD-Einheitszellen (Simulation nichtaffiner Deformationen) in einer größeren Zelle dargestellt, die eine affine Deformation über die Einheitszellen verteilt. Es wurde festgestellt, dass diese Vorgehensweise für die Multiskala-Simulationen des Orientierungsprozesses verwendet werden können, sofern die Einheitszellen eine genaue Beschreibung der Wechselwirkungen zwischen den Komponenten darstellen. Der Vergleich dieser Methodik mit dem Modell des Dehnungsreduktionsfaktors weist den Erfolg der Multiskalen-Simulation bei der Charakterisierung des Wachstums der Orientierungs-

parameter abhängig von der Scherdehnung nach. Es hat sich auch herausgestellt, dass das Verfahren das Wachstum der Mikrostrukturen nicht erfasst, wenn die Einheitszellen das Material nicht exakt darstellen. Die weiteren Herausforderungen, wie Optimierung, Erweiterung und Verallgemeinerung des entwickelten Multiskalenalgorithmus, wurden ebenfalls angesprochen.

Schlüsselwörter: Computersimulationen, Rechenverfahren, dissipative Partikeldynamik, Multiskalen Modellierung, hierarchische Strukturen, Polymer-Nanokomposit, Schichtsilikat, Wachstum der Mikrostrukturen, Morphologie, Orientierung, Strömungsfeld

Abstract

Polymer nanocomposites (PNCs) display distinguished characteristics which originate from the interplay of phenomena at different length and time scales. Further development of these materials critically relies on a comprehensive understanding of the fundamentals of their hierarchical structure and behaviors. As such, their inherent multiscale nature is only reflected properly by a multiscale analysis which accounts for all important mechanisms. The fundamental concepts of multiscale simulations of polymeric materials along with relevant research outlooks are thoroughly addressed in this thesis. It is explained that in spite of all efforts, a framework for dynamic bridging of microstructure evolutions to macroscopic models had been hindered so far.

In this PhD research, a theoretical framework was developed based on well-credited mesoscopic dissipative particle dynamics (DPD) models in order to propose a solution to this problem. First, the dynamic conformation change of linear polymer chains in response to startup of a steady shear flow was investigated. Second, the orientation patterns of anisometric layered silicate particles were studied under various shear flows. The influence of the interactions between layered silicates and polymer chains on the orientation process was carefully explored. Finally, the results of these works were incorporated to develop DPD models in order to build an upscaling method for the mesoscopic orientation patterns to the macroscopic flows. This upscaling method was tested successfully against the available standard orientation models from the literature. In this strategy, the trajectories of the orientation process of weakly-interacting layered silicates are parametrized as a function of the applied shear strain instead of the time, based on the experiments which propose strain-dependent rather than time-dependent structural evolutions in such non-Brownian materials. Benefitting from the notion that the orientation kinetics is simply the rate of change with respect to strain rather than time, the applied strain was selected to pass the orientation parameters to an upper scale through a simple combination of affine and nonaffine deformations. This combination was pictured in its simplest form to be a random mixing of DPD unit cells (simulating nonaffine deformations) in a larger cell which distributes an affine deformation over the unit cells. It was noted that this strategy could be used to perform multiscale simulations of orientation process provided that the unit cells represent a precise description of the interactions between the components. A comparison of this methodology with the strain reduction factor model showed the success of the multiscale simulation of the evolution of orientation parameters against the applied shear strain. It was also shown that the method fails to capture the microstructure evolutions if the unit cells do not provide an accurate representation of the material. The remaining research challenges which must be overcome in order to improve, extend, and generalize the developed multiscale algorithm were addressed before closing the discussion.

Keywords: computer simulations, computational methods, dissipative particle dynamics, multiscale modelling, hierarchical structures, polymer nanocomposite, layered silicate, microstructure evolution, morphology, orientation, flow field

Table of Contents

1. Introduction

1.1 Motivations and Goals

It is well-established that the development of PNCs relies largely on our understanding of the structure–property relationship of the materials which requires a multiscale model to predict the material properties from the information of particle properties, molecular structure, molecular interactions and mesoscale morphology [229]. The current research in modelling and simulation of PNCs is largely limited to individual length and time scale. However, it should be noted that some efforts have recently been made to develop multiscale strategies for predicting the multiscale level of structure, properties, and processing performance of PNCs based on nanoparticle reinforcement [9, 52, 58, 75, 106, 166, 229].

The main challenge for PNCs is to predict accurately their hierarchical structures and behaviors and to capture the phenomena on length scales that span typically 5 – 6 orders of magnitude and time scales that can span a dozen orders of magnitude. For example, a clay particle with a diameter of 0.5 mm and 100 layers would have about 85 million atoms. If such a particle is dispersed into polymer matrix to form PNCs containing 5 % of clay in weight, the system would then have about 3 billion of atoms. Thus, it is too large for classical molecular dynamics (MD) and enormously too large for quantum mechanics (QM). Moreover, the observable properties of the materials depend on a hierarchy of structures, including chemical details at the atomistic level, individual chains, microscopic features involving aggregates of chains and clusters of clay platelets, up to continuum phenomena at the macroscale. As a result, the complete description of a PNC typically requires a wide range of length scales from the chemical bond, at around one angstrom in length, up to chain aggregates extending for many hundreds of angstroms and beyond. There is also a wide range of time scales, with chemical bond vibrations occurring over tens of femtoseconds and, at the other extreme, collective motions of many chains taking seconds or much longer. From this point of view, new strategies for multiscale modelling and simulation are essential to predict accurately the physical/chemical properties and material behavior which links the methods from microscale to mesoscale and macroscale levels.

With the exception of isolated instances, most of the studies so far have primarily dealt with the studies and developments related to the equilibrium aspects of polymer–nanoparticle mixtures. However, nonequilibrium effects resulting from filler aggregation and/or external fields (such as stress fields involved in the extrusion processing of PNCs) are important for many applications of PNCs. The time and length scales which can be probed through present-day computer simulations do not necessarily overlap with experimental regimes. Moreover, issues unique to PNCs, such as the anisotropy of the fillers, potentially long-ranged interparticle interactions (mediated by the polymers), and the dynamical and rheological response of the polymer matrix, do not have direct counterparts in the composites literature pertinent to micron sized and larger particles. Hence, there is a need for the development of appropriate theoretical models and computational frameworks which can enable the study of nonequilibrium issues as well as the influence of external fields on the structure and dispersion of nanoparticles in polymer matrices.

The setting up and performing of a multiscale simulation is however difficult when it comes to dynamics and rheology of PNCs. Among the multiscale methods, the concurrent approach is severely limited when it comes to simulating flow problems because of the fact that these methods often necessitate extreme computational costs [126]. For the adaptive resolution schemes on the other hand, one should note that the method is fundamentally developed for quiescent conditions and the application of flow is yet to be added to these schemes. Even for the simulation of equilibrium conditions, these schemes show noticeable discontinuities in pressure and density profiles at the transition region between the high and low resolutions [156]. Finally, the sequential methods in their current form offer the possibility to conveniently couple several methods and benefit from their advantages. However, it should be emphasized that this coupling often means a single-step passing of information from one method to the other [22, 23, 183, 188, 203, 207, 232]. Thus, for a dynamic simulation of microstructure evolutions under flow an innovative strategy is needed to efficiently generate and pass the information between the mesoscale and macroscale models. Such a strategy principally should utilize a hybrid scheme based on elements from both sequential and concurrent approaches to perform the message-passing. In this PhD research, I focus on developing an efficient algorithm for accelerated passing of microstructure information and flow characteristics between the meso and macro scales.

1.2 Hypothesis and Approach

It has been shown before that the dissipative particle dynamics (DPD) method is an adequate mesoscopic model to represent both thermodynamic and hydrodynamic interactions in soft matter [79, 80, 118]. In this research, it is assumed that DPD provides a natural flexibility in the design and testing of PNCs with various initial configurations. The main hypothesis of the present thesis is that DPD is also capable to capture the microstructure evolutions of PNCs correctly during an applied flow field. For this idea to be true, it is necessary that the constituents of the model PNCs, i.e. polymer chains and nanoparticles, are simulated both accurately and efficiently. Therefore, an important objective of this research is to ensure such criteria and test them for the PNC components separately and collectively. The multiscale strategy can only then be constructed on such mesoscopic models. In addition, the main idea in the scale bridging approach of the developed multiscale method is that the microstructure evolutions in non-Brownian PNCs are strain-dependent rather than time-dependent. This hypothesis can reduce the amount of simulations significantly and allow for a fast data transfer between mesoscopic and macroscopic models.

In this thesis, I will focus on the formation of anisotropic (preferentially oriented) structures of layered silicate nanoparticles within the polymer matrix. For a PNC system, the dynamics and orientation of the major constituent, the polymer chains, are critically important to the overall microstructure developments of the entire system including the nanoparticles. Therefore, it is necessary not only to determine their response to the application of shear flows, but also to examine the limitations of the applied modelling technique (i.e. DPD). For this reason, DPD models of monodispersed and polydispersed linear polymer chains were simulated under shear flows and their results were tested with results from literature. This work is described in details in the paper titled "*Coupled Orientation and Stretching of Chains*

in Mesoscale Models of Polydisperse Linear Polymers in Startup of Steady Shear Flow Simulations." The results of this work showed that while the standard DPD models are capable to model the dynamics of polymer chains, they need to be improved in future research.

In addition to the dynamics of polymer chains, the interactions between polymer chains and layered silicate particles determine the final morphology of the PNCs. Consequently, it was necessary to study the influence of these interactions on the orientation patterns developed under shear flows in DPD models. A comprehensive study was conducted in order to investigate the orientation of layered silicates in uncompatibilized and compatibilized polymer melts. The details are explained in the paper titled "*Orientation of Anisometric Layered Silicate Particles in Uncompatibilized and Compatibilized Polymer Melts Under Shear Flow: A Dissipative Particle Dynamics Study.*" It was shown that the DPD models were capable to correctly predict the morphological evolutions under a variety of shear flows.

Finally, a simple but effective upscaling strategy was proposed based on previous experiments which made it possible to pass the orientation information from the mesoscale to the macroscale. In a previous study, a method based on optimization of the action functional was proposed to extend the time scale of MD simulations by several orders of magnitude [49]. In this method, instead of parameterizing the trajectory as a function of time, the trajectory is parametrized as a function of length. Inspired by this method, a strategy was developed in this thesis in which the trajectories of the orientation process of weakly-interacting layered silicates (the particles have little influence on the movements of each other) were parametrized as a function of the applied shear strain instead of the time [76]. The idea of using the applied strain was based on the experiments which propose strain-dependent rather than time-dependent structural evolutions in such non-Brownian materials [109, 112, 133, 189]. Benefitting from the notion that the orientation kinetics is simply the rate of change with respect to strain rather than time [205], the applied strain is selected to pass the orientation parameters to an upper scale through a simple combination of affine and nonaffine deformations. This combination was pictured in its simplest form to be a random mixing of DPD unit cells (simulating nonaffine deformations) in a larger cell which distributes an affine deformation among the unit cells. It was noted that this strategy could be used to perform multiscale simulations of orientation process, provided that the unit cells represent a precise description of the interactions between the components [76]. A comparison of this methodology with strain reduction factor model (with coefficients based on previous experiments from others [134, 179]) was used to examine the success of the multiscale simulation of the evolution of orientation parameters against the applied shear strain. It was also shown that the method fails to capture the microstructure evolutions if the unit cells do not provide an accurate representation of the material, for instance in the case of strongly-interacting PNCs. Further details of this technique are provided in the paper titled "*Dissipative Particle Dynamics Models of Orientation of Weakly-Interacting Anisometric Silicate Particles in Polymer Melts under Shear Flow: Comparison with the Standard Orientation Models.*"

Before closing this section, it should be noted that the simulations in this research were conducted on a 12-core Intel® Xeon CPU workstation with a calculation frequency of

2.80 GHz. The simulations were running for approximately 6 months (combined) in order to obtain the required results. The computer was equipped with 48 GB of DDR3 RAM.

1.3 Outline of the Thesis

In this introduction, an overview to the relevant topics of the thesis is provided. I will start by explaining the necessity of multiscale simulation and modelling of materials with emphasis on PNCs. The interdependent relation of morphology and rheology is highlighted and the standard simulation and modelling techniques of the morphology at the mesoscale are explained. Here, I have restricted the mesoscopic simulation techniques to DPD due to its use in this thesis. Then, the most important characteristics of multiscale simulation techniques are outlined along with proper examples of their use in polymer science. It should be noted here that this introduction is, for the most part, a rework of my published research papers which follow in the next chapters. The purpose of this rework is to structure the thesis appropriately while briefly introducing the most important topics relevant to this research. With this declaration, I wish to avoid any ethical conflicts.

The rest of the thesis consists of five papers and a conclusions section which are categorized in three main chapters. In the first chapter, *Fundamental Concepts in Multiscale Simulations of Polymer Systems*, an exhaustive review of the simulation methods in polymeric materials is provided with emphasis on PNCs. This paper titled "*A Review of Multiscale Computational Methods in Polymeric Materials*" presents the most up-to-date and comprehensive literature review on the topic of multiscale modelling techniques. In this review, the state of the art is addressed and the results of the present PhD research are also included. This will help to emphasize clearly on the progress resulted by this study in the vast field of multiscale modelling and simulation. Furthermore, this research enabled us to find appropriate streamlines in this field and spot the advantages and shortcomings of available methods. Afterwards, I briefly address the current possibilities in the multiscale simulation of PNCs in processing in the paper titled "*Multiscale Simulation of Polymer Nanocomposites in Processing: Challenges and Outlooks*". In this paper, it is shown that a dynamic microstructure development under flow can be envisioned using DPD models.

The second chapter, *Development of Suitable Methods for Multiscale Simulation of Polymer/Layered Silicate Nanocomposites Under Shear Flow*, includes three research papers. It deals with the development of a multiscale method based on DPD simulations which accounts for a dynamic evolution of orientation patterns on PNCs. The first paper, "*Coupled Orientation and Stretching of Chains in Mesoscale Models of Polydisperse Linear Polymers in Startup of Steady Shear Flow Simulations*", focuses on the major constituent in a PNC, i.e. the polymer chains. It investigates the dynamic conformation change of linear polymer chains in response to startup of a steady shear flow. Then, the orientation patterns of anisometric layered silicates are thoroughly studied in the second paper titled "*Orientation of Anisometric Layered Silicate Particles in Uncompatibilized and Compatibilized Polymer Melts Under Shear Flow: A Dissipative Particle Dynamics Study*". In this paper, the role of interactions between layered silicates and polymer chains on the orientation dynamics are explored. Finally, the results of these works are incorporated to develop well-credited DPD models in order to build an upscaling method for the mesoscopic orientation patterns to the

macroscopic flows. In the paper "*Dissipative Particle Dynamics Models of Orientation of Weakly-Interacting Anisometric Silicate Particles in Polymer Melts under Shear Flow: Comparison with the Standard Orientation Models*", this upscaling method is introduced and tested successfully against the available standard orientation models from the literature.

At the end of the thesis, a short chapter is dedicated in the third chapter to address the main outcomes of this study, as well as the remaining challenges which must be overcome in order to improve, extend, and generalize the developed multiscale algorithm.

2. Multiscale Modelling in Materials Science

Some of the most fascinating problems in all fields of materials science involve multiple spatial or temporal scales. Processes that occur at a certain scale govern the behavior of the system across several (usually larger) scales. The notion and practice of multiscale modelling can be traced back to the beginning of modern science. In many problems of materials science this notion arises quite naturally. The ultimate microscopic constituents of materials are atoms, and the interactions among them at the microscopic level (on the order of nanometers and femtoseconds) determine the behavior of the material at the macroscopic scale (on the order of centimeters and milliseconds and beyond), with the latter being the scale of interest for technological applications. Therefore, the idea of modelling materials across several characteristic length and timescales has obvious appeal as a tool of potentially great effect on technological innovation. The advent of ever-more-powerful computers that can handle such simulations provides further argument that such an approach can address realistic situations and can be a worthy partner to the traditional approaches of theory and experiment.

The challenge in modern simulations of materials science and engineering is that real materials usually exhibit phenomena on one scale that require a very accurate and computationally expensive description of phenomena on another scale for which a coarser description is satisfactory and, in fact, necessary to avoid prohibitively large computations. Since a single-scale modelling method would not suffice to describe the entire system, the goal becomes to develop models that combine different methods specialized at different scales, effectively distributing the computational power where it is needed most. There is great hope that a multiscale approach is the answer to such a quest, and it is by definition an approach that takes advantage of the multiple scales present in a material and builds a unified description by linking the models at the different scales. At the same time, the unified approach can retain the accuracy that the individual approaches provide in their respective scales, allowing, for instance, for very high accuracy in particular regions of the systems where it is required. As effective theories, multiscale models are also useful for gaining physical insight that might not be apparent from brute-force computations. Specifically, a multiscale model can be an effective way to facilitate the reduction and analysis of data, which sometimes can be overwhelming. Overall, the goal of multiscale approaches is to predict the performance and behavior of materials across all relevant length and timescales, striving to achieve a balance among accuracy, efficiency, and realistic description.

2.1 Multiscale Modelling of PNCs

The incorporation of nanoparticles in polymers has attracted substantial academic and industrial interest due to the dramatic improvements in the properties of the matrix polymers. However, from the experimental point of view, a thorough structural characterization and a tailored fabrication of these hybrid nanostructure materials remain a grand challenge. Nanomaterials are both exciting and puzzling at the same time, as they involve components at "uncommon" characteristic scales at which conventional theories may fail. Understanding the behavior of materials at different scales is important both from the standpoint of basic science and future applications. The development of such materials is still in its infancy and, as such, largely empirical. Thus, a fine degree of control of the resulting macroscopic properties cannot be achieved so far. Moreover, as the ultimate properties of these hybrid systems commonly depend on their structure at the nanoscale, it is of particular interest to establish the mesoscopic morphology of the final composite and to link this characteristic to the material performance. To this purpose, the development of theories and the application of computer simulation techniques have opened avenues for the design of these materials, and the a priori prediction/optimization of their structures and properties.

The addition of only 1 - 10 vol% nanoparticles has been shown to enhance various properties of the neat polymers [30, 37, 67, 73, 119, 122, 136]. These changes are often introduced additionally into the polymer matrix while many advantages of the neat polymer such as high processability are still preserved [103, 178]. Therefore, PNCs are ideal candidates for multiple applications like medical devices, aerospace applications, automobile industries, and coatings. Experience has shown that, besides the filler content, the property enhancement in PNCs is directly linked to the nanoparticles arrangement and dispersion [103, 149]. A precise morphology control is of great significance in PNCs, otherwise the full property potential of these materials could not be achieved. The fact that many of the common nanoparticles possess strong van der Waals interactions promotes their aggregation and consequently diminishes their effectiveness. On the other hand, the role of polymer-particle interactions could either facilitate or complicate the aggregation process. Moreover, the geometrical characteristics of the nanoparticles, such as aspect ratio and structural flexibility, add to the complexity of their impact on the properties since it can alter surface energies as well as surface-to-volume ratio [127]. Therefore, the structural characterization and the precise evaluation of the fabrication of PNCs are crucial to achieve the desired properties. Many studies are devoted to understand the effects of processing conditions on the final microstructure and the resulting properties of the PNCs [73, 74, 103, 110, 127, 136, 149, 184]. The multiscale nature of PNCs simply divulges, if one considers the interplaying role of the fabrication stage with macroscopic characteristics and the aforementioned submicron phenomena involved in the final performance of PNCs.

In order to find appropriate predictive tools, several theories and computational methods were developed which could introduce new possibilities to design and optimize the structures and properties of these materials. At present, no single theory or computational method can cover various scales involved in PNCs. As a result, the bridging of length and time scales via a combination of various methods in a multiscale simulation framework is considered to be one of the most important topics in computational materials research. The resulting

multiscale method is preferably supposed to predict macroscopic properties of PNCs from fundamental molecular processes. In order to build a multiscale simulation, often models and theories from four characteristics length and time scales are combined. They are roughly divided into the following scales.

1. The quantum scale ($\sim 10^{-10}$ m, $\sim 10^{-12}$ s): The nuclei and electrons are the particles of interest at this scale and quantum mechanics (QM) methods are used to model their state. The possibility to study the phenomena associated with formation and rupture of chemical bonds, the changes in electrons configurations, and other similar phenomena are typical advantages of modelling at quantum scale.

2. The atomistic scale ($\sim 10^{-9}$ m, $\sim 10^{-9}$ - 10^{-6} s): All atoms or small groups of atoms are explicitly represented and treated by single sites in atomistic simulations. The potential energy of the system is estimated using a number of different interactions which are collectively known as force fields. The typical interactions include the bonded and nonbonded interactions. The bonded interactions often consist of the bond length, the bond angle, and the bond dihedral potentials. The most typically used nonbonded interactions are Coulomb interactions and dispersion forces. MD and Monte Carlo (MC) simulation techniques are often used at this level to model atomic processes involving a larger group of atoms compared with QM.

3. The mesoscopic scale ($\sim 10^{-6}$ m, $\sim 10^{-6}$ - 10^{-3} s): At mesoscopic scale, a molecule is usually described with a field or a microscopic particle generally known as a bead. In this way the molecular details are introduced implicitly which provides the opportunity to simulate the phenomena on longer length and time scales hardly accessible by atomistic methods. A good example for the field-based description of polymer systems is the Flory-Huggins model for the free energy of mixing in which the details of the system are summed up in model parameters. On the other hand, in particle-based models collections of particles are accumulated in beads through a coarse-graining procedure. The interactions between the beads are then used to characterize the system. Various methods have been developed to study the mesoscale structures in polymeric materials including Brownian dynamics (BD), dissipative particle dynamics (DPD), lattice Boltzmann (LB), time-dependent Ginzburg-Landau (TDGL) theory, and dynamic density functional theory (DDFT).

4. The macroscopic scale ($\sim 10^{-3}$ m, ~ 1 s): At this level, the physical system is considered as a continuous medium and the discrete atomic and molecular structures and their influence on the overall behavior of the system are ignored. The behavior of such a system is governed by constitutive laws which are often coupled with conservation laws to simulate various phenomena. All functions such as velocity and stress components are continuous except at a finite number of locations separating regions of continuity. The fundamental assumption at this scale is in representing a heterogeneous material as an equivalent homogeneous medium. The most important methods used to simulate systems at this scale are finite difference method (FDM), finite element method (FEM), and finite volume method (FVM).

The success of a multiscale simulation lies in an appropriate combination of methods from these scales in order to model the material as realistically as possible. This task is often

extremely complicated and necessitates a different strategy for every set of material/phenomena at hand.

2.2 Background and Significance of Polymer/Layered Silicate Nanocomposites

In the vast field of nanotechnology, polymer materials reinforced with nanofillers such as layered silicates (clay), have become a prominent area of current research and development. Generally speaking, nanocomposites are commonly defined as materials consisting of two or more dissimilar materials with well-defined interfaces, at least one of the materials being nanostructured (having structural features ranging in size from 1 to a few 100 nm) in one, two, or three dimensions. The same refers to the spacing between the networks and layers formed by polymeric and inorganic components. Depending on the strength of the interfacial tension between the polymeric matrix and the layered silicate (modified or not), which defines the extent of the separation of the silicate layers, polymer/layered silicate nanocomposites (PLNs) can be categorized into two types: (i) intercalated nanocomposites, in which the polymer chains are inserted between the layers of the clay such that the interlayer spacing is expanded, but the layers still bear a well-defined relationship to each other, and (ii) exfoliated nanocomposites, in which the layers of the clay have been completely separated, and the individual mineral sheets are randomly distributed throughout the polymeric matrix. A schematic representation of these structures is shown in Figure 1. The best performance of PLNs, regarding some properties such as the mechanical behavior, is generally achieved for systems characterized by a high degree of clay exfoliation within the polymeric matrix.

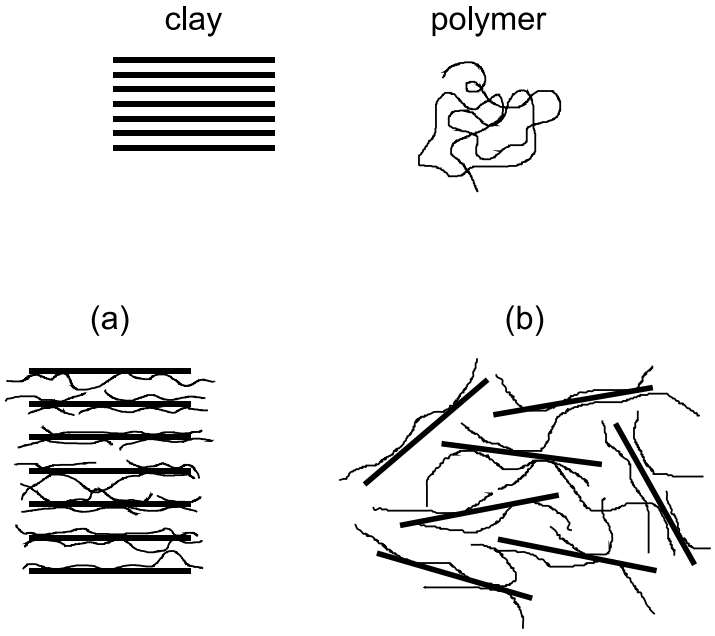

Figure 1: Schematic representation of different types of PLNs (a) intercalated, and (b) exfoliated structures.

The incorporation of non-spherical particles in PLNs has led to the development of advanced materials with anisometric properties [1, 30, 149, 184]. PLNs particularly exhibit superior

improvement in mechanical properties [67, 71, 119, 122, 220, 226], gas-barrier properties [37, 190], solvent resistance [149], and reduced flammability [67, 136, 164, 224] relative to their unfilled polymer matrices. This allows for the light-weight PLN to be processed by conventional techniques in much the same way as unfilled polymers. However, a well-dispersed microstructure of tactoids, i.e. the exfoliated structure, must be ensured in order to achieve the optimal performance of PLNs [30]. Unfortunately, it is indeed difficult to have such structures due to (i) the large aspect ratio of silicate layers, (ii) slow diffusion kinetics of polymer chains inside narrow silicate galleries, and (iii) the unfavorable mixing energy of silicate particles and polymer chains. Consequently, the fabrication of stable microstructures in PLNs has been the topic of many experimental and theoretical studies.

Melt intercalation is a widely-used commercial method of PLN production which relies on the mixing ability of silicate layers with polymer melt. This processing technique is the only method addressed in this work. Many approaches have been taken in order to promote the intermixing of silicate and polymers. This includes modification of the silicate surface [35, 123, 220], changing the molecular structure of the polymer [223], and incorporation of compatibilizing molecules in the matrix [13, 31, 115]. In compatibilized PLNs, the silicate layers are usually modified with surfactant molecules such as alkylammonium. This promotes the compatibility of the layers with the compatibilizing molecules. The compatibilizing molecules could be polymers such as maleic anhydride grafted polypropylene (MA-g-PP). The improved compatibility leads to the improved dispersion of silicate layers in the polymer matrix. Such a mechanism is absent in uncompatibilized PLNs resulting in the formation of aggregated microstructures. The application of dispersive stresses of shear and/or extensional types is also found to help achieve finer dispersions [30, 195]. As a result, the evolution of microstructure under flow has always been an intriguing subject.

The production of PLNs in an efficient and cost-effective manner poses significant challenges, which can be appreciated by considering the structure of the clay particles. Montmorillonite (MMT) is a prime example of the layered silicates commonly used in nanocomposites. These layers organize themselves to form stacks with a regular van der Waals gap in between them, called the interlayer region or gallery. Isomorphic substitution of some elements within the layers generates negative charges that are counter-balanced by alkali or alkaline earth metal cations situated in the interlayers. The lateral dimensions of these layers can vary from approximately 200 Å to several micrometers, depending on the particular composition of the silicate, while the spacing between the closely packed sheets is on the order of 1 nm, which is smaller than the radius of gyration of typical polymers, see Figure 2. Consequently, there is a large entropic barrier that inhibits the polymer's penetrating this gap and becoming intermixed with the clay.

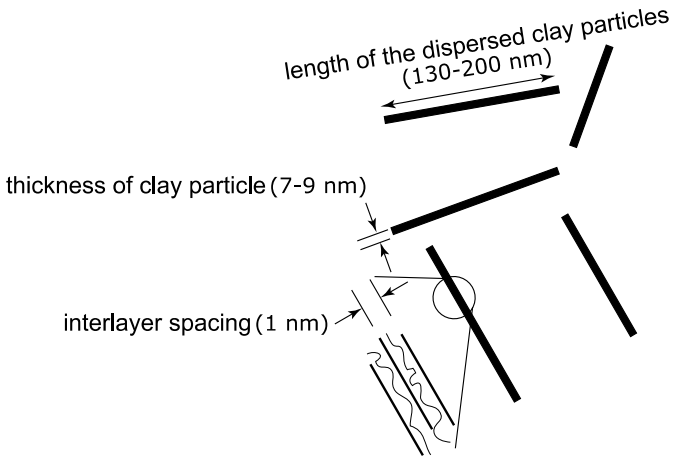

Figure 2: Schematic representation of hierarchical morphology and characteristic dimensions of clays in PLNs.

To enhance polymer-clay interaction, a cation-exchange process is employed in which hydrophilic cations are exchanged by a surface modifier, usually selected from a group of organic substances having at least one alkyl group, most commonly quaternary ammonium salts. The role of this organic component in organosilicates is to lower the surface energy of the inorganic host and improve the wetting characteristic with the polymer. Intuitively, the nature and the structure of these "compatibilizers" determine the hydrophobicity of the silicate layers and hence their extent of exfoliation.

Indeed, the real commercial production of such complex systems involves the application of severe external flow fields during the processing of the PLNs in order to facilitate the exfoliation through convective forces. Extrusion processing is undoubtedly a well-known mixing operation which can provide high production rates for industrial purposes. In an extruder, the coupling of multiple phenomena including the stress transport from the rotary screw to the material bulk as well as the instinctive thermodynamics of the system play a key role in the determination of the final microstructure of the PNC. Therefore, it is necessary to consider such interactive factors in the modelling and simulation of the extrusion processing of PNCs as indeed it is nowadays one of the most common processing machinery in the commercial production of the aforementioned systems. However, the complexity of the description of such systems which can take all the relevant phenomena into account has always hindered the research.

During the processing of PLNs, the material experiences a variety of flow deformations which could cause translation, rotation, bending, and breaking of layered silicates. These phenomena influence the properties of the final part which are highly dependent on the microstructural characteristics and particles orientation. The modelling of spherical [194, 195] and non-spherical suspensions such as fibers [168, 169] and sheets [54, 55], has been the subject of several publications over the past few decades. The mesoscopic standard orientation model is based on the Jeffery's equation for the motion of a single fiber in an infinite Newtonian matrix [88]. Later, it was modified by Folgar and Tucker to account for fiber-fiber interactions [59]. Afterwards, Advani and Tucker improved it by the introduction of the second-order moment tensor of the probability density function for orientation [5].

More recently, various versions of this model have been developed to account for phenomena such as slow orientation kinetics [205] and semiflexibility of the fibers [138].

In recent years, the rapid development of the computer technology has made complicated numerical simulations possible [125, 180]. Computer simulations have made significant contributions to our understanding of shear-induced microstructural evolutions within the limitation of the model complexity and the accessible time and length scales [129, 193]. Detailed molecular simulations have shown great potential to model complex phenomena at an atomistic level [90, 172, 186, 202, 212]. Coarse-graining technique has been successfully applied to MD method in order to access longer time and length scales [11, 143 - 145]. Anderson et al. [7] utilized coarse-grained molecular dynamics (CGMD) to explore the intermolecular interactions that influence mesoscale morphology development in PLNs. Sinsawat et al. [185] also used CGMD to investigate aspects of the polymer matrix that promote the formation of intercalated or exfoliated structures. More recently, Kalra et al. [94] incorporated CGMD to study spherical nanoparticle dispersions in polymer melts under shear flows. Such studies have shown the capability of computer simulations to help distinguish the phenomena involved in the formation of microstructures in PNCs.

The unique insights available through simulation of materials at a range of scales, from the quantum and molecular, via the mesoscale, to the finite element level, can produce a wealth of knowledge. It can significantly reduce the number of experiments, allowing products and processes to be optimized while permitting large numbers of candidate materials to be screened prior to production. Therefore, multiscale computational approaches covering all methods for each length and time scales can play an ever-increasing role in predicting and designing material properties, and guiding such experimental work as production and characterization.

Several multiscale computational approaches, spanning different length/time scale domains have been proposed in recent years for the characterization of PLNs. Multiscale modelling has been shown to be a valuable tool for the characterization and/or prediction of macroscopic properties of PNCs with different fillers, such as layered clays, carbon and boron nanotubes, fibers, and spheres. In spite of these efforts devoted to the multiscale simulation of nanostructured systems, a thorough, systematic and comprehensive study dealing with multiscale modelling and simulations of PNCs covering all length scales with the final aim to study morphology phenomena and prediction of macroscopic effective property still exists.

With the ambitious aim of filling this gap, recent efforts in nanocomposites simulation were initially concerned with binding energy evaluations for well-characterized polymer/clay systems using atomistic MD methods. At the same time, some researches were focused on the development and application of mesoscale simulation recipes to polymer blends and nanocomposites morphology investigations on one side, and on the integration of these tools with both lower scales and higher scales on the other.

Central to the above described multiscale modelling recipe is the mesoscopic level where material time-space spans from nanometers to micrometers in length scale and investigates relaxation phenomena up to microseconds in the time domain. In mesoscale modelling, the familiar atomistic description of the molecules is coarse grained, leading to beads of material (representing the collective degree of freedom of many atoms). These beads interact

through pair-potentials which capture the underlying interactions of the constituent atoms. The primary output of mesoscale modelling is material phase morphologies with size up to the micron level. These morphologies are of interest per se, although little prediction of the material properties can be obtained with the mesoscale tools. FEM then comes into play, and the material properties of interest can be calculated accordingly by mapping the material structures formed at the nano/micrometer scale onto the finite element grid and coupling this information with the properties of the pure components that comprise the complex system. Using standard solvers, the FEM code can then calculate the properties of the realistic structured material.

In a comprehensive computational procedure to investigate such complex systems, the interactions between all individual components (filler, polymer and surface modifier/compatibilizer) for each nanocomposite, which occur at a molecular level, must be calculated using atomistic simulations as a first step. Similarly, using other MD based protocols, the spacings of the clay stacks in PLNs have to be derived. Secondly, the information obtained from the atomistic simulations must be expanded by employing mesoscale models for the prediction of density profiles and system morphologies. To this purpose, the MD data should be mapped onto the corresponding mesoscale models via the respective interaction parameters, and the results generated at both length scales have to be then compared for consistency. Lastly, the density profiles and the morphologies resulting from the mesoscale simulations must be imported into a FEM code, and some characteristic macroscopic properties of these systems may be predicted as functions of filler loading and/or a given degree of dispersion in PLNs and later compared with the corresponding experimental values.

In this work, an attempt is made to overcome such complications with reasonable assumptions which can provide the researchers with a well-defined theme for multiscale modelling and simulation of PLNs experiencing external shearing flows. Although several issues must be addressed to optimize the production of PLNs, of foremost importance is to identify conditions that enable a dynamic passing of morphological information between the scales.

3. Morphology of PNCs

The properties of PNCs are highly related to their overall morphologies. For example, in clay-based PNCs, the optimal mechanical performance is generally obtained from exfoliated structure other than intercalated structure [30, 103, 184]. The morphology of PNCs depends on not only the physics of the components and the interactions among the components but also the volume fraction of nanoparticles and processing conditions [184]. Therefore, it is important to understand the effects of various factors on the macroscopic morphology of the materials, such as the size and shape of nanoparticles, the clustering of nanoparticles, polymer architecture, hydrodynamic interactions, and eventually establish the correlations between the morphology of the resulting composites and their properties, for instance, mechanical properties, gas permeability, electrical conductivity, and rheology.

The latter is critically important due to the fact that it has an interchangeable relation with the morphology and microstructure of PNCs [73, 74, 109, 112, 133, 184, 189]. There are a

number of simulations in the literature focusing on this relation [6, 229]. For instance, Paul and co-workers [44, 61, 62] examined the effects of polymer rheology and processing conditions on the formation of PNCs via melt intercalation processing. Simulation techniques are particularly useful when unveiling the physical origins of certain rheological behaviors of PNCs [6, 229]. The origins of linear viscoelasticity of PNCs [163], the shear-rate dependence of viscosity of PNCs [93], and the dispersion of nanoparticles under applied flows [94, 193] are some examples for this application.

3.1 Rheological Orientation Models

It is a well-known fact that the local orientation of anisometric particles determines the local mechanical and physical properties in a reinforced composite material [1, 21]. Thus, any useful prediction of the structural performance or dimensional accuracy of the final part necessitates a precise prediction of the flow-induced particle orientation. Consequently, it is of great significance to be able to predict the orientation patterns which arise during processing of such complex materials. For this reason, several particle orientation models have been developed and combined with traditional continuum calculations to simulate injection molding [12, 139], compression molding [4, 221], and extrusion processes [8].

The standard orientation model is based on Jeffery's equation for the motion of an ellipsoid [88]. This model is applicable to dilute suspensions and has been used in most orientation models to account for the hydrodynamic contributions in orientation. If the unit vector directed along the fiber axis, $\mathbf{p}$, is used to denote the fiber orientation, the time derivative of this vector, $\dot{\mathbf{p}}$, following the particle can be written as

$$\dot{\mathbf{p}} = \mathbf{W}\cdot\mathbf{p} + \lambda\left(\mathbf{D}\cdot\mathbf{p} - \mathbf{D}:\mathbf{ppp}\right), \qquad (1)$$

where $\mathbf{W} = \frac{1}{2}\left(\mathbf{L} - \mathbf{L}^{\mathrm{T}}\right)$ is the vorticity tensor and $\mathbf{D} = \frac{1}{2}\left(\mathbf{L} + \mathbf{L}^{\mathrm{T}}\right)$ is the rate-of-deformation tensor. $\mathbf{L}$ represents the velocity gradient tensor with components $\mathrm{L}_{ij} = \frac{\partial \mathrm{v}_i}{\partial \mathrm{x}_j}$ where v_i is the component of velocity in x_j direction. $\lambda = \left(\mathrm{r}^2 - 1\right)/\left(\mathrm{r}^2 + 1\right)$ is a constant that depends on the particle aspect ratio, r. In Jeffery's model, the first term corresponds to the fiber rotation due to the vorticity of the flow. The second term represents a rotation of the fiber axis toward the direction of maximum elongation rate.

Orientation calculations often use the second- and fourth-order orientation tensors, $\mathbf{A}_2$ and $\mathbf{A}_4$ respectively, introduced by Advani and Tucker [5]. These tensors are given by

$$\mathbf{A}_2 = \oint \mathbf{pp}\psi(\mathbf{p})\mathrm{d}\mathbf{p} \qquad \text{and} \qquad \mathbf{A}_4 = \oint \mathbf{pppp}\psi(\mathbf{p})\mathrm{d}\mathbf{p}. \qquad (2)$$

Here, $\psi(\mathbf{p})$ is the probability density function for fiber orientation and the integral is performed over all orientation states. In order to model concentrated suspensions of non-Brownian particles, Folgar and Tucker [60] added the diffusion term to the Jeffery's equation. The Folgar-Tucker (FT) model for the orientation change in terms of the orientation tensors can be written as

$$\dot{\mathbf{A}}_2 = \mathbf{W}\cdot\mathbf{A} - \mathbf{A}\cdot\mathbf{W} + \lambda\left(\mathbf{D}\cdot\mathbf{A} + \mathbf{A}\cdot\mathbf{D} - 2\mathbf{A}_4:\mathbf{D}\right) + 2\mathrm{C_I}\dot{\gamma}\left(\mathbf{I} - 3\mathbf{A}\right). \qquad (3)$$

In this equation, $\dot{\mathbf{A}}_2$ is the material derivative of the second-order orientation tensor. $\mathrm{C_I}$ is a phenomenological coefficient called the interaction coefficient which models the

randomization effect of interactions between particles. $\dot{\gamma} = (2\mathbf{D}:\mathbf{D})^{\frac{1}{2}}$ is the scalar magnitude of $\mathbf{D}$ typically known as the shear-rate in simple shear flows. The last term in this equation represents an isotropic rotary diffusion which models the effect of particle-particle interactions on the orientation. A consequence of adding this term to the orientation model is that the steady orientation state for large strains does not necessarily depict a perfect alignment.

It has been shown that the kinetics of orientation in materials with anisometric particles such as fibers or layered silicates is significantly slower than FT model predicts [179]. To overcome this problem and provide a better prediction for the experimental results, a simple strategy is to modify the right-hand side of equation (3) by some factor $k<1$ [87]

$$\dot{\mathbf{A}}_2 = k[\mathbf{W}\cdot\mathbf{A} - \mathbf{A}\cdot\mathbf{W} + \lambda\left(\mathbf{D}\cdot\mathbf{A} + \mathbf{A}\cdot\mathbf{D} - 2\mathbf{A}_4:\mathbf{D}\right) + 2C_I\dot{\gamma}\left(\mathbf{I} - 3\mathbf{A}\right)]. \quad (4)$$

In this model, the $1/k$ is often referred to as the *strain reduction factor*. The idea behind this model, known as the SRF model, was also proved by the work of Sepehr et al. [179] who proposed the slip coefficient k to empirically modify the FT model. They suggest that the shear strain applied on the fibers γ_s after time t is $\gamma_s = k\dot{\gamma}t$. For short fibers in a polypropylene (PP) matrix, they report slip coefficient values in the range of 0.33 to 0.38.

On a mesoscopic level, Rajabian et al. [168 - 170] developed a rheological model for ellipsoid particles in viscoelastic polymeric fluids by adding a dissipation function to the Jeffery's model. They described such dissipations as a function of the overall free energy with respect to the conformation tensors $\mathbf{\Phi}_{\mathbf{A}_2}$ and $\mathbf{\Phi}_{\mathbf{C}}$. The conformation tensors are further formulated utilizing two second-order symmetric structure tensors $\mathbf{A}_2$ and $\mathbf{C}$, i.e. the orientation tensor of the particles (the same as equation (2) by Advani and Tucker [5]) and the tensor describing the extension of polymer molecules, respectively. The evolutions of the components of these structure tensors with time is then given by

$$\dot{A}_{ij} = A_{ik}W_{kj} - W_{ik}A_{kj} + \lambda\left(A_{ik}D_{kj} + D_{ik}A_{kj} - 2D_{kl}A_{ijkl}\right) - \frac{2}{3}(D_{lm}D_{ml})^{\frac{1}{2}}\Lambda_p\left(A_{il}\Phi_{A_{lj}} + A_{lj}\Phi_{A_{il}}\right) + \frac{4}{9}(D_{lm}D_{ml})^{\frac{1}{2}}\Lambda_p A_{ij}\Phi_{A_{kk}}, \text{ and} \quad (5)$$

$$\dot{C}_{ij} = -C_{jk}W_{ik} - W_{jk}C_{ik} + C_{jk}D_{ik} + D_{jk}C_{ik} - \Lambda_m\left(C_{kj}\Phi_{C_{ik}} + C_{ik}\Phi_{C_{kj}}\right). \quad (6)$$

The components of the conformation tensors are

$$\Phi_{C_{ij}} = -\frac{k_BT}{2}\left[n_m C_{ij}^{-1} - \frac{n_m b}{1\text{-}trC}\delta_{ij} - B_{pm}(n_p n_m)^{\frac{1}{2}}\left(\delta_{ij} - A_{ij}\right)\right], \text{ and} \quad (7)$$

$$\Phi_{A_{ij}} = -\frac{k_BT}{2}\left[n_p A_{ij}^{-1} - B_{pm}(n_p n_m)^{\frac{1}{2}}\left(trC\,\delta_{ij} - C_{ij}\right) - 2B_{pp}n_p\left(\delta_{ij} - A_{ij}\right)\right]. \quad (8)$$

In these equations, $n_p = \frac{4\phi}{d^2 l}$ and $n_m = (1 - \phi)\frac{\rho N_0}{M_w}$ where ϕ, l and d are the volume fraction, length and diameter of the particles, respectively. M_w and ρ are the molecular weight and density of the polymer and N_0 is the Avogadro's number. B_{pm} and B_{pp} are phenomenological parameters determined by experiments which denote the interactions between particle-macromolecule and particle-particle pairs, respectively. Λ_p and Λ_m are the mobility parameters for the particles and macromolecules. The parameter b is defined by $b = \frac{2HR_0^2}{k_BT}$

where H is the spring constant and R_0 is the maximum spring length for the modelled polymer chains utilizing the finitely extensible nonlinear elastic (FENE) springs. Here, k_B is the Boltzmann's constant and T is the absolute temperature. In the evolution equations, the initial conditions are the equilibrium solutions obtained by solving $\Phi_{C_{ij}} = 0$ and $\Phi_{A_{ij}} = 0$. The governing equations of this mesoscopic model (MM) can be readily solved in the case of an imposed flow. Moreover, the model is adaptable to nano-sized particles considering the fact that the model addresses the particle-macromolecule interactions in both the free energy and mobility coefficients.

Although these models have proved to be efficient in the prediction of particle orientation, they cannot provide a detailed description of the system microstructure but only an average evaluation. Furthermore, the influence of aggregating and dispersing mechanisms on the formation of oriented structures (and vice versa) is not directly and dynamically included in these models. These limitations verify the importance of detailed computer simulations to study this field.

3.2 Simulation at the Mesoscale

Atomistic simulations of complex systems including polymeric materials provide a detailed picture of, for instance, the interactions between components and conformational dynamics. Such information is often missing in macroscale models. On the other hand, the description of hydrodynamic behavior is relatively straightforward to handle in macroscale methods while it is difficult and expensive to treat in atomistic models. Between the domains of these scale ranges, there is the intermediate mesoscopic scale which extends the time scale of atomistic methods. Simulating the wide range of time scales in a single atomistic model needs large-scale computational resources. Consequently, the various mesoscale methods are developed to link atomistic and macroscale techniques and compensate for their shortcomings. DPD is one such mesoscopic method which enables taking into account the influence of hydrodynamics on the morphology developments in PNCs. Here, the details of DPD are further discussed due to its indispensable role in this research.

DPD is a relatively new mesoscopic particle simulation method proposed by Hoogerbrugge and Koelman in 1992 [142]. In its core, DPD is similar to MD except that the individual DPD particles, i.e. beads, represent the collective dynamic behavior of several molecules. This coarse-graining approach as well as softer interaction potentials between DPD beads allow for the simulation of dynamic phenomena over longer time scales [72, 79].

Benefiting from this advantage, Kim et al. [99] incorporated DPD in order to investigate the conformational behavior of a pH-responsive polymer and its effect on the permeability in PLNs. By the implementation of plane Couette flow with the Lees-Edwards periodic boundary conditions into DPD, the method has been widely used as the standard virtual rheometer in particle simulations to obtain steady-state shear properties. It has been utilized in many works to study the rheology of different systems including polymer solutions [230], surfactant solutions [124], entangled polymer melts [222], and suspensions [15, 28, 56, 146]. While the method has proved promising in many systems, it still suffers from the intrinsic instabilities at very low or very high shear-rates and needs further improvements [56, 124].

The rheology of dispersed particles in solutions or polymer melts has already been treated with DPD [15, 28, 146, 211]. The presence of non-spherical solid particles with complex geometries in the matrix usually leads to more difficult and time-consuming calculations. A common method to overcome such problems, the freezing technique, has been employed in several works [28]. In the freezing technique, a large solid particle is constructed out of smaller spherical particles by aggregating them as a rigid entity. While this approach has been shown to entail significant savings in computational costs, it loses an important physical characteristic of non-spherical particles with high aspect ratios, i.e. semiflexibility and bending of the particles.

In standard DPD, each bead is subject to the sum of three central, pairwise, additive forces. For bead i with the mass m_i and position vector $\mathbf{r}_i$, the Newton's equation of motion becomes

$$\mathrm{m}_i \frac{\mathrm{d}^2\mathbf{r}_i}{\mathrm{dt}^2} = \sum_j \left(\mathrm{F}_{ij}^{\mathrm{C}} + \mathrm{F}_{ij}^{\mathrm{D}} + \mathrm{F}_{ij}^{\mathrm{R}}\right), \qquad (9)$$

in which $\mathrm{F}_{ij}^{\mathrm{C}}$, $\mathrm{F}_{ij}^{\mathrm{D}}$, and $\mathrm{F}_{ij}^{\mathrm{R}}$ are respectively the conservative, the dissipative, and the random forces between bead i and its neighboring beads within a certain force cutoff radius r_{cut}. These forces are defined as [79]

$$\mathrm{F}_{ij}^{\mathrm{C}} = \mathbb{A}_{ij}\chi_{ij}\left(1-\frac{\mathrm{r}_{ij}}{r_{cut}}\right)\hat{\mathbf{r}}_{ij}, \qquad (10)$$

$$\mathrm{F}_{ij}^{\mathrm{D}} = -\xi_{ij}\omega^{\mathrm{D}}(\mathrm{r}_{ij})\mathrm{r}_{ij}\left[(\mathbf{v}_i-\mathbf{v}_j)\cdot\hat{\mathbf{r}}_{ij}\right]\hat{\mathbf{r}}_{ij}, \qquad (11)$$

$$\mathrm{F}_{ij}^{\mathrm{R}} = \sigma_{ij}\omega^{\mathrm{R}}(\mathrm{r}_{ij})\mathrm{r}_{ij}\zeta_{ij}\hat{\mathbf{r}}_{ij}. \qquad (12)$$

Here, r_{ij} is the distance between the beads i and j, $\hat{\mathbf{r}}_{ij}$ is the unit vector pointing from the center of bead j to that of bead i, χ_{ij} equals 1 for beads with a distance less than r_{cut} and equals 0 otherwise. $\mathbf{v}_i$ and $\mathbf{v}_j$ are the velocity vectors of the ith and jth beads, respectively. ζ_{ij} is a Gaussian random number with zero mean and unit variance. $\mathbb{A}_{ij}$ is the maximum repulsion between bead i and bead j. ξ_{ij} and σ_{ij} are the friction coefficient and the noise amplitude between bead i and bead j, respectively. $\omega^{\mathrm{D}}(\mathrm{r}_{ij})$ and $\omega^{\mathrm{R}}(\mathrm{r}_{ij})$ are dissipative and random weight functions, respectively. DPD simulations often obey the fluctuation-dissipation theorem in which one of the two weight functions fixes the other one [141]. This theory dictates that the random and dissipative terms must be administered in a particular way in order to maintain the correct Boltzmann distribution in equilibrium. As a consequent of this theory, one has

$$\omega^{\mathrm{D}}(\mathrm{r}_{ij}) = \left[\omega^{\mathrm{R}}(\mathrm{r}_{ij})\right]^2, \qquad (13)$$

$$\sigma_{ij}{}^2 = 2\xi_{ij}\mathrm{k}_B\mathrm{T}. \qquad (14)$$

These relationships ensure an equilibrium distribution of bead velocities for thermodynamic equilibrium. In many studies, the weight functions are

$$\omega^{\mathrm{D}}(\mathrm{r}_{ij}) = \left[\omega^{\mathrm{R}}(\mathrm{r}_{ij})\right]^2 = \chi_{ij}\left(1-\frac{\mathrm{r}_{ij}}{r_{cut}}\right)^2. \qquad (15)$$

Due to the pairwise nature of the forces involved in DPD framework, all of the beads obey Newton's third law [80]. As a result, the sum of all forces in the system vanishes. Furthermore, any given volume of beads in the system is only accelerated by the sum of all forces that cross its boundaries. This is the fundamental assumption which results in the Navier-Stocks equations. Consequently, DPD formulation conserves hydrodynamics [78 - 80].

At every time step during the simulation, the set of positions and velocities of the beads is updated utilizing the positions and velocities at the earlier time. In principle, all algebraic update algorithms from MD can be used in DPD. However, the dependence of forces on velocity in DPD complicates the algorithm. A common approach to solve this problem is to use a modified version of the velocity-Verlet algorithm [79, 209, 210]. For bead i with unit mass and the overall force $\mathbf{f}_i$ over a short interval of time Δt, the algorithm suggests

$$\mathbf{r}_i(t+\Delta t) \approx \mathbf{r}_i(t) + \mathbf{v}_i(t)\,\Delta t + \tfrac{1}{2}\mathbf{f}_i(t)(\Delta t)^2, \qquad (16)$$

$$\tilde{\mathbf{v}}_i(t+\Delta t) \approx \mathbf{v}_i(t) + \lambda\,\mathbf{f}_i(t)\,\Delta t, \qquad (17)$$

$$\mathbf{f}_i(t+\Delta t) \approx \mathbf{f}_i\big(\mathbf{r}_i(t+\Delta t), \tilde{\mathbf{v}}_i(t+\Delta t)\big), \qquad (18)$$

$$\mathbf{v}_i(t+\Delta t) \approx \mathbf{v}_i(t) + \tfrac{1}{2}\Delta t\,(\mathbf{f}_i(t) + \mathbf{f}_i(t+\Delta t)). \qquad (19)$$

In this algorithm, the velocity in the next time step is first estimated by a predictor method, i.e. $\tilde{\mathbf{v}}_i(t+\Delta t)$, and then corrected in the last step, i.e. $\mathbf{v}_i(t+\Delta t)$. If the forces were independent of velocity, the actual velocity-Verlet algorithm would be recovered for $\lambda = 0.5$. The parameter λ has been shown to affect the temperature in DPD simulations by Den Otter and Clarke [43]. Based on empirical observations, some authors suggest $\lambda = 0.65$ would yield an accurate temperature control probably due to the cancellation of errors [80].

Recently, some modifications for standard DPD formulation have been proposed. Pan et al. [146] developed a new formulation of DPD in the spirit of fluid particle model in such a way that the dissipative forces were explicitly divided into central and shear components. It allowed them to redistribute and balance these forces to obtain the correct hydrodynamics in the study of Brownian colloidal suspensions. In order to capture the physics of entangled polymer melts, Yamanoi et al. [222] used entanglement forces instead of conservative forces and were able to reproduce both static and dynamic properties of linear polymer systems. Despite these attempts, the standard DPD has also shown that it is quite capable of simulating complex systems such as compatibilized and uncompatibilized PLNs under shear flows [76, 77]. Various polymeric systems have been successfully treated in the DPD framework such as blood rheology [57, 231], rheology of ultrahigh molecular weight polymers [65], lipid bilayers [68], adsorption characteristics of confined PE glycols dissolved in water [70], structure of thermoset polymers near an alumina substrate [91, 92], graphene structure [97], surfactant aggregation [111], photo degradation process of polymer coatings [120], distribution of nanoparticles in lamellar and hexagonal diblock copolymer matrices [121, 154], and electrical percolation threshold in packed assemblies of oriented fiber suspensions [167].

4. Multiscale Strategies

The ultimate purpose of a multiscale modelling is to predict the macroscopic behavior from the first principles at the quantum scale. Finding appropriate protocols for multiscale simulations is on the other hand a very challenging topic. This is due to the fact that polymeric materials often exhibit phenomena on one scale that require a precise description of other phenomena on another scale. Since none of the methods at individual scales would suffice alone to describe an entire multiscale system nor they are designed for such a purpose, the goal becomes to develop a proper combination of various methods specialized at different scales in a multiscale scheme.

In general, there are three main categories of multiscale approaches: sequential, concurrent, and adaptive resolution schemes. The sequential approach links a hierarchy of computational methods in which the operative methods at a larger scale utilize the coarse-grained (CG) representations with information obtained from more detailed, smaller scale methods. Sequential approaches have also been referred to as serial, implicit, or message-passing methods. The second category of multiscale methods, the concurrent approaches, attempt to link methods appropriate at each scale together in a combined model, where the different scales of the system are considered concurrently and communicate with some type of handshaking procedure. Concurrent methods are also called parallel or explicit approaches. It is noteworthy that multiscale simulations could principally utilize a hybrid scheme based on elements from both sequential and concurrent approaches. More recently, a new concept for multiscale simulations has been developed which resembles some characteristics of concurrent methods. In this approach, single atoms or molecules can freely move in the simulation domain and switch smoothly from one resolution to another, for instance based on their spatial coordinates, within the same simulation run. Consequently, these methods are generally referred to as the adaptive resolution simulations. Details of such techniques are provided in the following sections.

Finally, it should be noted that there are a number of advanced techniques which allow to extend the reach of a single-scale technique such as MD within certain conditions. Such methods are also reviewed briefly for the sake of completeness.

4.1 Sequential Multiscale Approaches

In sequential approaches, calculations are often performed at a smaller (finer) scale and the resulting data are passed to a model at a larger (coarser) scale after leaving out unnecessary details for instance by coarse-graining. In some cases the reverse procedure can also be done. A sequential multiscale model requires a complete knowledge of the fundamental processes involved at the finest scale to yield accurate information. Afterwards, it is also necessary to have a reliable strategy to introduce this information into the coarser scales. Such a strategy is often achieved by utilizing phenomenological theories which contain a few key parameters. These parameters are then used as the linking bridges between the scales when their values are determined from the calculated data of the finer scale simulations. This message-passing approach can be performed in sequence for multiple scales. It is obvious that in this sequential approach the accuracy of the simulations at the coarser scale

critically depends on the accuracy of the information from the finer scale simulations. Furthermore, the model at the coarser scale must be accurate itself so that it can provide reliable results. In this strategy, the relations between the scales must be invertible so that the results of the coarser scale simulations can be used to suggest the best choice for the finer scale parameters.

The sequential approach has generally proved effective in systems where the different scales are weakly coupled. Therefore, appropriate systems for such a methodology often share a common character by which the large-scale variations appear homogeneous and quasi-static from the small-scale perspective. The majority of the multiscale simulations that have been actually incorporated in materials research are in fact sequential. In order to highlight the sequential message-passing in a range of polymeric systems, a few examples are outlined here.

To predict the morphology and mechanical properties of mixtures of diblock copolymers and rod-like nanoparticles, Shou et al. [183] coupled the self-consistent field theory with DFT to provide input information for the lattice spring model (LSM). In their sequential algorithm, the spatial morphology of different phases is mapped onto the coarser-scale lattice and the force constants are derived for the three-dimensional network of springs. In similar approaches, other methods including LB [203], MC [232], and MD [188, 207], have also been used to produce appropriate morphological information for LSM in various systems including polymer blends and nanocomposite coatings. Recently, the classical fluids density functional theory was linked to MD simulations by Brown et al. [20] to study microphase separated states of both typical diblock and tapered diblock copolymers. The fluids density functional theory can predict the equilibrium density profiles of polymeric systems. The authors used the resulting density profiles of this theory to initialize MD simulations with a close to equilibrated structure and could speed up the simulations. In a study on the influence of self-assembly on the mechanical and electrical properties of PNCs, Buxton and Balazs [22, 23] used a combination of Cahn-Hillard theory and BD at the finer scale to produce morphological data. The data were later fed either into LSM in order to determine the mechanical properties, or into FDM to calculate the electrical conductivity.

A number of studies have been devoted to characterize PLNs at different scales, spanning from quantum mechanical scale up to the macroscale. One such algorithm was developed by Suter et al. [198] starting at the parameter-free density functional level of quantum theory, transferring key data through atomistic classical MD to a CG representation. This sequential procedure allowed for the study of the intercalation of molten polymers, poly(ethylene glycol) and poly(vinyl alcohol), within MMT tactoids and the subsequent larger scale assembly of these bridged tactoids, see Figure 3. In a separate study, Scocchi et al. [176] used a multiscale method to evaluate rescaled self and mixed DPD energies from binding and nonbinding energies of MD simulations. In this manner, they were able to reproduce the maximum repulsion parameters for DPD simulations of polyamide (PA)/clay and PP/clay nanocomposites and reproduce experimentally observed microstructures. The same methodology was also applied in following works and was extended into the macroscale realm by linking to FEM in order to derive mechanical properties of PLNs as a function of the degree of exfoliation [150, 177].

The most common serial transfer of information from a finer scale method to a coarser one can be envisioned in the systematic development of CG models of polymer systems. The CG models are often designed to reproduce the configurations of more detailed descriptions in atomistic simulations as accurately as possible. In this way, a CG model with much less degrees of freedom is achieved which can access longer time scales appropriate for instance in dynamics simulations. It is worthy to note that the final conformations of such CG simulations could be translated back to its atomistic details based on a specific backmapping algorithm. These sequential procedures represent general characteristics of sequential multiscale approaches and could also be extended to more complex systems.

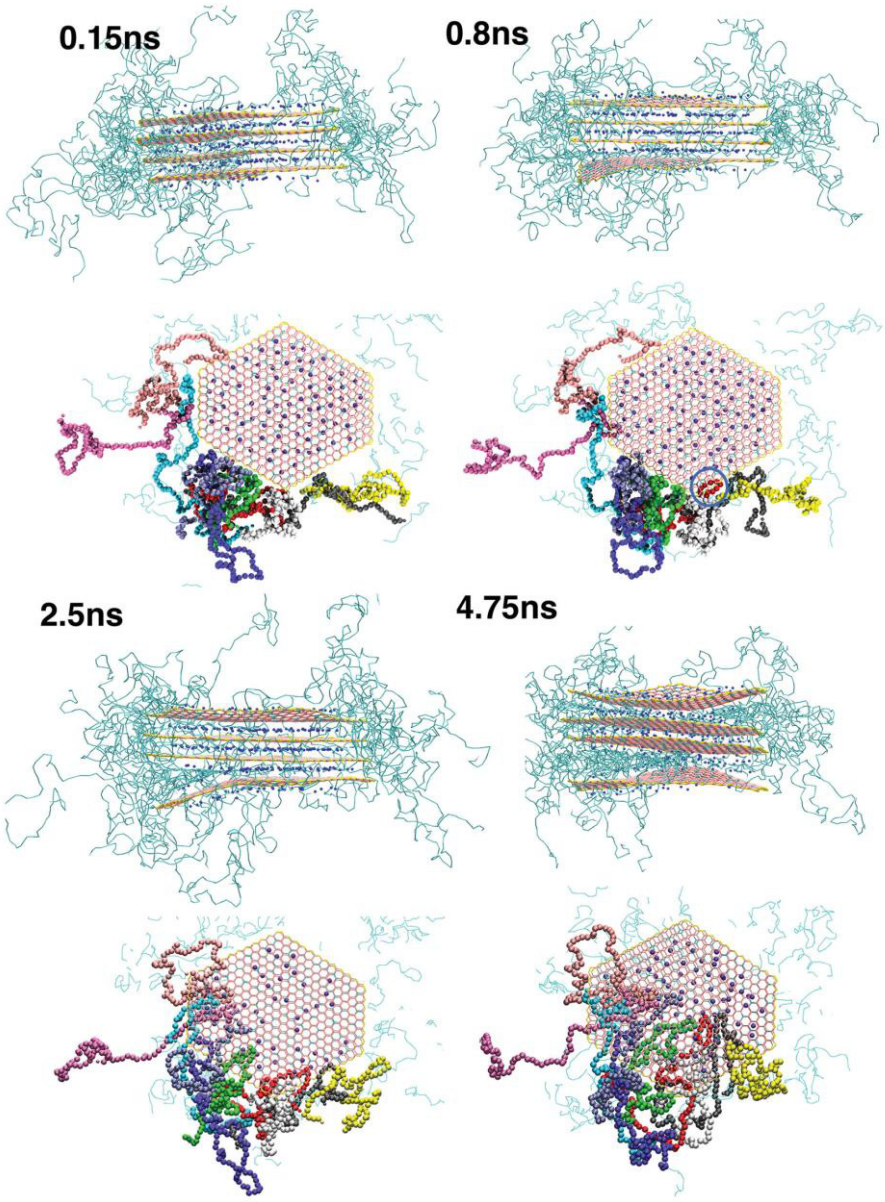

Figure 3: Pictorial overview of the intercalation of poly(vinyl alcohol) chains into a clay tactoid. The side and top views of the tactoids are illustrated at relevant snapshots, for the simulation times shown. In the side views, the macromolecules are represented by the green bonds; for the clay CG particles the colors are: neutral clay is pink, charged clay is cyan, edge clay is yellow, and sodium is blue.

For each time frame, the side view illustrates the bending that the lowermost clay sheet undergoes to accommodate the intercalating poly(vinyl alcohol) chain. For the top view, the polymers that intercalate into the spacing between the lowermost sheets are colored according to their molecule number, such that they can be differentiated during visualization. It is observed that the polymer initially starts intercalating as short loops (an example is circled in blue at the 0.8 ns snapshot), and progresses further into the interlayer and forms a relatively linear chain on the clay surface. Reprinted from Suter et al. [198] under the terms of the Creative Commons Attribution License.

4.1.1 Systematic Coarse-Graining Methods

A serious problem with polymeric materials in a sequential multiscale scheme is that the coarse-graining method from atomistic scale to mesoscale or from mesoscale to macroscale is not a straightforward procedure. The coarsening from QM to MD follows basic principles which can be formulated in a computational framework while it is system-specific at higher scales. All approaches are based on the application of a force field that transforms information from quantum scale to atomistic simulations. From atomistic simulations to mesoscale model, essential features of the system such as the structure and/or thermodynamics have to be maintained while reducing the degrees of freedom. The linking of scales through the mesoscale is addressed by many authors as the most challenging step towards developing reliable multiscale frameworks. Systematic coarse-graining methods are therefore developed to address these challenges.

Systematic coarse-graining methods attempt to extend the length and time scales of atomistic MD simulations by replacing several atoms with a single super atom and thus reducing the degrees of freedom. These approaches strictly attempt to preserve intrinsic properties of polymers such as radius of gyration, diffusion coefficient, etc. As a consequence, the results of such CG models can be directly compared with experiments. Depending on how many atoms are lumped into a single super atom, i.e. the degree of coarse-graining, the systemic coarse-graining methods can be roughly divided into three major blocks; (i) low coarse-graining degrees where one or two monomers are coarse-grained into one super atom, for instance, in an iterative Boltzmann inversion (IBI) scheme, (ii) medium coarse-graining degrees where ten to twenty monomers are coarse-grained into one blob or bead, for instance, used in the so-called "blob model", and (iii) high coarse-graining degrees where the whole chain is mapped to a single soft colloid in super coarse-graining methods. These variations provide access to a range of length/time scales from 10^{-6} s/10^{-6} m to 10^{-2} s/10^{-2} m, particularly precious to simulate dynamic properties of polymeric systems [117]. In addition to the reduced number of degrees of freedom, CG models often benefit from simpler forms of interactions compared with the detailed models. This feature can promote the computational efficiency to a large extend. Besides, the free energy profiles of CG models are usually smoother due to the fact that many interaction centers are replaced with only a single site. Finally, the parametrization of the CG interactions is simpler than that of full atomistic systems since many chemistry-specific details are ignored during coarse-graining. Such features of CG models make them particularly appealing for many applications in polymer systems.

4.1.2 Reverse Mapping

While the coarse-graining procedure helps accessing longer time scales in simulations, it also removes detailed atomistic features necessary for precise evaluations of the structure. Since CG models have proved extremely useful in various simulations, such as generating equilibrated structures for further analysis and simulation runs [147, 174, 187, 192], there is a general tendency towards employing them upon possibility. Consequently, a reverse mapping is also needed to reproduce atomistic details such as chemical characteristics from the CG model. The reverse mapping procedure is also referred to as fine-graining or backmapping in the literature [25, 29].

Early attempts for reverse mapping are dated back to Tschöp et al. [204] and Kotelyanskii et al. [104]. In general, a reverse mapping operation includes (i) the reconstruction of CG particles with possible atomistic structures from a bank of templates, followed by (ii) performing energy minimization (EM), MD, or MC simulations to guarantee collectively and locally relaxed atomistic structures. In the first step, the fitting templates are often extracted from a preceding atomistic equilibrium simulation. The chosen template for a given CG particle should not only fit the contour of the underlying CG molecule, but also allow the best superposition for the neighborhood CG particles. In order to achieve a high backmapping efficiency, the fitting procedure is usually based only on geometrical criteria and no force and energy calculations are involved. In some cases where the CG particle represents a complex structure with bulky side groups, one must be careful to avoid interlocking of side groups [174]. In the second step, it is necessary to run post-processing calculations due to the fact that the CG force field is derived from average atomic distributions and therefore may easily lead to overlapping structures [84]. Such artefacts could happen more frequently in coarser CG models.

Several backmapping algorithms have been proposed for different polymers in the literature [85, 96, 165, 174, 204, 219]. Often, when the CG model is tailored on the atomistic contour using atomistic distributions to build up the CG force field, the zoom-in back to the atomistic description is a simple geometrical problem [96]. However, a more sophisticated procedure must be followed in some cases where the model is particularly coarse or the CG particles contain asymmetric atoms and the polymer chain has a specific tacticity [174, 219]. An example for the first case was given by Karimi-Varzaneh et al. [96] who used a simple backmapping algorithm to reinsert the atomistic details of a PA-66 in its corresponding CG model. As for the latter, Wu [219] utilized a special backmapping procedure to capture tacticity effects on the structure and dynamics of PMMA melts. Moreover, a general backmapping technique to prepare equilibrated polymer melts was proposed by Carbone et al. [25] which consists of (i) the generation of continuum random walks characterized by different Kuhn lengths and (ii) the insertion of the atomistic units on the parent random walk chains. The steps of this approach for PA-66 is shown in Figure 4. The authors showed that melts of PE, atactic PS and PA-66 are well-equilibrated with this technique and their long and short range structural properties can be successfully compared with previous all-atomistic (AA) simulation and experimental data. Some cases with special reverse mapping algorithms are also found in literature. For instance, in order to generate realistic amorphous polymer surfaces, Handgraaf et al. [82] developed a special mapper which takes the CG structure as

input and uses the MC technique to generate the atomistic structure. The mapped atomistic structure is later equilibrated by performing a short MD simulation.

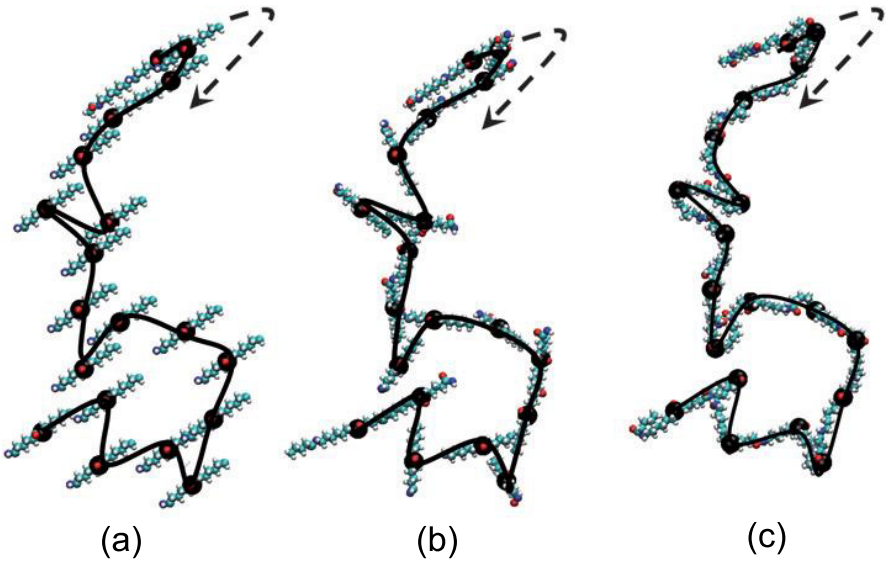

Figure 4: Steps of the reverse-mapping procedure for the case of PA-66: (a) insertion of the atomistic fragments (colored beads) on the parent random walk (solid black line); (b) orientation of the atomistic fragments; (c) final configuration of the rebuilt atomistic model. The arrow indicates the direction of the growing chain. Reproduced from Carbone et al. [25] with permission of The Royal Society of Chemistry.

It should be noted here that the reverse mapping of a nonequilibrium CG system differs from an equilibrium run to some extent. Since molecular deformations are recorded in the CG model during the nonequilibrium simulations, a proper backmapping procedure should translate these deformations into the atomistic model. Furthermore, the deformation energy stored in the polymer chain of the CG model should be passed to the atomistic level. Obviously, a simple backmapping cannot meet these requirements since during the post-processing step, i.e. EM or MD or MC simulations, the energetically unstable deformed structure relaxes quickly. A backmapping method was proposed by Chen et al. [29] to overcome this problem for polymer models under sheared nonequilibrium conditions. Their methodology mixes the general concepts of backmapping with the new idea of applying position restraints to preserve the deformed configurations. In order to retain the globally stretched configuration from the CG simulation, position restraints with a harmonic potential are applied to all those atoms which coincide with locations of CG particles. The globally deformed structure is allowed to relax locally through a molecular mechanics approach [14]. By changing the position restraint scheme and re-optimizing the structure through an iterative procedure, it is possible to minimize the isolation of segments from the rest of the chain. The workflow of the backmapping procedure of Chen et al. [29] is illustrated in Figure 5.

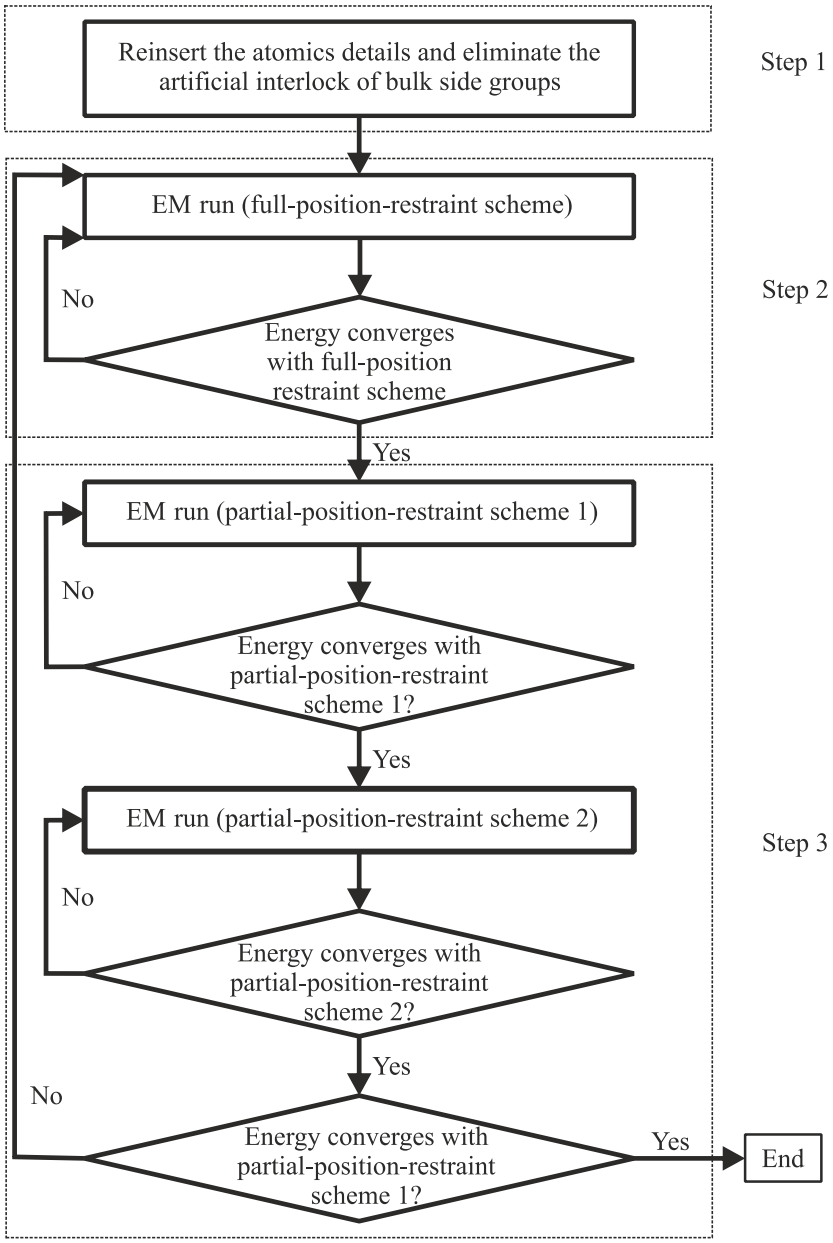

Figure 5: The workflow of the backmapping procedure of CG sheared nonequilibrium models as proposed by Chen et al. [29]. Notice that schemes 1 and 2 in step 3 are two variants of the main scheme in step 2 in order to minimize the isolation of segments from the rest of the chain. Reproduced from Chen et al. [29] with permission of the PCCP Owner Societies.

Finally, the validity of a reverse-mapped atomistic structure is often tested by comparing relevant structural information obtained from atomistic simulations run after the reinsertion of the atoms with the original atomistic simulations used to develop the CG force field [25, 69, 96]. Radial distribution function of a specific chemical group, bond and angle distributions, torsion angle distribution, and the number of hydrogen bonds are mostly used for such comparisons. In some studies, the results of a reverse-mapped atomistic simulation are also directly compared with the available experimental data [25].

4.2 Concurrent Multiscale Approaches

The concurrent approaches define the system under consideration through a genius combination of several methods and solve them simultaneously instead of a hierarchical procedure as in sequential approaches. The resolution of the solution is adapted to provide an accurate representation of those regions of the system which are of particular interest. A common field of application for such strategies is the analysis of crack propagation in materials. During the crack propagation the immediate neighborhood of the crack tip, where the bond breaking is taking place, demands a higher precision in the models representation whereas a coarser model could suffice for further away from this region. An example of the concurrent methodology used in the crack analysis is shown in Figure 6. In this multiscale simulation, the concurrent approach combines tight binding (TB), MD, and FEM techniques to study crack propagation in silicon [3]. The vicinity of the crack should be simulated at a finer resolution since it exhibits significant nonlinearity. Therefore, atomistic MD method could provide a more precise representation of the crack surrounding whereas FEM can still accurately describe the rest of the system further away from the crack. The treatment of formation and the breaking of covalent bonds at the atomic scale is not reliable with any empirical potential, since bonds between atoms are essentially quantum mechanical phenomena arising from the sharing of valence electrons [196]. Consequently, it is necessary to include a TB approach in the simulations of a small region in the immediate neighborhood of the crack tip, where bond breaking is prevalent during fracture, whereas further away from this region the empirical potential description of MD is adequate.

The concurrent approach is best suitable for the systems with an inherent multiscale character. In such systems, the behavior at each scale depends strongly on the phenomena at other scales. Moreover, this approach can be of a more general nature due to the fact that it does not often rely on any system-specific assumptions such as a particular coarse-graining model. Therefore, a well-defined concurrent model can be applied to many different systems within the limits of common phenomena involved as long as it incorporates all the relevant features at each level. In contrast to sequential methods, concurrent models are not usually constructed based on a detailed prior knowledge of the physical quantities and processes involved. As a result, such models are particularly useful when dealing with new emerging problems about which little is known, for instance, at the atomistic level and its connection to larger scales. However, the coupling between the different regions treated by different methods is a critical challenge remaining in the core of concurrent approaches. A successful multiscale model seeks a smooth coupling between these regions. Here, I address some of the concepts and strategies developed in the concurrent framework.

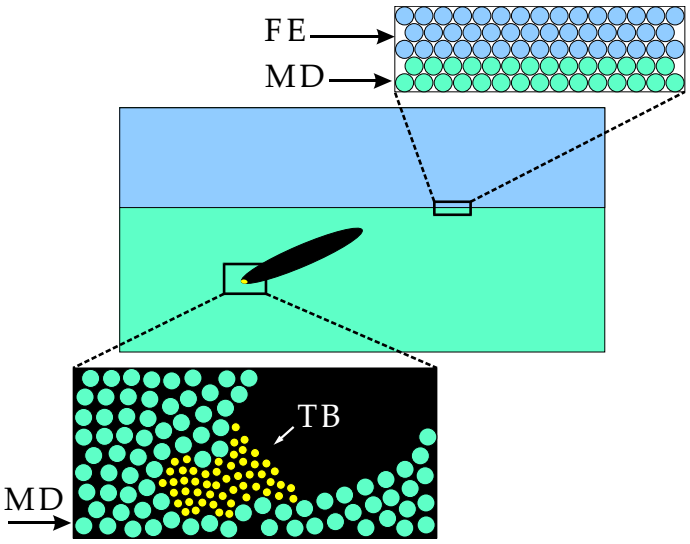

Figure 6: A hybrid FEM/MD/TB simulation. The FEM, MD, and TB approaches compute forces on particles (either FEM nodes or atoms) in their respective domains of application. The simulation then uses these forces in a time-stepping algorithm to update the positions and velocities of the particles.

4.2.1 The Concept of Handshaking

In concurrent simulations, often two distinct domains with different scales are linked together benefitting from a region called the "handshake" region. The handshake region generally bridges the atomistic and continuum domains of the multiscale model [132, 173]. However, there are studies where it has been used to link quantum mechanical TB calculations to atomistic domains [19, 132] or atomistic MD models to their equivalent CG descriptions [173].

The handshake region transfers information from one domain to the other and thus provides the possibility to overlap, usually, atomistic and continuum domains. The overlap is defined with a field variable, normally the potential energy, taking the form of a weighted combination of the magnitude of the same variable in the continuum and atomistic domains. The weight is normally a function that decreases monotonically from unity to zero through the overlap so that variable starts with a value equal to the same variable in one domain and gradually takes on the value of the same variable in the other domain. The form of the weighting function is arbitrary rather than an outcome of the formulation. Consequently, the modelling quality of the handshake region is strongly dependent on a smooth and gradual transition of field variables from one domain to the other domain. In the handshake algorithm, it is assumed that the properties of each domain are independent from one another. Due to this assumption, one has to be concerned particularly whether or not the material properties of both domains are truly equivalent. In addition, physical complications in the handshake region might necessitate more complex algorithms to obtain a precise representation of it. For instance, nodal displacements of the continuum domain should be influenced by the displacements of molecules inside the neighboring atomistic domain if the node and the molecules are within the cutoff distance of the molecular interactions.

The handshaking approach has been applied to combine TB/MD/FEM in order to study crack propagation and crystal impact in silicon [19, 132]. A combination of TB/MD/FEM has also been utilized in a handshaking framework to characterize submicron micro-electro-mechanical systems by Rudd et al. [173]. Based on the works of Abraham et al. [2, 19] the unifying theme for such a multiscale model is the total Hamiltonian H_{tot} defined throughout the entire system. This Hamiltonian is a function of the atomic positions $\mathbf{r}_j$ and their velocities $\mathbf{v}_j$ in the TB and MD regions for all j atoms, and the displacements $\mathbf{u}_\alpha$ and their time rates of change $\dot{\mathbf{u}}_\alpha$ in the finite element (FE) regions for all α nodes. Within this framework, it is the Hamiltonian that is partitioned into FE, MD, TB and handshaking contributions from FE/MD and MD/TB during the domain decomposition. It is assumed that the atomic and nodal displacements do not necessarily fall into a unique domain, but their interactions do. In this way, H_{tot} may be written as

$$\begin{aligned}\mathrm{H}_{tot} &= \mathrm{H}_{FE}(\mathbf{u}_\alpha,\dot{\mathbf{u}}_\alpha) + \mathrm{H}_{FE/MD}\left(\mathbf{r}_j,\mathbf{v}_j,\mathbf{u}_\alpha,\dot{\mathbf{u}}_\alpha\right) \\ &+ \mathrm{H}_{MD}\left(\mathbf{r}_j,\mathbf{v}_j\right) + \mathrm{H}_{MD/TB}\left(\mathbf{r}_j,\mathbf{v}_j\right) + \mathrm{H}_{TB}\left(\mathbf{r}_j,\mathbf{v}_j\right),\end{aligned} \qquad (20)$$

with the Hamiltonian of different contributions depicted with appropriate indices. Rudd et al. [173] explain that the FE/MD as well as MD/TB handshakes must successfully address the basic issues of (i) matching the degrees of freedom and (ii) defining consistent forces at the corresponding interfaces. Despite this similarity, it should be emphasized that each handshake obliges a somewhat different approach in order to answer the requirements. This is due to the fact that the MD/TB handshake takes place across an interface consisting of atoms whereas the interface at the FE/MD handshake is between planes of atoms [173]. Equations of motion for all the relevant degrees of freedom are obtained by taking the appropriate derivatives of this Hamiltonian in a standard Euler-Lagrange procedure. The time evolution of all the variables then marches forward in lock-step using the same integrator. Thus, the entire time history of the system may be obtained numerically given an appropriate set of initial conditions. Further information can be obtained from the work of Rudd et al. [173].

4.2.2 Linking Atomistic and Continuum Models

It is frequently observed in large-scale atomistic simulations that only a small subset of atoms actively participate in the evolving phenomenon. This allows for the majority of atoms to be effectively represented by continuum models. Hence, a considerable reduction of computation and storage resources is guaranteed if only novel multiscale approaches could reduce the number of degrees of freedom in atomistic simulations. Various concurrent multiscale modelling methods were developed in the last twenty years which couple atomistic simulations such as MD with continuum simulations such as FEM. Detailed comparative reviews of such approaches can be found in references [34, 126]. The idea behind these methods, not unlike all multiscale strategies, is to focus the available computation power where it is needed by applying atomistic simulations, whereas an approximate solution is provided for the rest of the system by continuum simulations. Therefore, both atomistic details as well as the macroscopic properties of materials can be

obtained simultaneously from these simulations. Such models are mostly designed for crystalline materials such as metals or carbon nanomaterials. Unfortunately, their application in polymeric materials is still limited, possibly due to the unfamiliarity of these models to polymer researchers. It is noteworthy that some authors have referred to such methods in recent reports on polymer simulations [98, 117].

Certain categories of problems such as fracture and nanoindentation possess the characteristics of localized deformation where it is possible to address the system by a dual-domain or partitioned-domain approach; one with an atomistic description B^A, and the other with continuum approximation B^C. The two domains are linked by an interfacial region B^I across which compatibility and equilibrium are enforced. An important distinction among various methods is the way they treat the interfacial region. Most methods adopt one of the strategies depicted in Figure 7. The interfacial region is shown by the dashed lines. In part (a) of the figure, B^I has been further subdivided into two parts: (i) the handshake region B^H, and (ii) the padding region B^P. As explained before, the handshake region provides a mixing between the two scales. The padding region is continuum in nature and provides the boundary conditions to the atoms in B^A and B^H with a certain range of atomistic interactions, r_{cut}. The thickness of this region depends on r_{cut} and the motions of atoms in B^P are determined from the continuum displacement fields at the position of the padding atoms, in different ways for different methods. It is also possible to eliminate the handshake region as shown in part (b) of Figure 7. Most models that do not include a handshake region require a direct atom-node correspondence along the edge of the FE region to impose the displacement compatibility across the interface. This necessitates that the mesh is refined down to the atomic scale on the continuum side of the interface and hence introduces difficulties in mesh generation.

The coupling between the B^A and B^C regions requires compatibility conditions in each direction. This means providing some prescription for finding the displacements of atoms in B^P, from the nodal displacement information in B^C, as well as a way to determine the displacement boundary conditions for the B^C nodes along the edge of the mesh closest to the B^A. Compatibility can be imposed in a strong or weak sense. Strong compatibility is imposed by the continuum on the atoms when the padding atoms move in the same as the finite elements in which they reside. In the other direction, the strong compatibility is imposed by the atomistic region on the continuum by defining a subset of nodes that coincide with some of the atoms in B^A. The displacement boundary condition is therefore imposed on B^C with the motion of the overlaying atoms from B^A. In the weak compatibility, displacement boundary conditions are enforced only in some average sense, or with some type of penalty method approach. Strong compatibility introduces complexity in mesh generation near the interface while it also yields relatively more accurate results [126].

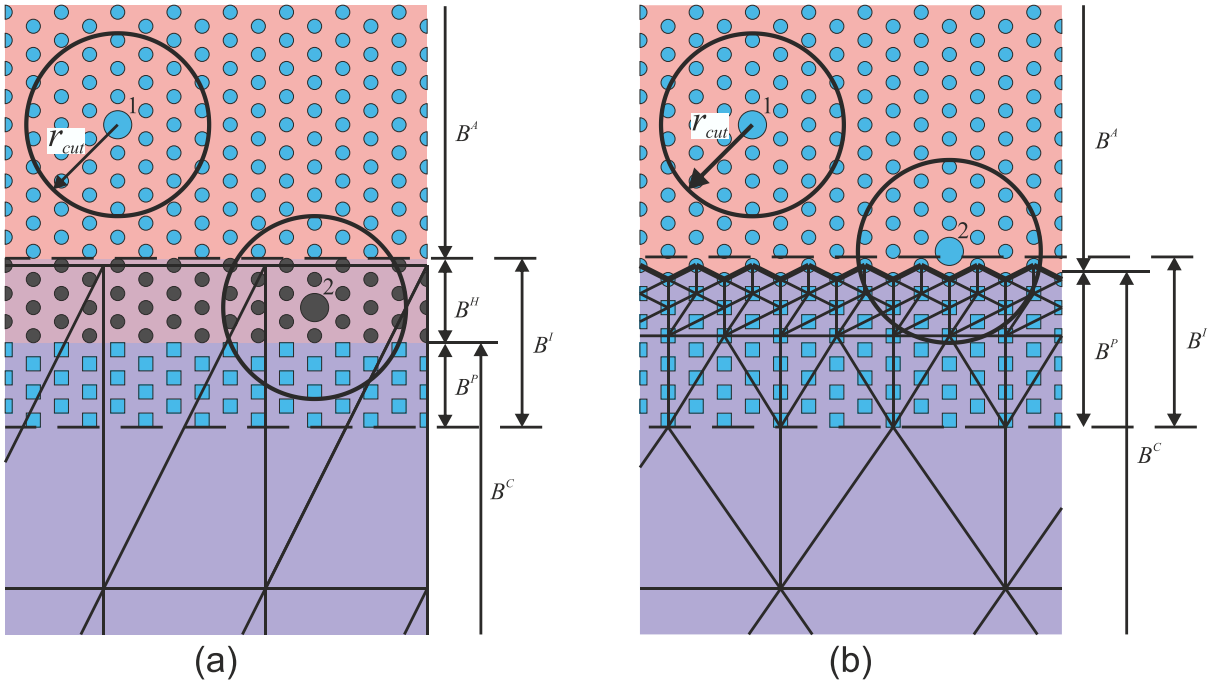

Figure 7: A generic interface in a coupled atomistic/continuum problem. The finite cutoff radius of the atoms means that an atom like 1 cannot 'see' into the continuum, while atom 2 can. Thus there is the need for a 'padding' region as discussed in the text. The model on the left includes a handshake region, B^H , while the model on the right does not. Padding atoms are shown as blue squares, handshake atoms as black circles and regular atoms as blue circles.

The simulation algorithm often finds the equilibrium by either minimizing an energy functional or driving the set of forces on all degrees of freedom to zero. Consequently, there are two major categories of the governing formulation i.e. the energy-based and the force-based approaches. The disadvantage of the energy-based approach is that it is extremely difficult to eliminate the non-physical side effects of the coupled energy functional. This problem, often referred to as the "ghost forces", stems from trying to combine two energy functionals from different models into a single coupled energy expression [10, 126, 181]. The force-based approaches, on the other hand, have no well-defined total energy functional and are considered to be non-conservative in general. These approaches can be numerically slow and unstable and could converge to unstable equilibrium states. However, force-based methods can eliminate the ghost forces due to access to the direct definition of the forces.

Several methods are proposed in literature to correct the ghost forces artifact in energy-based models. These methods take various actions in order to eliminate or at least mitigate for ghost forces [45, 100, 116, 140, 182]. One such approach with general characteristics is the deadload ghost force correction [181]. In this approach, the ghost forces are explicitly computed and the negative of these forces are added as deadloads to the affected atoms or nodes. The deadload ghost force correction has shown great promise in some static simulations [126]. However, the deadload correction is only an approximation for the simulations where ghost forces change during the calculation progress.

The general algorithm for energy-based methods defines the total potential energy of the entire system U^{tot} as the sum of the potential energies of the atomistic U^{A}, continuum U^{C} and handshake U^{H} regions, as

$$\mathrm{U}^{tot} = \mathrm{U}^{A} + \mathrm{U}^{C} + \mathrm{U}^{H}, \qquad (21)$$

and minimizes it to reach equilibrium. These energies are described by [126]

$$\mathrm{U}^{A} = \sum_{\alpha \in B^{A}} \mathrm{E}_{\alpha} - \sum_{\alpha \in B^{A}} \mathbf{f}_{\alpha} \cdot \mathbf{u}_{\alpha}, \qquad (22)$$

$$\mathrm{U}^{C} \approx \sum_{e=1}^{N_e} \sum_{q=1}^{N_q} \omega^{q} \mathrm{V}_{e} \mathrm{W}\left(\mathbf{\Delta}(\mathbf{r}_{e}^{q})\right) - \bar{\mathbf{f}}^{\mathrm{T}} \mathbf{u}, \qquad (23)$$

$$\mathrm{U}^{H} \approx \sum_{\alpha \in B^{H}} (1-\Theta(\mathbf{r}_{\alpha})) \mathrm{E}_{\alpha} + \sum_{e \in B^{H}} \Theta(\mathbf{r}_{e}^{cent}) \mathrm{W}\left(\mathbf{\Delta}(\mathbf{r}_{e}^{cent})\right), \qquad (24)$$

where the energy, spatial coordinates, displacement and applied forces of atom α are shown by E_{α}, $\mathbf{r}_{\alpha}$, $\mathbf{u}_{\alpha}$, and $\mathbf{f}_{\alpha}$, respectively. N_e is the number of elements, V_e is the volume of element e, N_q is the number of quadrature points in the numerical integration, $\mathbf{r}_{e}^{q}$ is the position of quadrature point q of element e in the reference configuration, and ω^{q} is the associated Gauss quadrature weights. $\bar{\mathbf{f}}$ and $\mathbf{u}$ are the vector of applied forces and nodal displacements in the FE region, respectively. W is a function of the deformation gradient $\mathbf{\Delta}$. $\mathbf{r}_{e}^{cent}$ is the coordinates of the Gauss point in element e which is taken at the centroid of the triangular elements in this specific case shown in Figure 7. One should notice that the energy of the continuum region is approximated due to the fact that a continuous integral has been replaced by a discrete numerical method. Consequently, the handshake region is also approximated since it also uses such a numerical approach for the continuum energy contribution. In the energy equation for the handshake region, both the continuum and atomistic energies are used in a weighted fashion according to a function Θ which varies linearly from one at the edge of B^{H} closest to the continuum region, to zero at the edge closest to the atomistic region. Indeed, for methods with no handshake region, U^{H} is taken zero and only the continuum and atomistic regions contribute to U^{tot}. Moreover, one should note that the padding atoms have no contribution to the formulation of the potential energy. Therefore, these atoms only provide an appropriate boundary condition for the atoms in B^{A}.

The force-based methods are based on two independent potential energy functionals. The first one calculates an energy functional U^{atom} assuming the entire system is modelled using atoms. The second energy functional U^{FE}, on the other hand, provides a description of the system if it was modelled entirely in a FEM framework. The forces for the all α atoms, $\mathbf{f}_{\alpha}$, and all i nodes, $\mathbf{f}_{i}$, are simply found by differentiating the corresponding energies with respect to the atomic or nodal displacements, $\mathbf{u}_{\alpha}$ and $\mathbf{u}_{i}$ respectively, as

$$\mathbf{f}_{\alpha} = \frac{\partial \mathrm{U}^{atom}}{\partial \mathbf{u}_{\alpha}}, \qquad (25)$$

$$\mathbf{f}_{i} = \frac{\partial \mathrm{U}^{FE}}{\partial \mathbf{u}_{i}}. \qquad (26)$$

It is important to note that the difference between energy-based and force-based methods stems from the fact that in the second approach one does not attempt to minimize the combined energy functional.

4.2.3 Applications of Concurrent Methods to Polymeric Materials

In this part, I give several examples for the applications of coupled atomistic/continuum models in polymeric systems. In the studies outlined here, one can find applications of the methods explained so far; either it is directly used, or a modified version is developed to capture the correct physics involved, or a concept is borrowed to propose new models for polymers.

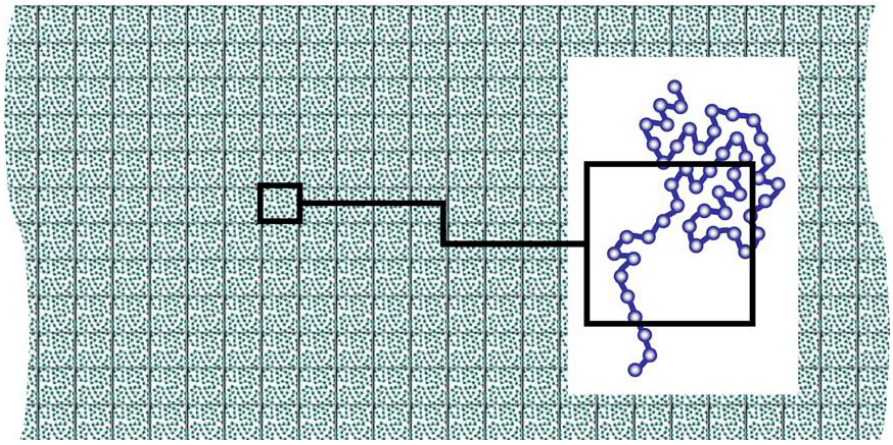

Figure 8: Construction of initial polymer domain from amorphous cells. Reprinted from Tan et al. [199]. Copyright 2016, with permission from Elsevier.

Generally, it is more difficult to model polymers than crystalline materials due to their semi-crystalline nature. A methodology to solve this problem was formulated by Theodorou and Suter [200, 201] in which a parent chain of atoms is attached to a cell known as an Amorphous Cell (AC). The AC is then subjected to deformations assuming periodic boundary conditions on all sides of the cell. Tan et al. [199] incorporated the concept of AC and developed it based on the adaptive scaling resolution ideas and introduced the Pseudo Amorphous Cell (PAC) multiscale approach for amorphous polymers. PAC algorithm includes: (i) the construction of a configuration of polymer chains in the domain, (ii) linearization of molecular mechanics equations for regions with small deformations, (iii) reduction of the number of degrees of freedom in small deformation regions, and (iv) coupling of linear and nonlinear molecular mechanics equations. In their method, the regions with large deformations are represented with nonlinear molecular mechanics and thus provide a finer solution, see Figure 8. The authors showed that PAC can successfully simulate the nanoindentation of amorphous polymers and the indentation force was predicted with a good precision comparable to a full molecular mechanics simulation [199]. Later Su et al. [197] applied the PAC approach to correlate the displacements of atoms within a representative volume element (RVE) of amorphous material to the deformation of the RVE.

The ground idea of projection methods was first introduced in details by Hughes et al. [86] as the variational multiscale methods (VMS) which allows a complete model to be described by orthogonal subscale models. Utilizing this property, Codina [33] presented a method to deal with numerical instability of the Stocks problem due to the incompressibility constraint and convection. He proposed using orthogonal subscales in FEM through the pressure gradient projection. This approach has been developed recently by Castillo and Codina [26, 27] to present VMS stabilized formulations for the stationary three-field incompressible flow

problem for viscoelastic fluids as well as fluids with nonlinear viscosity. The authors were able to successfully capture the distributions of streamlines in a sudden contraction flow as shown in Figure 9 for an Oldroyd-B fluid at Re of 1 at various Weissenberg numbers (We). It was observed that the size of the vortex appearing in the bottom corner decreases as We increases.

In a recent MD study of brittle fracture in epoxy-based thermoset polymers under mechanical loading, Koo et al. [102] introduced an EM step into the virtual deformation test to maintain the system temperature at zero. They stated in the paper that this idea was borrowed from quasicontinuum (QC) method which bridges atomistic scale to continuum scale by decoupling temperature effects. The possibilities of incorporating multiscale approaches to connect MD and FEM such as QC in investigations of structure at epoxy-silica interface are also emphasized by Büyüköztürk et al. [24].

Jo and Yang [89] utilized an atomistic/continuum model to predict the mechanical properties of semicrystalline poly(trimethylene terephthalate) (PTT). Their approach includes an EM process similar to energy-based methods. The system for semicrystalline PTT consists of an amorphous matrix described as a continuum, and a spherical inclusion representing the crystalline phase modelled in atomistic detail. The crystallinity of PTT can be controlled by varying the volume fraction of an inclusion.

In order to model the compressive behavior of carbon nanotube PNCs, Li and Chou [113, 114] developed a multiscale strategy in which the nanotube is modelled at the atomistic scale, and the matrix deformation is analyzed by the continuum FEM. Their methodology is similar to other atomistic/continuum coupling themes except for the fact that they adopt a so-called truss rod model to correctly represent van der Waals interactions at the interface. Figure 10 illustrates the truss rods connecting carbon atoms with nodes in finite elements. The multiscale scheme developed by Li and Chou was later incorporated by Montazeri and Naghdabadi [128] to study the stability of carbon nanotube PNCs with a viscoelastic matrix. They coupled molecular structural mechanics to FEM and simulated the buckling behavior of the system.

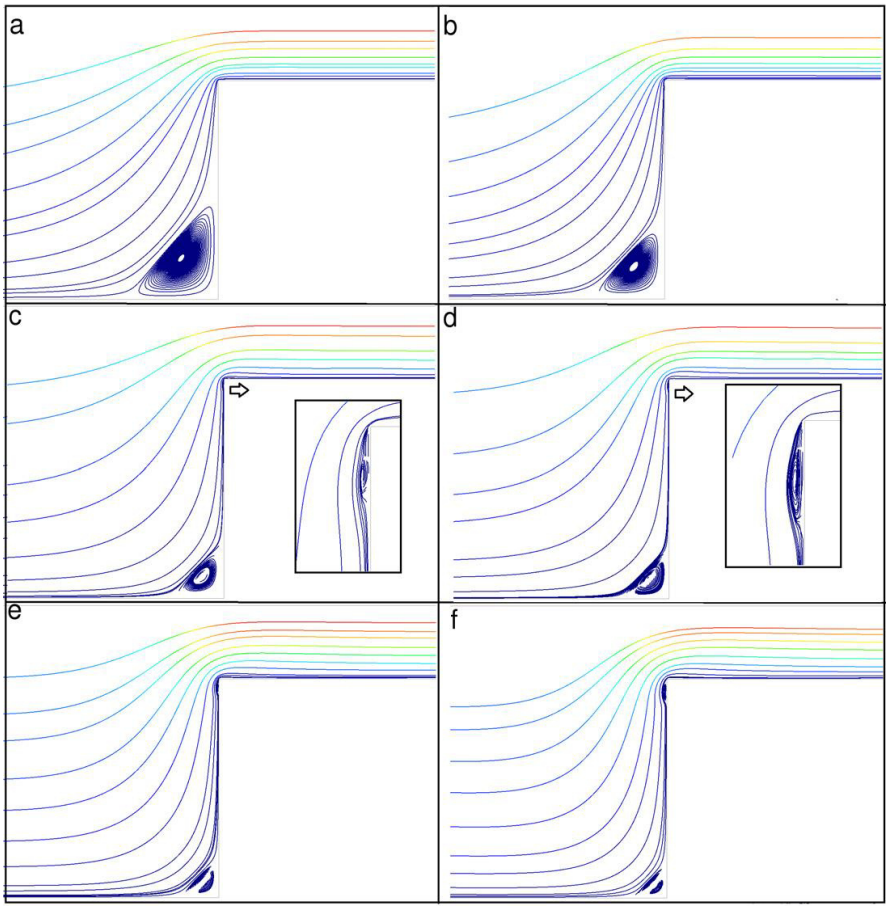

Figure 9: Distributions of streamlines near the corner for (a) We = 0, (b) We = 0.5, (c) We = 2.5, (d) We = 3, (e) We = 4 and (f) We = 5. Reprinted from Castillo and Codina [27]. Copyright 2016, with permission from Elsevier.

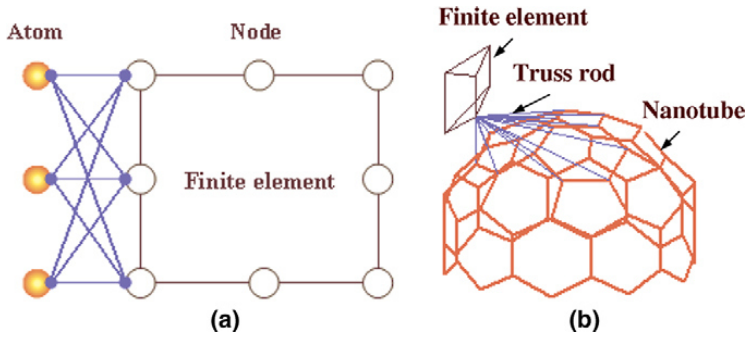

Figure 10: Illustrations of truss rods connecting nodes in finite elements with carbon atoms: (a) on the nanotube lateral surface and (b) on the nanotube end cap region. Reprinted from Li and Chou [114]. Copyright 2016, with permission from Elsevier.

A multiscale simulation strategy was proposed by De et al. [36] to determine the mesoscale velocity evolution in polymer fluids with large stress relaxation times. In such systems the use of a constitutive equation of viscosity is not sufficient to produce the correct rheology. The authors introduced a scale bridging concept in which small parts of the system were simulated with MD. These parts could communicate with each other through a continuum

approach. The passing of information is schematically shown in Figure 11. As it is observed, the continuum approach provides accurate means of interpolating between these points. They described the coupling of atomistic and continuum regions in a Lagrangian framework so that the memory effects, and the consequent dependence of properties on the overall deformation are included in the calculations.

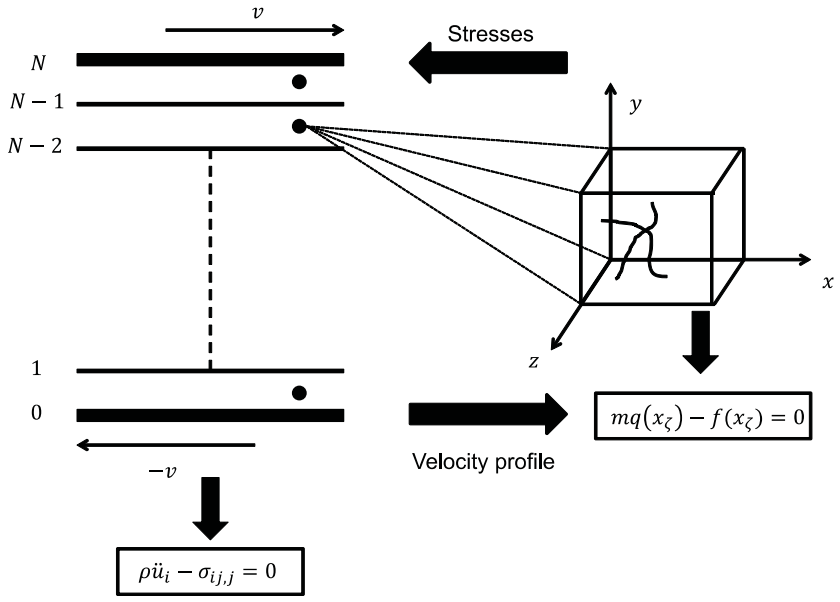

Figure 11: Schematic representation of the proposed multiscale method. The stresses calculated from the MD simulations are used in the coarse grained methods, while the coarse grained methods yield velocity profiles which are used in the next set of MD simulations. Reprinted with permission from De et al. [36]. Copyright 2016 by The American Physical Society.

4.3 Adaptive Resolution Simulations

It was already discussed in the concurrent multiscale approaches that there is a category of systems in which the phenomenon of interest is focused in a subregion of the entire domain. Consequently, it would be computationally efficient if the irrelevant AA representation of molecules far from this subregion were replaced with an alternative less expensive model. However, the common feature and limitation in all concurrent methods (introduced so far) is that the regions of the system treated at different resolution levels are fixed and do not allow for particle exchange. The relatively new class of multiscale simulation approaches, i.e. the adaptive resolution simulations, provides this possibility. Several papers have been devoted to address different aspects of these methods in recent years showing their increasing popularity [81, 105, 156, 218, 228]. It should be noted that these methods can be principally considered to be concurrent since they often couple the simultaneous run of two techniques with different levels of resolution using a transition region. Furthermore, the transition region usually uses an either force or energy interpolation criterion to link different resolutions somewhat similar to the concurrent methods. However, in adaptive resolution simulations, an atom or a molecule is free to smoothly switch its resolution within the same simulation run depending on its spatial coordinates. Therefore, it allows for an adaptive modification of the resolution within the coexisting models which promotes the accuracy

where needed and provides the required precision. In concurrent approaches, on the other hand, different scales are coupled often by a step-wise transfer of information between different methods, for instance I refer to Youn Park et al. [225]. Therefore, some authors introduce adaptive resolution simulations as a separate class of multiscale approaches to emphasize these different aspects [98]. Here, I also follow this notion.

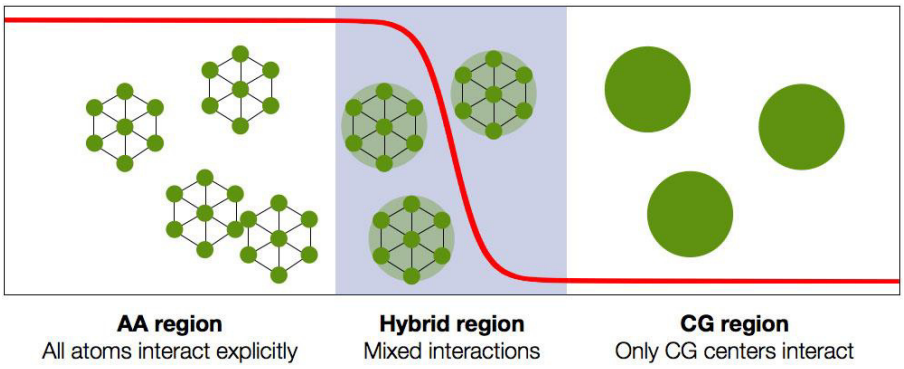

Figure 12: Typical scheme of an adaptive resolution simulation: a high-resolution region, where molecules are described at the atomistic level, is coupled to a low-resolution region where a simpler, CG model is employed. These two subregions of the system are interfaced via a transition region, in which the molecule's representation smoothly changes from one to the other, depending on their positions. It is on this last region and its properties (i.e., the way molecules change resolution) that the complexity of adaptive resolution schemes concentrates. Reprinted from Potestio et al. [156] under the terms of the Creative Commons Attribution License.

The adaptive resolution simulations often divide a domain into an AA and a CG region and link them using a transition region, see Figure 12, hence are sometimes referred to as the double-resolution simulation methods. Examples for the appropriate systems to investigate with such a strategy include the studies of macromolecules embedded in a solvent (see Figure 13) [157], and liquids near surfaces [137]. The transition region allows for a smooth interpolation from a given representation of the molecule's structure/interaction to another depending on the properties that have to be preserved in the CG region. A complete methodology should address the interactions between the atoms or molecules in different domains as well as the property change in crossing the transition region. Moreover, it is central to adaptive resolution simulations that the molecules should be free to diffuse from any region of the simulation box to any other. Other constraints could include thermal equilibrium and uniform density profile across the entire domain which along with certain region-specific properties lead to a formulation of an adaptive resolution scheme.

The Adaptive Resolution Scheme (AdResS) was developed by Kremer and co-workers [41, 157 - 162] as the first effective and computationally efficient method to simulate a system where an AA and a CG model are simultaneously employed in different subregions of the simulation domain. These subregions are interfaced in such a way to allow atoms and molecules to freely diffuse from one region to the other. AdResS is principally based on the assumption that Newton's third law should be satisfied everywhere in the simulation domain. Additionally, the method assumes that a molecule in the CG region loses completely its

atomistic details and interacts with other molecules, either in AA or CG regions, only via its center of mass. An interpolation scheme for the force field across the domain defining the force $\mathbf{f}_{\alpha\beta}$ acting between molecules α and β can be formulated considering the aforementioned assumptions as

$$\mathbf{f}_{\alpha\beta} = \psi(\mathbf{R}_\alpha)\,\psi(\mathbf{R}_\beta)\,\mathbf{f}_{\alpha\beta}^{\mathrm{AA}} + (1 - \psi(\mathbf{R}_\alpha)\,\psi(\mathbf{R}_\beta))\,\mathbf{f}_{\alpha\beta}^{\mathrm{CG}}, \qquad (27)$$

where $\mathbf{R}_\alpha$ and $\mathbf{R}_\beta$ are the center of mass coordinates of molecules α and β, respectively. $\mathbf{f}_{\alpha\beta}^{\mathrm{AA}}$ and $\mathbf{f}_{\alpha\beta}^{\mathrm{CG}}$ are the atomistic and CG forces acting on molecule α due to the interaction with molecule β, respectively. Here, ψ is a spatial interpolation function that goes from 1 in the AA region to 0 in the CG region smoothly. In the transition region, atomistic details are explicitly integrated and the CG force is computed between the centers of mass of the molecules and then redistributed to the atoms weighted by the ratio of the atom's mass to the mass of molecule [64]. In the CG region, the CG force is directly applied to the center of mass coordinates of the molecules and there is no need to conserve the molecules internal structure. When a molecule enters the CG region its atomistic details are removed and reintroduced again, through some sort of reservoir of equilibrated atomistic structures, as soon as it approaches the transition region.

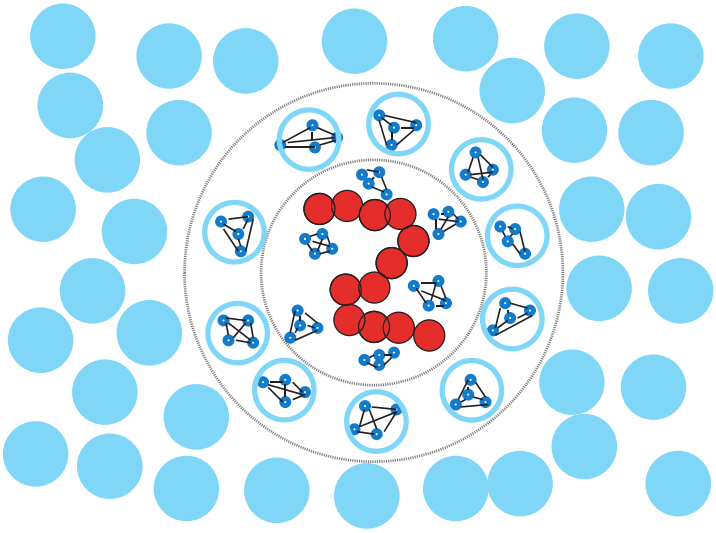

Figure 13: A schematic plot of a solvated generic polymer. The solvent is modelled on different levels of detail. Solvent molecules within a certain radius from the polymer's center of mass are represented with a high resolution while a lower resolution is used for the more distant solvent. The high resolution sphere moves with the polymer's center of mass. The polymer beads are represented smaller than the solvent molecules to preserve clarity. Reprinted from Praprotnik et al. [157] with the permission of AIP Publishing.

The central requirement of satisfying Newton's third law in AdResS is demonstrated to rule out any form of potential energy interpolation and vice versa [42]. Consequently, energy-conserving simulations in the microcanonical ensemble cannot be performed using AdResS. Due to the non-conservative nature of the forces in the transition region, molecules receive an unreal excess energy when crossing this region. This energy can be removed utilizing a local thermostat in order to keep the temperature constant everywhere in the system. The

equilibrium configurations of the system are then sampled according to Boltzmann distribution [63, 152, 157 - 159, 162].

The different resolution of the utilized models typically results in a pressure difference between the corresponding regions which further leads to a non-uniform density profile in the system. Kremer and co-workers [64, 131, 151] modified the CG potential by introducing a thermodynamic force $\mathbf{f}^{th}$ which counterbalances the high pressure of the CG model. This force is obtained in an iterative procedure as

$$\mathbf{f}_{i+1}^{th} = \mathbf{f}_{i}^{th} - \frac{\nabla \rho_i(\mathrm{r})}{\rho^* \mathrm{k}_T}, \qquad (28)$$

where ρ^* is the reference molecular density, k_T is the system's isothermal compressibility and $\rho_i(\mathrm{r})$ is the molecular density profile as a function of the position in the direction perpendicular to the CG/AA interface. The iterative procedure converges once the density profile is flat, i.e. $\nabla\rho(\mathrm{r}) = 0$. The resulting thermodynamic force produces a flat density profile and preserves the thermal compressibility of the system as well as the structure of the system in the CG region. Principally, this method allows one to use any arbitrary CG force field, with pressure and structure completely different from the target atomistic ones. Consequently, the AA region behaves as an open system that exchanges energy and molecules with a reservoir and thus producing the molecule number fluctuations, the pressure and all other thermodynamically relevant quantities the same as if the AA region were simply cut from a large AA simulation [64]. This condition can be established irrespective of the specific model used in the CG region only because of the thermodynamic force.

AdResS provides the possibility to perform numerical experiments in which the spatial extension of correlations in the system is investigated. Particularly, the structural properties of the AA region can be monitored as a function of its size in order to examine their dependency on the interactions with molecules in the bulk region. For instance, Lambeth et al. [108] used this notion to study the ordering degree of the hydrogen bond network of a molecule with both hydrophilic and hydrophobic bonds solvated in water as a function of the size of the AA region. The same strategy has also been applied to investigate the extent of spatial correlations in low-temperature para-hydrogen [153, 155]. In some systems, it is critical to have access to a large number of particles, for instance, to correctly reproduce the solvation free energies in mixtures. Thus, a standard AA simulation could lead to extremely costly computations in such cases. Naturally, AdResS has shown to be a viable candidate for these systems as well, as evidenced in some works on methanol-water mixtures [130], and triglycine in aqueous urea [131].

4.4 Extending Atomistic Simulations

Besides the methods that are explicitly designed to link computational techniques from different realms together, there are some approaches to extend the reaches of a specific technique such as MD. As it was noted before, MD plays a critical role in the modelling of materials problems because MD simulations can follow the actual dynamical evolution of the system along its deterministic pathway. However, MD is strictly limited to very short time scales due to its full atomistic representation of the molecules. Therefore, some researchers

studied different methods to address the time scale problem including hyperdynamics [213 - 215], parallel replica dynamics [216], and temperature-accelerated dynamics [191]. These methods are based on the transition state theory in which the system trajectory is simulated to find an appropriate pathway to escape from an energy well [83, 213]. The simulation walks through this pathway with a process that takes place much faster than the direct MD.

The hyperdynamics approach is designed to accelerate MD simulations without any prior knowledge of neither the location of the dividing surface, i.e. the surface in the phase space separating the initial and final states, nor the states through which the system may evolve. For this purpose, the energy of the system in regions other than at the dividing surfaces is raised by applying a bias potential which leads to an accelerated transition from one equilibrium state to another equilibrium state [213]. The parallel replica dynamics method was incorporated for a system with infrequent events in which successive transitions are uncorrelated [216]. In such a system, running a number of independent MD simulations in parallel gives the exact dynamical evolution between the states. For a system with correlated crossing events, the state-to-state transition sequence is still correct. However, the error associated with the simulation time should be eliminated. Finally, in the temperature-accelerated dynamics method, the state-to-state transition is accelerated by increasing the temperature followed by filtering out the transitions that should not have occurred at the original temperature [191]. Consistent with other accelerated dynamics methods, the trajectory of the system is allowed to wander on its own to find an appropriate escape path. Consequently, no prior information is required about the nature of the involved phenomena [213].

The accelerated dynamics methods are formulated in order to find transition pathways between two known equilibrium states via effective MD simulations. Other approaches to extend atomistic simulations are also available which often require no preconceived mechanism or transition state. One such method attempts to find the transition pathway by minimizing the average value of the potential energy along the path rather than trying to find the path with the lowest barrier [49 - 51]. Another approach utilizes statistical sampling of the dynamical paths i.e. MC sampling of MD trajectories introducing transition path-sampling methods [18, 32, 38, 53, 101]. In addition to these methods, an alternative finite-temperature string method is proposed that represents transition paths by their intrinsic parameterization to efficiently evolve and sample paths in the path space [46 - 48, 171]. The string method performs a constrained sampling of the equilibrium distribution of the system in hyperplanes normal to the transition pathways of a CG potential. The collection of the hyperplanes is parametrized by a string that is updated self-consistently until it approximates locally the correct coordinate associated with the phenomenon. The region in these planes in which the equilibrium distribution is concentrated determines a transition tube in the configuration space in which a transition takes place with high probability. Finally, some works try to find dynamical paths that could connect an initial state to a final state in general terms [17, 39, 40, 148, 175, 217, 227]. Such methods often offer good numerical stability, efficient parallelizability, and high quality trajectories.

A class of methods attempts to address the systems with a free-energy surface which may possess multiple local minima separated by large barriers. These strategies are generally known as the methods to escape the free-energy local minima [107]. One such method

combines the ideas of CG dynamics on the free-energy surface with those of adaptive bias potential methods [107]. The method allows the system to escape from local minima in the free-energy surface and at the same time achieves a quantitative determination of the free-energy surface through the integrated process. This method has especially found application in biological systems [95, 135, 208].

In a category of systems an inherent dispersity in some characteristic details results in a natural disparity in time scales. A well-known example of such a case is the Born–Oppenheimer approximation [16], in which the electron motion is separated from that of the nuclei because of the large disparity between their masses. Another scenario for the separation of time scales occurs when some subset of forces present in the system is much stronger compared with the rest of the forces, while the masses of the constituents are about the same. In order to deal more efficiently with such systems, various integration algorithms with multiple time steps have been developed [206]. This idea is particularly useful in polymers in which the bond vibrations usually occur at a much faster rate than bond translation and rotations. Consequently, the configuration space as well as the forces can be divided into fast and slow components. This separation yields a set of coupled equations of motion for the evolution of the fast and slow degrees of freedom. Instead of solving this set of equations simultaneously, the multiple-time-step integration uses a small time step Δt to advance the fast processes by n steps while holding the slow variables fixed. The slow processes are then updated using a time step of $n\Delta t$. In the case that an analytic solution of high-frequency motions is available, this solution can be incorporated into an integration scheme for the entire system. Therefore, a time step can be defined based on the slow processes and used for the simulation of entire system with a much smaller number of cycles [206].

Finally, a method based on optimization of the action functional was proposed by Elber et al. [49] to extend the time scale of MD simulations by several orders of magnitude. In this method, instead of parameterizing the trajectory as a function of time, the trajectory is parametrized as a function of length. Instead of solving the Newton equations in MD simulations, an action term, i.e. the stochastic difference equation with respect to time, is optimized.

5. Fundamental Concepts in Multiscale Simulations of Polymer Systems

In this chapter, I focus on the current status of multiscale simulation methods in polymer science. The existing possibilities are addressed and special attention is paid to polymer nanocomposites. Moreover, the shortcomings of various approaches are discussed and research directions are reviewed.

Two papers are presented in this chapter. They are:

5.1 A Review of Multiscale Computational Methods in Polymeric Materials

[Gooneie A., Schuschnigg S., Holzer C.: A Review of Multiscale Computational Methods in Polymeric Materials, Polymers 9 (1), 2017, pp. 16]

5.2 Multiscale Simulation of Polymer Nanocomposites in Processing: Challenges and Outlooks

[Gooneie A., Mattausch H., Witschnigg A., Schuschnigg S., Holzer C.: Multiscale simulation of polymer nanocomposites in processing: Challenges and outlooks, Key Engineering Materials 651, 2015, pp. 533–538]

polymers

MDPI

Review

A Review of Multiscale Computational Methods in Polymeric Materials

Ali Gooneie *, Stephan Schuschnigg and Clemens Holzer

Chair of Polymer Processing, Montanuniversitaet Leoben, Otto Gloeckel-Strasse 2, 8700 Leoben, Austria; stephan.schuschnigg@unileoben.ac.at (S.S.); clemens.holzer@unileoben.ac.at (C.H.)

* Correspondence: ali.gooneie@unileoben.ac.at; Tel.: +43-3842-402-3509

Academic Editor: Xianqiao Wang

Received: 20 October 2016; Accepted: 22 December 2016; Published: 9 January 2017

Abstract: Polymeric materials display distinguished characteristics which stem from the interplay of phenomena at various length and time scales. Further development of polymer systems critically relies on a comprehensive understanding of the fundamentals of their hierarchical structure and behaviors. As such, the inherent multiscale nature of polymer systems is only reflected by a multiscale analysis which accounts for all important mechanisms. Since multiscale modelling is a rapidly growing multidisciplinary field, the emerging possibilities and challenges can be of a truly diverse nature. The present review attempts to provide a rather comprehensive overview of the recent developments in the field of multiscale modelling and simulation of polymeric materials. In order to understand the characteristics of the building blocks of multiscale methods, first a brief review of some significant computational methods at individual length and time scales is provided. These methods cover quantum mechanical scale, atomistic domain (Monte Carlo and molecular dynamics), mesoscopic scale (Brownian dynamics, dissipative particle dynamics, and lattice Boltzmann method), and finally macroscopic realm (finite element and volume methods). Afterwards, different prescriptions to envelope these methods in a multiscale strategy are discussed in details. Sequential, concurrent, and adaptive resolution schemes are presented along with the latest updates and ongoing challenges in research. In sequential methods, various systematic coarse-graining and backmapping approaches are addressed. For the concurrent strategy, we aimed to introduce the fundamentals and significant methods including the handshaking concept, energy-based, and force-based coupling approaches. Although such methods are very popular in metals and carbon nanomaterials, their use in polymeric materials is still limited. We have illustrated their applications in polymer science by several examples hoping for raising attention towards the existing possibilities. The relatively new adaptive resolution schemes are then covered including their advantages and shortcomings. Finally, some novel ideas in order to extend the reaches of atomistic techniques are reviewed. We conclude the review by outlining the existing challenges and possibilities for future research.

Keywords: computer simulations; computational methods; multiscale modelling; hierarchical structures; multiple scales; bridging strategies; polymers; nanocomposites

Contents

1. Introduction

Polymeric materials display distinguished characteristics which range from the angstrom level of an individual bond, to tens of nanometers of the chain gyration radius, to micrometers, millimeters and larger in melts, blends, solutions and polymer nanocomposites (PNCs). The corresponding time scales of the dynamics relevant to different material properties span an even wider range from femtoseconds to seconds or even hours for large-scale ordering processes such as phase separation in blends. In order to highlight the inherent multiscale nature of polymer systems, two interesting cases from the literature are briefly outlined. Indeed, many other examples from various fields of polymer science can be found elsewhere [1–13]. We believe that the selected examples should suffice to serve the purpose as well as the brevity.

As the first example, PNCs are considered due to their importance to many applications. The incorporation of nanoparticles in polymers has attracted substantial academic and industrial interest due to the dramatic improvements in the properties of the host polymers. The addition of only 1–10 vol % nanoparticles has been shown to be able to enhance various properties of the neat polymers [14–20]. These changes are often introduced into the polymer matrix while many benefits of the neat polymer including rather easy processability are still preserved [21,22]. Therefore, PNCs are ideal candidates for multiple applications like medical devices, aerospace applications, automobile industries, coatings, etc. Experience has shown that the property enhancement in PNCs is directly linked to the nanoparticles arrangement and dispersion [21,23]. A precise morphology control is of great significance in PNCs, otherwise the full property potential of these materials cannot be achieved.

The fact that many of the common nanoparticles possess strong van der Waals interactions promotes their aggregation and consequently diminishes their effectiveness. On the other hand, the role of polymer-particle interactions can either facilitate or complicate the aggregation process. Moreover, the geometrical characteristics of the nanoparticles, such as aspect ratio and structural flexibility, add to the complexity of their impact on the properties since it can alter surface energies as well as surface-to-volume ratio [24]. Therefore, the structural characterization and the detailed evaluation of the fabrication of PNCs are crucial to achieve the desired properties. Many studies are devoted to understand the effects of processing conditions on the final microstructure and the resulting properties of the PNCs [19–21,23–27]. The multiscale nature of PNCs simply divulges if one considers the interplaying role of the fabrication stage with macroscopic characteristics and the aforementioned submicron phenomena involved in the final outcome of PNCs.

A fascinating field of application for multiscale methods is in biological systems [3,4,7]. For instance, we take a single hair strand. It is well known that hairs, i.e., keratin fibers, exhibit a complex structure [28]. Filaments with a diameter of approximately 8 nm are tightly packed in a matrix, filling the approximately 2 nm gap in between which are later assembled into a so-called macrofibril. Often, several hundred filaments form one macrofibril. Various macrofibrils can be categorized based on how packed they are. These macrofibrils constitute the main part of the hair cells in the cortex. The remaining volume of the cell is comprised of the remnants and pigment granules. The cross-section of a hair typically has almost 100 cells, contained by a cell-membrane structure. Finally, the cortex is encapsulated by the cuticle which forms the surface of a hair fiber. It is of significance to be able to find the relation between the mechanical properties of these fibers and the structure of the keratin proteins, temperature, humidity and deformation rate. Obviously, such analysis necessitates a multiscale approach to capture the precise behavior of the hair mechanics as suggested by Akkermans and Warren [28].

In order to find appropriate solutions to these questions, several theories and computational methods were developed which could introduce new possibilities to design, predict and optimize the structures and properties of materials. At present, no single theory or computational method can cover various scales involved in polymeric materials. As a result, the bridging of length and time scales via a combination of various methods in a multiscale simulation framework is considered to be one of the most important topics in computational materials research. The resulting multiscale method is preferably supposed to predict macroscopic properties of polymeric materials from fundamental molecular processes. In order to build a multiscale simulation, often models and theories from four characteristics length and time scales are combined. They are roughly divided into the following scales.

1. The quantum scale (~10^{-10} m, ~10^{-12} s): The nuclei and electrons are the particles of interest at this scale and quantum mechanics (QM) methods are used to model their state. The possibility to study the phenomena associated with formation and rupture of chemical bonds, the changes in electrons configurations, and other similar phenomena are typical advantages of modelling at quantum scale.

2. The atomistic scale (~10^{-9} m, ~10^{-9}–10^{-6} s): All atoms or small groups of atoms are explicitly represented and treated by single sites in atomistic simulations. The potential energy of the system is estimated using a number of different interactions which are collectively known as force fields. The typical interactions include the bonded and nonbonded interactions. The bonded interactions often consist of the bond length, the bond angle, and the bond dihedral potentials. The most typically used nonbonded interactions are Coulomb interactions and dispersion forces. Molecular dynamics (MD) and Monte Carlo (MC) simulation techniques are often used at this level to model atomic processes involving a larger group of atoms compared with QM.

3. The mesoscopic scale (~10^{-6} m, ~10^{-6}–10^{-3} s): At mesoscopic scale, a molecule is usually described with a field or a microscopic particle generally known as a bead. In this way the molecular details are introduced implicitly which provides the opportunity to simulate the phenomena on longer length and time scales hardly accessible by atomistic methods. A good example for the field-based

description of polymer systems is the Flory-Huggins model for the free energy of mixing in which the details of the system are summed up in model parameters. On the other hand, in particle-based models collections of particles are accumulated in beads through a coarse-graining procedure. The interactions between the beads are then used to characterize the system. Various methods have been developed to investigate the mesoscopic structures in polymeric systems including dissipative particle dynamics (DPD), Brownian dynamics (BD), lattice Boltzmann (LB), dynamic density functional theory (DDFT), and time-dependent Ginzburg-Landau (TDGL) theory.

4. The macroscale (~10^{-3} m, ~1 s): At this scale, the system is treated as a continuous medium and the discrete characteristics of atoms and molecules are ignored. The behavior of such a system is governed by constitutive laws which are often coupled with conservation laws to simulate various phenomena. All functions such as velocity and stress components are continuous except at a finite number of locations which separate continuity regions. The fundamental assumption at this scale is in replacing a heterogeneous material with an equivalent homogeneous model. The most important methods used to simulate systems at this scale are finite difference method (FDM), finite element method (FEM), and finite volume method (FVM).

Although several review papers are available on the topic of multiscale simulations in materials [1–12,29–31], a comprehensive discussion of its various aspects in polymer science is still needed. Some reports approach the objective by introducing different case studies and never actually detailing various categories of multiscale methods, while some others focus only on a specific topic in multiscale simulations such as coarse-graining or concurrent simulations. Here, we aim to provide an opportunity for the interested reader to explore how such techniques might be applied in their own area of specialty by focusing on the core concepts of major trends in this field all in one place. Consequently, we outline the basics of the methods and illustrate each one with a few examples from the vast field of polymeric systems. We organize the review as follows. In Section 2, we introduce some of the most significant computational methods used so far to model different scales. This part is not intended to provide detailed description of each method. Instead, we aim to emphasize different approaches, challenges, restrictions, and opportunities that models of each scale could generally possess. Since such models are the building blocks for the multiscale methods, it is important to note how they convey their characteristics into a multiscale approach. We strongly advice the interested reader to refer to relevant literature, some significant ones introduced here, for further information. In Section 3, we discuss in detail various ideas to link scales in a multiscale package. Four major blocks are presented in this part: Sequential Multiscale Approaches, Concurrent Multiscale Approaches, Adaptive Resolution Simulations, and Extending Atomistic Simulations. This section is the core of the paper and therefore we attempt to deliver the most recent advances in each instance. In every case, the applications in polymer science are highlighted to serve the topic. It was a serious concern of ours to cite the outstanding studies that could cover from the classic fundamental works up to the latest publications. We hope this eases further pursue of the relevant works. It should be noted that the topic at hand is massive and there might be some significant studies which are left out despite our attempts. Finally, we conclude the review by emphasizing the current challenges and future research directions. Overall, the present review is meant to put forth the major directions in multiscale simulation strategies in polymer science.

2. Simulation Methods

In general, computational methods are categorized into either particle-based or field-based approaches [32,33]. The particle-based methods incorporate particles to represent the building blocks of polymers such as atoms, molecules, monomers, or even an entire polymer chain. These particles (and their combinations in the form of bonds, angles, dihedrals and so on) often interact with each other through certain forces which form a force field altogether [34]. By the application of a statistical mechanical sampling method, the particles are allowed to move within a certain thermodynamic ensemble and hence simulate a desired process [35]. Perhaps the most well-known

particle-based techniques are MD and its coarser versions such as DPD. In the second category, i.e., the field-based approaches, the system is typically described in terms of effective potentials, collective dynamic variables, and density fields which determine the degrees of freedom of the model [36]. Therefore, a reduced representation of the system is developed based on some phenomenological approximation [32]. The famous Flory approximation of the free energy of a polymer is a good example of the field-based strategy [37]. Another valuable field-based method is the polymer reference interaction site model (PRISM) which attempts to realize the polymer structure in terms of density correlation functions [38]. Other examples of such methods include density functional theory (DFT) [38–40], self-consistent field theory (SCFT) [32,33,38], and phase-field techniques [41–43]. In this section, we outline the details of some of the most important methods at different scales. These methods mainly belong to the particle-based approaches due to their relevance to the rest of the discussion as well as to our own research interest. For more details on the field-based methods, the reader is referred to the cited literature.

2.1. Quantum Mechanics

A precise treatment of atomistic scale phenomena requires the solution of the Schrödinger wave equations for all electrons and nuclei on the basis of a quantum scale modelling [44]. In QM, the time-independent form of the wave equation $\phi(\mathbf{r})_k$ for a particle in an energy eigenstate E_k in a potential $U(\mathbf{r})$ having coordinates vector $\mathbf{r}$ and mass m is

$$-\frac{h^2}{8\pi^2 m}\nabla^2\phi(\mathbf{r})_k + U(\mathbf{r})\phi(\mathbf{r})_k = E_k\phi(\mathbf{r})_k, \tag{1}$$

where h is Planck's constant. It can be shown that for a material having i electrons with mass m_{el} and the negative unit charge of $-e$ and the coordinates $\mathbf{r}_{el_i}$, and j nuclei with mass m_n and a positive unit charge of $z_n e$ with z_n being the atomic number, and the spatial coordinates $\mathbf{r}_{n_j}$, Equation (1) becomes

$$\begin{aligned} &-\frac{h^2}{8\pi^2 m_{el}}\sum_i \nabla_i^2\phi(\mathbf{r}_{el_1},\mathbf{r}_{el_2},\ldots,\mathbf{r}_{el_i},\mathbf{r}_{n_1},\mathbf{r}_{n_2},\ldots,\mathbf{r}_{n_j})_k \\ &-\frac{h^2}{8\pi^2}\sum_j \frac{1}{m_{n_j}}\nabla_j^2\phi(\mathbf{r}_{el_1},\mathbf{r}_{el_2},\ldots,\mathbf{r}_{el_i},\mathbf{r}_{n_1},\mathbf{r}_{n_2},\ldots,\mathbf{r}_{n_j})_k \\ &+\left(\sum_{\substack{i_1,i_2\\ i_1\neq i_2}}\frac{e^2}{|\mathbf{r}_{el_{i1}}-\mathbf{r}_{el_{i2}}|}+\sum_{i,j}\frac{z_j e^2}{|\mathbf{r}_{el_i}-\mathbf{r}_{n_j}|}+\sum_{\substack{j_1,j_2\\ j_1\neq j_2}}\frac{z_{j1}z_{j2}e^2}{|\mathbf{r}_{n_{j1}}-\mathbf{r}_{n_{j2}}|}\right)\phi(\mathbf{r}_{el_1},\mathbf{r}_{el_2},\ldots,\mathbf{r}_{el_i},\mathbf{r}_{n_1},\mathbf{r}_{n_2},\ldots,\mathbf{r}_{n_j})_k \\ &= E_k\phi(\mathbf{r}_{el_1},\mathbf{r}_{el_2},\ldots,\mathbf{r}_{el_i},\mathbf{r}_{n_1},\mathbf{r}_{n_2},\ldots,\mathbf{r}_{n_j})_k. \end{aligned} \tag{2}$$

In 1927, Born and Oppenheimer [45] proposed a strategy to separate the wave functions of the light electrons from the heavy nuclei considering that the electrons typically relax to some orders of magnitude faster than the nuclei. This strategy, known as the adiabatic Born-Oppenheimer approximation, assumes that the electrons always remain in their ground state irrespective of the positions of the nuclei by adiabatically adjusting to the movements of the nuclei. As a result of this assumption, one can define the wave function ϕ in Equation (2) as the product of two independent wave functions. In this approach, one function describes the dynamics of the electrons ϖ and the other function describes the dynamics of the nuclei φ. This can be shown as

$$\phi(\mathbf{r}_{el_1},\mathbf{r}_{el_2},\ldots,\mathbf{r}_{el_i},\mathbf{r}_{n_1},\mathbf{r}_{n_2},\ldots,\mathbf{r}_{n_j}) = \varpi(\mathbf{r}_{el_1},\mathbf{r}_{el_2},\ldots,\mathbf{r}_{el_i})\,\varphi(\mathbf{r}_{n_1},\mathbf{r}_{n_2},\ldots,\mathbf{r}_{n_j}). \tag{3}$$

Consequently, the corresponding wave function of the electrons with the eigenstate energy $E_{k_{el}}$ is

$$\left(-\frac{h^2}{8\pi^2 m_{el}} \sum_i \nabla_i^2 + \sum_{\substack{i1,i2 \\ i1 \neq i2}} \frac{e^2}{|\mathbf{r}_{el_{i1}} - \mathbf{r}_{el_{i2}}|} + \sum_{i,j} \frac{z_j e^2}{|\mathbf{r}_{el_i} - \mathbf{r}_{n_j}|} \right) \varpi(\mathbf{r}_{el_1}, \mathbf{r}_{el_2}, \ldots, \mathbf{r}_{el_i})_{k_{el}} = E_{k_{el}}^{el} \varpi(\mathbf{r}_{el_1}, \mathbf{r}_{el_2}, \ldots, \mathbf{r}_{el_i})_{k_{el}}, \quad (4)$$

and the corresponding wave function of the nuclei with the eigenstate energy E_{k_n} is

$$\left(-\frac{h^2}{8\pi^2} \sum_j \frac{1}{m_n} \nabla_j^2 + \sum_{i,j} \frac{z_j e^2}{|\mathbf{r}_{el_i} - \mathbf{r}_{n_j}|} + \sum_{\substack{j1,j2 \\ j1 \neq j2}} \frac{z_{j1} z_{j2} e^2}{|\mathbf{r}_{n_{j1}} - \mathbf{r}_{n_{j2}}|} \right) \varphi(\mathbf{r}_{n_1}, \mathbf{r}_{n_2}, \ldots, \mathbf{r}_{n_j})_{k_n} = E_{k_n}^{n} \varphi(\mathbf{r}_{n_1}, \mathbf{r}_{n_2}, \ldots, \mathbf{r}_{n_j})_{k_n}. \quad (5)$$

It is worthy to note at this point that the use of the adiabatic Born-Oppenheimer approximation is justified only when the energy gap between ground and excited electronic states is larger than the energy scale of the nucleus motion. This assumption has been shown to fail in materials with zero energy gaps such as metals [46,47] and the free-state graphene [48]. Despite this, the adiabatic Born-Oppenheimer approximation has proved effective in the atomistic simulations of some metallic [49] and graphene-based systems [50] as well.

The quantum mechanical many-body problem was formulated by Kohn and Sham [40] in the density functional theory (DFT). In DFT, electrons were replaced by effective electrons with the same total density moving in the potential generated by the other electrons and ion cores. Later, DFT was modified by Car and Parrinello [51] which allowed for the movements to be incorporated into the DFT scheme, thus leading to the so-called ab initio MD (AIMD). Such methods have found useful applications in polymer science such as the simulation of mechanics of polyethylene (PE) macromolecules [52–54], conduction in polymers [55–57], polymerization [58,59], crystal structures [60], disordered conformations of poly(tetra fluoro ethylene) chains [61], and diffusion in polymers [62].

2.2. *Atomistic Techniques*

Atomistic scale simulations often benefit from Equation (5) to predict the initial atomic configurations assuming that the electrons are instantaneously equilibrated during the movements of the nuclei. The approximation methods of this equation are mainly divided into stochastic and deterministic approaches. The stochastic approaches are often referred to as MC methods which are well-credited to evaluate equilibrium states for certain distribution functions or to solve the equations of motion in their corresponding integral form. The deterministic approaches are typically referred to as MD which are mainly used to discretely solve the equation of motion. In general, simulations at this scale provide an atomistic picture of the interactions between components and conformational dynamics which could help uncover the underlying phenomena. By the way of illustration, we consider an example of the application of MD to PNCs in the work of Piscitelli et al. [63] who investigated the functionalization of sodium montmorillonite (Na-MMT) using three aminosilanes characterized by different lengths of the alkyl chains. It is known that the presence of negative charges on the surface of each MMT layer as well as counteracting cations such as sodium or potassium located in the vicinity of the platelets within the galleries produce highly polar pristine structures of Na-MMT [14,21,23]. These structures further lead to their incompatibility with the majority of polymers. Consequently, a simple dispersion of Na-MMT in a polymer results in the formation of aggregated structures within the matrix which is followed by the deterioration of the property enhancement in these PNCs. In order to avoid these structures, chemical functionalization of Na-MMT platelets like silylation reaction is often performed [14]. The X-ray diffraction (XRD) patterns of Piscitelli et al. [63] indicated that the silylation reaction results in the Na-MMT galleries to open up regardless of the type of the aminosilane. However,

it was observed that the *d*-spacing in the modified Na-MMT was reduced as the organic chain of the aminosilane molecule became longer. This outcome might not be expected before the experiments and therefore MD was incorporated to illuminate the underlying phenomena. The simulations revealed the increasing tendency of aminosilane molecules with increasing their length to interact among themselves by intermolecular hydrogen bonding as well as hydrophobic interactions. These interactions could eventually lead to the bridging of aminosilane molecules between two Na-MMT layers for longer chains. This situation not only does not improve the *d*-spacing of the modified Na-MMT compared with the unmodified nanoparticles, but also acts against any attempts from polymer macromolecules to open up the layers. As observed in these simulations, MD can play a key role in the understanding of molecular mechanisms involved in the intercalation process in polymer/clay nanocomposites. Without a thorough vision of such molecular processes in aminosilane-functionalized Na-MMTs, the designed PNC would fail due to this general belief that longer organic chains normally result in higher interlayer spacing. In the following, MC and MD techniques are revisited.

2.2.1. Monte Carlo

In general, the MC methods include a large number of stochastic computer experiments by incorporating uncorrelated random numbers. MC can be used to mimic stationary ensembles by exploring a multitude of states in the corresponding phase space. Therefore, one can obtain pseudo-time-averaged statistical data by calculating ensemble averages along trajectories in the phase space assuming the ergodic system behavior [64–66]. It should be noted that the MC methods are not restricted to the atomistic scale but can be used at any scale if an appropriate probabilistic model is provided.

MC methods often consist of three characteristic steps. These steps are: (i) translation of the physical phenomena under investigation into an analogous probabilistic or statistical model; (ii) solving the resulting probabilistic model by a large number of numerical stochastic sampling experiments; and (iii) analyzing the generated data utilizing statistical methods. The sampling method can follow either a simple sampling algorithm or a weighted sampling algorithm. The simple sampling uses an equal distribution of the random numbers while the weighted sampling develops random numbers based on a distribution which is accommodated to the problem being investigated. The weighted sampling algorithm is the underlying principle of the so-called Metropolis MC algorithm [67].

In Metropolis MC for canonical and/or microcanonical ensembles with N atoms, a new configuration of the atoms is achieved by randomly or systematically choosing one atom and moving it from its initial position i to the temporary trial position j. Consequently, the initial state $\mathbf{\Gamma}_i$ of the system in the corresponding phase space is changed to the trial state $\mathbf{\Gamma}_j$. This displacement alters the Hamiltonian of the system from $\mathrm{H}(\mathbf{\Gamma}_i)$ to $\mathrm{H}(\mathbf{\Gamma}_j)$ according to the particular interactions being considered in the model. Therefore, the change in the system Hamiltonian $\Delta\mathrm{H}(\mathbf{\Gamma}_{i\to j})$ is

$$\Delta\mathrm{H}(\mathbf{\Gamma}_{i\to j}) \;=\; \mathrm{H}(\mathbf{\Gamma}_j) \;-\; \mathrm{H}(\mathbf{\Gamma}_i). \tag{6}$$

If the imposed movement of the chosen atom brings the system to a lower state of energy, i.e., $\Delta\mathrm{H}(\mathbf{\Gamma}_{i\to j}) \;<\; 0$, the movement is accepted and the displaced atom remains in its new position. Otherwise, the imposed movement is only accepted with a certain probability $\mathrm{p}_{i\to j}$ which is proportional to

$$\mathrm{p}_{i\to j} \;\propto\; \exp\left(-\frac{\Delta\mathrm{H}(\mathbf{\Gamma}_{i\to j})}{\mathrm{k}_B\mathrm{T}}\right), \tag{7}$$

where k_B is Boltzmann's constant, and T is temperature. In Metropolis MC, a random number ζ between 0 and 1 is generated and used to test the new configuration. The imposed movement is accepted only if $\zeta \leq \exp\left(-\frac{\Delta H(\Gamma_{i\rightarrow j})}{k_B T}\right)$. If the movement is not accepted, the initial position is assumed to be the new position and the entire procedure is repeated by considering another randomly chosen atom.

The Metropolis MC also suggests using the same strategy for the grandcanonical ensemble where the number of initial atoms might change. For this purpose, the change in the system energy due to the exchange of an arbitrarily chosen atom by an atom of a different kind is taken into account to determine whether the new configuration is accepted or not. The methodology is the same as before.

As a final remark on MC, it should be noted that the original MC methods were intrinsically designed to simulate the equilibrium states of a system. The extension of the MC predictions to the simulation of microstructure evolution was first promoted by the incorporation of Ising lattice model in Potts-type MC models [68–70]. In the sense of using an internal kinetic measure such as the number of MC steps, this class of MC models is often referred to as kinetic MC models [71–75].

MC simulations have been utilized to describe a variety of phenomena in polymeric materials. Its application covers a wide range of problems including study of polymer degradation [71,73], development of surface morphology in thin films [76–80], heterophase interfaces [81–94], crystal growth and melting [95–98], morphology evolution [99–106], fracture behavior [107], diffusion [108–111], study of polymer melt viscoelasticity by nonequilibrium MC [112,113], and prediction of phase diagrams [114,115].

2.2.2. Molecular Dynamics

The MD method is a deterministic simulation technique for the simulation of many-body interaction phenomena at the atomistic scale. It is based on substituting the quantum mechanical expression for the kinetic energy in Equation (5) by the classic momentum term and solving it for a nucleon using Newton's law of motion. Consequently, the simulation of a many-body system would require the formulation and solution of equations of motion of all constituting particles. The equation of motion of a particle *i* is

$$m_i \frac{d^2 \mathbf{r}_i}{dt^2} = \mathbf{f}_i, \tag{8}$$

where m_i is the particle mass and $\mathbf{r}_i$ is the particle position vector. $\mathbf{f}_i$ is the force acting on the *i*th particle at time t which is obtained as the negative gradient of the interaction potential U, i.e., $\mathbf{f}_i = -\nabla U = -\left(\frac{\partial U}{\partial x}\mathbf{i} + \frac{\partial U}{\partial y}\mathbf{j} + \frac{\partial U}{\partial z}\mathbf{k}\right)$. The underlying potentials are often quantified in terms of the relative position of two or more particles. This means that these potentials together with their parameters, i.e., the so-called force field, describe how the potential energy of a many-body system depends on the coordinates of the particles [34,116]. Such a force field can be obtained by QM, empirical methods, and quantum-empirical methods. It should be noted that the criteria for selecting an adequate force field should address the necessary precision in the system description, transferability, and computational speed.

The overall algorithm of MD is to simulate the evolution of particle configurations based on an adequate force field by integrating the equations of motion over discrete steps in time. The procedure is simply to calculate the position and velocity of every particle at present and a time step later. The system of equations of motion of N particles can be solved by utilizing FDM. The Verlet technique is possibly the most common integration scheme among all [117,118]. Utilizing the Taylor expansion, it uses the positions $\mathbf{r}_i(t)$ and accelerations $\mathbf{a}_i(t)$ at time t, and positions $\mathbf{r}_i(t - \Delta t)$ from the previous time step $t - \Delta t$, to calculate the new positions $\mathbf{r}_i(t + \Delta t)$ at the next time $t + \Delta t$ according to

$$\mathbf{r}_i(t + \Delta t) \approx 2\mathbf{r}_i(t) - \mathbf{r}_i(t - \Delta t) + \mathbf{a}_i(t)(\Delta t)^2. \tag{9}$$

The velocities $\mathbf{v}_i(t)$ and $\mathbf{v}_i\left(t + \frac{1}{2}\Delta t\right)$ at times t and $t + \frac{1}{2}\Delta t$ can be estimated as

$$\mathbf{v}_i(t) \approx \frac{\mathbf{r}_i(t + \Delta t) - \mathbf{r}_i(t - \Delta t)}{2\Delta t}, \tag{10}$$

$$\mathbf{v}_i\left(t + \frac{1}{2}\Delta t\right) \approx \frac{\mathbf{r}_i(t + \Delta t) - \mathbf{r}_i(t)}{\Delta t}. \tag{11}$$

A typical interaction potential U may consist of a number of bonded and nonbonded interaction terms. The bonded interactions may include bond stretching, bond angle bending, dihedral angle torsion, and inversion interaction potentials described by various functions such as harmonic functions. The nonbonded interactions contain electrostatic and van der Waals contributions and may consist of various potential types such as Lennard-Jones potential, Buckingham potential, Coulombic potential, etc. The concept of using interaction potentials makes it possible to carry out atomistic MD simulations which reveal the atomistic mechanisms and intrinsic structural properties by considering a relatively large number of particles.

While MD is shown to be a promising and reliable method in atomistic scale modelling, it has statistical limitations. A comparison of MC and MD methods suggests that in a phase space with 6N degrees of freedom, N being the total number of particles, MC allows one to investigate many more states than MD. Therefore, the validity of ensemble averages obtained by MD is limited to the assumption of system ergodicity; an assumption which is not unambiguously proven [64]. Still, the great power of MD is its proficiency to predict microstructure dynamics along its deterministic trajectory at an atomistic level. Applications of MD in the field of polymeric materials include topics such as macromolecular dynamics [119–124], intercalation phenomena in polymer/clay nanocomposites [63], structure of interfaces [125–127], polymer membranes [128,129], crystal structures [130–132], diffusion phenomena [133–136], segregation phenomena [137], tribological properties and crack propagation [138–140], thin films and surfaces [141–144], liquid crystalline polymers [145,146], rheology of polymeric systems [147–150], application of elongational flows on polymers using nonequilibrium MD [151,152], and the simulations of reactive systems such as crosslinking and decomposition of polymers using the ReaxFF force field [153–156].

2.3. Mesoscale Techniques

Atomistic simulations of complex systems including polymeric materials provide a detailed picture of, for instance, the interactions between components and conformational dynamics. Such information is often missing in macroscale models. On the other hand, the description of hydrodynamic behavior is relatively straightforward to handle in macroscale methods while it is challenging and expensive to address in atomistic models. Between the domains of these scale ranges, there is the intermediate mesoscopic scale which extends the time scale of atomistic methods. To show the importance of the time scale in the observed phenomena in soft matters, we take the lipid bilayers as an example. Bonds and angles of lipid molecules fluctuate within a time scale of a few picoseconds [157]. If the time scale is increased by an order of magnitude, trans-gauche isomerizations of dihedrals take place [158]. By further increasing the time scale to a few nanoseconds, the phospholipid molecule rotates around its axis. Moving on to longer time scales, two lipids can switch places in a bilayer on a time scale of tens of nanoseconds. Moreover, the individual lipid molecules orient and form membranes protrusions [159]. The peristaltic motions and undulations take place on a scale of 100 ns [160]. Finally, the steady transverse diffusion of lipids dominates on a time scale of 2 ms [161]. Simulating such a wide range of time scales in a single atomistic MD model needs large-scale computational resources. Consequently, the various mesoscale methods are developed which attempt to link atomistic and macroscale techniques and compensate for their shortcomings. Here, we briefly review BD, DPD and LB techniques which are often used at this scale. In addition to these methods, we also refer the interested reader to the stochastic multiparticle collision

model developed by Malevanets and Kapral [162] to investigate complex fluids such as polymers. This method was recently coupled with MD and an adaptive resolution hybrid model was achieved which is particularly interesting to study transport and hydrodynamic properties [163].

2.3.1. Brownian Dynamics

The motions of colloidal particles in dilute dispersions are a common example to introduce the BD method. Since the solvent molecules are often much smaller than the colloidal particles, the characteristic time of the motions of the solvent molecules is much smaller than that of the particles. Therefore, if one observes such dispersions based on the characteristic time of the solvent molecules in a MD framework, the suspended particles seem quiescent. In this case, a very long simulation time is necessary in order to observe the motions of particles. Hence, performing MD simulations is unrealistic when it is necessary, for instance, to trace a particle in time in order to calculate the diffusion coefficient. BD method overcomes this difficulty by replacing the explicit solvent molecules in MD with an implicit continuum medium. In BD simulations, the effects of the solvent molecules on the colloidal particles are defined by dissipative and random forces.

If the dispersion is dilute enough to neglect the hydrodynamic interactions between particles, the Brownian motion of particle i is generally described by the Langevin equation as [164]

$$m_i \frac{d^2 \mathbf{r}_i}{dt^2} = \mathbf{f}_i - \xi \mathbf{v}_i + \mathbf{f}_i^B. \tag{12}$$

In this equation, m_i, $\mathbf{r}_i$ and $\mathbf{v}_i$ are the mass, position and velocity vectors of the particle i, $\mathbf{f}_i$ is the sum of the forces exerted on particle i by the other particles, and ξ is the friction coefficient. Here, $\mathbf{f}_i^B$ is the random force inducing the Brownian motions of the particle due to the motions of solvent molecules. The random force should be independent of the particle position and velocity and is described by its stochastic properties

$$\left\langle \mathbf{f}_i^B(t) \right\rangle = 0, \tag{13}$$

$$\left\langle \mathbf{f}_i^B(t) \cdot \mathbf{f}_i^B(t') \right\rangle = A\delta(t - t'), \tag{14}$$

where $\delta(t - t')$ is the Dirac delta function and $A = 6\xi k_B T$. The position and velocity of each particle in time is therefore described as

$$\mathbf{r}_i(t + \Delta t) = \mathbf{r}_i(t) + \frac{m_i}{\xi}\mathbf{v}_i(t)\left(1 - e^{-\frac{\xi}{m_i}\Delta t}\right) + \frac{1}{\xi}\mathbf{f}_i(t)\left(\Delta t - \frac{m_i}{\xi}\left(1 - e^{-\frac{\xi}{m_i}\Delta t}\right)\right) + \delta\mathbf{r}_i^B(t + \Delta t), \tag{15}$$

$$\mathbf{v}_i(t + \Delta t) = \mathbf{v}_i(t)e^{-\frac{\xi}{m_i}\Delta t} + \frac{1}{\xi}\mathbf{f}_i(t)\left(1 - e^{-\frac{\xi}{m_i}\Delta t}\right) + \delta\mathbf{v}_i^B(t + \Delta t). \tag{16}$$

The terms $\delta\mathbf{r}_i^B(t + \Delta t)$ and $\delta\mathbf{v}_i^B(t + \Delta t)$ represent a random displacement and velocity change due to the random forces. One can utilize a two-dimensional normal distribution to sample these terms based on random numbers [165]. Consequently, the positions and velocities of the particles can be updated in every time step during the simulations. It should be noted that the momentum is not conserved in the formulation of BD due to the random noise terms. As a result, BD cannot reproduce correct hydrodynamics and is limited to the prediction of diffusion properties [164,166,167].

If the dispersion is not dilute and the hydrodynamic interactions between the particles are not negligible, the above equations should be modified. Ermak and McCammon [168] have introduced such effects into BD. In their method, the diffusion tensor is utilized to re-write the Langevin equation. Recently, Ando et al. [169] suggested to use Krylov subspaces for computing Brownian random noise vectors. Their method facilitates performing large-scale BD simulations with hydrodynamic interactions. They showed that only low accuracy is required in the Brownian noise vectors to accurately evaluate dynamic and static properties of model polymer and monodisperse suspensions. BD has been incorporated to study a variety of phenomena including particle dispersions [170–177],

polymer solutions [178–181], confined suspensions [182], peeling behavior of polymer molecules from a surface [183], and translocation of complex molecules through nanopores [184,185].

2.3.2. Dissipative Particle Dynamics

DPD is a relatively new mesoscopic particle simulation method proposed by Hoogerbrugge and Koelman in 1992 [186]. Fundamentally, DPD is similar to MD except for the fact that individual DPD particles (which are often referred to as beads in the literature) represent the dynamic behavior of several atoms or molecules. This coarse-graining strategy along with the softer potential functions incorporated to represent bead-bead interactions allow for the simulation of dynamic processes over longer time scales [187,188].

In DPD, the motion of each bead is dominated by three pairwise forces. For bead i with the mass m_i and position vector $\mathbf{r}_i$, the Newton's equation of motion becomes

$$m_i \frac{d^2 \mathbf{r}_i}{dt^2} = \sum_j (F_{ij}^C + F_{ij}^D + F_{ij}^R), \tag{17}$$

in which F_{ij}^C, F_{ij}^D, and F_{ij}^R are respectively the conservative, the dissipative, and the random forces between bead i and its neighboring beads within a certain force cutoff radius r_{cut}. These forces are defined as [187]

$$F_{ij}^C = \mathbb{A}_{ij}\chi_{ij}\left(1 - \frac{r_{ij}}{r_{cut}}\right)\hat{\mathbf{r}}_{ij}, \tag{18}$$

$$F_{ij}^D = -\xi_{ij}\omega^D(\mathbf{r}_{ij})\mathbf{r}_{ij}[(\mathbf{v}_i - \mathbf{v}_j)\cdot\hat{\mathbf{r}}_{ij}]\hat{\mathbf{r}}_{ij}, \tag{19}$$

$$F_{ij}^R = \sigma_{ij}\omega^R(\mathbf{r}_{ij})\mathbf{r}_{ij}\zeta_{ij}\hat{\mathbf{r}}_{ij}. \tag{20}$$

Here, $\mathbf{r}_{ij}$ is the distance between the beads i and j, is the unit vector pointing from the center of bead j to that of bead i, χ_{ij} equals 1 for beads with a distance less than r_{cut} and equals 0 otherwise. $\mathbf{v}_i$ and $\mathbf{v}_j$ are the velocity vectors of the ith and jth beads, respectively. ζ_{ij} is a Gaussian random number with zero mean and unit variance. $\mathbb{A}_{ij}$ is the maximum repulsion between bead i and bead j. ξ_{ij} and σ_{ij} are the friction coefficient and the noise amplitude between bead i and bead j, respectively. $\omega^D(\mathbf{r}_{ij})$ and $\omega^R(\mathbf{r}_{ij})$ are dissipative and random weight functions, respectively. DPD simulations often obey the fluctuation-dissipation theorem in which one of the two weight functions fixes the other one [189]. This theory dictates that the random and dissipative terms must be administered in a particular way in order to maintain the correct Boltzmann distribution in equilibrium. As a consequent of this theory, one has

$$\omega^D(r_{ij}) = \left[\omega^R(r_{ij})\right]^2, \tag{21}$$

$$\sigma_{ij}{}^2 = 2\xi_{ij}k_BT. \tag{22}$$

These relationships ensure an equilibrium distribution of bead velocities for thermodynamic equilibrium. In many studies, the weight functions are

$$\omega^D(r_{ij}) = \left[\omega^R(r_{ij})\right]^2 = \chi_{ij}\left(1 - \frac{r_{ij}}{r_{cut}}\right)^2. \tag{23}$$

Due to the pairwise nature of the forces involved in DPD framework, all of the beads obey Newton's third law [190]. As a result, the sum of all forces in the system vanishes. Furthermore, any given volume of beads in the system is only accelerated by the sum of all forces that cross its boundaries. This is the fundamental assumption which results in the Navier-Stokes equation. Consequently, DPD formulation conserves hydrodynamics [187,190,191]. If the random force was not pairwise as in BD formulation see Equation (12), momentum would not be conserved [164,165].

At every time step during the simulation, the set of positions and velocities of the beads is updated utilizing the positions and velocities at the earlier time. In principle, all algebraic update algorithms from MD can be used in DPD. However, the dependence of forces on velocity in DPD complicates the algorithm. A common approach to solve this problem is to use a modified version of the velocity-Verlet algorithm [117,118,187]. For bead i with unit mass and the overall force $\mathbf{f}_i$ over a short interval of time Δt, the algorithm suggests

$$\mathbf{r}_i(t + \Delta t) \approx \mathbf{r}_i(t) + \mathbf{v}_i(t)\,\Delta t + \frac{1}{2}\mathbf{f}_i(t)(\Delta t)^2, \tag{24}$$

$$\widetilde{\mathbf{v}}_i(t + \Delta t) \approx \mathbf{v}_i(t) + \lambda\,\mathbf{f}_i(t)\,\Delta t, \tag{25}$$

$$\mathbf{f}_i(t + \Delta t) \approx \mathbf{f}_i(\mathbf{r}_i(t + \Delta t), \widetilde{\mathbf{v}}_i(t + \Delta t)), \tag{26}$$

$$\mathbf{v}_i(t + \Delta t) \approx \mathbf{v}_i(t) + \frac{1}{2}\Delta t\,(\mathbf{f}_i(t) + \mathbf{f}_i(t + \Delta t)). \tag{27}$$

In this algorithm, the velocity in the next time step is first estimated by a predictor method, i.e., $\widetilde{\mathbf{v}}_i(t + \Delta t)$ and then corrected in the last step, i.e., $\mathbf{v}_i(t + \Delta t)$. If the forces were independent of velocity, the actual velocity-Verlet algorithm would be recovered for $\lambda = 0.5$. The parameter λ has been shown to affect the temperature in DPD simulations by Den Otter and Clarke [192]. Based on empirical observations, some authors suggest $\lambda = 0.65$ would yield an accurate temperature control probably due to the cancellation of errors [190].

In recent years, modified versions of DPD formulation have been developed. For instance, Pan et al. [193] formulated DPD by borrowing ideas from fluid particle model. This approach enabled an explicit separation of dissipative forces into central and shear components. As a further consequence of this methodology, the hydrodynamics of Brownian colloidal suspensions were correctly captured by redistributing and balancing the forces. In another study, Yamanoi et al. [194] replaced the conservative forces with entanglement forces in the force field to reproduce the physics of entangled polymers. In this way, they could successfully simulate static as well as dynamic behavior of linear polymer melts. Despite these efforts, the standard DPD has also shown quite capable of simulating complex systems such as compatibilized and uncompatibilized polymer/clay nanocomposites under shear flows [195,196]. Various polymeric systems have been successfully treated in the DPD framework such as blood rheology [197–199], rheology of ultrahigh molecular weight polymers [200], lipid bilayers [161], adsorption characteristics of confined PE glycols dissolved in water [201], crosslinking of thermoset resins and formation of a network in the bulk [202], structure of thermoset polymers near an alumina substrate [203], graphene structure [204], surfactant aggregation [205], photo degradation process of polymer coatings [71], distribution of nanoparticles in lamellar and hexagonal diblock copolymer matrices [206,207], surface segregation and self-repairing systems [208–210], and electrical percolation threshold in packed assemblies of oriented fiber suspensions [211].

2.3.3. Lattice Boltzmann

While BD and DPD techniques borrow ideas from MD to tackle the challenges at the mesoscale, some other methods such as lattice gas cellular automata (LGCA) and LB incorporate kinetic theory concepts. In this part of the paper, we briefly point out the fundamental ideas of LGCA at first and afterwards introduce LB as a pre-averaged version of LGCA.

LGCA was initially designed to overcome the computational limitations in the study of fluids at high Reynolds numbers (Re) [212]. In this method, the particles of fluid are bound to move on the nodes of a discrete lattice at discrete time steps. At each time step particles can move from one lattice node to a neighboring node according to a set of prescribed velocity vectors $\{\mathbb{v}_k\}$ which connect the neighboring nodes. In addition, only single occupancy is allowed for each possible velocity at a given node. The dynamics has two steps according to LGCA: (i) a propagation step, and (ii) a collision step. In the propagation step, also known as the streaming step, the particles move from their current node to an empty neighboring node with respect to their velocity. In the collision step, the particles collide and scatter according to certain rules which honor the mass and momentum conservation. In this way the Navier-Stokes equations are simulated correctly provided that the lattice and the velocity space are chosen carefully [164,165]. Although LGCA is unconditionally stable, it does not allow as large Re as it was initially thought [166].

LB inherits the discretized lattice dynamics based on propagation and collision steps from LGCA. However, it incorporates a one-particle distribution function as the relevant dynamic variable instead of the particle-based dynamics in LGCA. Initially, the collisions in LB is modelled by pre-averaging the collision schemes in the underlying LGCA model [213]. The resulting collision mechanism is then presented by a linearized collision matrix in which the distribution function relaxes toward a local equilibrium distribution [214,215]. In the LB scheme, thermal noises are not present which makes it much more efficient in comparison with LGCA for hydrodynamic problems. On the other hand, the intrinsic stability of LGCA is lost in LB. It should be noted that both LGCA and LB methods suffer from Galilean invariance problems and should be corrected for these limitations [166].

The particle distribution function $\Psi_i(\mathbf{r}, t)$ used in LB gives the density of particles at node $\mathbf{r}$ at time t moving with velocity $\mathbb{v}_i$ in the i-direction. The lattice in which this density moves is characterized by both the sets of constructing nodes and the velocity subspace $\{\mathbb{v}_k\}$. The velocity subspace determines the neighboring nodes to which a given density will be able to move in a time step. The lattice symmetry and the minimum allowed set of velocities should satisfy the requirement of a minimum set of symmetry properties. Otherwise, the underlying anisotropy of the lattice might affect the hydrodynamic behavior of the system. Figure 1 shows two lattice examples often used in two- and three-dimensional LB simulations. These lattices define 9 and 19 allowed velocities (including the quiescent state) and are thus named D2Q9 and D3Q19, respectively.

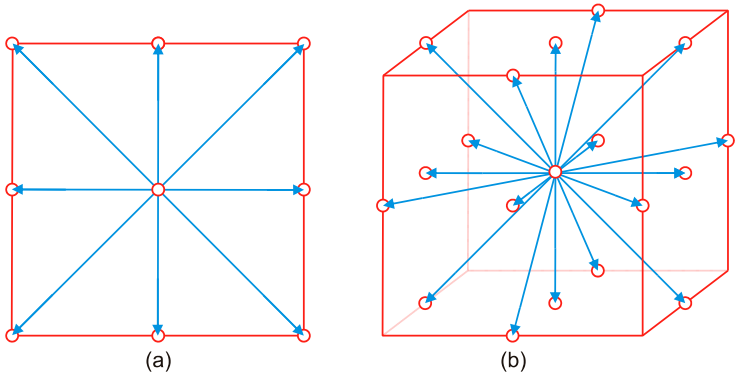

Figure 1. Two typical lattices often used in LB simulations: (**a**) D2Q9; and (**b**) D3Q19.

The densities $\Psi_i(\mathbf{r}, t)$ are the elementary dynamical variables in LB. The macroscopic local density $\rho(\mathbf{r}, t)$ and velocity $\mathbf{v}(\mathbf{r}, t)$ at position $\mathbf{r}$ can be evaluated based on $\Psi_i(\mathbf{r}, t)$ as

$$\rho(\mathbf{r}, t) = \sum_k \Psi_k(\mathbf{r}, t), \tag{28}$$

$$\rho(\mathbf{r},t)\,\mathbf{v}(\mathbf{r},t) \;=\; \sum_k \mathbb{v}_k \Psi_k(\mathbf{r},t), \tag{29}$$

in which the summation is performed over all allowed velocities. It is obvious that the local macroscopic properties can be evaluated with time, if the evolution of the particle distribution function is known. In LB the elementary two-step evolution (i.e., propagation and collision) of the particle distribution function after a time step Δt can be written in a condensed format as

$$\Psi_i(\mathbf{r} \,+\, \mathbb{v}_k \Delta t\,,\; t \,+\, \Delta t) \;=\; \Psi_i(\mathbf{r},t) \,+\, \sum_k \mathbf{\Lambda}_{ik}(\Psi_k(\mathbf{r},t) \,-\, \Psi_k^{eq}(\mathbf{r},t)), \tag{30}$$

where the index k spans the velocity subspace, $\Psi_k^{eq}(\mathbf{r},t)$ is the equilibrium distribution function and $\mathbf{\Lambda}_{ik}$ is the collision matrix. The simplest form of the collision matrix was proposed by Bhatnagar, Gross, and Krook (BGK) as $\mathbf{\Lambda}_{ik} \;=\; -\frac{1}{\tau}\delta_{ik}$ where τ is the collision time [216,217]. This method produces reasonably accurate solutions despite its simplicity [164]. The simplified form of Equation (30), i.e., the BGK-LB method, consequently is

$$\Psi_i(\mathbf{r} \,+\, \mathbb{v}_k \Delta t\,,\; t \,+\, \Delta t) \;=\; \Psi_i(\mathbf{r},t) \,+\, \frac{1}{\tau}(\Psi_i^{eq}(\mathbf{r},t) \,-\, \Psi_i(\mathbf{r},t)). \tag{31}$$

The equilibrium distribution function $\Psi_i^{eq}(\mathbf{r},t)$ needs to be defined before one can use Equation (31) to simulate a system. This is done by requiring that mass and momentum must be conserved [166]. A suitable form for the equilibrium distribution is often a quadratic function in velocities as [164]

$$\Psi_i^{eq} = \;\rho \mathrm{w}_i \left[1 \,+\, 3\frac{\mathbb{v}_i\cdot\mathbf{v}}{\mathbb{v}^2} \,-\, \frac{3}{2}\cdot\frac{\mathbf{v}^2}{\mathbb{v}^2} \,+\, \frac{9}{2}\cdot\frac{(\mathbb{v}_i\cdot\mathbf{v})^2}{\mathbb{v}^4}\right]. \tag{32}$$

Here, $\mathbb{v} \;=\; \sqrt{3}\,\mathbb{v}_s$ where $\mathbb{v}_s$ is the speed of sound, and w_i is the weighting constant. For D2Q9 lattice, w_i is

$$\mathrm{w}_i \;=\; \begin{cases} \frac{4}{9} & \text{for } i \;=\; 0 \\ \frac{1}{9} & \text{for } i \;=\; 1,\,2,\,3,\,4 \\ \frac{1}{36} & \text{for } i \;=\; 5,\,6,\,7,\,8 \end{cases} \quad \text{and } |\mathbb{v}_i| \;=\; \begin{cases} 0 & \text{for } i \;=\; 0 \\ \mathbb{v} & \text{for } i \;=\; 1,\,2,\,3,\,4 \\ \sqrt{2}\mathbb{v} & \text{for } i \;=\; 5,\,6,\,7,\,8 \end{cases}, \tag{33}$$

and for D3Q19 lattice, it is defined as

$$\mathrm{w}_i \;=\; \begin{cases} \frac{1}{3} & \text{for } i \;=\; 0 \\ \frac{1}{18} & \text{for } i \;=\; 1,\,2,\,\ldots,\,6 \\ \frac{1}{36} & \text{for } i \;=\; 7,\,8,\,\ldots,\,18 \end{cases} \quad \text{and } |\mathbb{v}_i| \;=\; \begin{cases} 0 & \text{for } i \;=\; 0 \\ \mathbb{v} & \text{for } i \;=\; 1,\,2,\,\ldots,\,6 \\ \sqrt{2}\mathbb{v} & \text{for } i \;=\; 7,\,8,\,\ldots,\,18 \end{cases}. \tag{34}$$

In the algorithm of BGK-LB method, one also needs to provide precise description of the boundaries of the system [164,165]. The discrete distribution function of LB on the boundaries has to be taken carefully so that it represents correct macroscopic boundaries of the system. LB has found various applications in polymer science [218], for instance, polymer solutions [133,178,219,220], simulation of complex flows [221,222], polymer electrolyte fuel cells [223], liquid crystals [224–226], deformation of droplets containing polymers and nanoparticles [227], and thermal conductivity and permeability of fibrous materials [228,229].

2.4. Macroscale Techniques

At the macroscopic scale, it is a common practice to disregard the discrete atomistic and molecular structures and assume that the material is continuously distributed throughout its volume. This approach is applicable provided that the behavior of the collections of atoms and molecules of the materials can be homogenized based on a proper understanding of the structures at the finer scales. Consequently, this scale is often referred to as the continuum scale in the literature. The continuum material is often assumed to possess average physical properties such as density, heat capacity, thermal

conductivity, etc. and can be subjected to body forces such as gravity and surface forces such as contact between two bodies.

In general, the macroscale methods obey several fundamental laws [2,30]. These laws are (i) conservation of mass; (ii) equilibrium, based on Newton's second law; (iii) the moment of momentum law, in which the moment is equal to the time derivative of angular momentum with respect to a reference point; (iv) conservation of energy; and finally (v) the conservation of entropy. Although these principles define the fundamentals for a macroscale model, they still need to be completed with suitable constitutive laws and the equations of state to provide all the information necessary in order to solve a macroscopic problem. It is noteworthy that the derivation of proper constitutive equations for polymeric systems has been an intriguing topic ever since the viscoelasticity concepts were introduced [230]. Various models are put forward with advantages as well as shortcomings often as a result of being limited to a certain class of either polymer systems or phenomena. Moreover, the implementation of usually complex viscoelastic constitutive equations results in extremely heavy calculations.

The continuum models often lead to a set of partial differential equations. In simple cases, it might be possible to find a closed-form analytical solution for the problem. However, it is often necessary to utilize appropriate numerical approaches to evaluate the solution due to the complexity of the involved phenomena. Finite difference method (FDM) is the simplest numerical method developed so far from a mathematical point of view. This simplicity comes with the price of losing flexibility for use with complicated geometries and phenomena compared with more elaborate numerical schemes such as finite element method (FEM) and finite volume method (FVM). It should be emphasized that all of these approaches are merely mathematical methods to estimate the solution of a set of partial differential equations and do not include a definite physical meaning in their bare core. Hence, they are not solely limited to the macroscale phenomena and the founding ideas behind them can also be applied to other scales. These numerical schemes ultimately transform the set of partial differential equations into a system of linear algebraic equations and solve it using either direct approaches, such as Gauss' method, or iterative approaches, such as Gauss-Seidel method [231].

It should be noted that the macroscale techniques do not always deal with a continuous medium. For instance, smoothed particle hydrodynamics (SPH) is one such particle-based method which has been applied to study a number of phenomena including viscoelastic flows [232,233]. Moreover, the thermodynamically consistent version of SPH is named smoothed dissipative particle dynamics (SDPD) and has been implemented in multiscale frameworks to link the macroscopic SPH to the mesoscopic DPD method [234–236]. In its essence, SPH utilizes particles moving with the flow which make it possible to evaluate hydrodynamic properties at particle positions by a weighted averaging of the local values. Therefore, every particle is practically "smoothed" over a finite volume with fixed mass. For this part of the paper, we focus our attention to two widely-used mathematical methods in macroscale calculations, i.e., FEM and FVM.

2.4.1. Finite Element Method

FEM is a powerful method to solve equations in integral form. Two possibilities exist for the application of FEM. In the first case, there exists an integral form of the physical problem. This integral form can be a result of a variational principle, the minimum of which corresponds to the solution, or more generally an integral equation to solve [231]. In the second case, an integral formulation must be obtained from an initial system of partial differential equations by a weak formulation, also called the weighted residual method [231].

A prerequisite of utilizing FEM is to decompose the spatial domain under consideration into a set of elements of arbitrary shape and size. This discretization is often called a grid or a mesh. In the decomposition procedure, the only restriction is that elements cannot overlap nor leave any zone of the domain uncovered. The definition of a mesh for FEM is more free compared with FDM for which the grid follows a coordinate system. For each element in FEM, a certain number of points, called nodes, must be defined which can be situated either on the edges of the element or inside it. The nodes are then used to construct the approximations of the functions under consideration over the entire domain by interpolation.

The approximation of a function $\mathrm{u}(\mathbf{r})$, where $\mathbf{r}$ is the vector of spatial coordinates, on a geometric domain meshed with finite elements is obtained as a linear combination of interpolation functions $\psi_n(\mathbf{r})$ associated with the mesh. If $\mathrm{u}_h(\mathbf{r})$ is the approximation of the function $\mathrm{u}(\mathbf{r})$ under consideration, it can be expressed in the form of a sum over the nodes of the domain by

$$\mathrm{u}_h(\mathbf{r}) \;=\; \sum_{n=1}^{\mathrm{N}} \mathrm{u}^n \psi_n(\mathbf{r}), \tag{35}$$

in which N is the total number of nodes. The interpolation functions $\psi_n(\mathbf{r})$ can be of diverse forms with different degrees of continuity and differentiability. In the standard FEM, these functions are defined locally at the level of each element. Therefore, if the node n belongs to element e, and if ψ_n^e is used to denote the restriction of ψ_n within the element, for every coordinate vector $\mathbf{r}$ outside the element e, one has

$$\psi_n^e(\mathbf{r}) \;=\; 0, \tag{36}$$

and for every coordinate vector $\mathbf{r}$ inside the element e,

$$\mathrm{u}_h(\mathbf{r}) \;=\; \sum_{n\,=\,1}^{\mathrm{N}} \mathrm{u}^n \psi_n(\mathbf{r}) \;=\; \sum_{n\in\, e} \mathrm{u}^n \psi_n^e(\mathbf{r}). \tag{37}$$

The last sum is performed only over the nodes that constitute the element e. Consequently, the interpolation used for approximation is locally defined at the level of each finite element. This way of decomposition and approximation thus distinguishes the standard FEM from other methods using interpolation functions defined over the entire domain. Moreover, in the standard FEM, the coefficients u^n are the values of the function u_h at the nodes of the mesh. As a result, the interpolation functions must satisfy two conditions in addition to Equation (36). First, if n and p are two nodes of the same element e, and $\mathbf{r}^p$ is the position vector of the node p, then

$$\psi_n^e(\mathbf{r}^p) \;=\; \delta_{np}, \tag{38}$$

where δ_{np} is the Kronecker delta function. Second, to exactly represent constant functions, for all $\mathbf{r}$ inside the element e including the borders

$$\sum_{n\in\, e} \psi_n^e(\mathbf{r}) \;=\; 1. \tag{39}$$

In most cases, the integral form of the problem should be also constructed from partial differential equations. For a simple case where the problem is limited to solve one partial differential equation of the form $\mathrm{R}(\mathrm{u}) \;=\; 0$ on domain Ω, one can utilize the weighted residual method to obtain the equivalent integral form. In the context of FEM, $\mathrm{R}(\mathrm{u})$ is often called the residual value. Obviously, the solution of the problem zeros the residual and simultaneously satisfies the boundary conditions at $\partial\Omega$. The basic idea in FEM is to search for functions u which zero the integral form

$$\Phi(\mathrm{u}) = \int_{\Omega} \rho\, \mathrm{R}(\mathrm{u})\, \mathrm{dV} \;=\; 0, \tag{40}$$

for every weighting function ρ belonging to a set of functions $\{S_\rho\}$, while u satisfies the boundary conditions at $\partial\Omega$. The equivalence between $R(u) = 0$ on Ω and Equation (40) is only true if the set $\{S_\rho\}$ has infinite dimensions and is composed of independent functions [231]. Otherwise, if $\{S_\rho\}$ is finite as in FEM, the solution u which satisfies Equation (40) is only an approximate solution to the problem.

It should be noted that the weighted residual method is not the only method which can be used to search for a function that zeros the residual $R(u)$ on Ω. For instance, the least-squares method can be applicable in some cases despite its limitations. The principle of least-squares consists of searching for the function u that minimizes the integral

$$f(u) = \int_\Omega (R(u))^2 \, dV, \tag{41}$$

and that respects the boundary conditions. However, it is often difficult to employ the boundary conditions in this formalism. Furthermore, the order of derivatives in R cannot be reduced which leads to high differentiability conditions on the finite element discretization [231]. For these reasons, the method of weighted residuals is often preferred.

For the discretization of the obtained integral form, N independent weighting functions ρ_1, ρ_2, ρ_3, ... , ρ_N are utilized. There are different approaches to define the type of ρ_i functions. The most used approach is the Galerkin method which defines the weighting functions precisely the same as the interpolation functions ψ_n of the approximation by finite elements [231]. Therefore, Equation (40) can be written as

$$\Phi(u) = \int_\Omega \psi_n \, R(\textstyle\sum_{n=1}^{N} u^n \psi_n) \, dV = 0. \tag{42}$$

This integral equation is later turned into a sum of finite series over the nodes of the domain. The boundary conditions are usually implemented into this integral form benefitting from the divergence theorem [231]. In the algorithm of FEM, for every element e a mapping can be defined between the element in physical space and a reference element, which allows defining the interpolation functions universally for the diverse elements regardless of their coordinates [231]. This notion facilitates programming profoundly.

FEM has been implemented in several simulation packages and consequently can be easily used by both academic and industrial communities, in a variety of applications. To name a few instances in polymer science, we note the prediction of the failure behavior of adhesives [237,238], the study of elastic modulus of polymer/clay nanocomposites [239], the prediction of temperature distribution in a tissue-mimicking hydrogel phantom during the application of therapeutic ultrasound [240], the wall slippage in the extrusion of highly-filled wood/polymer composites [241,242], the torsional friction behavior in hydrogels [243], permeation analysis in polymer membranes [244], viscoelastic flow analysis [245–247], and droplet deformation [248]. A significant improvement of the precision of FEM was achieved by Patera [249] when it was combined with spectral techniques. The resulting algorithm is generally known as the spectral element method (SEM). SEM is more stable and accurate than FEM under a relatively broad range of conditions [250]. Due to its power and versatility, SEM has shown to be a promising candidate to solve the viscoelastic models in the simulations of complex polymer flows [251,252].

2.4.2. Finite Volume Method

FDM and FEM are admittedly the two most important classes of numerical methods for partial differential equations. However, they both suffer from serious shortcomings. The main defects of FDM are: (i) the considerable geometrical error of the approximation of curved domains by rectangular grids; (ii) the lack of an effective approach to deal with natural and internal boundary conditions; and (iii) the difficulty to construct difference schemes with high accuracy unless the difference equation is allowed to relate more nodal points and thus further complicating the incorporation of boundary conditions.

Classic FEM methods, i.e., Galerkin FEM (GFEM), perform successfully in fields such as solid mechanics and heat conduction where the problem is governed by self-adjoint elliptic or parabolic partial differential equations. Unfortunately, this success did not continue in the field of fluid dynamics. The reason was ascribed to the convection operators in the Eulerian formulation of the governing equations which render the system of equations non-self-adjoint [253]. Consequently, solutions to non-self-adjoint fluid dynamic problems by GFEM often suffer from node to node oscillations. This problem has motivated the development of alternatives to the GFEM which preclude oscillations without requiring mesh or time step refinement. The streamline-upwind/Petrov-Galerkin (SUPG) [254,255] and the least-squares finite element [231,256] methods are two examples of such approaches. Some authors also attempted to develop a strategy in FEM which employs a least-squares method for first-order derivatives and a Galerkin method for second-order derivatives in the governing Navier-Stokes equations [257]. Nevertheless, the simplicity of calculations and development of simulation algorithms is usually hindered by such approaches.

As a result, the search for a simple yet accurate alternative to FEM was carried out benefiting from FDM concepts and coupling it with finite element spaces in order to derive the so-called generalized differences methods (GDM) [253]. GDM provides several advantages such as small geometrical errors, easy handling of natural boundary conditions, and maintaining conservation of mass. With GDM, one is supplied with a method with the computational effort greater than classic FDM and less than FEM while the accuracy is higher than FDM and nearly the same as FEM. Due to its advantages, in particular its inheritance of the mass conservation law, GDM was rapidly developed in computational fluid dynamics (CFD) most popularly called FVM. FVM is also referred to as the finite control volume method which is a discrete estimation of a certain control equation in an integral form [258–260]. Hence, FVM is basically equivalent to GDM with piecewise constants and piecewise linear elements. Using FVM to develop numerical algorithms for nonlinear equations is in fact generalizing the classical difference schemes to irregular meshes. The equivalence of FDM and FVM has been shown in simple cases for instance by Rappaz et al. [231].

Although FVM has been applied to many applications including magnetohydrodynamics [261–263], structural dynamics [264,265], and semiconductor theory [266,267], its main field of application has been CFD mainly due to its conservative nature. Consequently, we restrict ourselves to this field in the rest of this section. Similar to FDM and FEM, FVM changes a set of partial differential equations with a system of linear algebraic equations. In order to do this, FVM utilizes a two-step discretization procedure [268]. First, the partial differential equations are transformed into balance equations by integration. In this transformation the surface and volume integrals are changed into discrete algebraic equations over individual elements benefitting from an integration quadrature. A set of semi-discretized equations is then produced. Second, the local values of the variables in the elements are approximated by using suitable interpolation profiles. For a general scalar variable ϑ, one can write the steady state conservation equation as

$$\nabla\cdot(\rho\mathbf{v}\vartheta) \;=\; \nabla\cdot(\mathbf{D}^{\vartheta}\nabla\vartheta) + Q^{\vartheta}, \tag{43}$$

where ρ is the fluid density, **v** is the fluid velocity vector, $\mathbf{D}^{\vartheta}$ is the diffusion coefficient of ϑ, and Q^{ϑ} is the generation/destruction of ϑ in the control volume per unit volume. By integrating the above equation over the element e and utilizing the divergence theorem, one finds

$$\oint_{\partial V_e} (\rho \mathbf{v} \vartheta) \cdot d\mathbf{S} = \oint_{\partial V_e} (\mathbf{D}^{\vartheta} \nabla \vartheta) \cdot d\mathbf{S} + \int_{V_e} Q^{\vartheta} \, dV, \tag{44}$$

in which **S** represents the surface vector, and ∂V_e shows that the integration is performed over all the surfaces surrounding the volume V_e. The semi-discrete steady state equation for e can be finally simplified to [268]

$$\sum_{\varepsilon \sim neighboring\ cells\ of\ e} (\rho \mathbf{v} \vartheta - \mathbf{D}^{\vartheta} \nabla \vartheta)_{\varepsilon} \cdot \mathbf{S}_{\varepsilon} = Q_{\varepsilon}^{\vartheta} V_{\varepsilon}, \tag{45}$$

by using the mid-point integration approximation. The summation is performed over the faces surrounding element e with its neighboring cells. Here, Q_e^{ϑ} is the contribution of element e to Q^{ϑ}. If one denotes the convection and diffusion flux terms by $\mathbf{J}^{\vartheta,C}$ and $\mathbf{J}^{\vartheta,D}$, respectively, one can write Equation (45) in the form

$$\sum_{\varepsilon \sim neighboring\ cells\ of\ e} (\mathbf{J}^{\vartheta,C} + \mathbf{J}^{\vartheta,D})_{\varepsilon} \cdot \mathbf{S}_{\varepsilon} = Q_{\varepsilon}^{\vartheta} V_{\varepsilon}, \tag{46}$$

where $\mathbf{J}^{\vartheta,C} = \rho \mathbf{v} \vartheta$ and $\mathbf{J}^{\vartheta,D} = -\mathbf{D}^{\vartheta} \nabla \vartheta$. In FVM, the transported variable ϑ is conserved in the discretized solution domain since the fluxes at a face of an element are calculated using the values of the elements which share that face [268]. As a result, for any mutual surface of two elements, the outwards flux from a face of an element is precisely equal to the inwards flux from the other element through that same face. Consequently, such fluxes are equal in magnitude but with opposite signs.

To get the fully-discretized steady state finite volume equation for element e, one needs to adjust proper interpolation profiles. The interpolation profiles are often different for diffusive and convective terms due to the distinct physical phenomena that these terms represent. For the diffusive term, a linear interpolation profile is often used [268]. The selection of an interpolation profile for the convective terms could be more challenging. The simplest interpolation scheme, i.e., the symmetrical linear profile or the central difference scheme, could be applied here. Despite its simplicity, this scheme can result in unbounded unphysical behavior at high Peclet numbers (Pe) due to the fact that it cannot describe the directional preference of convection [268]. Consequently, the upwind scheme was introduced to account for this directional preference and provide a better stability at the cost of the accuracy. This is due to the fact that the upwind scheme has a first order of accuracy whereas the linear scheme has a second order of accuracy [269]. In order to enhance the precision and stability of advection schemes, higher-order upwind biased interpolation profiles were incorporated in the calculations. Such higher-order schemes often produce at least a second-order accurate solution, while they are unconditionally stable. An example of such attempts is the quadratic upstream interpolation for convective kinematics (QUICK) scheme developed by Leonard [270]. In this method, the value of the dependent variable is interpolated at each element face using a quadratic polynomial biased towards the upstream direction. Further details can be found elsewhere [268].

In recent years, the application of FVM in CFD has been significantly accelerated, mostly because of the emerging open source software packages such as OpenFOAM® (Open Source Field Operation and Manipulation) [271,272]. Analysis of viscoelastic fluids [273–279], viscoelastic two-phase flows [280], mold filling in water-assisted injection molding of viscoelastic polymers [281], gas permeation in glassy polymer membranes [282], blood flow [283], development of droplet and co-continuous binary polymer microstructures [284] are some examples of FVM applications in polymer science.

3. Multiscale Strategies

The ultimate purpose of a multiscale modelling is to predict the macroscopic behavior from the first principles at the quantum scale. Finding appropriate protocols for multiscale simulations is on

the other hand a very challenging topic. This is due to the fact that polymeric materials often display phenomena on one scale that necessitate a precise description of other phenomena on another scale. Since none of the methods discussed before is sufficient alone to describe a multiscale system nor they are designed for such a purpose, the goal becomes to develop a proper combination of various methods specialized at different scales in a multiscale scheme. This scheme is also supposed to effectively distribute the computational power where it is needed most. By definition, such a multiscale approach can take advantage of the various methods it envelops at multiple scales and reaches the length and time scale that the individual methods fail to achieve. At the same time, this approach can retain the precision provided by the individual methods in their respective scales. Moreover, the multiscale approach should be flexible enough to allow for high accuracy in particular regions of the systems as required. Therefore, the overall objective of multiscale models is to predict the behavior of materials across all significant length and time scales while preserving a balance among precision, efficiency, and realistic description.

In general, there are three main categories of multiscale approaches: sequential, concurrent, and adaptive resolution schemes. The sequential approach links a series of computational schemes in which the operative methods at a larger scale utilize the coarse-grained (CG) representations based on detailed information attained from smaller scale methods. Sequential approaches are also known as implicit, serial, or message-passing methods. The second group of multiscale approaches, the concurrent methods, are designed to bridge the suitable schemes of each individual scale in a combined model. Such a model accounts for the different scales involved in a physical problem concurrently and incorporates some sort of a handshaking procedure to communicate between the scales. Concurrent methods are also called parallel or explicit approaches. It is noteworthy that multiscale simulations could principally utilize a hybrid scheme based on elements from both sequential and concurrent approaches. More recently, a new concept for multiscale simulations has been developed which resembles some characteristics of concurrent methods. In this approach, single atoms or molecules can freely move in the simulation domain and switch smoothly from one resolution to another, for instance based on their spatial coordinates, within the same simulation run. Consequently, these methods are generally referred to as the adaptive resolution simulations. Details of such techniques are provided in the following sections. Finally, there are a number of advanced techniques which allow for extending the reach of a single-scale technique such as MD within certain conditions. Such methods are also reviewed for the sake of completeness before closing the discussion of multiscale strategies.

3.1. Sequential Multiscale Approaches

In sequential approaches, calculations are often performed at a smaller scale (the more detailed, finer scale) and the resulting data are passed to a coarser model at a larger scale after leaving out unnecessary details for instance by coarse-graining. However, it will be shown that in some cases the reverse procedure can also be done. A sequential multiscale model requires a thorough understanding of the fundamental processes dominating the finest scale to yield accurate information. Afterwards, it is also crucial to have a well-founded approach to introduce this information into the coarser scales. Such a strategy is usually achieved by utilizing phenomenological theories which contain some key parameters. These parameters are then used as the linking bridges between the scales when their values are determined from the calculated data of the finer scale simulations. This message-passing method can be performed in sequence for multiple length scales. It is obvious that in this sequential approach the accuracy of the simulations at the coarser scale critically depends on the accuracy of the information from the finer scale simulations. Furthermore, the model at the coarser scale must be accurate itself so that it can provide reliable results. In this strategy, the relations between the scales must be invertible so that the results of the coarser scale simulations can be used to suggest the best choice for the finer scale parameters.

The sequential approach has generally proven effective in systems where the different scales are weakly coupled. Therefore, appropriate systems for such a methodology often share a common character by which the large-scale variations appear homogeneous and quasi-static from the small-scale perspective. The majority of the multiscale simulations that have been actually incorporated in materials research are in fact sequential. In order to highlight the sequential message-passing in a range of polymeric systems, a few examples are outlined here. To predict the morphology and mechanical properties of mixtures of diblock copolymers and rod-like nanoparticles, Shou et al. [285] coupled the self-consistent field theory with DFT to provide input information for the lattice spring model (LSM). In their sequential algorithm, the spatial morphology of different phases is mapped onto the coarser-scale lattice and the force constants are derived for the three-dimensional network of springs. In similar approaches, other methods including LB [286], MC [287], and MD [288,289], have also been used to produce appropriate morphological information for LSM in various systems including polymer blends and nanocomposite coatings. Recently, the classical fluids density functional theory was linked to MD simulations by Brown et al. [290] to study microphase separated states of both typical diblock and tapered diblock copolymers. The fluids density functional theory can predict the equilibrium density profiles of polymeric systems. The authors used the resulting density profiles of this theory to initialize MD simulations with a close to equilibrated structure and could speed up the simulations. In a study on the influence of self-assembly on the mechanical and electrical properties of PNCs, Buxton and Balazs [291,292] used a combination of Cahn-Hillard theory and BD at the finer scale to produce morphological data. The data were later fed either into LSM in order to determine the mechanical properties, or into FDM to calculate the electrical conductivity.

A number of studies have been devoted to characterize polymer/clay nanocomposites at different scales, spanning from quantum mechanical scale up to the macroscale. One such algorithm was developed by Suter et al. [293] which starts with the quantum theory, and transfers the key information through atomistic classical MD to a CG representation. This sequential procedure allowed for the study of the intercalation of molten polymers, poly(ethylene glycol) and poly(vinyl alcohol), within MMT tactoids and the larger scale ordering of these bridged tactoids, see Figure 2. In a separate multiscale study, Scocchi et al. [294] evaluated the rescaled energies of a CG DPD model from the energy values of their atomistic MD counterparts. Using this information, they could calculate the maximum repulsion coefficients for the corresponding DPD models of polyamide (PA)/clay and polypropylene (PP)/clay nanocomposites and reproduce experimentally observed microstructures. The same methodology was also applied in following works and was extended into the macroscale realm by linking to FEM in order to derive mechanical properties of polymer/clay nanocomposites as a function of the degree of exfoliation [295,296]. The DPD parameters of their work derived from MD simulations, were recently shown to be capable to capture the orientation dynamics of clays in polymer melts under various shearing flows, see Figure 3 [195].

The most common serial transfer of information from a finer scale method to a coarser one can be envisioned in the systematic development of CG models of polymer systems. The CG models are often designed to reproduce the configurations of more detailed descriptions in atomistic simulations as accurately as possible. In this way, a CG model with much less degrees of freedom is achieved which can access longer time scales appropriate for instance in dynamics simulations. It is worthy to note that the final conformations of such CG simulations could be translated back to its atomistic details based on a specific backmapping algorithm. These sequential procedures represent general characteristics of sequential multiscale approaches and could also be extended to more complex systems. Furthermore, these fields have witnessed a large amount of research activities in recent years. As a result, more details are provided on these topics to help the reader familiarize oneself with the underlying challenges and possibilities.

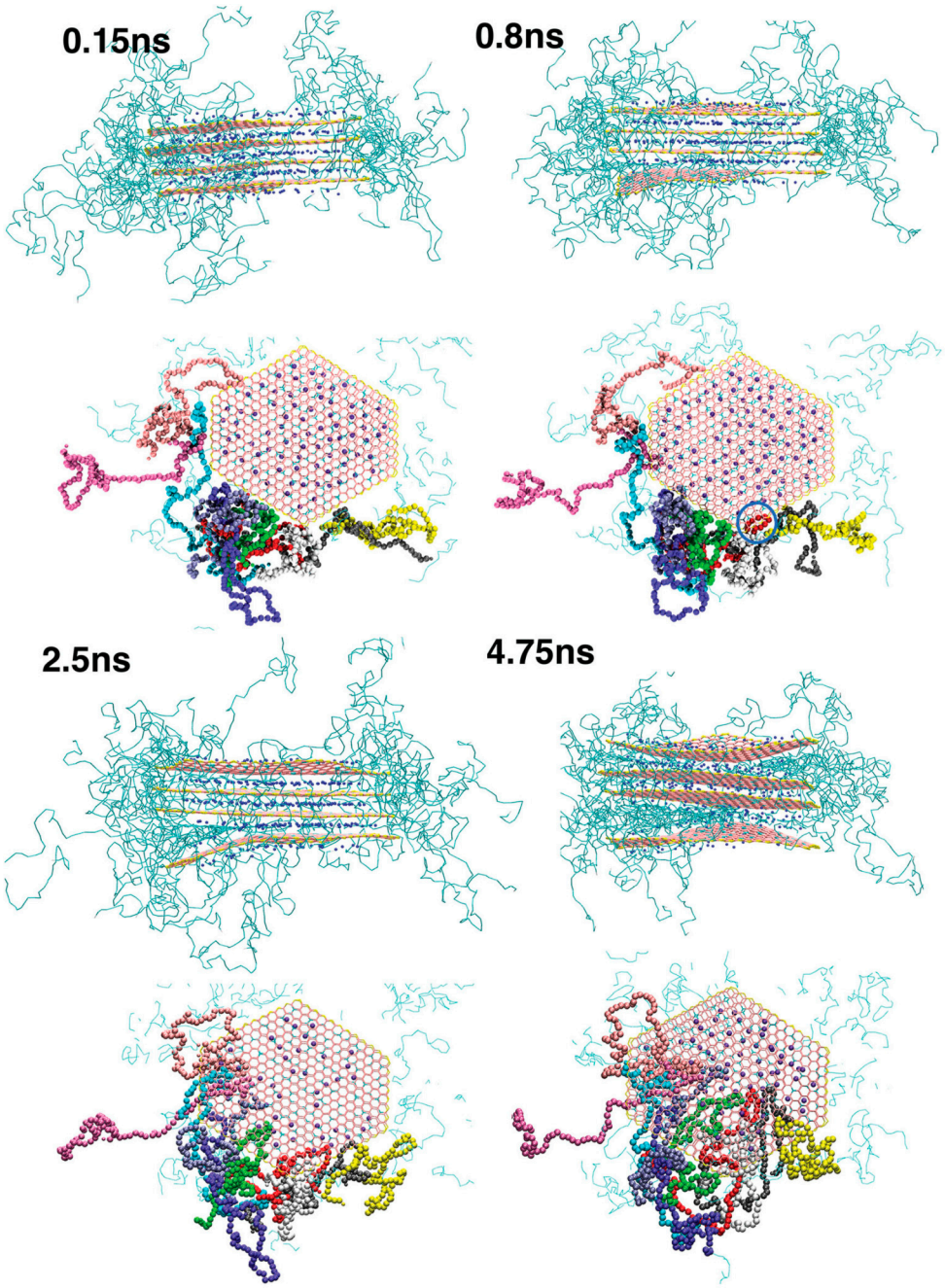

Figure 2. Pictorial overview of the intercalation of poly(vinyl alcohol) chains in a clay tactoid. The side and top views of the tactoids are illustrated at several snapshots. The macromolecules are shown by the green bonds in the side views. The color code for the clay particles are: pink: neutral clay; cyan: charged clay; yellow: edge of the clay; and blue: sodium. The bending of the lowermost clay due to the intercalation process of poly(vinyl alcohol) chains can be observed in the side view snapshots. For the top view, the intercalating polymers are colored based on their molecule number, to make the visualization easier. One can see that the polymer initially starts intercalating as short loops (for an instance see the blue circled chain at the 0.8 ns snapshot), and progresses further into the interlayer. Reprinted from Suter et al. [293] under the terms of the Creative Commons Attribution License.

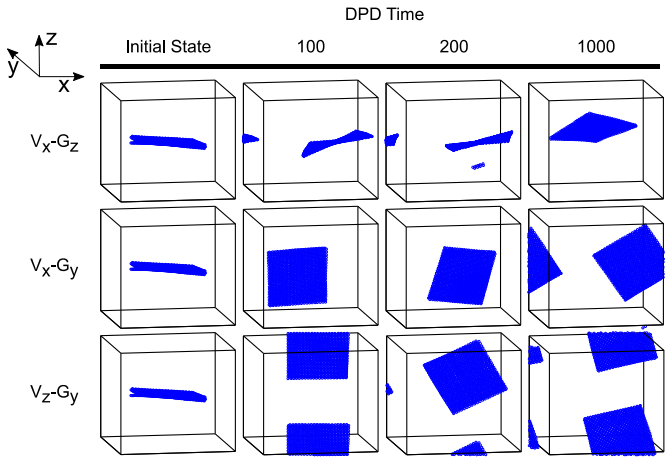

Figure 3. Snapshots of the clay platelets with time experiencing various flow directions. The applied shear-rate is 0.148 in DPD units and the flow of each row is defined in the figure; the velocity direction is shown by $V_{direction}$ and the velocity gradient direction by $G_{direction}$. Reprinted from Gooneie et al. [195]. Copyright 2016, with permission from John Wiley & Sons Inc.

3.1.1. Systematic Coarse-Graining Methods

A serious problem with polymeric materials in a sequential multiscale scheme is that the coarse-graining method from atomistic scale to mesoscale or from mesoscale to macroscale is not a straightforward procedure. The coarsening from QM to MD follows basic principles which can be formulated in a computational framework while it is system-specific at higher scales. All methods are based on the application of a force field which transforms information from quantum scale to atomistic simulations. From atomistic simulations to mesoscale model, critical features of the system such as the structure and/or thermodynamics have to be preserved while the degrees of freedom is reduced. The linking of scales through the mesoscale is addressed by many authors as the most challenging step towards developing reliable multiscale frameworks. Systematic coarse-graining methods are therefore developed to address these challenges. It is noteworthy that some mathematical aspects of various coarse-graining methods for equilibrium [297] and nonequilibrium [298] systems were addressed recently in details.

Systematic coarse-graining strategies attempt to extend the length and time scales of atomistic MD simulations by replacing several atoms with a single super atom and thus reducing the degrees of freedom. These approaches strictly attempt to preserve intrinsic properties of polymers such as radius of gyration, diffusion coefficient, etc. As a consequence, the results of such CG models can be directly compared with experiments. Depending on the number of atoms that are lumped into a single super atom, i.e., the degree of coarse-graining, the systemic coarse-graining methods are roughly divided into three major blocks; (i) low coarse-graining degrees where one or two monomers are coarse-grained into one super atom; for instance, in an iterative Boltzmann inversion (IBI) scheme; (ii) medium coarse-graining degrees where ten to twenty monomers are coarse-grained into one blob or bead, for instance, used in the so-called "blob model"; and (iii) high coarse-graining degrees where the whole chain is mapped to a single soft colloid in super coarse-graining methods. These variations provide access to a range of time and length scales from 10^{-6} s (10^{-6} m) to 10^{-2} s (10^{-2} m), particularly precious to simulate dynamic properties of polymeric systems [299]. In addition to the reduced number of degrees of freedom, CG models often benefit from simpler forms of interactions compared with the detailed models. This feature can promote the computational efficiency to a large extend. Besides, the free energy profiles of CG models are usually smoother due to the fact that many interaction centers are replaced with only a single site. Finally, the parametrization of the CG interactions is simpler than that of full atomistic systems since many chemistry-specific details are ignored during coarse-graining. Such features of CG models make them particularly appealing for many applications

in polymer systems. In the next sections, several methods for coarse-graining as well as various remaining challenges are discussed.

Low Coarse-Graining Degrees

Low degrees of coarse-graining with one or two monomers lumped into a single super atom are carried out by either parameterized or derived approaches [300]. The parameterized approaches utilize all-atomistic (AA) simulations to calculate some target property, such as a pair distribution function, and then the coarse-graining potentials are evaluated to reproduce the target quantities. One should note that the CG potentials can hardly reproduce all the original AA system specifications. On the other hand, in the derived methods the CG pair potentials are calculated in AA simulations from the direct interactions between the groups of atoms enveloped in super atoms. In these methods, the contribution of multibody interactions to the effective CG potentials is less significant in comparison with pair potentials. Consequently, the derived methods are often used to describe systems in which multibody interactions do not play a significant role. Examples of derived methods are the pair potential of mean force (pPMF) [301,302], the effective force CG (EFCG) [303], and the conditional reversible work (CRW) [300,304,305]. In the rest of this part, we focus on parametrized approaches since the derived methods are generally considered to be better-suited for small molecules even though they have recently found some applications in larger molecules [306,307].

The parameterized methods are divided into structure-based and force-based methods depending on the target quantities. As specified in the name, structure-based methods construct the CG potentials in order to reproduce a structural property of the AA system such as pair distribution functions [36,308–318]. The IBI method is undoubtedly the most significant example of such methods [308,319]. Other structure-based methods include the Kirkwood-Buff IBI method [320], the inverse Monte Carlo (IMC) method [309,310,313], the relative entropy method [321–324], and the generalized Yvon-Born-Green theory [325]. All of these methods are principally similar to the IBI method with minor differences in their optimization or mapping schemes. The force-based approaches, on the other hand, attempt to match the force distributions on a super atom from both the CG and AA representations. There are mainly two variations to force-based methods namely the force-matching method [3,326–331], and the multiscale coarse-graining method [328,329,332–335]. For the sake of completeness, we should mention that in some works a combination of the methods is used to derive the CG model. For instance, we refer to the recent study of Wu [336] who utilized a combination of IBI and CRW to find the CG potentials for morphological simulations of poly(vinyl chloride)/poly(methyl methacrylate) and PS/poly(methyl methacrylate) blends.

In the IBI method, one often assumes that the probability distribution function $\mathrm{p^R}$ depends on pair distance r, bond length l, bond angle θ, and dihedral angle $\mho$. These parameters are further taken to be independent from each other so that $\mathrm{p^R(r,}l,\theta,\mho) = \mathrm{p^R(r)} \times \mathrm{p^R}(l) \times \mathrm{p^R}(\theta) \times \mathrm{p^R}(\mho)$ and the CG potential function becomes $\mathrm{U^{CG}(r,}l,\theta,\mho) = \mathrm{U^{CG}(r)} + \mathrm{U^{CG}}(l) + \mathrm{U^{CG}}(\theta) + \mathrm{U^{CG}}(\mho)$. Through the simple Boltzmann inversion one has $\mathrm{U^{CG}(q)} = -\mathrm{k}_B\mathrm{T\ ln\ p^R(q)}$ with $\mathrm{q} = \mathrm{r},l,\theta,\mho$. The iterative algorithm in IBI compares the probability distribution functions of the CG model with the corresponding target probability distribution functions of AA simulations $\mathrm{p^R_{\mathit{target}}}$, and improves the calculated CG potential functions in a step-wise manner according to [299,337,338].

$$\mathrm{U^{CG}_{\mathit{i}+1}(q)} = \mathrm{U^{CG}_{\mathit{i}}(q)} + \mathrm{k}_B\mathrm{T\ ln}\frac{\mathrm{p^R_{\mathit{i}}(q)}}{\mathrm{p^R_{\mathit{target}}(q)}} \tag{47}$$

The potential correction term, i.e., the second term on the right hand side of the equation, is sometimes multiplied by a relaxation factor between zero and one to avoid overshooting in the numerical procedure. The number of iterations required to reach satisfactory property reproduction in IBI is system-specific and depends on various factors like polymer structure, the definition of the super atom, the degree of coarse-graining, etc. and can take from a few to hundreds of

iterations to converge [327]. Li et al. [339] used such a strategy to reproduce viscoelastic properties of *cis*-polyisoprene. In their work, the authors reproduced CG distribution functions and those obtained from AA simulations. In this way, they could optimize the potential functions for the four independent parameters separately.

The IBI method is not the only way to optimize a CG model based on AA simulations. Here we take a quick look at two other methods namely IMC and force-matching methods. IMC or the Newton inversion method incorporates rigorous statistical mechanical arguments to update the potential functions of the CG model [309,310,313]. The optimization procedure in IMC poses an interdependent updating algorithm for pair potentials in multicomponent systems whereas in IBI method these potentials are updated separately which could lead to convergence problems. However, this feature is often computationally very expensive [327]. In the force-matching method, a variational approach is used to construct the CG potentials based on the recorded forces from AA simulations [3,326–331]. In this method, the difference between the average AA force on a particle and the corresponding force in the CG counterpart is minimized in order to find the optimized CG force field. Thus, the force-matching approach actually projects the full many-body force field onto the definitive potential functions of the CG force field [340]. Due to the fact that the CG force field is merely an approximation of the AA force field, the force-matching method may or may not reproduce the structural properties of the AA system perfectly. The incorporation of higher-order interactions in the definition of the CG force field could resolve this problem at the cost of lower computational efficiencies [341]. It should be noted that IBI and similar methods are usually not helpful in systems with a diluted component since the interactions between the diluted molecules cannot be readily obtained. In such cases one should compute the effective potentials for these interactions with more rigorous sampling schemes such as thermodynamic integration or umbrella sampling [306,342–344].

In the coarse-graining procedure, there is usually more than one way to define super atoms. Several important issues regarding the definition of super atoms should be addressed carefully, i.e., the shape of the super atom, the position of the center of a super atom on a molecule, the number of atoms which are enveloped by it, as well as the number of different super atoms associated with a molecule. The super atom is defined to be a spherical particle in most studies, but there are also some works which offer generalizations for anisotropic potentials [345,346]. This enforces additional complexity on the definition of potential functions as well as the performance of CG simulations only for a slightly increased accuracy. Therefore, it is generally advised to achieve higher precisions by incorporating additional spherical super atoms to characterize the molecules instead of utilizing non-spherical super atoms [299]. Considering the other parameters mentioned for the definition of super atoms, there is no general rule applicable for different cases. There are various ways to define the super atoms to represent a CG model of a system. However, it is crucial to ensure that the final CG model is capable to reproduce the static, dynamic or thermodynamic properties correctly before it is further applied. To give an example, we consider the various possibilities to develop CG models of polystyrene (PS), which has been extensively studied with different approaches in the definition of super atoms as illustrated in Figure 4. Müller-Plathe and his co-workers [347–349] adopted the CG structure shown in Figure 4a and could successfully reproduces the gyration radius and the Flory characteristic ratio of PS in melts at 500 K. Nevertheless, the entanglement length was estimated to be much smaller than the experiments. Spyriouni et al. [350] modified the CG potential functions of this model and could predict the correct entanglement length of PS melts as well as the packing length and the tube diameter. Still, the isothermal compressibility was largely different from experimental values indicating the poor transferability of the developed potentials to pressures other than the one used in AA simulations. Another CG representation was developed by Sun and Faller [351,352] as depicted in Figure 4b which could obtain the entanglement length at 450 K in agreement with experimental observations. The mapping scheme shown in Figure 4c was developed by Qian et al. [353] which yields potentials capable of reproducing the isothermal compressibility as well as structural properties of the PS melts from 400 to 500 K. Finally, in order to include the tacticity effects on the structural

and dynamic properties of PS, Harmandaris et al. [354,355] and Fritz et al. [356] used the CG models shown in Figure 4d. This model has been applied to study both the mechanical properties of PS glasses [357,358] and the dynamic properties of PS melts [359,360]. These works manifest the influence of the definition of super atoms on the final outcome of the simulations. Consequently, a CG model should be tested and validated for its predictive features and merits before any further use [361].

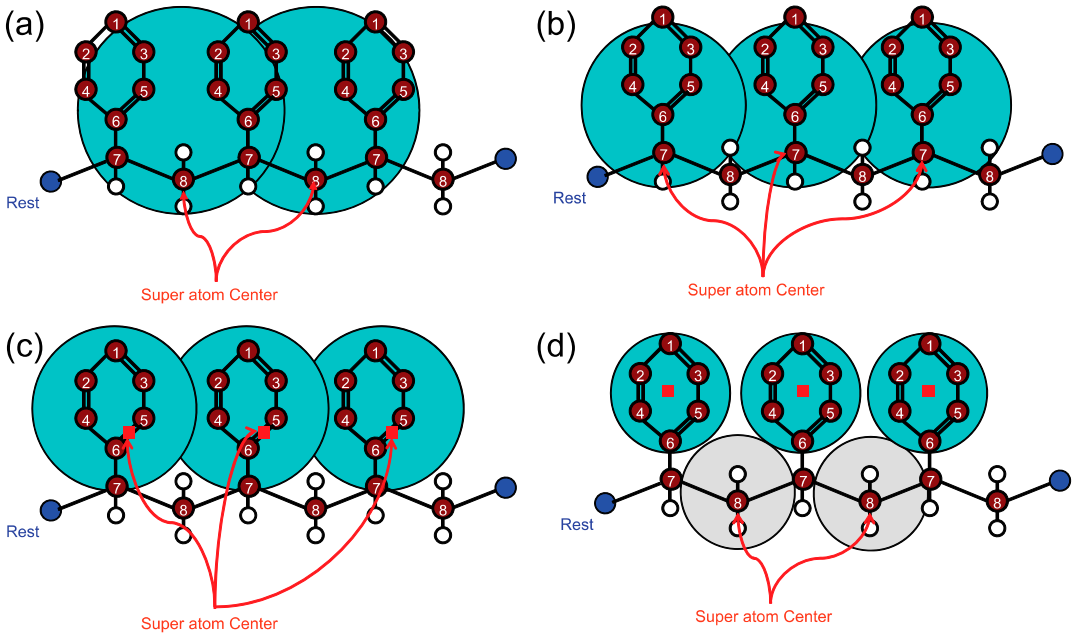

Figure 4. Different definitions for the super atoms of CG PS utilized by (**a**) Müller-Plathe and co-workers [347–349]; (**b**) Sun and Faller [351,352]; (**c**) Qian et al. [353]; and (**d**) Harmandaris et al. [354,355]. Reprinted from Li et al. [299] under the terms of the Creative Commons Attribution License.

The fact that several atoms are replaced with a super atom in CG models changes the entropy due to the deleted degrees of freedom. This leads to an altered internal dynamics after coarse-graining. This notion becomes more important as the degree of coarse-graining increases. In addition to this altered entropy, the coarse-graining procedure changes the amount of the surface of each molecule available to its surrounding molecules due to the fact that it simplifies a cluster of atoms into a spherical super atom. Consequently, the hydrodynamic radius of the CG super atom is strongly dependent on the coarse-graining methodology and in every case, it is different from its AA counterparts. Since the friction coefficient is related to the hydrodynamic radius according to Stokes's law [362], the coarse-graining procedure also changes the internal friction coefficient between monomers which leads to incorrect dynamic behavior of CG models [363–365]. Therefore, it is necessary to rescale the dynamics in order to simulate the correct behavior [366]. The dynamic rescaling can be performed utilizing a time-mapping factor defined, for instance, as the ratio of the friction coefficients [359,360], the ratio of decorrelation times utilizing the autocorrelation function [339], or numerically derived from the ratio of the mean square displacements (MSD) [354], between AA and CG models. In spite of these efforts, the correct definition of a time-mapping factor is still a challenge due to the fact that different modes of motions in a system should be scaled with different characteristic scaling factors, giving rise to the so-called "dynamical heterogeneity" issue [367–369].

Finally, the transferability and thermodynamic consistency of developed CG models should be ensured. In a coarse-graining procedure such as IBI, the effective potential functions are often evaluated based on target distribution functions, which are themselves derived for a specific set of thermodynamic conditions resembling a certain ensemble. Therefore, the derived potential functions from one state are not transferable to another state in most cases [337,370]. All CG models are

state-dependent and should not be transferred to another state without re-parametrization. The "state" contains information about temperature, density, concentration, system composition, phase, etc. as well as chemistry-specific details of the system. An example for the thermodynamic inconsistency of CG models and AA simulations is the missing long-range interactions between the super atoms leading to overestimations of the pressure. To compensate for such effects, some studies add a linear attractive tail function into the pair potential and recover the correct pressure for CG polymer systems [319,371,372]. Consequently, the effective potential functions should be optimized individually for each state of the CG system. Despite this general consideration, there are some instances in the literature where the effective potential functions of the CG model possess a range of transferability into a subset of thermodynamics states [353,373–375]. For instance, the effective CG potentials of homopolymer melts show a remarkable transferability over a large range of temperatures [376–378]. Such studies state that the definition of super atoms largely influences the transferability of the effective CG potentials derived by the IBI method. An interesting topic in the transferability of CG models is to find a methodology to derive CG potentials which are both thermodynamically and structurally consistent with the underlying AA description [317,318,338,344,379–382]. Such a method could ensure a certain state transferability for the constructed CG potentials. Using calibration methods in order to improve the transferability of derived CG potentials is also an interesting possibility. Recently, inspired by ideas from uncertainty quantification and numerical analysis, Patrone et al. [383] used a Bayesian correction algorithm [384] to efficiently generate transferable CG forces. Their method uses functional derivatives of CG simulations to rapidly recalibrate initial estimates of forces anchored by standard methods such as force-matching.

Medium Coarse-Graining Degrees

Since the definition of the super atom is not unique, it is possible to lump several monomers of the polymer chain into one single super atom. In this way, the approachable length and time scales of the CG simulations are significantly extended. Based on this idea, Padding and Briels lumped 20 monomers along a PE chain in a single spherical blob and developed the so-called "blob model" [385–387]. The potential functions of the blob model are optimized systematically based on AA simulations in a similar fashion to IBI. However, due to the larger number of lumped monomers in comparison with techniques for low coarse-graining degrees, the dihedral interactions between the blobs are negligible. Therefore, the potential functions of the blob model usually consist of nonbonded and bonded (i.e., bonds and bond angles) interactions. Padding and Briels write these interactions as

$$U^{CG}_{nonbonded}(r) = c_0 e^{-(\frac{r}{b_0})^2}, \quad (48)$$

$$U^{CG}_{bond}(l) = c_1 e^{-(\frac{r}{b_1})^2} + c_2 e^{-(\frac{r}{b_2})^2} + c_3 l^{\mu}, \quad (49)$$

$$U^{CG}_{angle}(\theta) = c_4(1 - \cos\theta)^{\nu}, \quad (50)$$

in which $U^{CG}_{nonbonded}(r)$, $U^{CG}_{bond}(l)$, and $U^{CG}_{angle}(\theta)$ are the potentials of nonbonded, bond and angle interactions, respectively. c_0 to c_4, b_0 to b_2, μ and ν are fitting parameters derived from AA simulations. The potential functions for nonbonded and bonded interactions Equations (48) and (49), respectively are optimized against AA results for the blob representation of PE illustrated in Figure 5. Blob model has been applied in a number of studies including the investigation of transient and steady shear flow rheological properties of polymer melts [388], chain dynamics of poly(ethylene-*alt*-propylene) melts [389], and entangled star PE melts [390]. In the blob model, it is also necessary to rescale the dynamics to capture the behavior of the polymer chains correctly. The rescaling can be performed by adjusting the friction coefficient of the Langevin equation to the simulated value from the AA model [386]. Based on this rescaling strategy, the correct diffusion coefficients and scaling laws of the zero-shear viscosity of PE polymer melts were predicted correctly in the blob model as shown in Figure 6 [386].

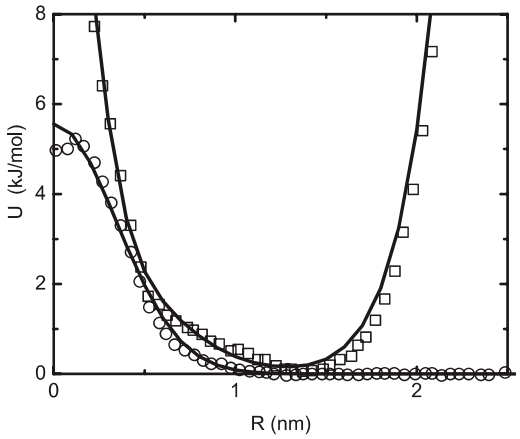

Figure 5. Potential functions for nonbonded (circles) and bonded (squares) interactions from AA simulations. The solid lines are fitted with Equations (48) and (49). Reproduced from Padding and Briels [385] with the permission of AIP Publishing.

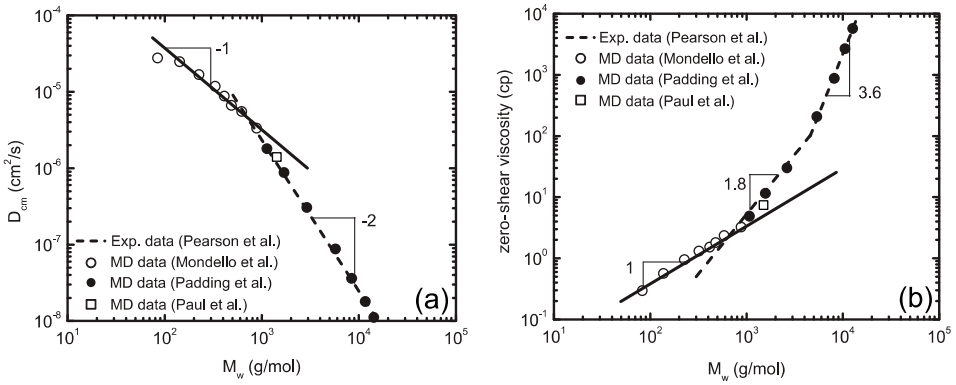

Figure 6. (**a**) Center-of-mass self-diffusion coefficient, D_{cm}; and (**b**) zero-shear viscosity versus molecular weight, M_w , for PE melts at 450 K. Reproduced from Padding and Briels [386] with the permission of AIP Publishing. For further information regarding the various sets of data shown in figure refer to the cited work and the references within it.

Another exciting method used to perform CG simulations with medium coarse-graining degrees is DPD which was introduced in Section 2.3.2. The conservative force in DPD algorithm was shown by Groot and Warren [187] to be connected to the Flory-Huggins parameters between components. This notion was further generalized to consider bead-size effects [391], variable bead volumes [392], as well as polymer blends [200]. The consideration of variable bead volumes in DPD facilitates the way to simulate more complex polymeric systems where beads can represent various functional chemical units with different volumes rather than polymers constructed from a single bead type [202]. In addition, an elaborate systematic strategy for parameterization of chain molecules in DPD simulations was recently proposed by Lee et al. [205] which successfully combines top-down and bottom-up approaches and benefits from experimental infinite dilution solubilities of the compounds to map the repulsion interaction parameters. There are rather simple relationships in the literature using which one can find the appropriate DPD conservative forces for all-fluid systems [202,203]. However, such relations cannot help in DPD studies where a fluid is interacting with a solid substrate. As a consequence, some authors developed an iterative approach to optimize the repulsive forces of DPD versus AA simulations based on a comparison of the density profiles of fluid particles on the solid substrate [201–203]. An example of such analysis is shown in Figure 7 for the parametrization of epoxy-alumina interactions as utilized by Kacar et al. [203]. A similar coarse-graining strategy was also incorporated by Johnston and

Harmandaris [393] to study model polystyrenes on a gold surface. In their methodology, the authors developed a hierarchical multiscale model in which DFT, MD, and CG models were combined to describe the interfacial properties.

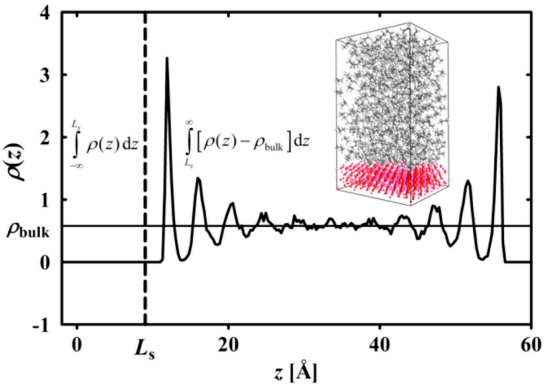

Figure 7. Number density profile from atomistic MD simulations. Molecular center-of-mass of a particular bead is used in computation of the profiles. Vertical line is the location of the substrate surface and defines the integration boundaries. A pictorial representation of the atomistic simulation box snapshot is given as the inset picture. Reprinted with permission from Kacar et al. [203]. Copyright 2016 American Chemical Society.

The distribution functions become broader as more atoms are coarse-grained into one super atom since more degrees of freedom are smeared out through averaging. Accordingly, the potential interactions become increasingly soft and therefore unphysical bond-crossings may occur in such systems. Such bond-crossings result in unrealistic predictions of the dynamics in the modelling of long polymer chains by reducing the number of entanglements. Hence, it is important to avoid the bond-crossing phenomenon in CG models. There are three main routes available to avoid (or to reduce in some cases) the bond-crossings in CG models. The first method was developed by Padding and Briels [385] for the blob model. They introduced an algorithm which prevents bond-crossings by considering a bond as an elastic band and applying the energy minimization (EM) criteria to predict the possible entanglement positions. The second method was proposed by Pan et al. [394] who added segmental repulsive forces to the force field in order to decrease the frequency of bond-crossings. Similar ideas were also put forward by Yamanoi et al. [194] and Sirk et al. [395]. While these approaches are promising, they are computationally expensive. Moreover, some parameters used in these models such as the cutoff distance of the segmental repulsions are physically ambiguous and need further explanation to avoid arbitrary choices. The third method was introduced by Nikunen et al. [396] who could prevent bond-crossings by incorporating simple topological constraints. Using this approach, Rouse as well as reptational dynamics [397] were simulated correctly for short and long chains, respectively. In spite of these attempts, there are still serious computational limitations regarding these methods which necessitate careful selection and implementation of such approaches [398].

High Coarse-Graining Degrees

The coarse-graining methods discussed so far often lump a few atoms up to several monomers into a single super atom. Since the polymer chain length is typically much longer than these coarse-graining limits, super coarse-graining models are necessary to approach extremely large spatial and temporal scales of polymers. In such models, an entire polymer chain is often represented by a single particle. The dynamics of polymer chains is strictly defined by the dynamics of the centers of mass of these particles and all the high-frequency motions associated with macromolecules are dropped out. Based on these ideas, a super CG model was developed by Murat and Kremer [399] in which polymer chains were replaced by soft ellipsoidal particles. The size and shape of the particles is determined based

on the conformations of the underlying chains. The internal energy of a particle with a given size is characterized by the probability of occurrence of that particle. Furthermore, the density of monomers within each particle is calculated from all conformations that have the same size. The spatial overlap of the monomer density distributions of two particles defines the interaction between them. For a large number of contacting particles, the interactions between the particles forces them to adjust the equilibrium size distribution. Their simulations showed that the generic Gaussian random walk scheme appropriately defines the behavior of the chains in the melt [399]. They argue that a large number of long chains can be simulated within a reasonable computation time on a single workstation processor due to the fact that the internal degrees of freedom of the chains are severely smeared out [399]. Extensions of this method are available in which a chain of such soft particles can be considered for the simulations of high molecular weight polymers [400–403]. For instance, Zhang et al. [403] used such a strategy in combination with the mapping of the density distributions onto a lattice in the framework of MC schemes and could develop a particle-to-mesh approach for high molecular weight polymers. The authors propose that such a grid-based scheme could be a viable candidate to produce equilibrated models of long polymer chains useful in the setting of a general multiscale study [403].

An interesting super CG model was developed by Kindt and Briels [404] in which a single particle was ambitiously used to study the dynamics of entangled polymer chains. In this model, a set of entanglement numbers are used for each pair of particles to describe the deviation of the CG model (with the ignored degrees of freedom) from the equilibrium state. Such deviations give rise to transient forces in the system. The displacements of the particles are governed by these transient forces as well as the conservative forces derived from the potential of mean force. This deviation-displacement analysis is performed for any given configuration of the centers of mass of the polymers. Due to the core role of the transient forces in the simulation strategy, it has been called the "transient force model" [405]. The authors applied this model to a melt of $C_{800}H_{1602}$ chains at 450 K and examined radial distribution functions, dynamic structure factors, and linear and nonlinear rheological properties. In general, they could achieve good qualitative, and to a large extent quantitative, agreement with experiments and more detailed simulations. Figure 8 illustrates typical linear and nonlinear rheological properties for $C_{800}H_{1602}$ chains at 450 K calculated by Kindt and Briels [404]. The surprising observation that a single particle could capture the correct reptation behavior was qualitatively linked to the transient forces being quadratic in the deviations of entanglement numbers and thus resembling the confined motions of a chain in a tube [405]. This model has been further applied to study rheological properties of various polymer systems [406–412].

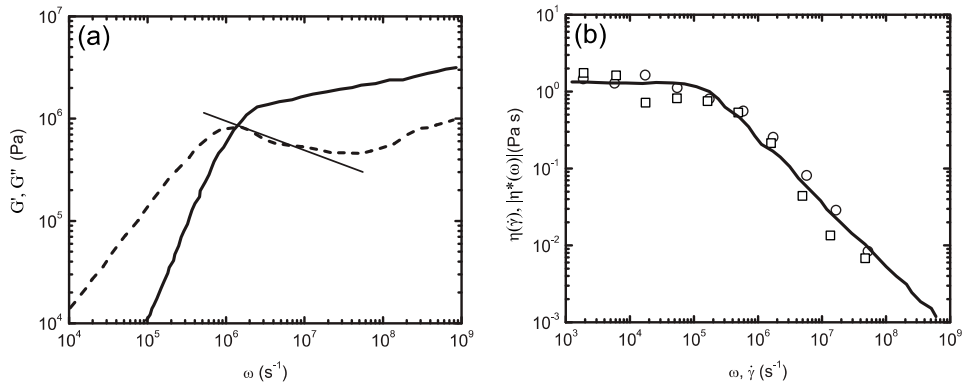

Figure 8. (**a**) Storage G' and loss G'' moduli (full and dashed lines, respectively); and (**b**) the flow curve for $C_{800}H_{1602}$ melt at 450 K. Reprinted from Kindt and Briels [404] with the permission of AIP Publishing. The solid line in (**b**) is derived in equilibrium simulations using the Cox-Merz rule. The circles and squares are simulation results under shear benefitting from linear background and variable flow field methods, respectively. For further information regarding the data shown in figure refer to the cited work and the references within it.

Based on analytical calculations through the Ornstein-Zernike equation [413], a super coarse-graining model was developed by Guenza and her co-workers [363–365,414–419] which does not need any further optimization against a more detained model. This model provides analytical expressions for various thermodynamic and physical quantities which are especially useful when dealing with rescaling issues. As it was noted before, once a molecule is coarse-grained its entropy as well as accessible surface to the surrounding molecules are changed. The entropy change becomes important in such super CG models in comparison with low coarse-graining degrees such as IBI. The present model provides analytic expressions for the scaling factors from each contribution as [363,365]

$$s_{entropy} = R_g \sqrt{\frac{3MN_c}{2k_BT}}, \tag{51}$$

$$s_{friction} = \frac{\xi}{N\xi_m}, \tag{52}$$

with $s_{entropy}$ and $s_{friction}$ as the rescaling factors for the entropy and surface changes, respectively. Here, M is the molecular weight of the chain with radius of gyration R_g, and N_c is the number of monomers per chain. ξ and ξ_m are the friction coefficients of the super CG and freely-rotating chain systems, respectively.

3.1.2. Reverse Mapping

While the coarse-graining procedure helps accessing longer time scales in simulations, it also removes detailed atomistic features necessary for precise evaluations of the structure. Since CG models have proven extremely useful in various simulations, such as generating equilibrated structures for further analysis and simulation runs [350,420–422], there is a general tendency towards employing them upon possibility. Consequently, a reverse mapping is also needed to reproduce atomistic details such as chemical characteristics from the CG model. The reverse mapping procedure is also referred to as fine-graining or backmapping in the literature [423,424].

Early attempts for reverse mapping are dated back to Tschöp et al. [425] and Kotelyanskii et al. [426]. In general, a reverse mapping operation includes (i) the reconstruction of CG particles with possible atomistic structures from a bank of templates; followed by (ii) performing EM, MD, or MC simulations to guarantee collectively and locally relaxed atomistic structures. In the first step, the fitting templates are often extracted from a preceding atomistic equilibrium simulation. The chosen template for a given CG particle should not only fit the contour of the underlying CG molecule, but also allow the best superposition for the neighborhood CG particles. In order to achieve a high backmapping efficiency, the fitting procedure is usually based only on geometrical criteria and no force and energy calculations are involved. In some cases where the CG particle represents a complex structure with bulky side groups, one must be careful to avoid interlocking of side groups [420]. In the second step, it is necessary to run post-processing calculations due to the fact that the CG force field is derived from average atomic distributions and therefore may easily lead to overlapping structures [427]. Such artefacts could happen more frequently in coarser CG models.

Several backmapping approaches are proposed for different polymers in the literature [420,425,428–431]. Often, when the CG model is constructed based on the atomistic simulations, the zoom-in back to the atomistic description is simply a geometrical problem [430]. However, a more sophisticated procedure must be followed in some cases where the model is significantly coarse or the CG particles include asymmetric atoms and the polymer chain shows a specific tacticity [420,431]. An example for the first case was given by Karimi-Varzaneh et al. [430] who used a simple backmapping algorithm to reinsert the atomistic details of a PA-66 in its corresponding CG model. As for the latter, Wu [431] utilized a special backmapping procedure to capture tacticity effects on the structure and dynamics of poly(methyl methacrylate) melts. Moreover, a general backmapping technique to prepare equilibrated polymer melts was proposed by Carbone et al. [424] which consists of (i) the generation of random

walk chains with various Kuhn lengths; and (ii) the insertion of atoms on the underlying random walk chains. The steps of this approach for PA-66 are shown in Figure 9. The authors showed that well-equilibrated melts of PE, atactic PS and PA-66 can be achieved using this method. The structural properties of such relaxed melts were shown to be in good agreement with previous AA simulations and experimental data on short as well as long spatial ranges. Some cases with special reverse mapping algorithms are also found in literature. For instance, in order to generate realistic amorphous polymer surfaces, Handgraaf et al. [432] developed a special mapper which takes the CG structure as input and uses the MC technique to generate the atomistic structure. The mapped atomistic structure is later equilibrated by performing a short MD simulation.

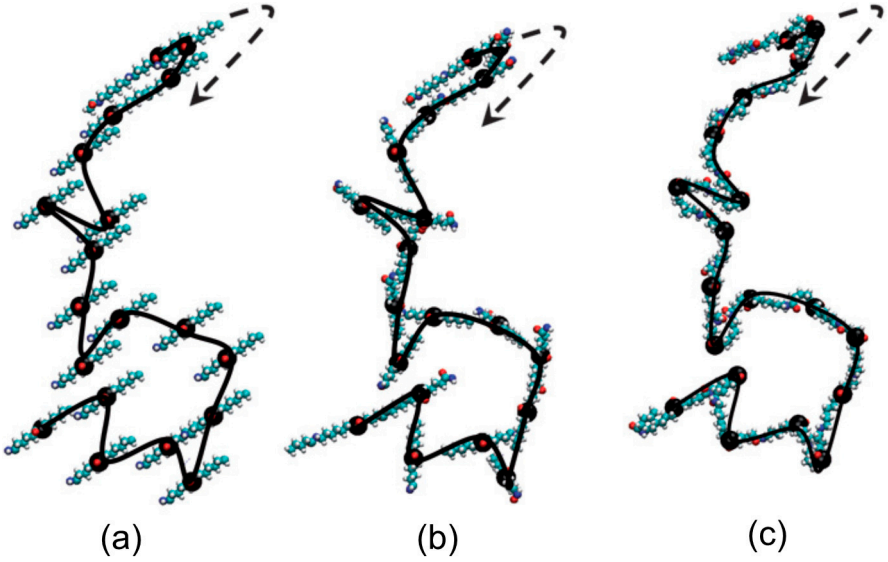

Figure 9. Reverse-mapping procedure for PA-66: (**a**) insertion of the atomistic segments (colored beads) on the underlying random walk chain (solid black line); (**b**) re-orientation of the atomistic segments; (**c**) final configuration of the reconstructed atomistic chain. The arrow indicates the grow direction of the chain. Reproduced from Carbone et al. [424] with permission of The Royal Society of Chemistry.

It should be noted here that the reverse mapping of a nonequilibrium CG system differs from an equilibrium run to some extent. Since molecular deformations are significant in the CG model due to the nonequilibrium simulations, a proper backmapping procedure should translate these deformations into the atomistic model. Furthermore, the atomistic model must also contain information about the stored deformation energy in the CG model of the polymer. Obviously, a simple backmapping cannot meet these requirements since during the post-processing step, i.e., EM or MD or MC simulations, the energetically unstable deformed structure relaxes quickly. A backmapping method was proposed by Chen et al. [423] to overcome this problem for polymer chains experiencing sheared nonequilibrium conditions. Their methodology mixes the general concepts of backmapping with the new idea of applying position restraints to preserve the deformed configurations. In order to preserve the stretched chain configuration obtained in the CG simulation, position restraints with a harmonic potential are applied to all the atoms coinciding with CG particles locations. The globally deformed structure is allowed to relax locally using a molecular mechanics approach [433]. By changing the position restraint scheme and re-optimizing the structure through an iterative procedure, it is possible to minimize the isolation of segments from the rest of the chain. The workflow of the backmapping procedure of Chen et al. [423] is illustrated in Figure 10.

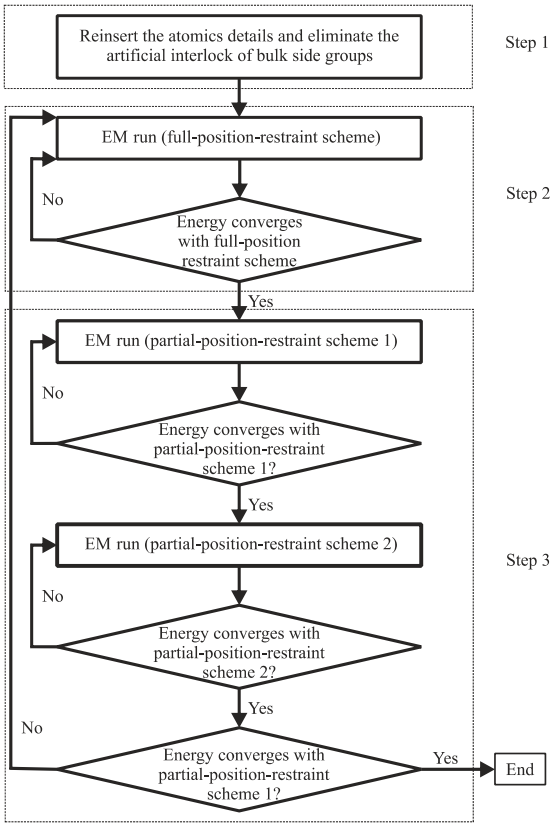

Figure 10. The workflow used in the backmapping procedure of nonequilibrium CG simulations as proposed by Chen et al. [423]. Notice that schemes 1 and 2 in step 3 are two variants of the main scheme in step 2 in order to minimize the isolation of segments from the rest of the chain. Reproduced from Chen et al. [423] with permission of the PCCP Owner Societies.

Finally, the validity of a reverse-mapped atomistic structure is often tested by comparing relevant structural information simulated using atomistic models based on the reverse-mapped configurations with the original AA simulations initially used to develop the CG force field [424,430,434]. Radial distribution function of a specific chemical group, bond and angle distributions, torsion angle distribution, and the number of hydrogen bonds are mostly used for such comparisons. In some studies, the results of a reverse-mapped atomistic simulation are also directly compared with the available experimental data [424].

3.2. Concurrent Multiscale Approaches

The concurrent approaches define the system under consideration through a genius combination of several methods and solve them simultaneously instead of a hierarchical procedure as in sequential approaches. The resolution of the solution is adapted to provide an accurate representation of those regions of the system which are of particular interest. A common field of application for such strategies is the analysis of crack propagation in materials. During the crack propagation the immediate neighborhood of the crack tip, where the bond breaking is taking place, demands a higher precision in the models representation whereas a coarser model could suffice for further away from this region. An example of the concurrent methodology used in the crack analysis is shown in Figure 11. In this multiscale simulation, the concurrent approach combines tight binding (TB), MD, and FEM techniques to study crack propagation in silicon [435]. The vicinity of the crack should be simulated at a finer resolution since it exhibits significant nonlinearity. Therefore, atomistic MD method could provide a more precise representation of the crack surrounding whereas FEM can still accurately describe

the rest of the system further away from the crack. In order to provide a reliable description of the underlying physics, the formation as well as the rupture of covalent bonds must be treated with quantum mechanics rather than empirical potentials. This is due to the fact that bonds are principally the sharing of valence electrons at a quantum mechanical scale [436]. Consequently, it is crucial to apply a TB modelling to a small region in the immediate vicinity of the crack tip, where bond breaking prevails during fracture, while the empirical potential description of MD is adequate further away from this region.

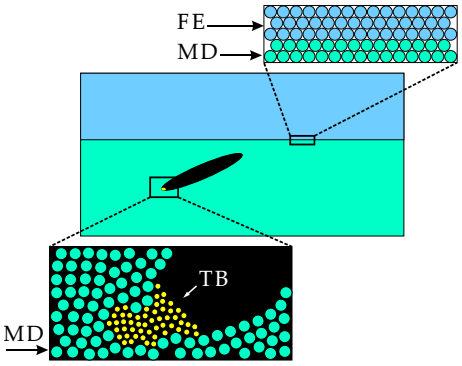

Figure 11. A hybrid FE/MD/TB simulation. The FE, MD, and TB approaches compute forces on particles (either FE nodes or atoms) in their respective domains of application. These forces are then incorporated to calculate the updated positions and velocities of the particles in a time-stepping algorithm.

The concurrent approach is best suitable for the systems with an inherent multiscale character. In such systems, the behavior at each scale depends strongly on the phenomena at other scales. Moreover, this approach can be of a more general nature due to the fact that it does not often rely on any system-specific assumptions such as a particular coarse-graining model. Therefore, a well-defined concurrent model can be applied to many different systems within the limits of common phenomena involved as long as it incorporates all the relevant features at each level. In contrast to sequential methods, concurrent models are not usually constructed based on a detailed prior knowledge of the physical quantities and processes involved. As a result, such models are particularly useful when dealing with new emerging problems about which little is known, for instance, at the atomistic level and its connection to larger scales. However, the coupling between the different regions treated by different methods is a critical challenge remaining in the core of concurrent approaches. A successful multiscale model seeks a smooth coupling between these regions. Here, we address some of the concepts and strategies developed in the concurrent framework.

3.2.1. The Concept of Handshaking

In concurrent simulations, often two distinct domains with different scales are linked together benefitting from a region called the "handshake" region. The handshake region generally bridges the atomistic and continuum domains of the multiscale model [437,438]. However, there are studies where it has been used to link quantum mechanical TB calculations to atomistic domains [438,439], or atomistic MD models to their equivalent CG descriptions [437].

The handshake region transfers information from one domain to the other and thus provides the possibility to overlap, usually, atomistic and continuum domains. This overlap is defined with a field variable, often the potential energy, taking a weighted form of the magnitude of the same variable in each domain. The weighting is usually in the form of a function which decreases monotonically from one to zero in the overlap. As a result, the control variable has its corresponding values in each domain with a gradual transition between the domains. The form of the weighting function is not determined by the formulation and is arbitrary. Consequently, the modelling quality of the handshake region is strongly dependent on a smooth and gradual shift of control variables from one domain to the other

domain. In the handshake algorithm, it is assumed that the properties of each domain are independent from one another. Due to this assumption, one has to be concerned particularly whether or not the material properties of both domains are truly equivalent. In addition, physical complications in the handshake region might necessitate more complex algorithms to obtain a precise representation of it. For instance, nodal displacements of the continuum domain should be influenced by the displacements of molecules inside the neighboring atomistic domain if the node and the molecules are within the cutoff distance of the molecular interactions.

The handshaking approach has been applied to combine TB/MD/FEM in order to study crack propagation and crystal impact in silicon [438,439]. A combination of TB/MD/FEM has also been utilized in a handshaking framework to characterize submicron micro-electro-mechanical systems by Rudd et al. [437]. Based on the works of Abraham et al. [439,440] the unifying theme for such a multiscale model is the total Hamiltonian H_{tot} defined throughout the entire system. This Hamiltonian is a function of the atomic positions $\mathbf{r}_j$ and their velocities $\mathbf{v}_j$ in the TB and MD regions for all j atoms, and the displacements $\mathbf{u}_\alpha$ and their time rates of change $\dot{\mathbf{u}}_\alpha$ in the finite element (FE) regions for all α nodes. Within this scheme, the Hamiltonian is divided into FE, MD, TB and handshaking contributions from FE/MD and MD/TB during the domain decomposition. It is assumed that the atomic and nodal movements are not necessarily exclusive to a single domain, but their interactions are. In this way, H_{tot} may be written as

$$H_{tot} = H_{FE}(\mathbf{u}_\alpha, \dot{\mathbf{u}}_\alpha) + H_{FE/MD}(\mathbf{r}_j, \mathbf{v}_j \mathbf{u}_\alpha, \dot{\mathbf{u}}_\alpha) + H_{MD}(\mathbf{r}_j, \mathbf{v}_j) + H_{MD/TB}(\mathbf{r}_j, \mathbf{v}_j) + H_{TB}(\mathbf{r}_j, \mathbf{v}_j)\,, \quad (53)$$

with the Hamiltonian of different contributions depicted with appropriate indices. Rudd et al. [437] explain that the FE/MD as well as MD/TB handshakes must successfully address the fundamental issues of (i) matching the degrees of freedom and (ii) defining consistent forces at the corresponding interfaces. Despite this similarity, it should be emphasized that each handshake obliges a somewhat different approach in order to answer the requirements. This is due to the fact that the MD/TB handshake occurs across an interface of atoms whereas the interface at the FE/MD handshake is between planes of atoms [437]. Appropriate derivatives of this Hamiltonian function can be used to define the equations of motion in a standard Euler-Lagrange routine. The time evolution of all the variables can then proceed to the next step using the same integrator. The interested reader is referred to the work of Rudd et al. [437] for further information.

3.2.2. Linking Atomistic and Continuum Models

It is frequently observed in large-scale atomistic simulations that only a small subset of atoms actively participate in the evolving phenomenon. This allows for the majority of atoms to be effectively represented by continuum models. Hence, a considerable reduction of computation and storage resources is guaranteed if only novel multiscale approaches could reduce the number of degrees of freedom in atomistic simulations. There is a tremendous amount of concurrent multiscale modelling methods developed in the last twenty years which couple atomistic simulations such as MD with continuum simulations such as FEM [441,442]. The idea behind these methods, not unlike all multiscale strategies, is to focus the available computation power where it is needed by applying atomistic simulations, whereas an approximate solution is provided for the rest of the system by continuum simulations. Therefore, both atomistic details as well as the macroscopic properties of materials can be obtained simultaneously from these simulations. Such models are mostly designed for crystalline materials such as metals or carbon nanomaterials. Unfortunately, their application in polymeric materials is still limited, possibly due to the unfamiliarity of these models to polymer researchers. Although some authors have referred to such methods in recent reports on polymer simulations [32,299], the fundamentals of the methods are not brought to discussion. We believe that the basic ideas of these methods can be extended to study polymeric materials. Here a brief description of these methods is provided with emphasis on the fundamentals. At the end of this section,

several studies in polymeric systems are listed where such methods or a modified version of them are incorporated to address the phenomena. It is our hope that it will help guide future improvements.

Certain categories of problems such as fracture and nanoindentation possess the characteristics of localized deformation where it is possible to address the system by a dual-domain or partitioned-domain approach; one with an atomistic description B^A, and the other with continuum approximation B^C. The two domains are linked by an interfacial region B^I across which compatibility and equilibrium are enforced. An important distinction among various methods is the way they treat the interfacial region. Most methods follow one of the strategies demonstrated in Figure 12. The interfacial region is shown by the dashed lines. In part (a) of the figure, B^I has been further subdivided into two parts: (i) the handshake region B^H, and (ii) the padding region B^P. As explained before, the handshake region provides a mixing between the two scales. The padding region is continuum in nature and provides the boundary conditions to the atoms in B^A and B^H with a certain range of atomistic interactions, r_{cut}. The thickness of this region depends on r_{cut} and the motions of atoms in B^P are calculated, in different ways for different methods, based on the continuum displacement fields at the positions of the padding atoms. It is also possible to eliminate the handshake region as shown in part (b) of Figure 12. Models that do not use a handshake region mostly incorporate a direct atom-node correspondence at the edge of the FE region to impose the displacement compatibility across the interface. This necessitates that the mesh is refined down to the atomic scale on the continuum side of the interface and hence introduces difficulties in mesh generation.

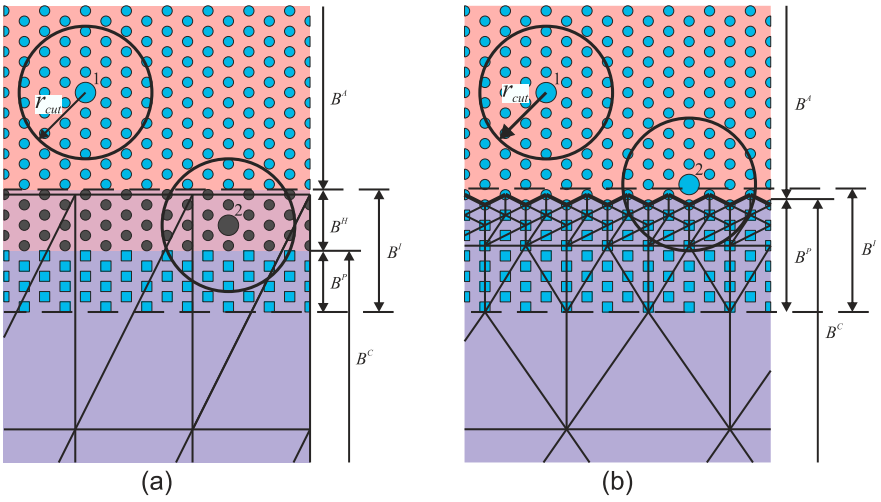

Figure 12. Schematic representation of generic interfaces used in coupled atomistic/continuum simulations: (**a**) with the handshake region; and (**b**) without the handshake region. Atom 1 does not influence the continuum directly (while atom 2 does) because of the finite cutoff length. Padding, handshake, and regular atoms are depicted by blue squares, black circles, and blue circles, respectively.

The coupling between the B^A and B^C domains necessitates compatibility conditions in each direction. Therefore, the displacements of atoms in B^P must be determined from the nodal displacements in B^C. Moreover, the displacement boundary conditions need to be defined for the B^C nodes at the edge of the mesh closest to the B^A. The compatibility criteria can be either strong or weak. The strong compatibility is when the padding atoms move in the same as the finite elements in which they reside. In this type of compatibility, subsets of nodes are defined that coincide with some of the atoms in B^A. The displacement boundary condition is therefore imposed on B^C with the motion of the overlaying atoms from B^A. The weak compatibility, on the other hand, utilizes some sort of an averaging or penalty method to enforce the displacement boundary conditions. Strong compatibility introduces complications in mesh definition near the interface while it also yields relatively more accurate results [442].

The simulation algorithm often finds the equilibrium by either minimizing an energy functional or driving the set of forces on all degrees of freedom to zero. Consequently, there are two major categories of the governing formulation i.e., the energy-based and the force-based approaches. The major drawback of the energy-based method is that it is extremely complicated to remove the non-physical artifacts of the coupled energy functional. This problem, often referred to as the "ghost forces", stems from trying to combine two energy functionals from different models into a single coupled energy expression [442–444]. The force-based approaches, on the other hand, have no well-defined total energy functional and are considered to be non-conservative in general. These approaches can be numerically slow and unstable and could converge to unstable equilibrium states. However, force-based methods can eliminate the ghost forces due to access to the direct definition of the forces.

Several methods are proposed in literature to correct the ghost forces artifact in energy-based models. These methods take various actions in order to eliminate or at least mitigate for ghost forces [445–449]. One such approach with general characteristics is the deadload ghost force correction [444]. In this approach, the ghost forces are explicitly computed and the negative of these forces are added as deadloads to the affected atoms or nodes. The deadload ghost force correction has shown great promise in some static simulations [442]. However, the deadload correction is only an approximation for the simulations where ghost forces change during the calculation progress.

The general algorithm for energy-based methods defines the total potential energy of the entire system U^{tot} as the sum of the potential energies of the atomistic U^{A}, continuum U^{C} and handshake U^{H} regions, as

$$\mathrm{U}^{tot} = \mathrm{U}^{A} + \mathrm{U}^{C} + \mathrm{U}^{H}, \tag{54}$$

and minimizes it to reach equilibrium. These energies are described by [442]

$$\mathrm{U}^{A} = \sum_{\alpha \in B^{A}} \mathrm{E}_{\alpha} - \sum_{\alpha \in B^{A}} \mathbf{f}_{\alpha} \cdot \mathbf{u}_{\alpha}, \tag{55}$$

$$\mathrm{U}^{C} = \sum_{e=1}^{N_e} \sum_{q=1}^{N_q} \omega^{q} \mathrm{V}_{e} \mathrm{W}(\Delta(\mathbf{r}_{e}^{q})) - \bar{\mathbf{f}}^{\mathrm{T}} \mathbf{u}, \tag{56}$$

$$\mathrm{U}^{H} \approx \sum_{\alpha \in B^{H}} (1 - \Theta(\mathbf{r}_{\alpha}))\mathrm{E}_{\alpha} + \sum_{e \in B^{H}} \Theta(\mathbf{r}_{e}^{cent}) \mathrm{W}(\Delta(\mathbf{r}_{e}^{cent})), \tag{57}$$

where the energy, spatial coordinates, displacement and applied forces of atom α are shown by E_{α}, $\mathbf{r}_{\alpha}$, $\mathbf{u}_{\alpha}$, and $\mathbf{f}_{\alpha}$, respectively. N_e is the number of elements, V_e is the volume of element e, N_q is the number of quadrature points in the numerical integration, $\mathbf{r}_{e}^{q}$ is the position of quadrature point q of element e in the reference configuration, and ω^{q} is the associated Gauss quadrature weights. $\bar{\mathbf{f}}$ and $\mathbf{u}$ are the vector of applied forces and nodal displacements in the FE region, respectively. W is a function of the deformation gradient Δ. $\mathbf{r}_{e}^{cent}$ is the coordinates of the Gauss point in element e which is taken at the centroid of the triangular elements in this specific case shown in Figure 12. One should notice that the energy of the continuum region is approximated due to the fact that a continuous integral has been replaced by a discrete numerical method. Consequently, the handshake region is also approximated since it also uses such a numerical approach for the continuum energy contribution. In the energy equation for the handshake region, both the continuum and atomistic energies are used in a weighted fashion according to a function Θ which varies linearly from one at the edge of B^{H} closest to the continuum region, to zero at the edge closest to the atomistic region. Indeed, for methods with no handshake region, U^{H} is taken zero and only the continuum and atomistic regions contribute to U^{tot}. Moreover, one should note that the padding atoms have no contribution to the formulation of the potential energy. Therefore, these atoms only provide an appropriate boundary condition for the atoms in B^{A}.

The force-based methods are based on two independent potential energy functionals. The first one calculates an energy functional U^{atom} assuming the entire system is modelled using atoms. The second energy functional U^{FE} on the other hand, provides a description of the system if it was modelled

entirely in a FEM framework. The forces for all α atoms, $\mathbf{f}_\alpha$, and all i nodes, $\mathbf{f}_i$, are simply found by differentiating the corresponding energies with respect to the atomic or nodal displacements, $\mathbf{u}_\alpha$ and $\mathbf{u}_i$ respectively, as

$$\mathbf{f}_\alpha = \frac{\partial \mathrm{U}^{atom}}{\partial \mathbf{u}_\alpha}, \tag{58}$$

$$\mathbf{f}_i = \frac{\partial \mathrm{U}^{FE}}{\partial \mathbf{u}_i}. \tag{59}$$

It is important to note that the difference between energy-based and force-based methods stems from the fact that in the second approach one does not attempt to minimize the combined energy functional. In the following, some relevant approaches which are used to link atomistic and continuum models are discussed.

Quasicontinuum Approach

Quasicontinuum (QC) method is a particularly interesting approach by Tadmor et al. [450–452] which seamlessly couples the atomistic and continuum realms. In QC approach, the atomistic description of the system is systematically coarsened by the introduction of kinematic constraints designed carefully so that the full atomistic resolution is preserved where required, for instance in the vicinity of large deformations, and to treat collectively large numbers of atoms in regions further away. QC was firstly developed to investigate defects in solids considering the interaction of dislocations [444,450,451,453–456]. However, it has also found applications in fracture and crack mechanics [457,458], and nanoindentation [459].

In QC method, there is no handshake region. Since there is no separation of the domains in QC, there are no needs for separate sets of material data in this multiscale approach. This is a significant advantage of QC. The calculation domain is partitioned into non-overlapping cells similar to the FEM. These cells then cover the constituting molecules of the material while their vertices coincide with some representative atoms from the molecules. The local density of such representative atoms is larger in regions with high deformations compared with the regions experiencing low deformations. Figure 13 shows an example for the selection of representative atoms in the vicinity of a crack. QC takes the degrees of freedom in a cell the same as the degrees of freedom of the representative atoms of that cell. In addition, the movement of molecules is usually calculated from the representative atoms utilizing interpolation functions. QC also approximates the average energy of a cell from its representative atoms. The method eventually looks for the arrangement of representative atoms which minimizes the potential energy of the domain.

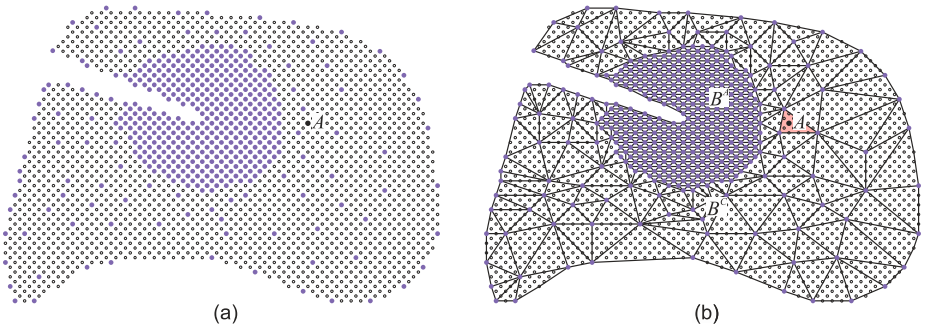

Figure 13. For an irregular domain which includes a crack, part (**a**) shows the representative atoms near the crack tip; Part (**b**) demonstrates the domain meshed by linear triangular elements. The density of representative atoms is adjusted to correspond to the variation in the deformation gradient. In order to calculate the displacement of atom A in part (**b**), one can use a linear interpolation of the displacements of the three representative atoms which form the highlighted element.

Variants of the QC model have been developed and applied in different situations [450,451,460,461]. In general, the QC approach includes three major blocks: (i) the constrained minimization of the atomistic energy of the system; (ii) the computation of the effective equilibrium equations based on appropriate summation rules; and (iii) the design of the computational mesh representing the structure of the system based on proper adaptation criteria. The QC model initially provides a full atomistic description of the system which is later scaled down to a subset of representative atoms. The positions of the remaining atoms are obtained by piecewise linear interpolations of the representative atoms. Afterwards, the effective equilibrium equations are obtained by minimizing the potential energy of the system based on the scaled-down configuration space. A precise evaluation of the total energy of the system E^{tot} is often performed over the full collection of atoms as

$$E^{tot} = \sum_{i=1}^{N} E_i, \tag{60}$$

in which N is the total number of atoms, and E_i is the energy of the ith atom at its corresponding position in the system. This comprehensive formula is approximated in QC models benefitting from the concept of representative atoms with

$$E^{tot} \approx \sum_{i=1}^{N_r} \omega_i \overline{E_i}, \tag{61}$$

where ω_i and $\overline{E_i}$ are the quadrature weight which shows the number of the atoms that a given representative atom stands for in the definition of the total energy, and the energy of the ith representative atom, respectively. Here, the summation is only performed over N_r representative atoms and thus the calculation effort is reduced. The representative atoms are usually adaptively selected so that an accurate description of the critical positions with larger deformation fields is obtained. QC approach often incorporates FEM to determine the displacement fields and combines it with an atomistic technique which is used to determine the energy of a given displacement field. One can compare it with the standard FEM in which a constitutive law is coupled with it through a phenomenological model.

The concepts of QC could be extended to include a coupling between atomistic calculations and QM as well. Such an strategy was initially introduced to study fracture in silicon and the method was named coupling of length scales (CLS) [437,439,440]. There are small differences between QC and CLS. Initially CLS method used a small strain approximation to describe the continuum region rather than the Cauchy-Born rule used in QC [442,462]. However, conceptually the methods are similar since the original CLS approach could be generalized to provide a nonlinear Cauchy-Born description for the continuum region. Furthermore, minor differences between the methods exist in the way they treat the interface. Still, these differences are believed to have slight influences on the error and rate of convergence [442,463].

QC suffers from the ghost forces like any other energy-based method. An idea to reduce these forces was initially put forward by introducing a handshake region to the QC models. This idea along with minor changes in the manipulation of forces at the interface constructed the bridging domain method (BDM) [464]. At the interface, BDM uses weak compatibility which eliminates the need for one-to-one correspondence between atoms and nodes. This weak compatibility imposes some loss of accuracy on BDM. Another approach to correct for ghost forces is the iterative minimization of two energy functionals used in composite grid atomistic/continuum method (CACM) [465]. CACM is a highly modular method with weak compatibility and no handshake region. It provides the possibility to separately solve energy functionals of different regions. However, this could lead to longer computation times especially for nonlinear problems.

Coarse-Grained Molecular Dynamics

Coarse-grained molecular dynamics (CGMD) was originally developed to model the nano-electro-mechanical systems (NEMS) [437,452,466]. In this technique, conventional MD is coupled

with a CG description of the system. The CG regions are modeled on a mesh in a formulation that generalizes conventional FEM of continuum elasticity. The significant aspect of CGMD is that it is derived solely from the MD model and has no continuum parameters. In other words, this method is notably different from the other coupled atomistic/continuum methods presented in this manuscript in the way that it constructs the continuum model only based on the atomistic information. As a result, it offers a smooth coupling and provides control of errors that arise at the coupling between the atomistic and CG regions. A more general version for the dynamics of CGMD is also proposed by Curtarolo and Ceder [467].

In CGMD the domain is partitioned into cells with variable sizes. This provides the possibility to assign a mesh node to each atom in important positions whereas in other regions the cells could contain several atoms and the nodes are not necessarily coincident with atoms. CGMD follows a detailed statistical coarse-graining prescription which particularly results in scale-dependent constitutive equations for different regions of the domain [466]. In CGMD, the CG mesh is refined to the atomic scale where it joins with the MD lattice. This refined mesh with no handshake region as well as the fact that CGMD adopts an effective field model suggests a strong resemblance to QC. In addition to the point made earlier on the use of atomistic constitutive equations in CGMD, this method is also designed for finite-temperature simulations. On the contrary, the classic QC is mainly applicable to zero-temperature simulations. It is interesting to note that according to Rudd and Broughton [466] the classic QC is closely related to the zero-temperature rigid approximation of CGMD. It should be noted that finite-temperature versions of QC are developed in recent years [468–470]. These methods often benefit from coarse-graining concepts similar to CGMD. Finally, CGMD is free from the ghost forces which is a desirable feature missing in QC.

Finite-Element/Atomistic Method

The finite-element/atomistic (FEAt) method is a force-based method first introduced by Kohlhoff et al. [471]. FEAt uses no handshake region and strong compatibility is enforced between the domains. To compensate for the absence of the handshake region, FEAt incorporates a nonlocal elasticity formulation in the finite elements and mitigates the abrupt transition from B^C to B^A. In general, the forces on every atom α in B^A and B^P are calculated independently from B^C, from the derivative with respect to atom positions of an energy functional $\mathrm{U}^{A\cup P}$ of the form

$$\mathrm{U}^{A\cup P} = \sum_{\alpha\in\{B^A\cup B^P\}} \mathrm{E}_\alpha - \sum_{\alpha\in\{B^A\cup B^P\}} \mathbf{f}_\alpha\cdot\mathbf{u}_\alpha. \tag{62}$$

This energy functional looks very similar to the one used in energy-based methods, but it is fundamentally different since it also contains the padding atoms. The energy functional of the continuum domain is similar to the energy functional of the energy-based methods described in Equation (56). The forces on the nodes are therefore simply obtained from its derivative with respect to nodal displacements. Based on these forces, the atoms and nodes are moved and the forces are re-calculated for the new atom and node positions.

Some variations to FEAt are found in the literature. In the presence of dislocations in the continuum, one can use discrete dislocation methods in the description of the continuum region. The resulting continuum region could be coupled with the atomistic region in a force-based algorithm just like FEAt to yield coupled atomistic and discrete dislocation (CADD) approach [472,473]. In order to remove the strong compatibility from FEAt and CADD, the hybrid simulation method (HSM) uses the same approach as BDM by including a handshake region in the system [474]. A variation of HSM is the concurrent atomistic/continuum (AtC) method in which a blending of forces is performed at the interface [443,475,476].

Bridging Scale Method

The bridging scale method (BSM) is an energy-based technique with no handshake region. In this method, the FE mesh exists throughout the entire domain in order to store a part of the final solution, see Figure 14. The central idea behind BSM is derived from classical works in decomposing a complete solution of the total displacement field into fine and coarse scales and solving for the fine scale only in regions that require it [477–479]. The coarse scale solution is that part of the solution which is normally represented by a set of FE shape functions. The fine scale solution on the other hand, is defined as the part of the solution whose projection onto the coarse scale is zero.

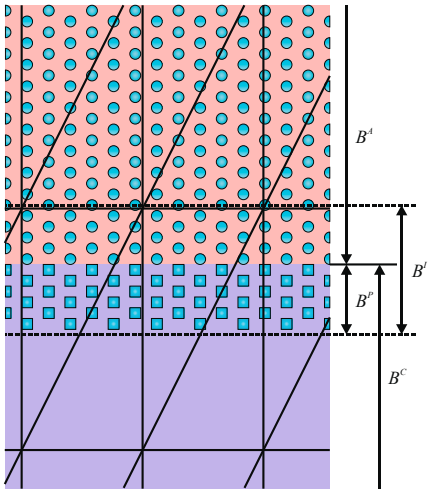

Figure 14. The BSM interfacial region. The interface has no handshake region and the finite elements cover the entire body which allows to store the coarse scale displacement field.

In BSM framework, the coarse scale solution $\gamma \mathbf{r}_\alpha$ is taken to be a function of the initial positions of the atoms $\mathbf{r}_\alpha$ and is defined by

$$\overline{\gamma}\mathbf{r}_\alpha = \sum_i \sigma_i^\alpha \mathbf{u}_i, \tag{63}$$

where σ_i^α is the shape function of node i evaluated at point $\mathbf{r}_\alpha$, and $\mathbf{u}_i$ is the FE nodal displacement associated with node i. Using a mass-weighted least-squares fitting of the coarse scale solution to the total solution, Park and Liu [480] showed that the fine scale solution γ' can be defined based on a projection matrix $\mathbf{P}$ as

$$\gamma' = \gamma - \mathbf{P}\gamma. \tag{64}$$

Here, γ is the exact solution determined from an underlying atomistic technique such as MD. Therefore, the total solution can be found by summing up both fine and coarse scale contributions. Such an approach is sometimes referred to as the projection method in the literature due to the fact that atomistic and continuum regions are coupled by projecting a fine scale solution onto a finite dimensional solution space [481].

Applications in Polymeric Materials

In this part of the paper, we give several examples for the applications of coupled atomistic/continuum models in polymeric systems. In the studies outlined here, one can find applications of the methods explained so far; either it is directly used, or a modified version is developed to capture the correct physics involved, or a concept is borrowed to propose new models for polymers. The reader should note that our goal is not to provide a comprehensive list here but merely to raise attention towards the opportunities. We hope that the polymer researcher finds it useful in order to navigate through these multiscale approaches and further develop new strategies for one's own problem.

Generally, it is more difficult to model polymers than crystalline materials due to their amorphous nature. A methodology to solve this problem was formulated by Theodorou and Suter [482,483] in which a parent chain of atoms is attached to an Amorphous Cell (AC). The AC then experiences deformations while periodic boundary conditions are applied to all sides. Tan et al. [481] incorporated the concept of AC and developed it based on the adaptive scaling resolution ideas similar to CGMD and introduced the Pseudo Amorphous Cell (PAC) multiscale approach for amorphous polymers. PAC algorithm includes: (i) generating a configuration of polymer chains in the domain; (ii) applying linear molecular mechanics for regions with small deformations; (iii) reducing the degrees of freedom in such regions; and (iv) coupling of linear and nonlinear molecular mechanics equations. In their method, the regions with large deformations are represented with nonlinear molecular mechanics and thus provide a finer solution. The authors showed that PAC can successfully simulate the nanoindentation of amorphous polymers and the indentation force was predicted with a good precision comparable to a full molecular mechanics simulation [481]. Later Su et al. [484] applied the PAC approach to correlate the movements of atoms of an amorphous material within a representative volume element (RVE) to the its overall deformation.

The ground idea of projection methods was first introduced in details by Hughes et al. [477] as the variational multiscale methods (VMS) which allows a complete model to be described by orthogonal subscale models. Utilizing this property, Codina [485] presented a method to deal with numerical instability of the Stokes problem due to the incompressibility constraint and convection. He proposed using orthogonal subscales in FEM through the pressure gradient projection. This approach has been developed recently by Castillo and Codina [486,487] to present stabilized VMS formulations to solve the quiescent three-field incompressible flow problems of viscoelastic fluids as well as fluids with nonlinear viscosity. The authors were able to successfully capture the distributions of streamlines in a sudden contraction flow for an Oldroyd-B fluid at Re of 1 at various Weissenberg numbers (We). It was observed that the size of the vortex appearing in the bottom corner decreases as We increases.

In a recent MD study of brittle fracture in epoxy-based thermoset polymers under mechanical loading, Koo et al. [488] introduced an EM step into the virtual deformation test to maintain the system temperature at zero. They stated in the paper that this idea was borrowed from QC which bridges atomistic scale to continuum scale by decoupling temperature effects. The possibilities of incorporating multiscale approaches to connect MD and FEM such as QC, in investigations of structure at epoxy-silica interface are also emphasized by Büyüköztürk et al. [489].

Jo and Yang [490] utilized an atomistic/continuum model to predict the mechanical properties of semicrystalline poly(trimethylene terephthalate) (PTT). Their approach includes an EM process similar to energy-based methods. The semicrystalline PTT includes an amorphous matrix represented as a continuum, and the crystalline phase represented by a spherical inclusion modelled in atomistic detail. The degree of crystallinity of PTT is altered by changing the volume fraction of an inclusion.

In order to model the compressive behavior of carbon nanotube PNCs, Li and Chou [491,492] developed a multiscale strategy in which the nanotube is modelled at the atomistic scale, and the matrix deformation is analyzed by the continuum FEM. Their methodology is similar to other atomistic/continuum coupling themes except for the fact that they adopt a so-called truss rod model to correctly represent van der Waals interactions at the interface. The multiscale scheme developed by Li and Chou was later incorporated by Montazeri and Naghdabadi [493] to study the stability of carbon nanotube PNCs with a viscoelastic matrix. They coupled molecular structural mechanics to FEM and simulated the buckling behavior of the system.

A multiscale simulation strategy was proposed by De et al. [494] to determine the mesoscopic velocity development in polymer fluids with large stress relaxation times. The incorporation of a constitutive viscosity equation is not sufficient in such systems to produce the correct rheology. The authors introduced a scale bridging concept in which small parts of the system were simulated with MD. These parts could communicate with each other through a continuum approach. During the passing of information, the continuum approach provides precise means of interpolating between these

points. They described the coupling of atomistic and continuum regions in a Lagrangian framework so that the memory effects are included in the calculations.

3.3. Adaptive Resolution Simulations

It was already discussed in the concurrent multiscale approaches that there is a category of systems in which the phenomenon of interest is focused in a subregion of the entire domain. Consequently, it would be computationally efficient if the irrelevant AA representation of molecules far from this subregion were replaced with an alternative less expensive model. However, the common limitation in all concurrent methods (introduced so far) is that particle exchange is not allowed in the fixed regions of the system treated at different resolutions. The relatively new class of multiscale simulation approaches, i.e., the adaptive resolution simulations, provides this possibility. Several papers have been devoted to address different aspects of these methods in recent years showing their increasing popularity [337,495–498]. It should be noted that these methods can be principally considered to be concurrent since they often couple the simultaneous run of two techniques with different levels of resolution using a transition region. Furthermore, the transition region usually uses an either force or energy interpolation criterion to link different resolutions somewhat similar to the concurrent methods. However, in adaptive resolution simulations, an atom or a molecule is free to smoothly switch its resolution within the same simulation run depending on its spatial coordinates. Therefore, it allows for an adaptive modification of the resolution within the coexisting models which promotes the accuracy where needed and provides the required precision. In concurrent approaches, on the other hand, different scales are coupled often by a step-wise transfer of information between different methods, for instance we refer to Youn Park et al. [499]. Therefore, some authors introduce adaptive resolution simulations as a separate class of multiscale approaches to emphasize these different aspects [32]. Here, we also follow this notion.

The adaptive resolution simulations often divide a domain into an AA and a CG region and link them using a transition region, see Figure 15, hence are sometimes referred to as the double-resolution simulation methods. Examples for the appropriate systems to investigate with such a strategy include the studies of macromolecules embedded in a solvent (see Figure 16) [500], and liquids near surfaces [501]. The transition region provides the basis for a smooth interpolation from a certain structural representation of a molecule to another depending on the properties that have to be preserved in the CG region. A complete methodology should address the interactions between the atoms or molecules in different domains as well as the property change in crossing the transition region. Moreover, it is central to adaptive resolution simulations that the molecules should be able to diffuse freely between different regions of the simulation box. Other constraints could include thermal equilibrium and uniform density profile across the entire domain which along with certain region-specific properties lead to a formulation of an adaptive resolution scheme.

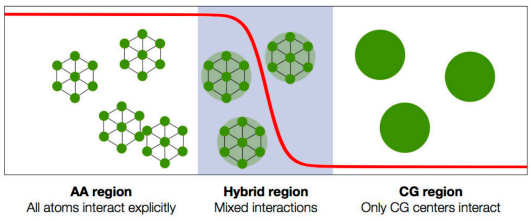

Figure 15. Representation of an adaptive resolution simulation in which a high-resolution region (AA region) is coupled to a low-resolution region (CG region). In the AA region, the structure of the molecules are described in their full atomistic details. In the CG region, however, a simpler representation of the structure and interactions of the molecules are utilized. A transition region is used to connect these regions. The novelty as well as difficulty of adaptive resolution schemes depends strongly on the properties of the transition region, i.e., the way molecules change their resolution. Reprinted from Potestio et al. [337] under the terms of the Creative Commons Attribution License.

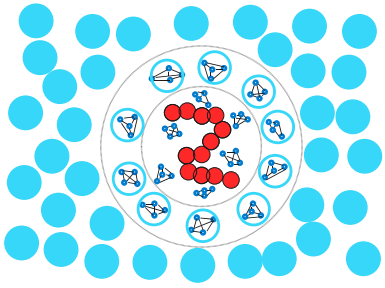

Figure 16. A schematic representation of a generic polymer solution. The structural resolution of the solvent molecules adaptively change based on their distance from the center of the mass of the polymer chain. The polymer beads are represented smaller than the solvent molecules to preserve clarity. Reprinted from Praprotnik et al. [500] with the permission of AIP Publishing.

3.3.1. The Adaptive Resolution Scheme

The Adaptive Resolution Scheme (AdResS) was developed by Kremer and co-workers [500,502–507] to simulate systems in which an AA and a CG model are incorporated to model different subregions of the simulation domain at the same time. The atoms and molecules are allowed to diffuse freely from one region to the other using a smooth transition region which links the subregions. AdResS is principally based on the assumption that Newton's third law should be satisfied the entire simulation box. Additionally, the method assumes that a molecule in the CG subregion contains no information about its atomistic details and interacts with other molecules, either in AA or CG regions, only via its center of mass. An interpolation scheme for the force field across the domain defining the force $\mathbf{f}_{\alpha\beta}$ acting between molecules α and β can be formulated considering the aforementioned assumptions as

$$\mathbf{f}_{\alpha\beta} = \psi(\mathbf{R}_\alpha)\,\psi(\mathbf{R}_\beta)\,\mathbf{f}^{\mathrm{AA}}_{\alpha\beta} + (1 - \psi(\mathbf{R}_\alpha)\,\psi(\mathbf{R}_\beta))\,\mathbf{f}^{\mathrm{CG}}_{\alpha\beta}, \tag{65}$$

where $\mathbf{R}_\alpha$ and $\mathbf{R}_\beta$ are the center of mass coordinates of molecules α and β, respectively. $\mathbf{f}^{\mathrm{AA}}_{\alpha\beta}$ and $\mathbf{f}^{\mathrm{CG}}_{\alpha\beta}$ are the atomistic and CG forces acting on molecule α due to the interaction with molecule β, respectively. Here, ψ is a spatial interpolation function that goes from 1 in the AA region to 0 in the CG region smoothly. In the transition region, atomistic details are explicitly integrated and the CG force is computed between the centers of mass of the molecules and then redistributed to the atoms weighted by the ratio of the atom's mass to the mass of molecule [508]. In the CG region, the CG force is directly applied to the center of mass coordinates of the molecules and there is no need to conserve the molecules internal structure. When a molecule enters the CG region its atomistic details are removed and reintroduced again, through some sort of reservoir of equilibrated atomistic structures, as soon as it approaches the transition region.

The central requirement of satisfying Newton's third law in AdResS is demonstrated to rule out any form of potential energy interpolation and vice versa [509]. Consequently, energy-conserving simulations in the microcanonical ensemble cannot be performed using AdResS. Due to the non-conservative nature of the forces in the transition region, molecules receive an unreal excess energy when crossing this region. This energy can be removed utilizing a local thermostat in order to keep the temperature constant everywhere in the system. The equilibrium configurations of the system are then sampled according to Boltzmann distribution [500,502,503,505,510,511].

The different resolution of the utilized models typically results in a pressure difference between the corresponding regions which further leads to a non-uniform density profile in the system. Kremer and co-workers [508,512,513] modify the CG potential by introducing a thermodynamic force $\mathbf{f}^{th}$ which counterbalances the high pressure of the CG model. This force is obtained in an iterative procedure as

$$\mathbf{f}^{th}_{i+1} = \mathbf{f}^{th}_{i} - \frac{\nabla \rho_i(\mathbf{r})}{\rho^* \mathrm{k}_T}, \tag{66}$$

where ρ^* is the reference molecular density, k_T is the system's isothermal compressibility and $\rho_i(r)$ is the molecular density profile. This profile is taken as a function of the position in the normal direction to the CG/AA interface. The iterative procedure converges once the density profile is flat, i.e., $\nabla\rho(r) = 0$. The resulting thermodynamic force produces a flat density profile and preserves the thermal compressibility of the system as well as the structure of the system in the CG region. Principally, this method allows one to use any CG force field. As a result, the AA region exchanges energy and molecules with a reservoir like an open system. Such an approach yields a relatively small AA region with the corresponding molecule number fluctuations and all relevant thermodynamic quantities the same as a large AA simulation [508]. It is only because of the thermodynamic driving force that this condition can be achieved independent of the CG model used.

AdResS provides the possibility to perform simulations of the spatial extension of correlations in the system. Particularly, the structural properties of the AA region can be monitored as a function of its size in order to examine their dependency on the interactions with molecules in the bulk region. For instance, Lambeth et al. [514] used this notion to study the ordering degree of the hydrogen bond network of a molecule with hydrophilic and hydrophobic bonds dissolved in water as a function of the size of the AA region. The extent of spatial correlations in low-temperature para-hydrogen has also been studied with the same approach [515,516]. In some systems, it is critical to have access to a large number of particles, for instance, to precisely evaluate the solvation free energies in mixtures. Thus, a standard AA simulation could lead to extremely costly computations in such cases. Naturally, AdResS has shown to be a viable candidate for these systems as well, as evidenced in some works on methanol-water mixtures [517], and triglycine in aqueous urea [513]. Another interesting possibility for such a case to even further accelerate the simulations was incorporated by Mukherji and Kremer [518] to study a coil-globule transition of a biomolecule in aqueous methanol. In their simulations, the usual closed boundary CG reservoir was replaced with a much smaller open boundary CG reservoir in which particles can be exchanged at the eight corners of the simulation domain, see Figure 17. Through this particle exchange adaptive resolution scheme (PE-AdResS), the depletion effects were avoided during the simulations. This type of *open system* MD simulations have raised attraction in recent years. We refer to the work of Agarwal et al. [519] for instance. Recently, a variation of AdResS formulation was developed by Alekseeva et al. [163] which presents a coupling strategy between the stochastic multiparticle collision dynamics and the deterministic MD methods. In this way, the authors were able to successfully demonstrate that hydrodynamic properties of the mixed fluid are conserved by a suitable coupling of the two particle-based methods.

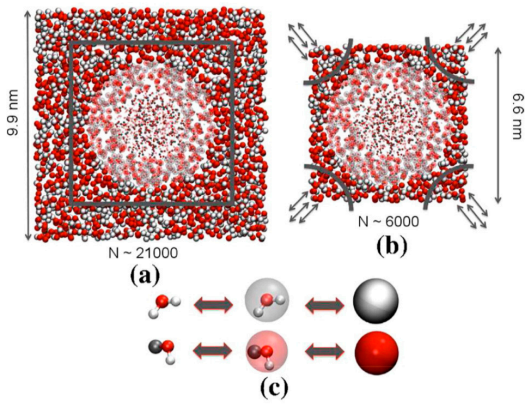

Figure 17. Simulations of a biomolecule dissolved in aqueous methanol: (**a**) Conventional AdResS approach; (**b**) PE-AdResS approach; and (**c**) Mapping scheme of the smooth transition between AA and CG representations. Reprinted with permission from Mukherji and Kremer [518]. Copyright 2016 American Chemical Society.

3.3.2. The Hamiltonian Adaptive Resolution Scheme

A theoretical analysis of the AdResS double-resolution scheme can show that with a local thermostat and the thermodynamic force the atomistic region is equivalent to an open region of a fully atomistic simulation up to second order correlation functions, i.e., the density profile and radial distribution functions [520]. Nonetheless, the lack of a global energy function makes it impossible to perform simulations in the microcanonical ensemble. Consequently, different strategies were employed to formulate an energy conserving version of adaptive resolution simulations including the healing region concept with a space-dependent interpolation of the AA and CG potential energies [521], and the combination schemes for the sum of the Lagrangians of all possible groupings of atomistic and CG molecules [522,523]. Unfortunately, these methods are either inaccurate or extremely complicated to be readily used [337,506]. Recently, an energy-based version of the AdResS method was developed namely the Hamiltonian adaptive resolution scheme (H-AdResS) [524,525]. H-AdResS defines the total Hamiltonian of each molecule with a position-dependent function H^{tot} as

$$H^{tot} = K + U^{int} + \sum_{\alpha} \left\{ \psi_{\alpha} U_{\alpha}^{AA} + (1 - \psi_{\alpha}) U_{\alpha}^{CG} \right\}, \tag{67}$$

in which K is the all-atom kinetic energy of the molecules, U^{int} is the contribution from internal interactions of the molecules, N is the number of molecules, and

$$U_{\alpha}^{AA} = \frac{1}{2} \sum_{\beta, \beta \neq \alpha}^{N} \sum_{ij} U^{AA}(|\mathbf{r}_{\alpha i} - \mathbf{r}_{\beta j}|), \tag{68}$$

$$U_{\alpha}^{CG} = \frac{1}{2} \sum_{\beta, \beta \neq \alpha}^{N} U^{CG}(|\mathbf{R}_{\alpha} - \mathbf{R}_{\beta}|), \tag{69}$$

$$\psi_{\alpha} = \psi(\mathbf{R}_{\alpha}). \tag{70}$$

U_{α}^{AA} and U_{α}^{CG} represent the potential energies of molecule α in its AA and CG representations, respectively. The force acting on atom i in molecule α can be obtained through differentiation of this Hamiltonian function [337,524,525]. The differentiation operation results in a drift force F_{α}^{drift} in the transition zone which is proportional to the difference between U_{α}^{AA} and U_{α}^{CG}, by

$$F_{\alpha}^{drift} = -\left[U_{\alpha}^{AA} - U_{\alpha}^{CG} \right] \nabla_{\alpha i} \psi_{\alpha}. \tag{71}$$

The definition of the drift force implies that the molecules are pushed into one of the regions if the potentials of the AA and CG regions are different. It is obvious from the mathematical expression of the drift force that it is not possible to write it as a sum of antisymmetric terms with molecule label exchange. Consequently, it results in a local breakdown of Newton's third law at the transition region. One can deduce that the drift force vanishes if the CG potential perfectly reproduces the many-body potential of mean force in the AA model. Since this is almost never true, a thermodynamic imbalance is always to be expected between the two regions in the form of different pressure and density levels [337,524]. Potestio et al. [524] used a compensation term $\Delta H(\psi_{\alpha})$ in the Hamiltonian, as was done in the AdResS method with the thermodynamic force, to correct for this imbalance. The Hamiltonian is therefore modified as [524]

$$\hat{H} = H^{tot} - \sum_{\alpha=1}^{N} \Delta H(\psi_{\alpha}). \tag{72}$$

The authors then obtained an approximate function $\Delta H(\psi_{\alpha})$ to cancel out the drift force on average, as

$$\Delta H(\psi_{\alpha}) = \frac{\Delta F(\psi_{\alpha})}{N}, \tag{73}$$

in which the suitable compensation term is related to the Kirkwood's thermodynamic integration for the free energy difference $\Delta F(\psi_\alpha)$ between a hybrid system with a position-independent coupling parameter ($\psi_\alpha \leq 1$) and a CG system ($\psi_\alpha = 0$) at the reference density ρ^* [524]. The authors include a further compensation term to ensure that both the AA and CG subregions coexist at the same reference density ρ^* by considering the effect of pressure difference along the interface $\Delta p(\psi_\alpha)$ and re-formulating $\Delta H(\psi_\alpha)$ in terms of the chemical potential gradient $\Delta\mu(\psi_\alpha)$, as [524]

$$\Delta H(\psi_\alpha) = \Delta\mu(\psi_\alpha) = \frac{\Delta F(\psi_\alpha)}{N} + \frac{\Delta p(\psi_\alpha)}{\rho^*} \quad (74)$$

The H-AdResS method was utilized with both a free energy and a chemical potential compensation strategy to study their effects on the density and pressure profiles [524]. The results showed that with the application of the free energy compensation Equation (73) the pressure profile became flat, but the density was still higher in the AA region. On the other hand, when the chemical potential compensation Equation (74) was applied, the densities of the AA and CG regions attained the same value with a small deviation due to the fluctuations present in the transition region. This was achieved by modifying pressures in each region to correspond to the desirable reference state of density and temperature.

The existence of a Hamiltonian in H-AdResS allows for the precise formulation of a statistical physics theory of double-resolution systems, providing a deep insight into the properties of a given AA model, its CG counterpart and the relation between them. In addition, H-AdResS makes it possible to perform simulation in the microcanonical ensemble as well. Some simulation techniques such as MC can also be incorporated in H-AdResS in contrast to AdResS [525]. It should be noted that H-AdResS along with its compensation strategy can be extended to multicomponent systems. In order to illustrate the routine, a simple case was outlined by Potestio et al. [337] for a liquid composed of two types of molecules.

3.4. Extending Atomistic Simulations

Besides the methods that are explicitly designed to link computational techniques from different realms together, there are some approaches to extend the reaches of a specific technique such as MD. As it was noted before, MD plays a critical role in the modelling of materials problems because MD simulations can follow the actual dynamical evolution of the system along its deterministic pathway. However, MD is strictly limited to very short time scales due to its full atomistic representation of the molecules. Therefore, some researchers studied different methods to address the time scale problem including hyperdynamics [526–528], parallel replica dynamics [529], and temperature-accelerated dynamics [530]. These methods are based on the transition state theory in which the system trajectory is simulated to find an appropriate pathway to escape from an energy well [528,531]. The simulation walks through this pathway with a process that takes place much faster than the direct MD.

The hyperdynamics is an accelerating approach for MD simulations which needs no prior information about the possible state trajectories of the system in the phase space. The method raises the energy of the system in regions other than at the dividing surfaces of the initial and final configurations in the phase space by applying a bias potential. Consequently, an accelerated transition is achieved from one equilibrium state to another equilibrium state [528]. The parallel replica dynamics method was incorporated for a system with infrequent events in which successive transitions are uncorrelated [529]. In such a system, running a number of independent MD simulations in parallel gives the exact dynamical evolution between the states. For a system with correlated crossing events, the state-to-state transition sequence is still correct. However, the error associated with the simulation time should be eliminated. Finally, in the temperature-accelerated dynamics method, the state-to-state transition is accelerated by increasing the temperature followed by filtering out the transitions that should not have occurred at the original temperature [530]. Consistent with other accelerated dynamics methods, the trajectory of the system is allowed to wander on its own to find an appropriate escape path. Consequently, no prior information is required about the nature of the involved phenomena [528].

The accelerated dynamics methods are formulated in order to find transition pathways between two known equilibrium states via effective MD simulations. Other approaches to extend atomistic simulations are also available which often require no preconceived mechanism or transition state. In order to find the transition pathway, one such method minimizes the average of the potential energy along the path instead of finding the path with the lowest barrier [532–534]. Another approach utilizes statistical sampling of the dynamical paths i.e., MC sampling of MD trajectories introducing transition path-sampling methods [535–539]. In addition to these methods, a finite-temperature string method is also available which represents the collection of the hyperplanes normal to the pathways of a system by a string [540–543]. In this method, the string is constantly updated during the simulations to capture the correct coordinate associated with the phenomenon. Finally, some works try to find dynamical paths that could connect an initial state to a final state in general terms [544–550]. Such methods often offer good numerical stability, efficient parallelizability, and high quality trajectories.

A class of methods attempts to address the systems with a free-energy surface which could possess several local minima in the free-energy surface. These strategies are generally known as the methods to escape the free-energy local minima [551]. For instance, a proper combination of CG dynamics with the adaptive bias potential methods could allow for the system to avoid local minima in the free-energy surface [551]. At the same time, the system provides a quantitative description of the free-energy surface through the integrated process. Such an approach has especially found application in biological systems [552–554].

In a category of systems an inherent dispersity in some characteristic details results in a natural disparity in time scales. A well-known example of such a case was already discussed in Section 2.1, i.e., the Born–Oppenheimer approximation [45], in which the electrons move independently from the nuclei due to their largely different masses. Another scenario which could lead to the separation of time scales is when a subset of forces is much stronger than the rest of the forces, while the masses of the constituents are almost equal. In order to deal more efficiently with such systems, various integration algorithms with multiple time steps have been developed [555]. This idea is particularly useful in polymers in which the bonds vibrate often much faster than they translate and rotate. Consequently, the configuration space as well as the forces can be divided into fast and slow components. As a result of this separation, a set of equations of motion are derived for the development of the fast and slow processes. This set of equations are solved using the multiple-time-step integration in which a small time step Δt to advance the fast processes by n steps while holding the slow variables fixed. The slow processes are then updated using a time step of $n\Delta$t. In the case that an analytic solution of high-frequency motions is available, this solution can be incorporated into an integration scheme for the entire system. Therefore, a time step can be defined based on the slow processes and used for the simulation of entire system with a much smaller number of cycles [555].

In order to extend the time scale of MD simulations, a method was developed based on optimization of the action functional [534]. The method parametrizes the system trajectory as a function of length rather than time. In order to achieve this goal, this approach optimizes an action term defined based on the stochastic time-dependent difference equation rather than solving the Newton equations in MD simulations. A similar idea was recently proposed in which the trajectories of the orientation process of weakly-interacting layered silicates were parametrized as a function of the shear strain instead of the time [196]. The idea of using the applied strain was motivated by the experimental reports supporting strain-dependent structure developments in such non-Brownian materials. Benefitting from the notion that the orientation kinetics is principally determined with respect to strain, the applied strain was selected to pass the orientation parameters to an upper scale through a simple combination of affine and nonaffine deformations, see Figures 18 and 19. This methodology could be also incorporated to develop multiscale models of orientation process provided that the interactions between the components are carefully defined in the unit cell.

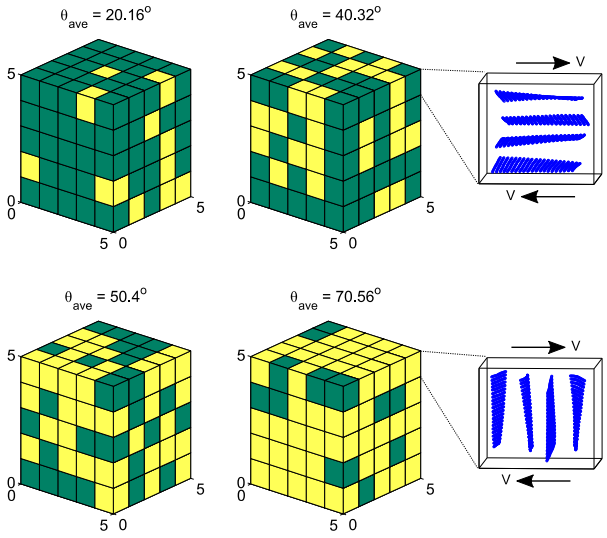

Figure 18. Examples of construction of a large cell for the upper scale simulation benefitting from a random mixing of unit cells resulting in various average initial orientation angles, θ_{ave}. The initial configurations of the unit cells before the flow starts are also given. Reprinted from Gooneie et al. [196]. Copyright 2016, with permission from John Wiley & Sons Inc.

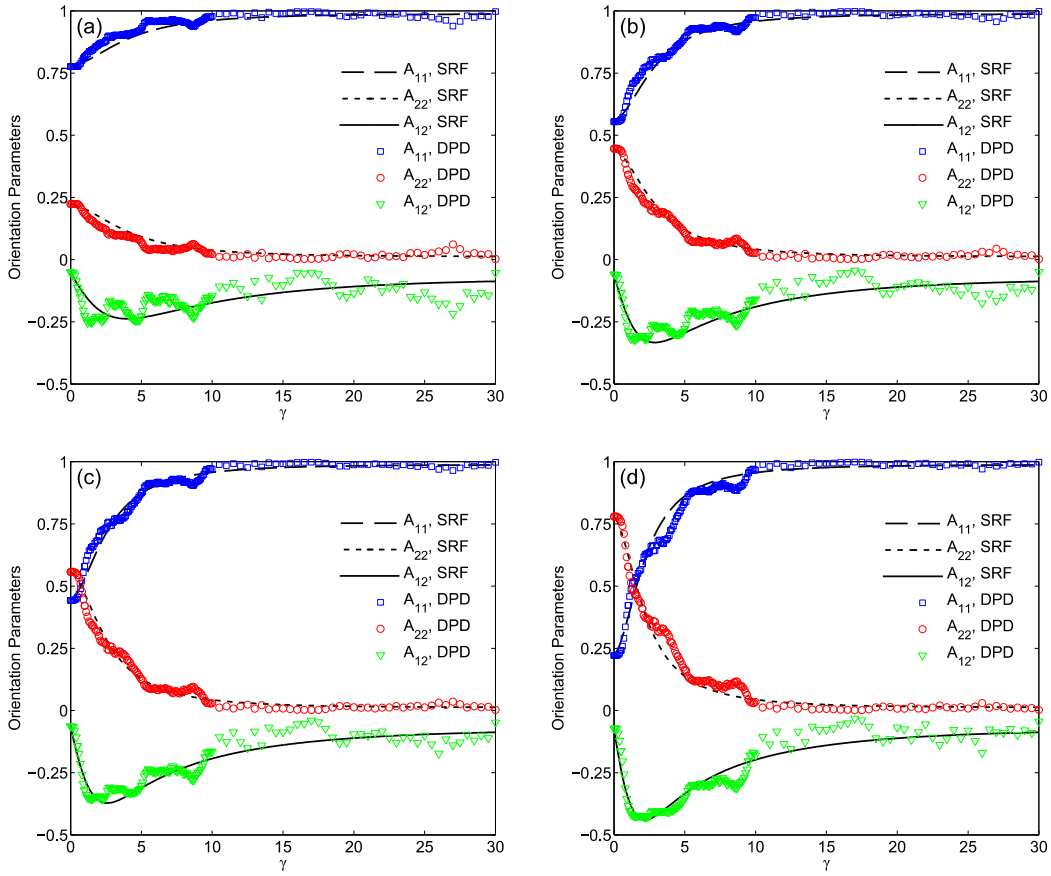

Figure 19. The orientation process defined by the orientation parameters as a function of the shear strain, γ. The results are derived from DPD models and strain reduction factor (SRF) model for various average initial orientation angles of (**a**) 20.16° ; (**b**) 40.32° ; (**c**) 50.40° ; and (**d**) 70.56° . Reprinted from Gooneie et al. [196]. Copyright 2016, with permission from John Wiley & Sons Inc.

4. Conclusions and Outlooks

The development of polymeric materials necessitates a comprehensive understanding of the phenomena at different time and length scales. This need has significantly accelerated the progress in theoretical and computational methods to capture the inherent hierarchical phenomena in such materials. In this field, the development of efficient multiscale approaches could lead to the design of materials simultaneously on many scales instead of trial-and-error experimentations. The present review attempted to survey the state-of-the-art of various multiscale simulation approaches as applied to polymer science.

Within the context of an overall multiscale simulation perspective, various approaches for modelling relevant processes in polymer science are classified into three major categories, namely sequential, concurrent, and adaptive resolution approaches. This classification provides the opportunity to easily examine these methods and the systems to which they have been often applied. It is fairly clear from this review that different multiscale approaches provide precious insights into the structure and dynamics of polymeric materials.

In general, the sequential techniques are more popular in polymer science. However, *a priori* knowledge of relevant physical quantities is a prerequisite in these methods. The bridging of various scales in a sequential method is often implicit. A successful sequential modelling depends critically on the accuracy of the finer scale model as well as the reliability of the message-passing algorithms. The link between QM data and atomistic models should be further developed to reproduce the correct structure and thermodynamics. Phenomena which might involve the breaking of bonds require a reactive force field of MD in combination with QM which further complicates the computations as well as the derivation of such a force field from the parametrization of QM data in the first place. Moreover, the construction of CG potentials from atomistic data might necessitate more rigorous strategies particularly in systems with variant local structures and properties. Systematic coarse-graining and backmapping schemes were revisited as major routes towards a sequential model generation in polymers. An inevitable question that arises with the coarse-graining procedure is the question of transferability of the final CG model. As an advantageous aspect, however, the investigation of transferability conditions could help to gain insight into fundamental principles that control the behavior of the system. It is expected that a general prescription for coarse-graining should be developed which ensures a wide range of transferability. In the context of systematic coarse-graining methods, it is interesting to extend super CG models to describe phenomena, such as flow birefringence and systems such as multicomponent mixtures.

The concurrent multiscale methods are a lot more complicated and computationally expensive than sequential approaches particularly when it comes to simulating flow problems. Nevertheless, they do not depend on *a priori* knowledge of relevant physical quantities supplied from smaller-scale simulations. In concurrent methods, it is significant that the problem is carefully posed to make the method practical. The common problem in a concurrent approach is usually associated with the partitioning of domains in the system. More importantly, an appropriate handshaking strategy in a concurrent approach between different domains, which is both mathematically accurate and physically consistent, is challenging and critical. There is no general consensus on what a proper coupling of domains is. Therefore, a general criterion that measures the quality of handshaking between domains would be extremely beneficial. Additionally, there is plenty of room for innovative research on the issue of domain coupling. Although many concurrent approaches exist which are very desirable and appealing in metals and carbon nanomaterials, their use in polymeric systems is still limited to a large extend. In this paper, we have devoted an entire section to cover the fundamentals of several concurrent methods and introduce the existing possibilities to polymer scientists. In order to better illustrate the outlooks, several examples from relevant areas of polymer research are provided so that the reader is persuaded to follow these highlights.

A third group of multiscale simulation strategies was also noted as the adaptive resolution schemes in which a molecule can freely move in space and change its resolution depending on

spatial criteria. There is plenty of room in this class of methods for future innovation, either in its methodological aspects or its extension to different materials and phenomena. The method is fundamentally developed for quiescent conditions and the application of flow is yet to be added to these schemes. Even for the simulation of equilibrium conditions, these schemes show noticeable discontinuities in pressure and density profiles at the transition region between the high and low resolutions. Furthermore, the combination of mixed resolution concurrent methods and adaptive resolution schemes can potentially become an increasingly robust multiscale simulation methodology for complex polymer systems. Future work in this area appears to be promising.

When dealing with computer simulations, the role of the computer itself should be also noted including both hardware and software characteristics. Computer technology develops at an astonishing rate. It is believed that the progress in graphics processing units (GPUs) along with the development of GPU-oriented molecular simulation algorithms should extend our reach to yet unexplored spatial and temporal scales in the simulations of polymer systems. Such computational resources along with advanced simulations schemes can closely mimic the problem at hand on engineering time scales in a computer experiment. As a possible area for future endeavors, it would be ideal to compile a combination of atomistic methods with mesoscale and even continuum methods within one simulation package instead of many scattered codes which are available today, each coming with its certain advantages and shortcomings. Such a package could ultimately use the strengths from various individual codes to mitigate for the shortcomings of others. Even more important is the development and implementation of seamless multiscale modelling techniques in this hypothetical package. In addition, it is expected that the qualitative description of fundamental processes will be replaced with the quantitative prediction of material properties with the introduction of exascale computing. First-principle simulations are expected to play an increasing role in these areas. However, the availability of increased computing power will not be sufficient on its own and advanced strategies and techniques are an indispensable part of extreme-scale computing architectures.

Although multiscale methods have brought about substantial developments in the field, the challenge of bridging the time scale of atomic motions to the typical experimental and engineering scales is still far from completion. For instance, in a number of polymer systems such as PNCs, suitable theoretical frameworks are still missing which can provide insights into the nonequilibrium phenomena and the impact of external fields on the morphology and dynamics of the system. Moreover, more rigorous and direct quantitative analysis of nonequilibrium atomistic polymeric models and their CG counterparts is still needed. Various topics still remain to be disclosed in future research including new emerging possibilities to pass the information from the atomic to macroscopic scale and back. Multiscale modelling techniques are yet to be applied to characterize many interesting systems such as polymer flow in dilute and concentrated solutions, characteristics of a polymer layer next to the surface of nanoparticles in PNCs, the molecular roots of the viscoelasticity in filled elastomers, dynamics of confined polymers, etc. These examples are just a few among many topics for the future research on polymer systems. With the progress in theoretical as well as experimental techniques, finding answers to such challenges shall result in a comprehensive knowledge of various material properties of polymeric systems across a range of length and time scales. Moreover, it will bring forth directions to design new systems with desired or yet unexplored properties in the future.

In the framework of multiscale methods, one should not forget that there is also a critical necessity to design new and improved simulation methods at individual time and length scales. From the discussions provided in this review, it is clear that multiscale modelling is a heavily active field in modern science with a multidisciplinary character. The actual power of multiscale strategies is only truly appreciated by overcoming traditional barriers between various scientific disciplines. The computational multiscale approaches should eventually fulfill their philosophy which is to enhance our knowledge of, and ability to control complex processes, even in life sciences. Developing proper multiscale methods is extremely difficult but undeniably represents the future of polymer science as well as computer simulation and modelling.

Author Contributions: Ali Gooneie performed the literature review and wrote the paper. Ali Gooneie and Stephan Schuschnigg reproduced the figures used in the context. Ali Gooneie, Stephan Schuschnigg and Clemens Holzer reviewed the manuscript at intermediate steps and contributed to the final manuscript.

Conflicts of Interest: The authors declare no conflict of interest.

Appendix A. Acronyms and Nomenclature

Acronyms

Acronym	Full phrase
AA	All-Atomistic
AC	Amorphous Cell method
AdResS	Adaptive Resolution Scheme
AIMD	Ab Initio Molecular Dynamics
AtC	Atomistic/Continuum method
BD	Brownian Dynamics
BDM	Bridging Domain Method
BGK-LB	Bhatnagar, Gross, And Krook LB method
BSM	Bridging Scale Method
CACM	Composite Grid Atomistic/Continuum Method
CADD	Coupled Atomistic and Discrete Dislocation method
CFD	Computational Fluid Dynamics
CG	Coarse-Grained
CGMD	Coarse-Grained Molecular Dynamics
CLS	Coupling of Length Scales method
CRW	Conditional Reversible Work
D2Q9	2-dimensional lattice with 9 allowed velocities used in LB simulations
D3Q19	3-dimensional lattice with 19 allowed velocities used in LB simulations
DDFT	Dynamic Density Functional Theory
DFT	Density Functional Theory
DPD	Dissipative Particle Dynamics
EFCG	Effective Force CG
EM	Energy Minimization
FDM	Finite Difference Method
FE	Finite Element
FEAt	Finite-Element/Atomistic method
FEM	Finite Element Method
FVM	Finite Volume Method
GDM	Generalized Differences Methods
GFEM	Galerkin Finite Element Method
GPU	Graphics Processing Unit
H-AdResS	Hamiltonian Adaptive Resolution Scheme
HSM	Hybrid Simulation Method
IBI	Iterative Boltzmann Inversion
IMC	Inverse Monte Carlo
LB	Lattice Boltzmann
LGCA	Lattice Gas Cellular Automata
LSM	Lattice Spring Model
MC	Monte Carlo
MD	Molecular Dynamics
Na-MMT	Sodium Montmorillonite

NEMS	Nano-Electro-Mechanical Systems
OpenFOAM	Open Source Field Operation And Manipulation
PA	Polyamide
PAC	Pseudo Amorphous Cell method
Pe	Peclet number
PE	Polyethylene
PNC	Polymer Nanocomposite
PP	Polypropylene
pPMF	Pair Potential of Mean Force
PRISM	Polymer Reference Interaction Site
PS	Polystyrene
PTT	Poly(Trimethylene Terephthalate)
QC	Quasicontinuum method
QM	Quantum Mechanics
QUICK	Quadratic Upstream Interpolation for Convective Kinematics
Re	Reynolds number
RVE	Representative Volume Element
SCFT	Self-Consistent Field Theory
SDPD	Smoothed Dissipative Particle Dynamics
SEM	Spectral Element Method
SPH	Smoothed Particle Hydrodynamics
SRF	Strain Reduction Factor model
SUPG	Streamline-Upwind/Petrov-Galerkin
TB	Tight Binding
TDGL	Time-Dependent Ginzburg-Landau
VMS	Variational Multiscale methods
We	Weissenberg number
XRD	X-Ray Diffraction

Nomenclature

Symbol	**Meaning**
A	$A = 6\xi k_B T$ in BD method
$\mathbb{A}_{ij}$	maximum repulsion between bead i and bead j in DPD method
a_i	acceleration of ith particle
B^A	atomistic domain in concurrent simulations
B^C	continuum domain in concurrent simulations
B^H	handshake region in concurrent simulations
B^I	interfacial region in concurrent simulations
B^P	padding region in concurrent simulations
b_i	fitting parameter
c_i	fitting parameter
D^ϑ	the diffusion term of ϑ
D_{cm}	center-of-mass self-diffusion coefficient
e	element
$\mathbb{e}$	absolute unit charge of an electron
E_f	Young's modulus
E_i	energy of atom, particle, or node i
$\overline{E_i}$	energy of the ith representative atom in QC method
E_k	eigenstate of energy
$E_{k_{el}}$	eigenstate energy of an electron

E_{k_n}	eigenstate energy of a nucleon
E^{tot}	total energy
$\Delta F(\psi_\alpha)$	free energy difference in H-AdResS method
F_{ij}^{C}	conservative force between bead i and its neighboring bead j within the force cutoff radius r_{cut}
F_{ij}^{D}	dissipative force between bead i and its neighboring bead j within the force cutoff radius r_{cut}
F_{ij}^{R}	random forces between bead i and its neighboring bead j within the force cutoff radius r_{cut}
F_{α}^{drift}	drift force of molecule α
$\bar{f}$	vector of applied forces in the FE region of a concurrent simulation
f_i	force acting on the ith atom, particle, or node
$f_{\alpha\beta}$	force acting between molecules α and β
f^{th}	thermodynamic force
f_i^{B}	Brownian random force acting on the ith particle
$f_{\alpha\beta}^{AA}$	atomistic forces acting on molecule α due to the interaction with molecule β
$f_{\alpha\beta}^{CG}$	CG forces acting on molecule α due to the interaction with molecule β
G'	storage modulus
G''	loss modulus
$H(\Gamma_i)$	Hamiltonian of the system at system state Γ_i
$\hat{H}$	modified Hamiltonian of the H-AdResS method
$\Delta H(\Gamma_{i\rightarrow j})$	change in the system Hamiltonian for going from system state Γ_i to Γ_j
$\Delta H(\psi_\alpha)$	compensation term in the Hamiltonian of the H-AdResS method
$H_{FE}(u_\alpha, \dot{u}_\alpha)$	Hamiltonian of the FE region as a function of the nodal displacements u_α, and time rate of nodal displacements $\dot{u}_\alpha$
$H_{FE/MD}(r_j, v_j, u_\alpha, \dot{u}_\alpha)$	Hamiltonian of the FE/MD handshake region as a function of the atomic positions r_j, atomic velocities v_j, nodal displacements u_α, and time rate of nodal displacements $\dot{u}_\alpha$
$H_{MD}(r_j, v_j)$	Hamiltonian of the MD region as a function of the atomic positions r_j, and atomic velocities v_j
$H_{MD/TB}(r_j, v_j)$	Hamiltonian of the MD/TB handshake region as a function of the atomic positions r_j, and atomic velocities v_j
$H_{TB}(r_j, v_j)$	Hamiltonian of the TB region as a function of the atomic positions r_j, and atomic velocities v_j
H_{tot}	total Hamiltonian
h	Planck's constant
$J^{\vartheta,C}$	convection flux term in FVM formulation
$J^{\vartheta,D}$	diffusion flux term in FVM formulation
K	the all-atom kinetic energy of the molecules
k_B	Boltzmann's constant
k_T	isothermal compressibility
l	bond length
M, M_w	molecular weight
m	mass of an atom or particle
m_{el}	mass of an electron
m_n	mass of a nucleon
N	number of atoms, particles, or nodes
N_c	number of monomers per chain
N_e	number of elements

N_q	number of quadrature points in the numerical integration
N_r	number of representative atoms in QC method
P	the projection matrix
$\Delta \mathrm{p}(\psi_\alpha)$	pressure difference along the interface in H-AdResS method
$\mathrm{p}_{i \to j}$	probability of accepting a new configuration for going from system state Γ_i to Γ_j
p^{R}	probability distribution function
$\mathrm{p}^{\mathrm{R}}_{target}$	the target probability distribution function of AA simulations
Q^{ϑ}	the generation/destruction of ϑ within the control volume per unit volume
$\mathrm{R}(\mathrm{u})$	residual form of a partial differential equation in terms of the unknown function u in FEM scheme
R_g	radius of gyration
R_i	center of mass coordinates of the ith molecule
$\mathbf{r}$	coordinates vector of an atom, or particle, or node
r	distance
r_{cut}	force cutoff radius
r_{el_i}	spatial coordinates of an electron
$\hat{\mathrm{r}}_{ij}$	unit vector pointing from the center of bead j to that of bead i
r_{n_j}	spatial coordinates of a nucleon
r_e^{cent}	coordinates of the Gauss point in element e taken at the centroid of the triangular elements
r_e^q	position of quadrature point q of element e in the reference configuration
$\delta \mathrm{r}_i^{\mathrm{B}}(\mathrm{t}+\Delta \mathrm{t})$	random displacement of the ith particle due to the random forces during time step Δt
S	surface vector
S_i	ith subregion
$\{\mathrm{S}_\rho\}$	set of weighting functions in FEM
$\mathrm{s}_{entropy}$	rescaling factor for the entropy change
$\mathrm{s}_{friction}$	rescaling factor for the friction change
T	temperature
t	time
Δt	time step
$\mathrm{U}(\mathrm{r})$	potential energy
U^A	potential energies of the atomistic region
U^{atom}	energy functional of a systems assuming it is entirely modelled using atoms
U^C	potential energies of the continuum region
$\mathrm{U}^{\mathrm{CG}}(\mathrm{r}, l, \theta, \mho)$	general form of the CG potential function in IBI method
U^{FE}	energy functional of a systems assuming it is entirely modelled using FEM
U^H	potential energies of the handshake region
U^{int}	energy of internal interactions
U^{tot}	total potential energy of the entire system
$\mathrm{U}^{\mathrm{CG}}_{angle}(\theta)$	bond angle potential in the blob model
$\mathrm{U}^{\mathrm{CG}}_{bond}(l)$	bond potential in the blob model
$\mathrm{U}^{\mathrm{CG}}_{nonbonded}(\mathrm{r})$	potential of nonbonded interactions in the blob model
$\mathrm{U}^{\mathrm{AA}}_\alpha$	potential energy of molecule α in the AA representation
$\mathrm{U}^{\mathrm{CG}}_\alpha$	potential energy of molecule α in the CG representation
u	vector of nodal displacements in the FE region of a concurrent simulation

$u(r)$	the unknown function in FEM which one needs to find
$u_h(r)$	approximation of the function $u(r)$ under consideration in FEM
u_α	displacements of atom, particle, or node α
$\dot{u}_\alpha$	rate of displacements of atom, particle, or node α
u^n	values of the function u_h at node n of the mesh
V_e	volume of element e
dV	volume element of the simulation domain in FEM
∂V_e	surfaces surrounding the volume v_e of element e
v	macroscopic velocity magnitude
$\mathbb{v}$	$\mathbb{v} = \sqrt{3}\,\mathbb{v}_s$ in LB method
$v(r,t)$	macroscopic local velocity at node r at time t in LB
$\widetilde{v}(t+\Delta t)$	estimated velocity in the next time step using a predictor method in DPD velocity-Verlet algorithm
$\delta v_i^B(t+\Delta t)$	Random velocity change of the ith particle due to the random forces during time step Δt
v_i	velocity of ith atom, particle, or node
$\lvert\mathbb{v}_i\rvert$	velocity magnitude in i-direction in LB method
$\{\mathbb{v}_k\}$	set of prescribed velocity vectors connecting the neighboring nodes in LB method
$\mathbb{v}_s$	speed of sound
W	a function of deformation gradient Δ
w_i	weighting constants used in LB method
$z_n e$	positive unit charge of a nucleon
Γ_i	system state in a phase space at position i
γ	exact solution in the projection method
$\dot{\gamma}$	shear-rate
$\overline{\gamma}(r_\alpha)$	coarse scale solution of a problem in the projection method
γ'	fine scale solution of a problem in the projection method
Δ	deformation gradient
δ	delta function
$\Delta\mu(\psi_\alpha)$	chemical potential gradient in H-AdResS method
ε	neighboring cells of a specific element in FVM
ζ	random number between 0 and 1 which is to determine the acceptance or rejection of a new configuration
ζ_{ij}	a Gaussian random number with zero mean and unit variance used in the definition of the random forces between beads i and j in DPD method
η	viscosity
Θ	a weighting function to link FE and atomistic models in concurrent simulations
θ	bond angle
θ_{ave}	averaged initial orientation angle
Λ_{ik}	collision matrix used in LB method
λ	multiplication parameter in in DPD velocity-Verlet algorithm
μ	fitting parameter
ν	fitting parameter
ϑ	a general conserved scalar variable in FVM scheme
ξ	friction coefficient between atoms or particles
ξ_{ij}	friction coefficient between bead i and bead j in DPD method
ξ_m	friction coefficient between particles of freely-rotating chains
ϖ	wave function of electrons

ρ	fluid density in CFD
$\rho(\mathrm{r},\mathrm{t})$	macroscopic local density at node r at time t in LB method
$\rho_i(\mathrm{r})$	molecular density profile in the ith iteration step as a function of the position in the direction perpendicular to the interface, in AdResS method
ρ^*	reference molecular density
ρ_i	ith weighting function in FEM
σ_{ij}	noise amplitude between bead i and bead j in DPD method
σ_i^α	shape function of node i evaluated at the point with coordinates r_α
τ	characteristic collision time in LB method
$\Phi(\mathrm{u})$	integral form of the weighted residuals in FEM
$\phi(\mathrm{r})_k$	wave function in Schrödinger's equation
φ	wave function of the nuclei
χ_{ij}	a parameter in DPD formulation which equals 1 for beads with a distance less than r_{cut} and equals 0 otherwise
$\Psi_i(\mathrm{r},\mathrm{t})$	particle distribution function used in LB at node r at time t moving with velocity $\mathbb{v}_i$ In the i-direction
$\Psi_i^{\mathrm{eq}}(\mathrm{r},\mathrm{t})$	equilibrium particle distribution function used in LB at node r at time t moving with velocity $\mathbb{v}_i$ In the i-direction
ψ	spatial interpolation function in AdResS method
$\psi_n(\mathrm{r})$	interpolation functions in FEM for node n
$\psi_n^e(\mathrm{r})$	interpolation functions in FEM for node n in element e
Ω	simulation domain in FEM
$\partial\Omega$	boundaries of the simulation domain in FEM
$\mho$	dihedral angle
ω	Frequency
ω_i	quadrature weight signifying how many atoms a given representative atom stands for in the description of the total energy, in QC method
$\omega^{\mathrm{D}}(\mathrm{r}_{ij})$	dissipative weight function in DPD method
ω^q	associated Gauss quadrature weights of quadrature point q of element e
$\omega^{\mathrm{R}}(\mathrm{r}_{ij})$	random weight function in DPD method

References

1. Elliott, J.A. Novel approaches to multiscale modelling in materials science. *Int. Mater. Rev.* **2011**, *56*, 207–225. [CrossRef]
2. Zeng, Q.H.; Yu, A.B.; Lu, G.Q. Multiscale modeling and simulation of polymer nanocomposites. *Prog. Polym. Sci.* **2008**, *33*, 191–269. [CrossRef]
3. Ayton, G.S.; Noid, W.G.; Voth, G.A. Multiscale modeling of biomolecular systems: In serial and in parallel. *Curr. Opin. Struct. Biol.* **2007**, *17*, 192–198. [CrossRef] [PubMed]
4. Ayyaswamy, P.S.; Muzykantov, V.; Eckmann, D.M.; Radhakrishnan, R. Nanocarrier hydrodynamics and binding in targeted drug delivery: Challenges in numerical modeling and experimental validation. *J. Nanotechnol. Eng. Med.* **2013**, *4*. [CrossRef] [PubMed]
5. Raabe, D. Challenges in computational materials science. *Adv. Mater.* **2002**, *14*, 639–650. [CrossRef]
6. Kremer, K.; Müller-Plathe, F. Multiscale problems in polymer science: Simulation approaches. *MRS Bull.* **2001**, *26*, 205–210. [CrossRef]
7. Murtola, T.; Bunker, A.; Vattulainen, I.; Deserno, M.; Karttunen, M. Multiscale modeling of emergent materials: Biological and soft matter. *Phys. Chem. Chem. Phys.* **2009**, *11*, 1869–1892. [CrossRef] [PubMed]
8. Peter, C.; Kremer, K. Multiscale simulation of soft matter systems—From the atomistic to the coarse-grained level and back. *Soft Matter* **2009**, *5*, 4357–4366. [CrossRef]
9. Sherwood, P.; Brooks, B.R.; Sansom, M.S. Multiscale methods for macromolecular simulations. *Curr. Opin. Struct. Biol.* **2008**, *18*, 630–640. [CrossRef] [PubMed]

10. Steinhauser, M.O.; Hiermaier, S. A review of computational methods in materials science: Examples from shock-wave and polymer physics. *Int. J. Mol. Sci.* **2009**, *10*, 5135–5216. [CrossRef] [PubMed]
11. Fermeglia, M.; Posocco, P.; Pricl, S. Nano tools for macro problems: Multiscale molecular modeling of nanostructured polymer systems. *Compos. Interfaces* **2013**, *20*, 379–394. [CrossRef]
12. Fermeglia, M.; Pricl, S. Multiscale molecular modeling in nanostructured material design and process system engineering. *Comput. Chem. Eng.* **2009**, *33*, 1701–1710. [CrossRef]
13. Johnston, K.; Harmandaris, V. Hierarchical simulations of hybrid polymer-solid materials. *Soft Matter* **2013**, *9*, 6696. [CrossRef]
14. Chiu, C.-W.; Huang, T.-K.; Wang, Y.-C.; Alamani, B.G.; Lin, J.-J. Intercalation strategies in clay/polymer hybrids. *Prog. Polym. Sci.* **2014**, *39*, 443–485. [CrossRef]
15. Gao, D.; Li, R.; Lv, B.; Ma, J.; Tian, F.; Zhang, J. Flammability, thermal and physical-mechanical properties of cationic polymer/montmorillonite composite on cotton fabric. *Compos. Part B* **2015**, *77*, 329–337. [CrossRef]
16. Lowe, D.J.; Chapman, A.V.; Cook, S.; Busfield, J.J.C. Micromechanical models of young's modulus of NR/organoclay nanocomposites. *J. Polym. Sci. Part B* **2011**, *49*, 1621–1627. [CrossRef]
17. Mattausch, H.; Laske, S.; Duretek, I.; Kreith, J.; Maier, G.; Holzer, C. Investigation of the influence of processing conditions on the thermal, rheological and mechanical behavior of polypropylene nanocomposites. *Polym. Eng. Sci.* **2013**, *53*, 1001–1010. [CrossRef]
18. Decker, J.J.; Meyers, K.P.; Paul, D.R.; Schiraldi, D.A.; Hiltner, A.; Nazarenko, S. Polyethylene-based nanocomposites containing organoclay: A new approach to enhance gas barrier via multilayer coextrusion and interdiffusion. *Polymer* **2015**, *61*, 42–54. [CrossRef]
19. Nguyen, Q.T.; Ngo, T.D.; Tran, P.; Mendis, P.; Bhattacharyya, D. Influences of clay and manufacturing on fire resistance of organoclay/thermoset nanocomposites. *Compos. Part A* **2015**, *74*, 26–37. [CrossRef]
20. Gooneie, A.; Nazockdast, H.; Shahsavan, F. Effect of selective localization of carbon nanotubes in PA6 dispersed phase of PP/PA6 blends on the morphology evolution with time, part 1: Droplet deformation under simple shear flows. *Polym. Eng. Sci.* **2015**, *55*, 1504–1519. [CrossRef]
21. Kotal, M.; Bhowmick, A.K. Polymer nanocomposites from modified clays: Recent advances and challenges. *Prog. Polym. Sci.* **2015**, *51*, 127–187. [CrossRef]
22. Sepahvand, R.; Adeli, M.; Astinchap, B.; Kabiri, R. New nanocomposites containing metal nanoparticles, carbon nanotube and polymer. *J. Nanopart. Res.* **2008**, *10*, 1309–1318. [CrossRef]
23. Pavlidou, S.; Papaspyrides, C.D. A review on polymer-layered silicate nanocomposites. *Prog. Polym. Sci.* **2008**, *33*, 1119–1198. [CrossRef]
24. Moniruzzaman, M.; Winey, K.I. Polymer nanocomposites containing carbon nanotubes. *Macromolecules* **2006**, *39*, 5194–5205. [CrossRef]
25. Gooneie, A.; Nazockdast, H.; Shahsavan, F. Effect of selective localization of carbon nanotubes in PA6 dispersed phase of PP/PA6 blends on the morphology evolution with time, part 2: Relaxation of deformed droplets after cessation of flow. *Polym. Eng. Sci.* **2016**, *56*, 51–60. [CrossRef]
26. Sinha Ray, S.; Okamoto, M. Polymer/layered silicate nanocomposites: A review from preparation to processing. *Prog. Polym. Sci.* **2003**, *28*, 1539–1641. [CrossRef]
27. Lecouvet, B.; Gutierrez, J.G.; Sclavons, M.; Bailly, C. Structure-property relationships in polyamide 12/halloysite nanotube nanocomposites. *Polym. Degrad. Stab.* **2011**, *96*, 226–235. [CrossRef]
28. Akkermans, R.; Warren, P.B. Multiscale modelling of human hair. *Philos. Trans. R. Soc. A Math. Phys. Eng. Sci.* **2004**, *362*, 1783–1793.
29. De Borst, R. Challenges in computational materials science: Multiple scales, multi-physics and evolving discontinuities. *Comput. Mater. Sci.* **2008**, *43*, 1–15. [CrossRef]
30. Gates, T.S.; Odegard, G.M.; Frankland, S.J.V.; Clancy, T.C. Computational materials: Multi-scale modeling and simulation of nanostructured materials. *Compos. Sci. Technol.* **2005**, *65*, 2416–2434. [CrossRef]
31. Karakasidis, T.E.; Charitidis, C.A. Multiscale modeling in nanomaterials science. *Mater. Sci. Eng. C* **2007**, *27*, 1082–1089. [CrossRef]
32. Khalatur, P.G. Molecular Dynamics Simulations in Polymer Science: Methods and Main Results. In *Polymer Science: A Comprehensive Reference, 10 Volume Set*; Elsevier: Spain, 2012; Volume 1, pp. 417–460.
33. Fredrickson, G.H. *The Equilibrium Theory of Inhomogeneous Polymers*, 2nd ed.; Clarendon Press: Oxford, UK, 2006.

34. González, M.A. Force fields and molecular dynamics simulations. *Écol. Thémat. Soc. Fr. Neutron.* **2011**, *12*, 169–200. [CrossRef]
35. Raabe, D. *Computational Materials Science*; Wiley-VCH Verlag: Darmstadt, Germany, 1998.
36. Müller-Plathe, F. Coarse-graining in polymer simulation: From the atomistic to the mesoscopic scale and back. *ChemPhysChem* **2002**, *3*, 754–769. [CrossRef]
37. Flory, P.J. *Principles of Polymer Chemistry*, 1st ed.; Cornell University Press: Ithaca, NY, USA, 1953.
38. Ganesan, V.; Jayaraman, A. Theory and simulation studies of effective interactions, phase behavior and morphology in polymer nanocomposites. *Soft Matter* **2014**, *10*, 13–38. [CrossRef] [PubMed]
39. Alkorta, I.; Elguero, J. Review on DFT and ab initio calculations of scalar coupling constants. *Int. J. Mol. Sci.* **2003**, *4*, 64–92. [CrossRef]
40. Kohn, W.; Sham, L.J. Self-consistent equations including exchange and correlation effects. *Phys. Rev.* **1965**, *140*, A1133–A1138. [CrossRef]
41. Steinbach, I. Phase-field models in materials science. *Model. Simul. Mater. Sci. Eng.* **2009**, *17*, 73001. [CrossRef]
42. Wang, X.; Ouyang, J.; Zhou, W.; Liu, Z. A phase field technique for modeling and predicting flow induced crystallization morphology of semi-crystalline polymers. *Polymers* **2016**, *8*, 230. [CrossRef]
43. Kim, J. Phase-field models for multi-component fluid flows. *Commun. Commut. Phys.* **2012**, *12*, 613–661. [CrossRef]
44. Schrödinger, E. Quantisierung als Eigenwertproblem. *Ann. Phys.* **1926**, *384*, 361–376. [CrossRef]
45. Born, M.; Oppenheimer, R. Zur quantentheorie der molekeln. *Ann. Phys.* **1927**, *389*, 457–484. [CrossRef]
46. Ponosov, Y.S.; Bolotin, G.A.; Thomsen, C.; Cardona, M. Raman scattering in Os: Nonadiabatic renormalization of the optical phonon self-energies. *Phys. Status Solidi B* **1998**, *208*, 257–269. [CrossRef]
47. White, J.D.; Chen, J.; Matsiev, D.; Auerbach, D.J.; Wodtke, A.M. Conversion of large-amplitude vibration to electron excitation at a metal surface. *Nature* **2005**, *433*, 503–505. [CrossRef] [PubMed]
48. Pisana, S.; Lazzeri, M.; Casiraghi, C.; Novoselov, K.S.; Geim, A.K.; Ferrari, A.C.; Mauri, F. Breakdown of the adiabatic Born-Oppenheimer approximation in graphene. *Nat. Mater.* **2007**, *6*, 198–201. [CrossRef] [PubMed]
49. Walker, B.G.; Molteni, C.; Marzari, N. Ab initio molecular dynamics of metal surfaces. *J. Phys.* **2004**, *16*, S2575–S2596. [CrossRef]
50. Rissanou, A.N.; Power, A.J.; Harmandaris, V. Structural and dynamical properties of polyethylene/graphene nanocomposites through molecular dynamics simulations. *Polymers* **2015**, *7*, 390–417. [CrossRef]
51. Car, R.; Parrinello, M. Unified approach for molecular dynamics and density-functional theory. *Phys. Rev. Lett.* **1985**, *55*, 2471–2474. [CrossRef] [PubMed]
52. Hageman, J.; Meier, R.J.; Heinemann, M.; de Groot, R.A. Young modulus of crystalline polyethylene from ab initio molecular dynamics. *Macromolecules* **1997**, *30*, 5953–5957. [CrossRef]
53. Serra, S.; Iarlori, S.; Tosatti, E.; Scandolo, S.; Santoro, G. Dynamical and thermal properties of polyethylene by ab initio simulation. *Chem. Phys. Lett.* **2000**, *331*, 339–345. [CrossRef]
54. Saitta, A.M.; Klein, M.L. First-principles molecular dynamics study of the rupture processes of a bulklike polyethylene knot. *J. Phys. Chem. B* **2001**, *105*, 6495–6499. [CrossRef]
55. Cavazzoni, C.; Colle, R.; Farchioni, R.; Grosso, G. Car-Parrinello molecular dynamics study of electronic and structural properties of neutral polyanilines. *Phys. Rev. B* **2002**, *66*, 165110. [CrossRef]
56. Wallace, D.S.; Stoneham, A.M.; Hayes, W.; Fisher, A.J.; Harker, A.H. Theory of defects in conducting polymers. I. Theoretical principles and simple applications. *J. Phys.* **1991**, *3*, 3879–3903. [CrossRef]
57. Wallace, D.S.; Stoneham, A.M.; Hayes, W.; Fisher, A.J.; Testa, A. Theory of defects in conducting polymers. II. Application to polyacetylene. *J. Phys.* **1991**, *3*, 3905–3920. [CrossRef]
58. Röthlisberger, U.; Sprik, M.; Klein, M.L. Living polymers: Ab initio molecular dynamics study of the initiation step in the polymerization of isoprene induced by ethyl lithium. *J. Chem. Soc. Faraday Trans.* **1998**, *94*, 501–508. [CrossRef]
59. Bernasconi, M.; Chiarotti, G.L.; Focher, P.; Parrinello, M.; Tosatti, E. Solid-state polymerization of acetylene under pressure: Ab Initio simulation. *Phys. Rev. Lett.* **1997**, *78*, 2008–2011. [CrossRef]
60. Quarti, C.; Milani, A.; Castiglioni, C. Ab initio calculation of the IR spectrum of PTFE: Helical symmetry and defects. *J. Phys. Chem. B* **2013**, *117*, 706–718. [CrossRef] [PubMed]
61. D'Amore, M.; Talarico, G.; Barone, V. Periodic and high-temperature disordered conformations of polytetrafluoroethylene chains: An ab initio modeling. *J. Am. Chem. Soc.* **2006**, *128*, 1099–1108.

62. Dai, L.; Yang, S.-W.; Chen, X.-T.; Wu, P.; Tan, V. Investigation of metal diffusion into polymers by ab initio molecular dynamics. *Appl. Phys. Lett.* **2005**, *87*. [CrossRef]
63. Piscitelli, F.; Posocco, P.; Toth, R.; Fermeglia, M.; Pricl, S.; Mensitieri, G.; Lavorgna, M. Sodium montmorillonite silylation: Unexpected effect of the aminosilane chain length. *J. Colloid Interface Sci.* **2010**, *351*, 108–115. [CrossRef] [PubMed]
64. Farquhar, I.E. *Ergodic Theory in Statistical Mechanics*; Interscience Publishers: New York, NY, USA, 1964.
65. Baumgärtner, A.; Burkitt, A.N.; Ceperley, D.M.; de Raedt, H.; Heermann, D.W.; Herrmann, H.J; Landau, D.P; Levesque, D.; von der Linden, W. *The Monte Carlo Method in Condensed Matter Physics*; Springer: Berlin, Germany, 2012.
66. Brin, M.; Stuck, G. *Introduction to Dynamical Systems*; Cambridge University Press: New York, NY, USA, 2002.
67. Metropolis, N.; Rosenbluth, A.W.; Rosenbluth, M.N.; Teller, A.H.; Teller, E. Equation of state calculations by fast computing machines. *J. Chem. Phys.* **1953**, *21*, 1087–1092. [CrossRef]
68. Potts, R.B. Some generalized order-disorder transformations. *Math. Proc. Camb. Philos. Soc.* **1952**, *48*, 106–109. [CrossRef]
69. Bortz, A.B.; Kalos, M.H.; Lebowitz, J.L. A new algorithm for Monte Carlo simulation of Ising spin systems. *J. Comput. Phys.* **1975**, *17*, 10–18. [CrossRef]
70. Gillespie, D.T. Exact stochastic simulation of coupled chemical reactions. *J. Phys. Chem.* **1977**, *81*, 2340–2361. [CrossRef]
71. Makki, H.; Adema, K.N.S.; Peters, E.A.J.F.; Laven, J.; Van Der Ven, L.G.J.; Van Benthem, R.A.T.M.; de With, G. A simulation approach to study photo-degradation processes of polymeric coatings. *Polym. Degrad. Stab.* **2014**, *105*, 68–79. [CrossRef]
72. Mermigkis, P.G.; Tsalikis, D.G.; Mavrantzas, V.G. Determination of the effective diffusivity of water in a poly (methyl methacrylate) membrane containing carbon nanotubes using kinetic Monte Carlo simulations. *J. Chem. Phys.* **2015**, *143*. [CrossRef] [PubMed]
73. Adema, K.N.S.; Makki, H.; Peters, E.A.J.F.; Laven, J.; Van Der Ven, L.G.J.; Van Benthem, R.A.T.M.; de With, G. Kinetic Monte Carlo simulation of the photodegradation process of polyester-urethane coatings. *Phys. Chem. Chem. Phys.* **2015**, *17*, 19962–19976. [CrossRef] [PubMed]
74. Kunz, L.; Kuhn, F.M.; Deutschmann, O. Kinetic Monte Carlo simulations of surface reactions on supported nanoparticles: A novel approach and computer code. *J. Chem. Phys.* **2015**, *143*. [CrossRef] [PubMed]
75. Zepeda-Ruiz, L.A.; Gilmer, G.H.; Walton, C.C.; Hamza, A.V.; Chason, E. Surface morphology evolution during sputter deposition of thin films—Lattice Monte Carlo simulations. *J. Cryst. Growth* **2010**, *312*, 1183–1187. [CrossRef]
76. Rysz, J. Monte Carlo simulations of phase separation in thin polymer blend films: Scaling properties of morphological measures. *Polymer* **2005**, *46*, 977–982. [CrossRef]
77. Galuschko, A.; Lang, M.; Kreer, T.; Sommer, J.-U. Monte carlo simulation of thin film polymer melts. *Soft Matter* **2014**, *12*, S49–S55. [CrossRef]
78. Ivanov, V.A.; Rodionova, A.S.; An, E.A.; Martemyanova, J.A.; Stukan, M.R.; Müller, M.; Paul, W.; Binder, K. Orientational ordering transitions of semiflexible polymers in thin films: A Monte Carlo simulation. *Phys. Rev. E* **2011**, *84*. [CrossRef] [PubMed]
79. Müller, M. Chain conformations and correlations in thin polymer films: A Monte Carlo study. *J. Chem. Phys.* **2002**, *116*, 9930–9938. [CrossRef]
80. Werner, A.; Schmid, F.; Müller, M.; Binder, K. Anomalous size-dependence of interfacial profiles between coexisting phases of polymer mixtures in thin-film geometry: A Monte Carlo simulation. *J. Chem. Phys.* **1997**, *107*, 8175–8188. [CrossRef]
81. Zykova-Timan, T.; Horbach, J.; Binder, K. Monte Carlo simulations of the solid-liquid transition in hard spheres and colloid-polymer mixtures. *J. Chem. Phys.* **2010**, *133*. [CrossRef] [PubMed]
82. Binder, K. Monte Carlo simulation of polymers at interfaces. *Phys. A Stat. Mech. Appl.* **1993**, *200*, 722–729. [CrossRef]
83. Bitsanis, I.A.; Brinke, G.T. A lattice Monte Carlo study of long chain conformations at solid-polymer melt interfaces. *J. Chem. Phys.* **1993**, *99*, 3100–3111. [CrossRef]
84. Jiang, J.; Liu, H.; Hu, Y. Lattice Monte Carlo simulation of polymer adsorption at an interface, 1: Monodisperse polymer. *Macromol. Theory Simul.* **1998**, *7*, 105–111. [CrossRef]

85. Jiang, J.; Liu, H.; Hu, Y. Lattice Monte Carlo simulation of polymer adsorption at an interface, 2: Polydisperse polymer. *Macromol. Theory Simul.* **1998**, *7*, 113–117.
86. John, A.; Nagel, J.; Heinrich, G. Monte Carlo simulation of polymer reactions at interfaces. *Macromol. Theory Simul.* **2007**, *16*, 430–440. [CrossRef]
87. Madden, W.G. Monte Carlo studies of the melt-vacuum interface of a lattice polymer. *J. Chem. Phys.* **1987**, *87*, 1405–1422. [CrossRef]
88. Müller, M. Reactions at polymer interfaces: A Monte Carlo simulation. *Macromolecules* **1997**, *30*, 6353–6357. [CrossRef]
89. Müller, M.; Binder, K.; Oed, W. Structural and thermodynamic properties of interfaces between coexisting phases in polymer blends: A Monte Carlo simulation. *J. Chem. Soc. Faraday Trans.* **1995**, *91*, 2369–2379. [CrossRef]
90. Müller, M.; MacDowell, L.G. Interface and surface properties of short polymers in solution: Monte Carlo simulations and self-consistent field theory. *Macromolecules* **2000**, *33*, 3902–3923. [CrossRef]
91. Müller, M.; Werner, A. Interfaces between highly incompatible polymers of different stiffness: Monte Carlo simulations and self-consistent field calculations. *J. Chem. Phys.* **1997**, *107*, 10764–10776. [CrossRef]
92. Reiter, J.; Zifferer, G.; Olaj, O.F. Monte Carlo studies of the interface between two polymer melts. *Macromolecules* **1990**, *23*, 224–228. [CrossRef]
93. Toral, R.; Chakrabarti, A. Monte Carlo study of polymer chains end-grafted onto a spherical interface. *Phys. Rev. E* **1993**, *47*, 4240–4246. [CrossRef]
94. Pandey, Y.N.; Doxastakis, M. Detailed atomistic Monte Carlo simulations of a polymer melt on a solid surface and around a nanoparticle. *J. Chem. Phys.* **2012**, *136*, 94901. [CrossRef] [PubMed]
95. Shu, R.; Zha, L.; Eman, A.A.; Hu, W. Fibril crystal growth in diblock copolymer solutions studied by dynamic monte carlo simulations. *J. Phys. Chem. B* **2015**, *119*, 5926–5932. [CrossRef] [PubMed]
96. Ren, Y.; Ma, A.; Li, J.; Jiang, X.; Ma, Y.; Toda, A.; Hu, W. Melting of polymer single crystals studied by dynamic Monte Carlo simulations. *Eur. Phys. J. E* **2010**, *33*, 189–202. [CrossRef] [PubMed]
97. Doye, J.; Frenkel, D. Kinetic Monte Carlo simulations of the growth of polymer crystals. *J. Chem. Phys.* **1999**, *110*, 2692–2702. [CrossRef]
98. Zhang, J.; Muthukumar, M. Monte Carlo simulations of single crystals from polymer solutions. *J. Chem. Phys.* **2007**, *126*. [CrossRef] [PubMed]
99. Aoki, K. Monte Carlo simulation of two-dimensional growth of conductive zones in interconversion of conducting polymer films involving random morphology. *J. Electroanal. Chem.* **1990**, *292*, 63–72. [CrossRef]
100. Balmer, J.A.; Mykhaylyk, O.O.; Schmid, A.; Armes, S.P.; Fairclough, J.P.A.; Ryan, A.J. Characterization of polymer-silica nanocomposite particles with core-shell morphologies using monte carlo simulations and small angle X-ray scattering. *Langmuir* **2011**, *27*, 8075–8089. [CrossRef] [PubMed]
101. Ruan, C.; Liu, C.; Zheng, G. Monte Carlo Simulation for the Morphology and Kinetics of Spherulites and Shish-Kebabs in Isothermal Polymer Crystallization. *Math. Probl. Eng.* **2015**, *2015*. [CrossRef]
102. Duda, Y.; Vázquez, F. Modeling of composite latex particle morphology by off-lattice Monte Carlo simulation. *Langmuir* **2005**, *21*, 1096–1102. [CrossRef] [PubMed]
103. He, X.; Liang, H.; Pan, C. Monte Carlo simulation of morphologies of self-assembled amphiphilic diblock copolymers in solution. *Phys. Rev. E* **2001**, *63*, 318041–318044. [CrossRef] [PubMed]
104. Nagpal, U.; Detcheverry, F.A.; Nealey, P.F.; De Pablo, J.J. Morphologies of linear triblock copolymers from Monte Carlo simulations. *Macromolecules* **2011**, *44*, 5490–5497. [CrossRef]
105. Raj Mohan, S.; Joshi, M.P.; Singh, M.P. Charge transport in disordered organic solids: A Monte Carlo simulation study on the effects of film morphology. *Org. Electron.* **2008**, *9*, 355–368. [CrossRef]
106. Narambuena, C.F.; Leiva, E.P.M.; Chávez-Páez, M.; Pérez, E. Effect of chain stiffness on the morphology of polyelectrolyte complexes. A Monte Carlo simulation study. *Polymer* **2010**, *51*, 3293–3302. [CrossRef]
107. Wang, X.; Chiang, M.; Snyder, C.R. Monte-Carlo simulation for the fracture process and energy release rate of unidirectional carbon fiber-reinforced polymers at different temperatures. *Compos. Part A* **2004**, *35*, 1277–1284. [CrossRef]
108. Li, J.; Ma, Y.; Hu, W. Dynamic Monte Carlo simulation of non-equilibrium Brownian diffusion of single-chain macromolecules. *Mol. Simul.* **2016**, *42*, 321–327. [CrossRef]

109. Neyertz, S.; Brown, D. A trajectory-extending kinetic Monte Carlo (TEKMC) method for estimating penetrant diffusion coefficients in molecular dynamics simulations of glassy polymers. *Macromolecules* **2010**, *43*, 9210–9214. [CrossRef]
110. Sikorski, A.; Adamczyk, P. Diffusion of polymer chains in porous media. A Monte Carlo study. *Polymer* **2010**, *51*, 581–586. [CrossRef]
111. Tüzel, E.; Kisacikoğlu, K.B.; Pekcan, Ö. Monitoring diffusion of reptating polymer chains by a direct energy transfer method: A Monte Carlo simulation. *Macromol. Theory Simul.* **2002**, *11*, 678–686. [CrossRef]
112. Mavrantzas, V.G.; Theodorou, D.N. Atomistic simulation of polymer melt elasticity. *Macromolecules* **1998**, *31*, 6310–6332. [CrossRef]
113. Baig, C.; Mavrantzas, V.G. Multiscale simulation of polymer melt viscoelasticity. *Phys. Rev. B* **2009**, *79*. [CrossRef]
114. Brindle, D.; Care, C.M. Phase diagram for the lattice model of amphiphile and solvent mixtures by Monte Carlo simulation. *J. Chem. Soc., Faraday Trans.* **1992**, *88*, 2163–2166. [CrossRef]
115. Ivanov, V.A.; Stukan, M.R.; Müller, M.; Paul, W.; Binder, K. Phase diagram of solutions of stiff-chain macromolecules: A Monte Carlo simulation. *J. Chem. Phys.* **2003**, *118*, 10333–10342. [CrossRef]
116. Guevara-Carrion, G.; Hasse, H.; Vrabec, J. Thermodynamic properties for applications in chemical industry via classical force fields. *Top. Curr. Chem.* **2012**, *307*, 201–250. [PubMed]
117. Verlet, L. Computer "experiments" on classical fluids. I. Thermodynamical properties of Lennard-Jones molecules. *Phys. Rev.* **1967**, *159*, 98–103. [CrossRef]
118. Verlet, L. Computer "experiments" on classical fluids. II. Equilibrium correlation functions. *Phys. Rev.* **1968**, *165*, 201–214. [CrossRef]
119. Kremer, K.; Grest, G.S. Dynamics of entangled linear polymer melts: A molecular-dynamics simulation. *J. Chem. Phys.* **1990**, *92*, 5057–5086. [CrossRef]
120. Aoyagi, T.; Doi, M. Molecular dynamics simulation of entangled polymers in shear flow. *Comput. Theor. Polym. Sci.* **2000**, *10*, 317–321. [CrossRef]
121. Durand, M.; Meyer, H.; Benzerara, O.; Baschnagel, J.; Vitrac, O. Molecular dynamics simulations of the chain dynamics in monodisperse oligomer melts and of the oligomer tracer diffusion in an entangled polymer matrix. *J. Chem. Phys.* **2010**, *132*. [CrossRef] [PubMed]
122. Harmandaris, V.A.; Mavrantzas, V.G.; Theodorou, D.N.; Kröger, M.; Ramírez, J.; Ottinger, H.C.; Vlassopoulos, D. Crossover from the rouse to the entangled polymer melt regime: Signals from long, detailed atomistic molecular dynamics simulations, supported by rheological experiments. *Macromolecules* **2003**, *36*, 1376–1387. [CrossRef]
123. Likhtman, A.E.; Sukumaran, S.K.; Ramirez, J. Linear viscoelasticity from molecular dynamics simulation of entangled polymers. *Macromolecules* **2007**, *40*, 6748–6757. [CrossRef]
124. Wang, Z.; Larson, R.G. Constraint release in entangled binary blends of linear polymers: A molecular dynamics study. *Macromolecules* **2008**, *41*, 4945–4960. [CrossRef]
125. Harmandaris, V.A.; Daoulas, K.; Mavrantzas, V.G. Molecular dynamics simulation of a polymer melt/solid interface: Local dynamics and chain mobility in a thin film of polyethylene melt adsorbed on graphite. *Macromolecules* **2005**, *38*, 5796–5809. [CrossRef]
126. Milano, G.; Santangelo, G.; Ragone, F.; Cavallo, L.; Di Matteo, A. Gold nanoparticle/polymer interfaces: All atom structures from molecular dynamics simulations. *J. Phys. Chem. C* **2011**, *115*, 15154–15163. [CrossRef]
127. Luo, T.; Lloyd, J.R. Enhancement of thermal energy transport across graphene/graphite and polymer interfaces: A molecular dynamics study. *Adv. Funct. Mater.* **2012**, *22*, 2495–2502. [CrossRef]
128. Neyertz, S.; Brown, D. Molecular dynamics study of carbon dioxide sorption and plasticization at the interface of a glassy polymer membrane. *Macromolecules* **2013**, *46*, 2433–2449. [CrossRef]
129. Lamas, E.J.; Balbuena, P.B. Molecular dynamics studies of a model polymer-catalyst-carbon interface. *Electrochim. Acta* **2006**, *51*, 5904–5911. [CrossRef]
130. Song, Y.; Feng, W.; Liu, K.; Yang, P.; Zhang, W.; Zhang, X. Exploring the folding pattern of a polymer chain in a single crystal by combining single-molecule force spectroscopy and steered molecular dynamics simulations. *Langmuir* **2013**, *29*, 3853–3857. [CrossRef] [PubMed]
131. Yamamoto, T. Molecular dynamics simulations of steady-state crystal growth and homogeneous nucleation in polyethylene-like polymer. *J. Chem. Phys.* **2008**, *129*. [CrossRef] [PubMed]

132. Yamamoto, T. Molecular dynamics of reversible and irreversible melting in chain-folded crystals of short polyethylene-like polymer. *Macromolecules* **2010**, *43*, 9384–9393. [CrossRef]
133. Hegde, G.A.; Chang, J.-F.; Chen, Y.-L.; Khare, R. Conformation and diffusion behavior of ring polymers in solution: A comparison between molecular dynamics, multiparticle collision dynamics, and lattice Boltzmann simulations. *J. Chem. Phys.* **2011**, *135*. [CrossRef] [PubMed]
134. Bahlakeh, G.; Nikazar, M.; Hafezi, M.-J.; Dashtimoghadam, E.; Hasani-Sadrabadi, M.M. Molecular dynamics simulation study of proton diffusion in polymer electrolyte membranes based on sulfonated poly (ether ether ketone). *Int. J. Hydrog. Energy* **2012**, *37*, 10256–10264. [CrossRef]
135. Liu, J.; Cao, D.; Zhang, L. Molecular dynamics study on nanoparticle diffusion in polymer melts: A test of the stokes-einstein law. *J. Phys. Chem. C* **2008**, *112*, 6653–6661. [CrossRef]
136. Zhao, X.-T.; Yang, H.; Sheng, Y.-Z.; Li, J.-Y.; Sun, M. Molecular dynamics simulation on the effect of the distance between SWCNTs for short polymers diffusion among single wall carbon nanotubes. *Comput. Mater. Sci.* **2014**, *95*, 446–450. [CrossRef]
137. Jang, S.S.; Molinero, V.; Çağin, T.; Goddard, W.A., III. Nanophase-Segregation and Transport in Nafion 117 from Molecular Dynamics Simulations: Effect of Monomeric Sequence. *J. Phys. Chem. B* **2004**, *108*, 3149–3157. [CrossRef]
138. Błoński, S.; Brostow, W. Molecular dynamics simulations of chain relaxation and crack propagation in polymer liquid crystals. *J. Chem. Phys.* **1991**, *95*, 2890–2896.
139. Brostow, W.; Cunha, A.M.; Quintanilla, J.; Simões, R. Crack formation and propagation in molecular dynamics simulations of polymer liquid crystals. *Macromol. Theory Simul.* **2002**, *11*, 308–314. [CrossRef]
140. Brostow, W.; Hinze, J.A.; Simões, R. Tribological behavior of polymers simulated by molecular dynamics. *J. Mater. Res.* **2004**, *19*, 851–856. [CrossRef]
141. Shagolsem, L.S.; Sommer, J.-U. Order and phase behavior of thin film of diblock copolymer-selective nanoparticle mixtures: A molecular dynamics simulation study. *Macromolecules* **2014**, *47*, 830–839. [CrossRef]
142. Hartmann, L.; Gorbatschow, W.; Hauwede, J.; Kremer, F. Molecular dynamics in thin films of isotactic poly(methyl methacrylate). *Eur. Phys. J. E* **2002**, *8*, 145–154. [CrossRef] [PubMed]
143. Chen, J.; Li, L.; Zhou, D.; Xu, J.; Xue, G. Effect of molecular chain architecture on dynamics of polymer thin films measured by the ac-chip calorimeter. *Macromolecules* **2014**, *47*, 3497–3501. [CrossRef]
144. Gooneie, A.; Gonzalez-Gutierrez, J.; Holzer, C. Atomistic Modelling of Confined Polypropylene Chains between Ferric Oxide Substrates at Melt Temperature. *Polymers* **2016**, *8*, 361. [CrossRef]
145. Egorov, E.A.; Zhizhenkov, V.V. Molecular dynamics and strengthening of liquid-crystal polymers. *Phys. Solid State* **2005**, *47*, 942–948. [CrossRef]
146. Stimson, L.M.; Wilson, M.R. Molecular dynamics simulations of side chain liquid crystal polymer molecules in isotropic and liquid-crystalline melts. *J. Chem. Phys.* **2005**, *123*. [CrossRef] [PubMed]
147. Daivis, P.J.; Matin, M.L.; Todd, B.D. Nonlinear shear and elongational rheology of model polymer melts by non-equilibrium molecular dynamics. *J. Non-Newton. Fluid Mech.* **2003**, *111*, 1–18. [CrossRef]
148. Hajizadeh, E.; Todd, B.D.; Daivis, P.J. A molecular dynamics investigation of the planar elongational rheology of chemically identical dendrimer-linear polymer blends. *J. Chem. Phys.* **2015**, *142*. [CrossRef] [PubMed]
149. Kairn, T.; Daivis, P.J.; Ivanov, I.; Bhattacharya, S.N. Molecular-dynamics simulation of model polymer nanocomposite rheology and comparison with experiment. *J. Chem. Phys.* **2005**, *123*. [CrossRef] [PubMed]
150. Jeng, Y.-R.; Chen, C.-C.; Shyu, S.-H. A molecular dynamics study of lubrication rheology of polymer fluids. *Tribol. Lett.* **2003**, *15*, 293–300. [CrossRef]
151. Todd, B.D.; Daivis, P.J. Nonequilibrium molecular dynamics simulations of planar elongational flow with spatially and temporally periodic boundary conditions. *Phys. Rev. Lett.* **1998**, *81*, 1118–1121. [CrossRef]
152. Baig, C.; Edwards, B.J.; Keffer, D.J.; Cochran, H.D.; Harmandaris, V.A. Rheological and structural studies of linear polyethylene melts under planar elongational flow using nonequilibrium molecular dynamics simulations. *J. Chem. Phys.* **2006**, *124*, 84902. [CrossRef] [PubMed]
153. Chenoweth, K.; Cheung, S.; van Duin, A.; Goddard, W.A., III; Kober, E.M. Simulations on the thermal decomposition of a poly(dimethylsiloxane) polymer using the ReaxFF reactive force field. *J. Am. Chem. Soc.* **2005**, *127*, 7192–7202. [CrossRef] [PubMed]
154. Chenoweth, K.; van Duin, A.; Goddard, W.A., III. ReaxFF reactive force field for molecular dynamics simulations of hydrocarbon oxidation. *J. Phys. Chem. A* **2008**, *112*, 1040–1053. [CrossRef] [PubMed]

155. Van Duin, A.; Dasgupta, S.; Lorant, F.; Goddard, W.A., III. ReaxFF: A reactive force field for hydrocarbons. *J. Phys. Chem. A* **2001**, *105*, 9396–9409. [CrossRef]
156. Odegard, G.M.; Jensen, B.D.; Gowtham, S.; Wu, J.; He, J.; Zhang, Z. Predicting mechanical response of crosslinked epoxy using ReaxFF. *Chem. Phys. Lett.* **2014**, *591*, 175–178. [CrossRef]
157. Tieleman, D.P.; Marrink, S.J.; Berendsen, H. A computer perspective of membranes: Molecular dynamics studies of lipid bilayer systems. *Biochim. Biophys. Acta Rev. Biomembr.* **1997**, *1331*, 235–270. [CrossRef]
158. Heller, H.; Schaefer, M.; Schulten, K. Molecular dynamics simulation of a bilayer of 200 lipids in the gel and in the liquid-crystal phases. *J. Phys. Chem.* **1993**, *97*, 8343–8360. [CrossRef]
159. Lipowsky, R.; Grotehans, S. Hydration vs. Protrusion Forces Between Lipid Bilayers. *Europhys. Lett.* **1993**, *23*, 599. [CrossRef]
160. Lindahl, E.; Edholm, O. Mesoscopic undulations and thickness fluctuations in lipid bilayers from molecular dynamics simulations. *Biophys. J.* **2000**, *79*, 426–433. [CrossRef]
161. Gao, L.; Shillcock, J.; Lipowsky, R. Improved dissipative particle dynamics simulations of lipid bilayers. *J. Chem. Phys.* **2007**, *126*. [CrossRef] [PubMed]
162. Malevanets, A.; Kapral, R. Mesoscopic model for solvent dynamics. *J. Chem. Phys.* **1999**, *110*, 8605. [CrossRef]
163. Alekseeva, U.; Winkler, R.G.; Sutmann, G. Hydrodynamics in adaptive resolution particle simulations: Multiparticle collision dynamics. *J. Comput. Phys.* **2016**, *314*, 14–34. [CrossRef]
164. Satoh, A. *Introduction to Molecular-Microsimulation for Colloidal Dispersions*, 1st ed.; Elsevier: Amsterdam, The Netherlands, 2003.
165. Satoh, A. *Introduction to Practice of Molecular Simulation*; Elsevier Inc.: Burlington, MA, USA, 2011.
166. Pagonabarraga, I. Lattice boltzmann modeling of complex fluids: Colloidal suspensions and fluid mixtures. In *Novel Methods in Soft Matter Simulations*; Karttunen, M., Vattulainen, I., Lukkarinen, A., Eds.; Springer: Berlin, Germany, 2004; pp. 279–309.
167. Sukop, M.; Throne, D.T. *Lattice Boltzmann Modeling: An Introduction for Geoscientists and Engineers*, 1st ed.; Springer: New York, NY, USA, 2006.
168. Ermak, D.L.; McCammon, J.A. Brownian dynamics with hydrodynamic interactions. *J. Chem. Phys.* **1978**, *69*, 1352–1360. [CrossRef]
169. Ando, T.; Chow, E.; Saad, Y.; Skolnick, J. Krylov subspace methods for computing hydrodynamic interactions in Brownian dynamics simulations. *J. Chem. Phys.* **2012**, *137*. [CrossRef] [PubMed]
170. Cerbelaud, M.; Lestriez, B.; Guyomard, D.; Videcoq, A.; Ferrando, R. Brownian dynamics simulations of colloidal suspensions containing polymers as precursors of composite electrodes for lithium batteries. *Langmuir* **2012**, *28*, 10713–10724. [CrossRef] [PubMed]
171. Patti, A.; Cuetos, A. Brownian dynamics and dynamic Monte Carlo simulations of isotropic and liquid crystal phases of anisotropic colloidal particles: A comparative study. *Phys. Rev. E* **2012**, *86*. [CrossRef] [PubMed]
172. Gu, L.; Xu, S.; Sun, Z.; Wang, J.T. Brownian dynamics simulation of the crystallization dynamics of charged colloidal particles. *J. Colloid Interface Sci.* **2010**, *350*, 409–416. [CrossRef] [PubMed]
173. Santos, P.; Campanella, O.H.; Carignano, M.A. Brownian dynamics study of gel-forming colloidal particles. *J. Phys. Chem. B* **2010**, *114*, 13052–13058. [CrossRef] [PubMed]
174. Saveyn, H.; de Baets, B.; Thas, O.; Hole, P.; Smith, J.; van der Meeren, P. Accurate particle size distribution determination by nanoparticle tracking analysis based on 2-D Brownian dynamics simulation. *J. Colloid Interface Sci.* **2010**, *352*, 593–600. [CrossRef] [PubMed]
175. Li, Y.; Zhu, Y.-L.; Li, Y.-C.; Qian, H.-J.; Sun, C.-C. Self-assembly of two-patch particles in solution: A Brownian dynamics simulation study. *Mol. Simul.* **2014**, *40*, 449–457. [CrossRef]
176. Mendes, M.J.; Schmidt, H.K.; Pasquali, M. Brownian dynamics simulations of single-wall carbon nanotube separation by type using dielectrophoresis. *J. Phys. Chem. B* **2008**, *112*, 7467–7477. [CrossRef] [PubMed]
177. Van Den Noort, A.; Briels, W.J. Brownian dynamics simulations of concentration coupled shear banding. *J. Non-Newton. Fluid Mech.* **2008**, *152*, 148–155. [CrossRef]
178. Jain, A.; Sunthar, P.; Dünweg, B.; Prakash, J.R. Optimization of a Brownian-dynamics algorithm for semidilute polymer solutions. *Phys. Rev. E* **2012**, *85*. [CrossRef] [PubMed]
179. Li, B.; Zhu, Y.-L.; Liu, H.; Lu, Z.-Y. Brownian dynamics simulation study on the self-assembly of incompatible star-like block copolymers in dilute solution. *Phys. Chem. Chem. Phys.* **2012**, *14*, 4964–4970. [CrossRef] [PubMed]

180. Zhang, Y.; de Pablo, J.J.; Graham, M.D. An immersed boundary method for Brownian dynamics simulation of polymers in complex geometries: Application to DNA flowing through a nanoslit with embedded nanopits. *J. Chem. Phys.* **2012**, *136*. [CrossRef] [PubMed]
181. Pham, T.T.; Bajaj, M.; Prakash, J.R. Brownian dynamics simulation of polymer collapse in a poor solvent: Influence of implicit hydrodynamic interactions. *Soft Matter* **2008**, *4*, 1196–1207. [CrossRef]
182. Delong, S.; Usabiaga, F.B.; Delgado-Buscalioni, R.; Griffith, B.E.; Donev, A. Brownian dynamics without Green's functions. *J. Chem. Phys.* **2014**, *140*. [CrossRef] [PubMed]
183. Iliafar, S.; Vezenov, D.; Jagota, A. Brownian dynamics simulation of peeling a strongly-Adsorbed polymer molecule from a frictionless substrate. *Langmuir* **2013**, *29*, 1435–1445. [CrossRef] [PubMed]
184. Lee, P.-H.; Helms, V.; Geyer, T. Coarse-grained Brownian dynamics simulations of protein translocation through nanopores. *J. Chem. Phys.* **2012**, *137*. [CrossRef] [PubMed]
185. Adhikari, R.; Bhattacharya, A. Driven translocation of a semi-flexible chain through a nanopore: A Brownian dynamics simulation study in two dimensions. *J. Chem. Phys.* **2013**, *138*. [CrossRef] [PubMed]
186. Hoogerbrugge, P.J.; Koelman, J.M.V.A. Simulating Microscopic Hydrodynamic Phenomena with Dissipative Particle Dynamics. *Europhys. Lett.* **1992**, *19*, 155. [CrossRef]
187. Groot, R.D.; Warren, P.B. Dissipative particle dynamics: Bridging the gap between atomistic and mesoscopic simulation. *J. Chem. Phys.* **1997**, *107*, 4423–4435. [CrossRef]
188. Gooneie, A.; Mattausch, H.; Witschnigg, A.; Schuschnigg, S.; Holzer, C. Multiscale simulation of polymer nanocomposites in processing: Challenges and outlooks. *Key Eng. Mater.* **2015**, *651*, 533–538. [CrossRef]
189. Español, P.; Warren, P. Statistical mechanics of dissipative particle dynamics. *Europhys. Lett.* **1995**, *30*, 191. [CrossRef]
190. Groot, R.D. Applications of Dissipative Particle Dynamics. In *Novel Methods in Soft Matter Simulations*; Karttunen, M., Vattulainen, I., Lukkarinen, A., Eds.; Springer: Berlin, Germany, 2004; pp. 5–38.
191. Groot, R.D.; Madden, T.J. Dynamic simulation of diblock copolymer microphase separation. *J. Chem. Phys.* **1998**, *108*, 8713–8724. [CrossRef]
192. Den Otter, W.K.; Clarke, J. The temperature in dissipative particle dynamics. *Int. J. Mod. Phys. C* **2000**, *11*, 1179–1193. [CrossRef]
193. Pan, W.; Caswell, B.; Karniadakis, G.E. Rheology, microstructure and migration in brownian colloidal suspensions. *Langmuir* **2010**, *26*, 133–142. [CrossRef] [PubMed]
194. Yamanoi, M.; Pozo, O.; Maia, J.M. Linear and non-linear dynamics of entangled linear polymer melts by modified tunable coarse-grained level Dissipative Particle Dynamics. *J. Chem. Phys.* **2011**, *135*, 44904. [CrossRef] [PubMed]
195. Gooneie, A.; Schuschnigg, S.; Holzer, C. Orientation of anisometric layered silicate particles in uncompatibilized and compatibilized polymer melts under shear flow: A dissipative particle dynamics study. *Macromol. Theory Simul.* **2016**, *25*, 85–98. [CrossRef]
196. Gooneie, A.; Schuschnigg, S.; Holzer, C. Dissipative particle dynamics models of orientation of weakly-interacting anisometric silicate particles in polymer melts under shear flow: Comparison with the standard orientation models. *Macromol. Theory Simul.* **2016**, *25*, 287–302. [CrossRef]
197. Fedosov, D.A.; Noguchi, H.; Gompper, G. Multiscale modeling of blood flow: From single cells to blood rheology. *Biomech. Model. Mechanobiol.* **2014**, *13*, 239–258. [CrossRef] [PubMed]
198. Zhang, P.; Zhang, N.; Deng, Y.; Bluestein, D. A multiple time stepping algorithm for efficient multiscale modeling of platelets flowing in blood plasma. *J. Comput. Phys.* **2015**, *284*, 668–686. [CrossRef] [PubMed]
199. Gooneie, A.; Schuschnigg, S.; Holzer, C. Dissipative particle dynamics simulations of orientation of layered silicate particles embedded in polymer melts under shear flows. *AIP Conf. Proc.* **2016**, *1779*, 50010.
200. Gai, J.-G.; Hu, G.-H.; Li, H.-L.; Zhu, S.-P.; Hoppe, S. Dissipative particle dynamics and flory-huggins theories for predicting the rheological behavior of ultrahigh molecular weight polyethylene blends. *Ind. Eng. Chem. Res.* **2010**, *49*, 11369–11379. [CrossRef]
201. Goicochea, A.G. Adsorption and disjoining pressure isotherms of confined polymers using dissipative particle dynamics. *Langmuir* **2007**, *23*, 11656–11663. [CrossRef] [PubMed]
202. Kacar, G.; Peters, E.; de With, G. Mesoscopic simulations for the molecular and network structure of a thermoset polymer. *Soft Matter* **2013**, *9*, 5785–5793. [CrossRef]
203. Kacar, G.; Peters, E.; de With, G. Structure of a thermoset polymer near an alumina substrate as studied by dissipative particle dynamics. *J. Phys. Chem. C* **2013**, *117*, 19038–19047. [CrossRef]

204. Kauzlari, D.; Meier, J.T.; Español, P.; Succi, S.; Greiner, A.; Korvink, J.G. Bottom-up coarse-graining of a simple graphene model: The blob picture. *J. Chem. Phys.* **2011**, *134*. [CrossRef] [PubMed]
205. Lee, M.-T.; Mao, R.; Vishnyakov, A.; Neimark, A.V. Parametrization of chain molecules in dissipative particle dynamics. *J. Phys. Chem. B* **2016**. [CrossRef] [PubMed]
206. Maly, M.; Posocco, P.; Pricl, S.; Fermeglia, M. Self-assembly of nanoparticle mixtures in diblock copolymers: Multiscale molecular modeling. *Ind. Eng. Chem. Res.* **2008**, *47*, 5023–5038. [CrossRef]
207. Posocco, P.; Posel, Z.; Fermeglia, M.; Lísal, M.; Pricl, S. A molecular simulation approach to the prediction of the morphology of self-assembled nanoparticles in diblock copolymers. *J. Mater. Chem.* **2010**, *20*, 10511–10520. [CrossRef]
208. Esteves, A.C.C.; Lyakhova, K.; Van Der Ven, L.G.J.; Van Benthem, R.A.T.M.; de With, G. Surface segregation of low surface energy polymeric dangling chains in a cross-linked polymer network investigated by a combined experimental-simulation Approach. *Macromolecules* **2013**, *46*, 1993–2002. [CrossRef]
209. Esteves, A.C.C.; Lyakhova, K.; van Riel, J.M.; Van Der Ven, L.G.J.; Van Benthem, R.A.T.M.; de With, G. Self-replenishing ability of cross-linked low surface energy polymer films investigated by a complementary experimental-simulation approach. *J. Chem. Phys.* **2014**, *140*, 124902. [CrossRef] [PubMed]
210. Lyakhova, K.; Esteves, A.C.C.; van de Put, M.W.P.; van der Ven, L.G.J.; van Benthem, R.A.T.M.; de With, G. Simulation-Experimental Approach to Investigate the Role of Interfaces in Self-Replenishing Composite Coatings. *Adv. Mater. Interfaces* **2014**, *1*, 1400053. [CrossRef]
211. Rahatekar, S.S.; Hamm, M.; Shaffer, M.; Elliott, J.A. Mesoscale modeling of electrical percolation in fiber-filled systems. *J. Chem. Phys.* **2005**, *123*. [CrossRef] [PubMed]
212. Frisch, U.; Hasslacher, B.; Pomeau, Y. Lattice-gas automata for the Navier-Stokes equation. *Phys. Rev. Lett.* **1986**, *56*, 1505–1508. [CrossRef] [PubMed]
213. Benzi, R.; Succi, S.; Vergassola, M. The lattice Boltzmann equation: Theory and applications. *Phys. Rep.* **1992**, *222*, 145–197. [CrossRef]
214. Higuera, F.J.; Jiménez, J. Boltzmann approach to lattice gas simulations. *Europhys. Lett.* **1989**, *9*, 663–668. [CrossRef]
215. Higuera, F.J.; Succi, S.; Benzi, R. Lattice gas dynamics with enhanced collisions. *Europhys. Lett.* **1989**, *9*, 345–349. [CrossRef]
216. Bhatnagar, P.L.; Gross, E.P.; Krook, M. A model for collision processes in gases. I. Small amplitude processes in charged and neutral one-component systems. *Phys. Rev.* **1954**, *94*, 511–525. [CrossRef]
217. Qian, Y.H.; D'Humières, D.; Lallemand, P. Lattice bgk models for navier-stokes equation. *Europhys. Lett.* **1992**, *17*, 479–484. [CrossRef]
218. Dünweg, B.; Ladd, A. Lattice Boltzmann Simulations of Soft Matter Systems. *arXiv*, **2009**, arXiv:0803.2826.
219. Usta, O.B.; Ladd, A.; Butler, J.E. Lattice-Boltzmann simulations of the dynamics of polymer solutions in periodic and confined geometries. *J. Chem. Phys.* **2005**, *122*. [CrossRef]
220. Ahlrichs, P.; Dünweg, B. Lattice-boltzmann simulation of polymer-solvent systems. *Int. J. Mod. Phys. C* **1998**, *9*, 1429–1438. [CrossRef]
221. Aidun, C.K.; Clausen, J.R. Lattice-boltzmann method for complex flows. *Annu. Rev. Fluid Mech.* **2010**, *42*, 439–472. [CrossRef]
222. Spaid, M.; Phelan, F.R., Jr. Lattice Boltzmann methods for modeling microscale flow in fibrous porous media. *Phys. Fluids* **1997**, *9*, 2468–2474. [CrossRef]
223. Sinha, P.K.; Mukherjee, P.P.; Wang, C.-Y. Impact of GDL structure and wettability on water management in polymer electrolyte fuel cells. *J. Mater. Chem.* **2007**, *17*, 3089–3103. [CrossRef]
224. Care, C.M.; Cleaver, D.J. Computer simulation of liquid crystals. *Rep. Prog. Phys.* **2005**, *68*, 2665–2700. [CrossRef]
225. Denniston, C.; Orlandini, E.; Yeomans, J.M. Lattice Boltzmann simulations of liquid crystal hydrodynamics. *Phys. Rev. E* **2001**, *63*, 056702. [CrossRef] [PubMed]
226. Marenduzzo, D.; Orlandini, E.; Cates, M.E.; Yeomans, J.M. Steady-state hydrodynamic instabilities of active liquid crystals: Hybrid lattice Boltzmann simulations. *Phys. Rev. E Stat., Nonlinear Soft Matter Phys.* **2007**, *76*. [CrossRef] [PubMed]
227. Usta, O.B.; Perchak, D.; Clarke, A.; Yeomans, J.M.; Balazs, A.C. Shear and extensional deformation of droplets containing polymers and nanoparticles. *J. Chem. Phys.* **2009**, *130*. [CrossRef] [PubMed]

228. Nabovati, A.; Llewellin, E.W.; Sousa, A. A general model for the permeability of fibrous porous media based on fluid flow simulations using the lattice Boltzmann method. *Compos. Part A* **2009**, *40*, 860–869. [CrossRef]
229. Wang, M.; He, J.; Yu, J.; Pan, N. Lattice Boltzmann modeling of the effective thermal conductivity for fibrous materials. *Int. J. Therm. Sci.* **2007**, *46*, 848–855. [CrossRef]
230. Bird, R.B.; Armstrong, R.C.; Hassager, O. *Dynamics of Polymeric Liquids*; John Wiley & Sons Inc.: Hoboken, NJ, USA, 1987.
231. Rappaz, M.; Bellet, M.; Deville, M. *Numerical Modeling in Materials Science and Engineering*; Springer: Leutershausen, Germany, 2003.
232. Ellero, M.; Español, P.; Flekkøy, E.G. Thermodynamically consistent fluid particle model for viscoelastic flows. *Phys. Rev. E* **2003**, *68*, 041504. [CrossRef] [PubMed]
233. Vázquez-Quesada, A.; Ellero, M.; Español, P. Smoothed particle hydrodynamic model for viscoelastic fluids with thermal fluctuations. *Phys. Rev. E* **2009**, *79*. [CrossRef] [PubMed]
234. Bian, X.; Litvinov, S.; Qian, R.; Ellero, M.; Adams, N.A. Multiscale modeling of particle in suspension with smoothed dissipative particle dynamics. *Phys. Fluids* **2012**, *24*. [CrossRef]
235. Vázquez-Quesada, A.; Ellero, M.; Español, P. Consistent scaling of thermal fluctuations in smoothed dissipative particle dynamics. *J. Chem. Phys.* **2009**, *130*. [CrossRef] [PubMed]
236. Petsev, N.D.; Leal, L.G.; Shell, M.S. Multiscale simulation of ideal mixtures using smoothed dissipative particle dynamics. *J. Chem. Phys.* **2016**, *144*. [CrossRef] [PubMed]
237. Pirondi, A.; Giuliese, G.; Moroni, F. Fatigue debonding three-dimensional simulation with cohesive zone. *J. Adhes.* **2016**, *92*, 553–571. [CrossRef]
238. Schiel, M.; Reh, S.; Schwienhorst, M.; Welters, T.; Stammen, E.; Dilger, K. Finite element modelling of cure-dependent mechanical properties by model-free kinetic analysis using a cohesive zone approach. *J. Adhes.* **2016**, *92*, 572–585. [CrossRef]
239. Heydari-Meybodi, M.; Saber-Samandari, S.; Sadighi, M. 3D multiscale modeling to predict the elastic modulus of polymer/nanoclay composites considering realistic interphase property. *Compos. Interfaces* **2016**, *23*, 641–661. [CrossRef]
240. Sun, M.-K.; Shieh, J.; Chen, C.-S.; Chiang, H.; Huang, C.-W.; Chen, W.-S. Effects of an implant on temperature distribution in tissue during ultrasound diathermy. *Ultrason. Sonochem.* **2016**, *32*, 44–53. [CrossRef] [PubMed]
241. Gooneie, A.; Schuschnigg, S.; Duretek, I.; Holzer, C. Numerical simulations of the flow of wood polypropylene composites with wall slipping in a profile die: The significance of material data. *Arch. Iran. Med.* **2015**, *1664*, 50014.
242. Duretek, I.; Schuschnigg, S.; Gooneie, A.; Langecker, G.R.; Holzer, C.; Gomze, L.A. Rheological properties of wood polymer composites and their role in extrusion. *J. Phys. Conf. Ser.* **2015**, *602*, 12014. [CrossRef]
243. Chen, K.; Zhang, D.; Yang, X.; Cui, X.; Zhang, X.; Wang, Q. Research on torsional friction behavior and fluid load support of PVA/HA composite hydrogel. *J. Mech. Behav. Biomed. Mater.* **2016**, *62*, 182–194. [CrossRef] [PubMed]
244. Ehrenhofer, A.; Bingel, G.; Paschew, G.; Tietze, M.; Schröder, R.; Richter, A.; Wallmersperger, T. Permeation control in hydrogel-layered patterned PET membranes with defined switchable pore geometry—Experiments and numerical simulation. *Sens. Actuators B* **2016**, *232*, 499–505. [CrossRef]
245. Baaijens, F. Mixed finite element methods for viscoelastic flow analysis: A review. *J. Non-Newton. Fluid Mech.* **1998**, *79*, 361–385. [CrossRef]
246. Verbeeten, W.; Peters, G.; Baaijens, F. Differential constitutive equations for polymer melts: The extended Pom-Pom model. *J. Rheol.* **2001**, *45*, 823–843. [CrossRef]
247. Yue, P.; Zhou, C.; Feng, J.J.; Ollivier-Gooch, C.F.; Hu, H.H. Phase-field simulations of interfacial dynamics in viscoelastic fluids using finite elements with adaptive meshing. *J. Comput. Phys.* **2006**, *219*, 47–67. [CrossRef]
248. Wilkes, E.D.; Phillips, S.D.; Basaran, O.A. Computational and experimental analysis of dynamics of drop formation. *Phys. Fluids* **1999**, *11*, 3577–3598. [CrossRef]
249. Patera, A.T. A spectral element method for fluid dynamics. *J. Comput. Phys.* **1984**, *54*, 468–488. [CrossRef]
250. Pozrikidis, C. *Introduction to Finite and Spectral Element Methods Using MATLAB*, 2nd ed.; CRC Press: Boca Raton, FL, USA, 2014.
251. Van Os, R.; Phillips, T.N. The prediction of complex flows of polymer melts using spectral elements. *J. Non-Newton. Fluid Mech.* **2004**, *122*, 287–301. [CrossRef]

252. Fiétier, N.; Deville, M.O. Time-dependent algorithms for the simulation of viscoelastic flows with spectral element methods. *J. Comput. Phys.* **2003**, *186*, 93–121. [CrossRef]
253. Li, R.; Chen, Z.; Wu, W. *Generalized Difference Methods for Differential Equations: Numerical Analysis of Finite Volume Methods*; Marcel Dekker: New York, NY, USA, 2000.
254. Hughes, T.; Brooks, A. Multi-dimensional upwind scheme with no crosswind diffusion. *Am. Soc. Mech. Eng.* **1979**, *34*, 19–35.
255. Hughes, T.; Mallet, M.; Akira, M. A new finite element formulation for computational fluid dynamics: II. Beyond SUPG. *Comput. Methods Appl. Mech. Eng.* **1986**, *54*, 341–355. [CrossRef]
256. Jiang, B.; Liao, G. The Least-Squares Meshfree Finite Element Method. In Proceedings of the Computational Mechanics: International Symposium on Computational Mechanic, Beijing, China, 30 July–1 August 2009; p. 341.
257. Kumar, R.; Dennis, B.H. A Least-Squares Galerkin Split Finite Element Method for Compressible Navier-Stokes Equations. In Proceedings of the 29th Computers and Information in Engineering Conference, San Diego, CA, USA, 30 August 30–2 September 2009.
258. Baliga, B.R.; Patankar, S.V. A control volume finite-element method for two-dimensional fluid flow and heat transfer. *Numer. Heat Transf.* **1983**, *6*, 245–261. [CrossRef]
259. Patankar, S.V. A calculation procedure for two-dimensional elliptic situations. *Numer. Heat Transf.* **1981**, *4*, 409–425. [CrossRef]
260. Prakash, C.; Patankar, S.V. A control volume-based finite-element method for solving the navier-stokes equations using equal-order velocity-pressure interpolation. *Numer. Heat Transf.* **1985**, *8*, 259–280. [CrossRef]
261. Balsara, D.S. Divergence-free reconstruction of magnetic fields and WENO schemes for magnetohydrodynamics. *J. Comput. Phys.* **2009**, *228*, 5040–5056. [CrossRef]
262. Powell, K.G.; Roe, P.L.; Linde, T.J.; Gombosi, T.I.; de Zeeuw, D.L. A Solution-Adaptive Upwind Scheme for Ideal Magnetohydrodynamics. *J. Comput. Phys.* **1999**, *154*, 284–309. [CrossRef]
263. Tóth, G. The $\bigtriangledown \cdot B = 0$ Constraint in Shock-Capturing Magnetohydrodynamics Codes. *J. Comput. Phys.* **2000**, *161*, 605–652. [CrossRef]
264. Liu, F.; Cai, J.; Zhu, Y.; Tsai, H.M.; Wong, A. Calculation of wing flutter by a coupled fluid-structure method. *J. Aircr.* **2001**, *38*, 334–342. [CrossRef]
265. Makhijani, V.B.; Yang, H.Q.; Dionne, P.J.; Thubrikar, M.J. Three-dimensional coupled fluid-structure simulation of pericardial bioprosthetic aortic valve function. *ASAIO J.* **1997**, *43*, M387–M392. [CrossRef] [PubMed]
266. Narumanchi, S.; Murthy, J.Y.; Amon, C.H. Submicron heat transport model in silicon accounting for phonon dispersion and polarization. *J. Heat Transf.* **2004**, *126*, 946–955. [CrossRef]
267. Voicolescu, I.; Andrew McGill, R.; Zaghloul, M.E.; Mott, D.; Stepnowski, J.; Stepnowski, S.; Summers, H.; Nguyen, V.; Ross, S.; Walsh, K.; et al. Micropreconcentrator for enhanced trace detection of explosives and chemical agents. *IEEE Sens. J.* **2006**, *6*, 1094–1103. [CrossRef]
268. Moukalled, F.; Mangani, L.; Darwish, M. *The Finite Volume Method in Computational Fluid Dynamics: An Advanced Introduction with OpenFOAM® and Matlab®*; Springer: Cham, Switzerland, 2016.
269. Patankar, S.V. *Numerical Heat Transfer and Fluid Flow*; Hemisphere Publishing: Washington, DC, USA, 1980.
270. Leonard, B.P. A stable and accurate convective modelling procedure based on quadratic upstream interpolation. *Comput. Methods Appl. Mech. Eng.* **1979**, *19*, 59–98. [CrossRef]
271. Weller, H.G.; Tabor, G.; Jasak, H.; Fureby, C. A tensorial approach to computational continuum mechanics using object-oriented techniques. *Comput. Phys.* **1998**, *12*, 620–631. [CrossRef]
272. Jasak, H. OpenFOAM: Open source CFD in research and industry. *Int. J. Nav. Archit. Ocean Eng.* **2009**, *1*, 89–94.
273. Favero, J.L.; Secchi, A.R.; Cardozo, N.; Jasak, H. Viscoelastic flow analysis using the software OpenFOAM and differential constitutive equations. *J. Non-Newton. Fluid Mech.* **2010**, *165*, 1625–1636. [CrossRef]
274. Favero, J.L.; Secchi, A.R.; Cardozo, N.; Jasak, H. Viscoelastic flow simulation: Development of a methodology of analysis using the software OpenFOAM and differential constitutive equations. *Comput. Aided Chem. Eng.* **2009**, *27*, 915–920.
275. Favero, J.L.; Secchi, A.R.; Cardozo, N.; Jasak, H. Viscoelastic fluid analysis in internal and in free surface flows using the software OpenFOAM. *Comput. Chem. Eng.* **2010**, *34*, 1984–1993. [CrossRef]

276. Holmes, L.; Favero, J.; Osswald, T. Numerical simulation of three-dimensional viscoelastic planar contraction flow using the software OpenFOAM. *Comput. Chem. Eng.* **2012**, *37*, 64–73. [CrossRef]
277. Yang, W.-J.; Yi, W.; Ren, X.-G.; Xu, L.-Y.; Xu, X.-H.; Yuan, X.-F. Toward large scale parallel computer simulation of viscoelastic fluid flow: A study of benchmark flow problems. *J. Non-Newton. Fluid Mech.* **2015**, *222*, 82–95. [CrossRef]
278. Lima, N.C.; D'ávila, M.A. Numerical simulation of electrohydrodynamic flows of Newtonian and viscoelastic droplets. *J. Non-Newton. Fluid Mech.* **2014**, *213*, 1–14. [CrossRef]
279. Cao, Y.; Ren, X.-G.; Guo, X.-W.; Wang, M.; Wang, Q.; Xu, X.-H.; Yang, X.-J. A new method to simulate free surface flows for Viscoelastic fluid. *Adv. Mater. Sci. Eng.* **2015**, *2015*. [CrossRef]
280. Habla, F.; Marschall, H.; Hinrichsen, O.; Dietsche, L.; Jasak, H.; Favero, J.L. Numerical simulation of viscoelastic two-phase flows using openFOAM®. *Chem. Eng. Sci.* **2011**, *66*, 5487–5496. [CrossRef]
281. Zhang, K.; Kuang, T.; Liu, H.; Zeng, X.; Deng, Y.; Jasak, H. Simulation and analysis of mold filling in water-assisted injection molding of viscoelastic polymers. *Gaofenzi Cailiao Kexue Yu Gongcheng* **2014**, *30*, 93–96.
282. Haddadi Sisakht, B.; Jordan, C.; Schretter, P.; Lassmann, T.; Harasek, M. Designing Better Membrane Modules Using CFD. *Chem. Prod. Process Model.* **2016**, *11*, 57–66. [CrossRef]
283. Wu, W.-T.; Yang, F.; Antaki, J.F.; Aubry, N.; Massoudi, M. Study of blood flow in several benchmark micro-channels using a two-fluid approach. *Int. J. Eng. Sci.* **2015**, *95*, 49–59. [CrossRef] [PubMed]
284. Carolan, D.; Chong, H.M.; Ivankovic, A.; Kinloch, A.J.; Taylor, A.C. Co-continuous polymer systems: A numerical investigation. *Comput. Mater. Sci.* **2015**, *98*, 24–33. [CrossRef]
285. Shou, Z.; Buxton, G.A.; Balazs, A.C. Predicting the self-assembled morphology and mechanical properties of mixtures of diblocks and rod-like nanoparticles. *Compos. Interfaces* **2003**, *10*, 343–368. [CrossRef]
286. Travasso, R.; Buxton, G.A.; Kuksenok, O.; Good, K.; Balazs, A.C. Modeling the morphology and mechanical properties of sheared ternary mixtures. *J. Chem. Phys.* **2005**, *122*, 194906. [CrossRef] [PubMed]
287. Zhao, X.; Deng, S.; Huang, Y.; Liu, H.; Hu, Y. Simulation of morphologies and mechanical properties of A/B polymer blend film. *Chin. J. Chem. Eng.* **2011**, *19*, 549–557. [CrossRef]
288. Smith, K.A.; Tyagi, S.; Balazs, A.C. Healing surface defects with nanoparticle-filled polymer coatings: Effect of particle geometry. *Macromolecules* **2005**, *38*, 10138–10147. [CrossRef]
289. Tyagi, S.; Lee, J.Y.; Buxton, G.A.; Balazs, A.C. Using nanocomposite coatings to heal surface defects. *Macromolecules* **2004**, *37*, 9160–9168. [CrossRef]
290. Brown, J.R.; Seo, Y.; Maula, T.; Hall, L.M. Fluids density functional theory and initializing molecular dynamics simulations of block copolymers. *J. Chem. Phys.* **2016**, *144*. [CrossRef] [PubMed]
291. Buxton, G.A.; Balazs, A.C. Predicting the mechanical and electrical properties of nanocomposites formed from polymer blends and nanorods. *Mol. Simul.* **2004**, *30*, 249–257. [CrossRef]
292. Buxton, G.A.; Balazs, A.C. Simulating the morphology and mechanical properties of filled diblock copolymers. *Phys. Rev. E Stat. Nonlinear Soft Matter Phys.* **2003**, *67*, 31802. [CrossRef] [PubMed]
293. Suter, J.L.; Groen, D.; Coveney, P.V. Chemically specifi C multiscale modeling of clay-polymer nanocomposites reveals intercalation dynamics, tactoid self-assembly and emergent materials properties. *Adv. Mater.* **2015**, *27*, 966–984. [CrossRef] [PubMed]
294. Scocchi, G.; Posocco, P.; Fermeglia, M.; Pricl, S. Polymer—Clay nanocomposites: A multiscale molecular modeling approach. *J. Phys. Chem. B* **2007**, *111*, 2143–2151. [CrossRef] [PubMed]
295. Scocchi, G.; Posocco, P.; Handgraaf, J.-W.; Fraaije, J.G.E.M.; Fermeglia, M.; Pricl, S. A complete multiscale modelling approach for polymer-clay nanocomposites. *Chem. Eur. J.* **2009**, *15*, 7586–7592. [CrossRef] [PubMed]
296. Pereira, S.P.; Scocchi, G.; Toth, R.; Posocco, P.; Nieto, D.R.; Pricl, S.; Fermeglia, M. Multiscale Modeling of Polymer/Clay Nanocomposites. *J. Multiscale Model.* **2011**, *3*, 151–176. [CrossRef]
297. Kalligiannaki, E.; Chazirakis, A.; Tsourtis, A.; Katsoulakis, M.A.; Plecháč, P.; Harmandaris, V. Parametrizing coarse grained models for molecular systems at equilibrium. *Eur. Phys. J. Spec. Top.* **2016**, *225*, 1347–1372. [CrossRef]
298. Harmandaris, V.; Kalligiannaki, E.; Katsoulakis, M.; Plecháč, P. Path-space variational inference for non-equilibrium coarse-grained systems. *J. Comput. Phys.* **2016**, *314*, 355–383. [CrossRef]
299. Li, Y.; Abberton, B.C.; Kröger, M.; Liu, W.K. Challenges in multiscale modeling of polymer dynamics. *Polymers* **2013**, *5*, 751–832. [CrossRef]

300. Brini, E.; Algaer, E.A.; Ganguly, P.; Li, C.; Rodríguez-Ropero, F.; van der Vegt, N. Systematic coarse-graining methods for soft matter simulations-a review. *Soft Matter* **2013**, *9*, 2108–2119. [CrossRef]
301. Hess, B.; Holm, C.; van der Vegt, N. Modeling multibody effects in ionic solutions with a concentration dependent dielectric permittivity. *Phys. Rev. Lett.* **2006**, *96*. [CrossRef] [PubMed]
302. Shen, J.-W.; Li, C.; van der Vegt, N.; Peter, C. Transferability of coarse grained potentials: Implicit solvent models for hydrated ions. *J. Chem. Theory Comput.* **2011**, *7*, 1916–1927. [CrossRef] [PubMed]
303. Wang, Y.; Noid, W.G.; Liu, P.; Voth, G.A. Effective force coarse-graining. *Phys. Chem. Chem. Phys.* **2009**, *11*, 2002–2015. [CrossRef] [PubMed]
304. Brini, E.; Marcon, V.; van der Vegt, N. Conditional reversible work method for molecular coarse graining applications. *Phys. Chem. Chem. Phys.* **2011**, *13*, 10468–10474. [CrossRef] [PubMed]
305. Brini, E.; van der Vegt, N. Chemically transferable coarse-grained potentials from conditional reversible work calculations. *J. Chem. Phys.* **2012**, *137*. [CrossRef] [PubMed]
306. Villa, A.; Peter, C.; van der Vegt, N. Self-assembling dipeptides: Conformational sampling in solvent-free coarse-grained simulation. *Phys. Chem. Chem. Phys.* **2009**, *11*, 2077–2086. [CrossRef] [PubMed]
307. Li, C.; Shen, J.; Peter, C.; van der Vegt, N. A chemically accurate implicit-solvent coarse-grained model for polystyrenesulfonate solutions. *Macromolecules* **2012**, *45*, 2551–2561. [CrossRef]
308. Tschöp, W.; Kremer, K.; Hahn, O.; Batoulis, J.; Bürger, T. Simulation of polymer melts. I. coarse-graining procedure for polycarbonates. *Acta Polym.* **1998**, *49*, 61–74. [CrossRef]
309. Lyubartsev, A.P.; Laaksonen, A. Calculation of effective interaction potentials from radial distribution functions: A reverse Monte Carlo approach. *Phys. Rev. E* **1995**, *52*, 3730–3737. [CrossRef]
310. Lyubartsev, A.P.; Laaksonen, A. Osmotic and activity coefficients from effective potentials for hydrated ions. *Phys. Rev. E* **1997**, *55*, 5689–5696. [CrossRef]
311. Reith, D.; Pütz, M.; Müller-Plathe, F. Deriving effective mesoscale potentials from atomistic simulations. *J. Comput. Chem.* **2003**, *24*, 1624–1636. [CrossRef] [PubMed]
312. Peter, C.; Delle Site, L.; Kremer, K. Classical simulations from the atomistic to the mesoscale and back: Coarse graining an azobenzene liquid crystal. *Soft Matter* **2008**, *4*, 859–869. [CrossRef]
313. Murtola, T.; Karttunen, M.; Vattulainen, I. Systematic coarse graining from structure using internal states: Application to phospholipid/cholesterol bilayer. *J. Chem. Phys.* **2009**, *131*. [CrossRef] [PubMed]
314. Savelyev, A.; Papoian, G.A. Molecular renormalization group coarse-graining of electrolyte solutions: Application to aqueous NaCl and KCl. *J. Phys. Chem. B* **2009**, *113*, 7785–7793. [CrossRef] [PubMed]
315. Savelyev, A.; Papoian, G.A. Molecular renormalization group coarse-graining of polymer chains: Application to double-stranded DNA. *Biophys. J.* **2009**, *96*, 4044–4052. [CrossRef] [PubMed]
316. Savelyev, A.; Papoian, G.A. Chemically accurate coarse graining of double-stranded DNA. *Proc. Natl. Acad. Sci. USA* **2010**, *107*, 20340–20345. [CrossRef] [PubMed]
317. Megariotis, G.; Vyrkou, A.; Leygue, A.; Theodorou, D.N. Systematic coarse graining of 4-Cyano-4′-pentylbiphenyl. *Ind. Eng. Chem. Res.* **2011**, *50*, 546–556. [CrossRef]
318. Mukherjee, B.; Delle Site, L.; Kremer, K.; Peter, C. Derivation of coarse grained models for multiscale simulation of liquid crystalline phase transitions. *J. Phys. Chem. B* **2012**, *116*, 8474–8484. [CrossRef] [PubMed]
319. Meyer, H.; Biermann, O.; Faller, R.; Reith, D.; Müller-Plathe, F. Coarse graining of nonbonded inter-particle potentials using automatic simplex optimization to fit structural properties. *J. Chem. Phys.* **2000**, *113*, 6264–6275. [CrossRef]
320. Ganguly, P.; Mukherji, D.; Junghans, C.; van der Vegt, N. Kirkwood-buff coarse-grained force fields for aqueous solutions. *J. Chem. Theory Comput.* **2012**, *8*, 1802–1807. [CrossRef] [PubMed]
321. Shell, M.S. The relative entropy is fundamental to multiscale and inverse thermodynamic problems. *J. Chem. Phys.* **2008**, *129*. [CrossRef] [PubMed]
322. Chaimovich, A.; Shell, M.S. Relative entropy as a universal metric for multiscale errors. *Phys. Rev. E* **2010**, *81*. [CrossRef] [PubMed]
323. Chaimovich, A.; Shell, M.S. Coarse-graining errors and numerical optimization using a relative entropy framework. *J. Chem. Phys.* **2011**, *134*. [CrossRef] [PubMed]
324. Chaimovich, A.; Shell, M.S. Anomalous waterlike behavior in spherically-symmetric water models optimized with the relative entropy. *Phys. Chem. Chem. Phys.* **2009**, *11*, 1901–1915. [CrossRef] [PubMed]
325. Mullinax, J.W.; Noid, W.G. Reference state for the generalized Yvon-Born-Green theory: Application for coarse-grained model of hydrophobic hydration. *J. Chem. Phys.* **2010**, *133*. [CrossRef] [PubMed]

326. Ercolesi, F.; Adams, J.B. Interatomic potentials from first-principles calculations: The force-matching method. *Europhys. Lett.* **1994**, *26*, 583–588. [CrossRef]
327. Rühle, V.; Junghans, C.; Lukyanov, A.; Kremer, K.; Andrienko, D. Versatile object-oriented toolkit for coarse-graining applications. *J. Chem. Theory Comput.* **2009**, *5*, 3211–3223. [CrossRef] [PubMed]
328. Izvekov, S.; Voth, G.A. A multiscale coarse-graining method for biomolecular systems. *J. Phys. Chem. B* **2005**, *109*, 2469–2473. [CrossRef] [PubMed]
329. Izvekov, S.; Chung, P.W.; Rice, B.M. The multiscale coarse-graining method: Assessing its accuracy and introducing density dependent coarse-grain potentials. *J. Chem. Phys.* **2010**, *133*. [CrossRef] [PubMed]
330. Zhou, J.; Thorpe, I.F.; Izvekov, S.; Voth, G.A. Coarse-grained peptide modeling using a systematic multiscale approach. *Biophys. J.* **2007**, *92*, 4289–4303. [CrossRef] [PubMed]
331. Hills, R.D., Jr.; Lu, L.; Voth, G.A. Multiscale coarse-graining of the protein energy landscape. *PLoS Comput. Biol.* **2010**, *6*, 1–15. [CrossRef] [PubMed]
332. Izvekov, S.; Voth, G.A. Multiscale coarse graining of liquid-state systems. *J. Chem. Phys.* **2005**, *123*. [CrossRef] [PubMed]
333. Noid, W.G.; Chu, J.-W.; Ayton, G.S.; Krishna, V.; Izvekov, S.; Voth, G.A.; Das, A.; Andersen, H.C. The multiscale coarse-graining method. I. A rigorous bridge between atomistic and coarse-grained models. *J. Chem. Phys.* **2008**, *128*, 244114. [CrossRef] [PubMed]
334. Noid, W.G.; Chu, J.-W.; Ayton, G.S.; Voth, G.A. Multiscale coarse-graining and structural correlations: Connections to liquid-state theory. *J. Phys. Chem. B* **2007**, *111*, 4116–4127. [CrossRef] [PubMed]
335. Noid, W.G.; Liu, P.; Wang, Y.; Chu, J.-W.; Ayton, G.S.; Izvekov, S.; Andersen, H.C.; Voth, G.A. The multiscale coarse-graining method. II. Numerical implementation for coarse-grained molecular models. *J. Chem. Phys.* **2008**, *128*, 244115. [CrossRef] [PubMed]
336. Wu, C. Phase morphologies of binary polymer blends predicted by systematically coarse-grained models. *Macromol. Theory Simul.* **2016**. [CrossRef]
337. Potestio, R.; Peter, C.; Kremer, K. Computer simulations of soft matter: Linking the scales. *Entropy* **2014**, *16*, 4199–4245. [CrossRef]
338. Rzepiela, A.J.; Louhivuori, M.; Peter, C.; Marrink, S.J. Hybrid simulations: Combining atomistic and coarse-grained force fields using virtual sites. *Phys. Chem. Chem. Phys.* **2011**, *13*, 10437–10448. [CrossRef] [PubMed]
339. Li, Y.; Tang, S.; Abberton, B.C.; Kröger, M.; Burkhart, C.; Jiang, B.; Papakonstantopoulos, G.J.; Poldneff, M.; Liu, W.K. A predictive multiscale computational framework for viscoelastic properties of linear polymers. *Polymer* **2012**, *53*, 5935–5952. [CrossRef]
340. Noid, W.G. Perspective: Coarse-grained models for biomolecular systems. *J. Chem. Phys.* **2013**, *139*. [CrossRef] [PubMed]
341. Rudzinski, J.F.; Noid, W.G. Investigation of coarse-grained mappings via an iterative generalized Yvon-Born-Green method. *J. Phys. Chem. B* **2014**, *118*, 8295–8312. [CrossRef] [PubMed]
342. Torrie, G.M.; Valleau, J.P. Nonphysical sampling distributions in Monte Carlo free-energy estimation: Umbrella sampling. *J. Comput. Phys.* **1977**, *23*, 187–199. [CrossRef]
343. Den Otter, W.K.; Briels, W.J. The calculation of free-energy differences by constrained molecular-dynamics simulations. *J. Chem. Phys.* **1998**, *109*, 4139–4146. [CrossRef]
344. Villa, A.; Peter, C.; van der Vegt, N. Transferability of nonbonded interaction potentials for coarse-grained simulations: Benzene in water. *J. Chem. Theory Comput.* **2010**, *6*, 2434–2444. [CrossRef] [PubMed]
345. Hahn, O.; Site, L.D.; Kremer, K. Simulation of polymer melts: From spherical to ellipsoidal beads. *Macromol. Theory Simul.* **2001**, *10*, 288–303. [CrossRef]
346. Xie, G.-L.; Zhang, Y.-H.; Huang, S.-P. Glass formation of n-butanol: Coarse-grained molecular dynamics simulations using gay-berne potential model. *Chin. J. Chem. Phys.* **2012**, *25*, 177–185. [CrossRef]
347. Müller-Plathe, F. Local structure and dynamics in solvent-swollen polymers. *Macromolecules* **1996**, *29*, 4782–4791. [CrossRef]
348. Milano, G.; Müller-Plathe, F. Mapping atomistic simulations to mesoscopic models: A systematic coarse-graining procedure for vinyl polymer chains. *J. Phys. Chem. B* **2005**, *109*, 18609–18619. [CrossRef] [PubMed]

349. Milano, G.; Goudeau, S.; Müller-Plathe, F. Multicentered Gaussian-based potentials for coarse-grained polymer simulations: Linking atomistic and mesoscopic scales. *J. Polym. Sci. Part B* **2005**, *43*, 871–885. [CrossRef]
350. Spyriouni, T.; Tzoumanekas, C.; Theodorou, D.; Müller-Plathe, F.; Milano, G. Coarse-grained and reverse-mapped united-atom simulations of long-chain atactic polystyrene melts: Structure, thermodynamic properties, chain conformation, and entanglements. *Macromolecules* **2007**, *40*, 3876–3885. [CrossRef]
351. Sun, Q.; Faller, R. Systematic coarse-graining of atomistic models for simulation of polymeric systems. *Comput. Chem. Eng.* **2005**, *29*, 2380–2385. [CrossRef]
352. Sun, Q.; Faller, R. Crossover from unentangled to entangled dynamics in a systematically coarse-grained polystyrene melt. *Macromolecules* **2006**, *39*, 812–820. [CrossRef]
353. Qian, H.-J.; Carbone, P.; Xiaoyu, C.; Karimi-Varzaneh, H.A.; Liew, C.C.; Müller-Plathe, F. Temperature-Transferable Coarse-Grained potentials for ethylbenzene, polystyrene, and their mixtures. *Macromolecules* **2008**, *41*, 9919–9929. [CrossRef]
354. Harmandaris, V.A.; Adhikari, N.P.; van der Vegt, N.; Kremer, K. Hierarchical modeling of polystyrene: From atomistic to coarse-grained simulations. *Macromolecules* **2006**, *39*, 6708–6719. [CrossRef]
355. Harmandaris, V.A.; Reith, D.; van der Vegt, N.; Kremer, K. Comparison between coarse-graining models for polymer systems: Two mapping schemes for polystyrene. *Macromol. Chem. Phys.* **2007**, *208*, 2109–2120. [CrossRef]
356. Fritz, D.; Harmandaris, V.A.; Kremer, K.; van der Vegt, N. Coarse-grained polymer melts based on isolated atomistic chains: Simulation of polystyrene of different tacticities. *Macromolecules* **2009**, *42*, 7579–7588. [CrossRef]
357. Mulder, T.; Harmandaris, V.A.; Lyulin, A.V.; van der Vegt, N.; Vorselaars, B.; Michels, M. Equilibration and deformation of amorphous polystyrene: Scale-jumping simulational approach. *Macromol. Theory Simul.* **2008**, *17*, 290–300. [CrossRef]
358. Mulder, T.; Harmandaris, V.A.; Lyulin, A.V.; van der Vegt, N.; Kremer, K.; Michels, M. Structural properties of atactic polystyrene of different thermal history obtained from a multiscale simulation. *Macromolecules* **2009**, *42*, 384–391. [CrossRef]
359. Harmandaris, V.A.; Kremer, K. Predicting polymer dynamics at multiple length and time scales. *Soft Matter* **2009**, *5*, 3920–3926. [CrossRef]
360. Harmandaris, V.A.; Kremer, K. Dynamics of polystyrene melts through hierarchical multiscale simulations. *Macromolecules* **2009**, *42*, 791–802. [CrossRef]
361. Karimi-Varzaneh, H.A.; van der Vegt, N.; Müller-Plathe, F.; Carbone, P. How good are coarse-grained polymer models? A comparison for atactic polystyrene. *ChemPhysChem* **2012**, *13*, 3428–3439. [CrossRef] [PubMed]
362. Batchelor, G.K. *An Introduction to Fluid Dynamics*; Cambridge University Press: New York, NY, USA, 2000.
363. Lyubimov, I.; Guenza, M.G. First-principle approach to rescale the dynamics of simulated coarse-grained macromolecular liquids. *Phys. Rev. E* **2011**, *84*. [CrossRef] [PubMed]
364. Lyubimov, I.Y.; McCarty, J.; Clark, A.; Guenza, M.G. Analytical rescaling of polymer dynamics from mesoscale simulations. *J. Chem. Phys.* **2010**, *132*. [CrossRef] [PubMed]
365. Lyubimov, I.Y.; Guenza, M.G. Theoretical reconstruction of realistic dynamics of highly coarse-grained cis-1,4-polybutadiene melts. *J. Chem. Phys.* **2013**, *138*. [CrossRef] [PubMed]
366. Fritz, D.; Koschke, K.; Harmandaris, V.A.; van der Vegt, N.; Kremer, K. Multiscale modeling of soft matter: Scaling of dynamics. *Phys. Chem. Chem. Phys.* **2011**, *13*, 10412–10420. [CrossRef] [PubMed]
367. Colmenero, J.; Arbe, A. Segmental dynamics in miscible polymer blends: Recent results and open questions. *Soft Matter* **2007**, *3*, 1474–1485. [CrossRef]
368. Roland, C.M.; Ngai, K.L. Dynamical heterogeneity in a miscible polymer blend. *Macromolecules* **1991**, *24*, 2261–2265. [CrossRef]
369. Harmandaris, V.A.; Kremer, K.; Floudas, G. Dynamic heterogeneity in fully miscible blends of polystyrene with oligostyrene. *Phys. Rev. Lett.* **2013**, *110*. [CrossRef] [PubMed]
370. Louis, A.A. Beware of density dependent pair potentials. *J. Phys.* **2002**, *14*, 9187–9206. [CrossRef]
371. Eslami, H.; Karimi-Varzaneh, H.A.; Müller-Plathe, F. Coarse-grained computer simulation of nanoconfined polyamide-6,6. *Macromolecules* **2011**, *44*, 3117–3128. [CrossRef]

372. Bayramoglu, B.; Faller, R. Coarse-grained modeling of polystyrene in various environments by iterative Boltzmann inversion. *Macromolecules* **2012**, *45*, 9205–9219. [CrossRef]
373. Fukunaga, H.; Takimoto, J.-I.; Doi, M. A coarse-graining procedure for flexible polymer chains with bonded and nonbonded interactions. *J. Chem. Phys.* **2002**, *116*, 8183–8190. [CrossRef]
374. Carbone, P.; Varzaneh, H.; Chen, X.; Müller-Plathe, F. Transferability of coarse-grained force fields: The polymer case. *J. Chem. Phys.* **2008**, *128*. [CrossRef] [PubMed]
375. Harmandaris, V.A.; Floudas, G.; Kremer, K. Temperature and pressure dependence of polystyrene dynamics through molecular dynamics simulations and experiments. *Macromolecules* **2011**, *44*, 393–402. [CrossRef]
376. Strauch, T.; Yelash, L.; Paul, W. A coarse-graining procedure for polymer melts applied to 1,4-polybutadiene. *Phys. Chem. Chem. Phys.* **2009**, *11*, 1942–1948. [CrossRef] [PubMed]
377. Vettorel, T.; Meyer, H. Coarse graining of short polythylene chains for studying polymer crystallization. *J. Chem. Theory Comput.* **2006**, *2*, 616–629. [CrossRef] [PubMed]
378. Yelash, L.; Müller, M.; Paul, W.; Binder, K. How well can coarse-grained models of real polymers describe their structure? The case of polybutadiene. *J. Chem. Theory Comput.* **2006**, *2*, 588–597. [CrossRef] [PubMed]
379. Fu, C.-C.; Kulkarni, P.M.; Scott Shell, M.; Gary Leal, L. A test of systematic coarse-graining of molecular dynamics simulations: Thermodynamic properties. *J. Chem. Phys.* **2012**, *137*. [CrossRef] [PubMed]
380. Baron, R.; Trzesniak, D.; de Vries, A.H.; Elsener, A.; Marrink, S.J.; van Gunsteren, W.F. Comparison of thermodynamic properties of coarse-grained and atomic-level simulation models. *ChemPhysChem* **2007**, *8*, 452–461. [CrossRef] [PubMed]
381. Betancourt, M.R.; Omovie, S.J. Pairwise energies for polypeptide coarse-grained models derived from atomic force fields. *J. Chem. Phys.* **2009**, *130*. [CrossRef] [PubMed]
382. Mullinax, J.W.; Noid, W.G. Extended ensemble approach for deriving transferable coarse-grained potentials. *J. Chem. Phys.* **2009**, *131*. [CrossRef]
383. Patrone, P.N.; Rosch, T.W.; Phelan, F.R., Jr. Bayesian calibration of coarse-grained forces: Efficiently addressing transferability. *J. Chem. Phys.* **2016**, *144*. [CrossRef] [PubMed]
384. Unadkat, J.D.; Beal, S.L.; Sheiner, L.B. Bayesian calibration. *Anal. Chim. Acta* **1986**, *181*, 27–36. [CrossRef]
385. Padding, J.T.; Briels, W.J. Uncrossability constraints in mesoscopic polymer melt simulations: Non-rouse behavior of C120H242. *J. Chem. Phys.* **2001**, *115*, 2846–2859. [CrossRef]
386. Padding, J.T.; Briels, W.J. Time and length scales of polymer melts studied by coarse-grained molecular dynamics simulations. *J. Chem. Phys.* **2002**, *117*, 925–943. [CrossRef]
387. Padding, J.T.; Briels, W.J.; Stukan, M.R.; Boek, E.S. Review of multi-scale particulate simulation of the rheology of wormlike micellar fluids. *Soft Matter* **2009**, *5*, 4367–4375. [CrossRef]
388. Padding, J.T.; Briels, W.J. Coarse-grained molecular dynamics simulations of polymer melts in transient and steady shear flow. *J. Chem. Phys.* **2003**, *118*, 10276–10286. [CrossRef]
389. Pérez-Aparicio, R.; Colmenero, J.; Alvarez, F.; Padding, J.T.; Briels, W.J. Chain dynamics of poly(ethylene-alt-propylene) melts by means of coarse-grained simulations based on atomistic molecular dynamics. *J. Chem. Phys.* **2010**, *132*. [CrossRef] [PubMed]
390. Liu, L.; Padding, J.T.; Den Otter, W.K.; Briels, W.J. Coarse-grained simulations of moderately entangled star polyethylene melts. *J. Chem. Phys.* **2013**, *138*. [CrossRef] [PubMed]
391. Maiti, A.; McGrother, S. Bead-bead interaction parameters in dissipative particle dynamics: Relation to bead-size, solubility parameter, and surface tension. *J. Chem. Phys.* **2004**, *120*, 1594–1601. [CrossRef] [PubMed]
392. Kacar, G.; Peters, E.; de With, G. A generalized method for parameterization of dissipative particle dynamics for variable bead volumes. *Europhys. Lett.* **2013**, *102*. [CrossRef]
393. Johnston, K.; Harmandaris, V. Hierarchical multiscale modeling of polymer-solid interfaces: Atomistic to coarse-grained description and structural and conformational properties of polystyrene-gold systems. *Macromolecules* **2013**, *46*, 5741–5750. [CrossRef]
394. Pan, G.; Manke, C.W. Developments toward simulation of entangled polymer melts by dissipative particle dynamics (DPD). *Int. J. Mod. Phys. B* **2003**, *17*, 231–235. [CrossRef]
395. Sirk, T.W.; Slizoberg, Y.R.; Brennan, J.K.; Lisal, M.; Andzelm, J.W. An enhanced entangled polymer model for dissipative particle dynamics. *J. Chem. Phys.* **2012**, *136*, 134903. [CrossRef] [PubMed]
396. Nikunen, P.; Vattulainen, I.; Karttunen, M. Reptational dynamics in dissipative particle dynamics simulations of polymer melts. *Phys. Rev. E* **2007**, *75*, 36713. [CrossRef] [PubMed]

397. Doi, M.; Edwards, S.F. *The Theory of Polymer Dynamics*; Clarendon Press: Oxford, UK, 1986.
398. Gooneie, A.; Schuschnigg, S.; Holzer, C. Coupled orientation and stretching of chains in mesoscale models of polydisperse linear polymers in startup of steady shear flow simulations. *Macromol. Theory Simul.* **2016**, *25*, 170–186. [CrossRef]
399. Murat, M.; Kremer, K. From many monomers to many polymers: Soft ellipsoid model for polymer melts and mixtures. *J. Chem. Phys.* **1998**, *108*, 4340–4348. [CrossRef]
400. D'Adamo, G.; Pelissetto, A.; Pierleoni, C. Coarse-graining strategies in polymer solutions. *Soft Matter* **2012**, *8*, 5151–5167. [CrossRef]
401. D'Adamo, G.; Pelissetto, A.; Pierleoni, C. Polymers as compressible soft spheres. *J. Chem. Phys.* **2012**, *136*. [CrossRef] [PubMed]
402. Vettorel, T.; Besold, G.; Kremer, K. Fluctuating soft-sphere approach to coarse-graining of polymer models. *Soft Matter* **2010**, *6*, 2282–2292. [CrossRef]
403. Zhang, G.; Daoulas, K.C.; Kremer, K. A New Coarse Grained Particle-To-Mesh Scheme for Modeling Soft Matter. *Macromol. Chem. Phys.* **2013**, *214*, 214–224. [CrossRef]
404. Kindt, P.; Briels, W.J. A single particle model to simulate the dynamics of entangled polymer melts. *J. Chem. Phys.* **2007**, *127*. [CrossRef] [PubMed]
405. Briels, W.J. Transient forces in flowing soft matter. *Soft Matter* **2009**, *5*, 4401–4411. [CrossRef]
406. Zhu, Y.-L.; Liu, H.; Lu, Z.-Y. A highly coarse-grained model to simulate entangled polymer melts. *J. Chem. Phys.* **2012**, *136*. [CrossRef] [PubMed]
407. Sprakel, J.; Padding, J.T.; Briels, W.J. Transient forces and non-equilibrium states in sheared polymer networks. *Europhys. Lett.* **2011**, *93*. [CrossRef]
408. Sprakel, J.; Spruijt, E.; van der Gucht, J.; Padding, J.T.; Briels, W.J. Failure-mode transition in transient polymer networks with particle-based simulations. *Soft Matter* **2009**, *5*, 4748–4756. [CrossRef]
409. Savin, T.; Briels, W.J.; öttinger, H.C. Thermodynamic formulation of flowing soft matter with transient forces. *Rheol. Acta* **2013**, *52*, 23–32. [CrossRef]
410. Padding, J.T.; van Ruymbeke, E.; Vlassopoulos, D.; Briels, W.J. Computer simulation of the rheology of concentrated star polymer suspensions. *Rheol. Acta* **2010**, *49*, 473–484. [CrossRef]
411. Padding, J.T.; Mohite, L.V.; Auhl, D.; Briels, W.J.; Bailly, C. Mesoscale modeling of the rheology of pressure sensitive adhesives through inclusion of transient forces. *Soft Matter* **2011**, *7*, 5036–5046. [CrossRef]
412. Padding, J.T.; Mohite, L.V.; Auhl, D.; Schweizer, T.; Briels, W.J.; Bailly, C. Quantitative mesoscale modeling of the oscillatory and transient shear rheology and the extensional rheology of pressure sensitive adhesives. *Soft Matter* **2012**, *8*, 7967–7981. [CrossRef]
413. Schweizer, K.S.; Curro, J.G. Integral equation theories of the structure, thermodynamics, and phase transitions of polymer fluids. *Adv. Chem. Phys.* **1997**, *98*, 1–142.
414. McCarty, J.; Guenza, M.G. Multiscale modeling of binary polymer mixtures: Scale bridging in the athermal and thermal regime. *J. Chem. Phys.* **2010**, *133*. [CrossRef] [PubMed]
415. McCarty, J.; Lyubimov, I.Y.; Guenza, M.G. Effective soft-core potentials and mesoscopic simulations of binary polymer mixtures. *Macromolecules* **2010**, *43*, 3964–3979. [CrossRef]
416. McCarty, J.; Lyubimov, I.Y.; Guenza, M.G. Multiscale modeling of coarse-grained macromolecular liquids. *J. Phys. Chem. B* **2009**, *113*, 11876–11886. [CrossRef] [PubMed]
417. Guenza, M.G. Theoretical models for bridging timescales in polymer dynamics. *J. Phys.: Condens. Matter* **2007**, *20*, 033101. [CrossRef]
418. Clark, A.J.; McCarty, J.; Lyubimov, I.Y.; Guenza, M.G. Thermodynamic consistency in variable-level coarse graining of polymeric liquids. *Phys. Rev. Lett.* **2012**, *109*. [CrossRef] [PubMed]
419. McCarty, J.; Clark, A.J.; Lyubimov, I.Y.; Guenza, M.G. Thermodynamic consistency between analytic integral equation theory and coarse-grained molecular dynamics simulations of homopolymer melts. *Macromolecules* **2012**, *45*, 8482–8493. [CrossRef]
420. Santangelo, G.; Di Matteo, A.; Müller-Plathe, F.; Milano, G. From mesoscale back to atomistic models: A fast reverse-mapping procedure for vinyl polymer chains. *J. Phys. Chem. B* **2007**, *111*, 2765–2773. [CrossRef] [PubMed]
421. Parker, A.J.; Rottler, J. Using soft potentials for the simulation of block copolymer morphologies. *Macromol. Theory Simul.* **2014**, *23*, 401–409. [CrossRef]

422. Sliozberg, Y.R.; Kröger, M.; Chantawansri, T.L. Fast equilibration protocol for million atom systems of highly entangled linear polyethylene chains. *J. Chem. Phys.* **2016**, *144*. [CrossRef] [PubMed]
423. Chen, X.; Carbone, P.; Santangelo, G.; Di Matteo, A.; Milano, G.; Müller-Plathe, F. Backmapping coarse-grained polymer models under sheared nonequilibrium conditions. *Phys. Chem. Chem. Phys.* **2009**, *11*, 1977–1988. [CrossRef] [PubMed]
424. Carbone, P.; Ali Karimi-Varzaneh, H.; Müller-Plathe, F. Fine-graining without coarse-graining: An easy and fast way to equilibrate dense polymer melts. *Faraday Discuss.* **2009**, *144*, 25–42. [CrossRef]
425. Tschöp, W.; Kremer, K.; Halm, O.; Batoulis, J.; Bürger, T. Simulation of polymer melts. II. From coarse-grained models back to atomistic description. *Acta Polym.* **1998**, *49*, 75–79. [CrossRef]
426. Kotelyanskii, M.; Wagner, N.J.; Paulaitis, M.E. Building large amorphous polymer structures: Atomistic simulation of glassy polystyrene. *Macromolecules* **1996**, *29*, 8497–8506. [CrossRef]
427. Harmandaris, V.A.; Mavrantzas, V.G.; Theodorou, D.N. Atomistic molecular dynamics simulation of stress relaxation upon cessation of steady-state uniaxial elongational flow. *Macromolecules* **2000**, *33*, 8062–8076. [CrossRef]
428. Queyroy, S.; Neyertz, S.; Brown, D.; Müller-Plathe, F. Preparing relaxed systems of amorphous polymers by multiscale simulation: Application to cellulose. *Macromolecules* **2004**, *37*, 7338–7350. [CrossRef]
429. Hess, B.; León, S.; van der Vegt, N.; Kremer, K. Long time atomistic polymer trajectories from coarse grained simulations: Bisphenol-A polycarbonate. *Soft Matter* **2006**, *2*, 409–414. [CrossRef]
430. Karimi-Varzaneh, H.A.; Carbone, P.; Müller-Plathe, F. Fast dynamics in coarse-grained polymer models: The effect of the hydrogen bonds. *J. Chem. Phys.* **2008**, *129*. [CrossRef] [PubMed]
431. Wu, C. Multiscale simulations of the structure and dynamics of stereoregular poly(methyl methacrylate)s. *J. Mol. Model.* **2014**, *20*. [CrossRef] [PubMed]
432. Handgraaf, J.-W.; Serral Gracia, R.; Nath, S.K.; Chen, Z.; Chou, S.-H.; Ross, R.B.; Schultz, N.E.; Fraaije, J. A multiscale modeling protocol to generate realistic polymer surfaces. *Macromolecules* **2011**, *44*, 1053–1061. [CrossRef]
433. Bleha, T.; Gajdos, J.; Karasz, F.E. Energetics of strain-induced conformational transitions in polymethylene chains. *Macromolecules* **1990**, *23*, 4076–4082. [CrossRef]
434. Ghanbari, A.; Böhm, M.C.; Müller-Plathe, F. A simple reverse mapping procedure for coarse-grained polymer models with rigid side groups. *Macromolecules* **2011**, *44*, 5520–5526. [CrossRef]
435. Abraham, F.F.; Broughton, J.Q.; Bernstein, N.; Kaxiras, E. Spanning the length scales in dynamic simulation. *Comput. Phys.* **1998**, *12*, 538–546. [CrossRef]
436. Stillinger, F.H.; Weber, T.A. Computer simulation of local order in condensed phases of silicon. *Phys. Rev. B Condens. Matter Mater. Phys.* **1985**, *31*, 5262–5271. [CrossRef]
437. Rudd, R.E.; Broughton, J.Q. Concurrent coupling of length scales in solid state systems. *Phys. Status Solidi B* **2000**, *217*, 251–291. [CrossRef]
438. Nakano, A.; Bachlechner, M.E.; Kalia, R.K.; Lidorikis, E.; Vashishta, P.; Voyiadjis, G.Z.; Campbell, T.J.; Ogata, S.; Shimojo, F. Multiscale simulation of nanosystems. *Comput. Sci. Eng.* **2001**, *3*, 56–66. [CrossRef]
439. Broughton, J.Q.; Abraham, F.F.; Bernstein, N.; Kaxiras, E. Concurrent coupling of length scales: Methodology and application. *Phys. Rev. B Condens. Matter Mater. Phys.* **1999**, *60*, 2391–2403. [CrossRef]
440. Abraham, F.F.; Broughton, J.Q.; Bernstein, N.; Kaxiras, E. Spanning the continuum to quantum length scales in a dynamic simulation of brittle fracture. *Europhys. Lett.* **1998**, *44*, 783–787. [CrossRef]
441. Curtin, W.A.; Miller, R.E. Atomistic/continuum coupling in computational materials science. *Model. Simul. Mater. Sci. Eng.* **2003**, *11*, R33–R68. [CrossRef]
442. Miller, R.E.; Tadmor, E.B. A unified framework and performance benchmark of fourteen multiscale atomistic/continuum coupling methods. *Model. Simul. Mater. Sci. Eng.* **2009**, *17*, 53001. [CrossRef]
443. Badia, S.; Parks, M.; Bochev, P.; Gunzburger, M.; Lehouc, Q. On atomistic-to-continuum coupling by blending. *Multiscale Model. Simul.* **2008**, *7*, 381–406. [CrossRef]
444. Shenoy, V.B.; Miller, R.; Tadmor, E.B.; Rodney, D.; Phillips, R.; Ortiz, M. An adaptive finite element approach to atomic-scale mechanics—The quasicontinuum method. *J. Mech. Phys. Solids* **1999**, *47*, 611–642. [CrossRef]
445. Li, X.; Ming, P. On the effect of ghost force in the quasicontinuum method: Dynamic problems in one dimension. *Commun. Comput. Phys.* **2014**, *15*, 647–676. [CrossRef]
446. Ortner, C.; Zhang, L. Atomistic/continuum blending with ghost force correction. *Siam J. Sci. Comput.* **2016**, *38*, A346–A375. [CrossRef]

447. Shimokawa, T.; Mortensen, J.J.; Schiøtz, J.; Jacobsen, K.W. Matching conditions in the quasicontinuum method: Removal of the error introduced at the interface between the coarse-grained and fully atomistic region. *Phys. Rev. B Condens. Matter Mater. Phys.* **2004**, *69*, 214104. [CrossRef]
448. Lu, J.; Yang, J.Z. Uniform accuracy of the quasicontinuum method. *Phys. Rev. B* **2006**, *74*. [CrossRef]
449. Klein, P.A.; Zimmerman, J.A. Coupled atomistic-continuum simulations using arbitrary overlapping domains. *J. Comput. Phys.* **2006**, *213*, 86–116. [CrossRef]
450. Tadmor, E.B.; Ortiz, M.; Phillips, R. Quasicontinuum analysis of defects in solids. *Philos. Mag. A Phys. Condens. Matter Struct. Defects Mech. Prop.* **1996**, *73*, 1529–1563. [CrossRef]
451. Tadmor, E.B.; Phillips, R.; Ortiz, M. Mixed atomistic and continuum models of deformation in solids. *Langmuir* **1996**, *12*, 4529–4532. [CrossRef]
452. Rudd, R.E.; Broughton, J.Q. Coarse-grained molecular dynamics and the atomic limit of finite elements. *Phys. Rev. B* **1998**, *58*, R5893–R5896. [CrossRef]
453. Shenoy, V.B.; Miller, R.; Tadmor, E.B.; Phillips, R.; Ortiz, M. Quasicontinuum models of interfacial structure and deformation. *Phys. Rev. Lett.* **1998**, *80*, 742–745. [CrossRef]
454. Rodney, D.; Martin, G. Dislocation pinning by small interstitial loops: A molecular dynamics study. *Phys. Rev. Lett.* **1999**, *82*, 3272–3275. [CrossRef]
455. Rodney, D.; Phillips, R. Structure and Strength of Dislocation Junctions: An Atomic Level Analysis. *Phys. Rev. Lett.* **1999**, *82*, 1704–1707. [CrossRef]
456. Tadmor, E.B.; Smith, G.S.; Bernstein, N.; Kaxiras, E. Mixed finite element and atomistic formulation for complex crystals. *Phys. Rev. B* **1999**, *59*, 235–245. [CrossRef]
457. Miller, R.; Ortiz, M.; Phillips, R.; Shenoy, V.; Tadmor, E.B. Quasicontinuum models of fracture and plasticity. *Eng. Fract. Mech.* **1998**, *61*, 427–444. [CrossRef]
458. Miller, R.; Tadmor, E.B.; Phillips, R.; Ortiz, M. Quasicontinuum simulation of fracture at the atomic scale. *Model. Simul. Mater. Sci. Eng.* **1998**, *6*, 607–638. [CrossRef]
459. Tadmor, E.B.; Miller, R.; Phillips, R.; Ortiz, M. Nanoindentation and incipient plasticity. *J. Mater. Res.* **1999**, *14*, 2233–2250. [CrossRef]
460. Binder, A.; Luskin, M.; Perez, D.; Voter, A.F. Analysis of transition state theory rates upon spatial coarse-graining. *Multiscale Model. Simul.* **2015**, *13*, 890–915. [CrossRef]
461. Eidel, B.; Stukowski, A. A variational formulation of the quasicontinuum method based on energy sampling in clusters. *J. Mech. Phys. Solids* **2009**, *57*, 87–108. [CrossRef]
462. Miller, R.E.; Tadmor, E.B. Hybrid continuum mechanics and atomistic methods for simulating materials deformation and failure. *MRS Bull.* **2007**, *32*, 920–926. [CrossRef]
463. Iacobellis, V.; Behdinan, K. Comparison of concurrent multiscale methods in the application of fracture in nickel. *J. Appl. Mech. Trans. ASME* **2013**, *80*. [CrossRef]
464. Xiao, S.P.; Belytschko, T. A bridging domain method for coupling continua with molecular dynamics. *Comput. Methods Appl. Mech. Eng.* **2004**, *193*, 1645–1669. [CrossRef]
465. Datta, D.K.; Picu, C.; Shephard, M.S. Composite Grid Atomistic Continuum Method: An Adaptive Approach to Bridge Continuum with Atomistic Analysis. *Int. J. Multiscale Comput. Eng.* **2004**, *2*, 71–90. [CrossRef]
466. Rudd, R.E.; Broughton, J.Q. Coarse-grained molecular dynamics: Nonlinear finite elements and finite temperature. *Phys. Rev. B Condens. Matter Mater. Phys.* **2005**, *72*. [CrossRef]
467. Curtarolo, S.; Ceder, G. Dynamics of an inhomogeneously coarse grained multiscale system. *Phys. Rev. Lett.* **2002**, *88*, 2555041–2555044. [CrossRef] [PubMed]
468. Dupuy, L.M.; Tadmor, E.B.; Miller, R.E.; Phillips, R. Finite-temperature quasicontinuum: Molecular dynamics without all the atoms. *Phys. Rev. Lett.* **2005**, *95*. [CrossRef] [PubMed]
469. Tang, Z.; Zhao, H.; Li, G.; Aluru, N.R. Finite-temperature quasicontinuum method for multiscale analysis of silicon nanostructures. *Phys. Rev. B Condens. Matter Mater. Phys.* **2006**, *74*. [CrossRef]
470. Marian, J.; Venturini, G.; Hansen, B.L.; Knap, J.; Ortiz, M.; Campbell, G.H. Finite-temperature extension of the quasicontinuum method using Langevin dynamics: Entropy losses and analysis of errors. *Model. Simul. Mater. Sci. Eng.* **2010**, *18*. [CrossRef]
471. Kohlhoff, S.; Gumbsch, P.; Fischmeister, H.F. Crack propagation in b.c.c. crystals studied with a combined finite-element and atomistic model. *Philos. Mag. A Phys. Condens. Matter Struct. Defects Mech. Prop.* **1991**, *64*, 851–878. [CrossRef]

472. Shilkrot, L.E.; Miller, R.E.; Curtin, W.A. Coupled atomistic and discrete dislocation plasticity. *Phys. Rev. Lett.* **2002**, *89*, 255011–255014. [CrossRef] [PubMed]
473. Shilkrot, L.E.; Miller, R.E.; Curtin, W.A. Multiscale plasticity modeling: Coupled atomistics and discrete dislocation mechanics. *J. Mech. Phys. Solids* **2004**, *52*, 755–787. [CrossRef]
474. Luan, B.Q.; Hyun, S.; Molinari, J.F.; Bernstein, N.; Robbins, M.O. Multiscale modeling of two-dimensional contacts. *Phys. Rev. E Stat. Nonlinear Soft Matter Phys.* **2006**, *74*. [CrossRef] [PubMed]
475. Badia, S.; Bochev, P.; Lehoucq, R.; Parks, M.L.; Fish, J.; Nuggehally, M.A.; Gunzburger, M. A force-based blending model foratomistic-to-continuum coupling. *Int. J. Multiscale Comput. Eng.* **2007**, *5*, 387–406. [CrossRef]
476. Fish, J.; Nuggehally, M.A.; Shephard, M.S.; Picu, C.R.; Badia, S.; Parks, M.L.; Gunzburger, M. Concurrent AtC coupling based on a blend of the continuum stress and the atomistic force. *Comput. Methods Appl. Mech. Eng.* **2007**, *196*, 4548–4560. [CrossRef]
477. Hughes, T.; Feijóo, G.R.; Mazzei, L.; Quincy, J.-B. The variational multiscale method—A paradigm for computational mechanics. *Comput. Methods Appl. Mech. Eng.* **1998**, *166*, 3–24. [CrossRef]
478. Qian, D.; Wagner, G.J.; Liu, W.K. A multiscale projection method for the analysis of carbon nanotubes. *Comput. Methods Appl. Mech. Eng.* **2004**, *193*, 1603–1632. [CrossRef]
479. Wagner, G.J.; Liu, W.K. Coupling of atomistic and continuum simulations using a bridging scale decomposition. *J. Comput. Phys.* **2003**, *190*, 249–274. [CrossRef]
480. Park, H.S.; Liu, W.K. An introduction and tutorial on multiple-scale analysis in solids. *Comput. Methods Appl. Mech. Eng.* **2004**, *193*, 1733–1772. [CrossRef]
481. Tan, V.; Zeng, X.S.; Deng, M.; Lim, K.M.; Tay, T.E. Multiscale modeling of polymers—The Pseudo Amorphous Cell. *Comput. Methods Appl. Mech. Eng.* **2008**, *197*, 536–554. [CrossRef]
482. Theodorou, D.N.; Suter, U.W. Detailed molecular structure of a vinyl polymer glass. *Macromolecules* **1985**, *18*, 1467–1478. [CrossRef]
483. Theodorou, D.N.; Suter, U.W. Geometrical considerations in model systems with periodic boundaries. *J. Chem. Phys.* **1985**, *82*, 955–966. [CrossRef]
484. Su, Z.C.; Tay, T.-E.; Chen, Y.; Tan, V. Multiscale modeling for amorphous materials—Mapping atomistic displacements to macroscopic deformation. *Intl. J. Appl. Mech.* **2012**, *4*. [CrossRef]
485. Codina, R. Stabilization of incompressibility and convection through orthogonal sub-scales in finite element methods. *Comput. Methods Appl. Mech. Eng.* **2000**, *190*, 1579–1599. [CrossRef]
486. Castillo, E.; Codina, R. Stabilized stress-velocity-pressure finite element formulations of the Navier-Stokes problem for fluids with non-linear viscosity. *Comput. Methods Appl. Mech. Eng.* **2014**, *279*, 554–578. [CrossRef]
487. Castillo, E.; Codina, R. Variational multi-scale stabilized formulations for the stationary three-field incompressible viscoelastic flow problem. *Comput. Methods Appl. Mech. Eng.* **2014**, *279*, 579–605. [CrossRef]
488. Koo, B.; Subramanian, N.; Chattopadhyay, A. Molecular dynamics study of brittle fracture in epoxy-based thermoset polymer. *Compos. Part B* **2016**, *95*, 433–439. [CrossRef]
489. Büyüköztürk, O.; Buehler, M.J.; Lau, D.; Tuakta, C. Structural solution using molecular dynamics: Fundamentals and a case study of epoxy-silica interface. *Int. J. Solids Struct.* **2011**, *48*, 2131–2140. [CrossRef]
490. Jo, W.H.; Yang, J.S. Molecular simulation approaches for multiphase polymer systems. In *Molecular Simulation Fracture Gel Theory*; Springer: Berlin, Germany, 2002.
491. Li, C.; Chou, T.-W. Elastic moduli of multi-walled carbon nanotubes and the effect of van der Waals forces. *Compos. Sci. Technol.* **2003**, *63*, 1517–1524. [CrossRef]
492. Li, C.; Chou, T.-W. Multiscale modeling of compressive behavior of carbon nanotube/polymer composites. *Compos. Sci. Technol.* **2006**, *66*, 2409–2414. [CrossRef]
493. Montazeri, A.; Naghdabadi, R. Study the effect of viscoelastic matrix model on the stability of CNT/polymer composites by multiscale modeling. *Polym. Compos.* **2009**, *30*, 1545–1551. [CrossRef]
494. De, S.; Fish, J.; Shephard, M.S.; Keblinski, P.; Kumar, S.K. Multiscale modeling of polymer rheology. *Phys. Rev. E* **2006**, *74*, 30801. [CrossRef] [PubMed]
495. Guenza, M.G. Advancements in multi scale modeling: Adaptive resolution simulations and related issues. *Eur. Phys. J.* **2015**, *224*, 2491–2495. [CrossRef]
496. Kreis, K.; Fogarty, A.C.; Kremer, K.; Potestio, R. Advantages and challenges in coupling an ideal gas to atomistic models in adaptive resolution simulations. *Eur. Phys. J.* **2015**, *224*, 2289–2304. [CrossRef]

497. Zavadlav, J.; Podgornik, R.; Praprotnik, M. Adaptive resolution simulation of a DNA molecule in salt solution. *J. Chem. Theory Comput.* **2015**, *11*, 5035–5044. [CrossRef] [PubMed]
498. Wang, H.; Agarwal, A. Adaptive resolution simulation in equilibrium and beyond. *Eur. Phys. J.* **2015**, *224*, 2269–2287. [CrossRef]
499. Youn Park, J.; Park, C.-H.; Shin Park, J.; Kong, K.-J.; Chang, H.; Im, S. Multiscale computations for carbon nanotubes based on a hybrid QM/QC (quantum mechanical and quasicontinuum) approach. *J. Mech. Phys. Solids* **2010**, *58*, 86–102. [CrossRef]
500. Praprotnik, M.; Delle Site, L.; Kremer, K. A macromolecule in a solvent: Adaptive resolution molecular dynamics simulation. *J. Chem. Phys.* **2007**, *126*, 134902. [CrossRef] [PubMed]
501. Nielsen, S.O.; Srinivas, G.; Klein, M.L. Incorporating a hydrophobic solid into a coarse grain liquid framework: Graphite in an aqueous amphiphilic environment. *J. Chem. Phys.* **2005**, *123*, 124907. [CrossRef] [PubMed]
502. Praprotnik, M.; Delle Site, L.; Kremer, K. Adaptive resolution molecular-dynamics simulation: Changing the degrees of freedom on the fly. *J. Chem. Phys.* **2005**, *123*. [CrossRef] [PubMed]
503. Praprotnik, M.; Delle Site, L.; Kremer, K. Adaptive resolution scheme for efficient hybrid atomistic-mesoscale molecular dynamics simulations of dense liquids. *Phys. Rev. E* **2006**, *73*. [CrossRef] [PubMed]
504. Praprotnik, M.; Matysiak, S.; Site, L.D.; Kremer, K.; Clementi, C. Adaptive resolution simulation of liquid water. *J. Phys.* **2007**, *19*. [CrossRef]
505. Praprotnik, M.; Site, L.D.; Kremer, K. Multiscale simulation of soft matter: From scale bridging to adaptive resolution. *Annu. Rev. Phys. Chem.* **2008**, *59*, 545–571. [CrossRef] [PubMed]
506. Praprotnik, M.; Poblete, S.; Delle Site, L.; Kremer, K. Comment on "adaptive multiscale molecular dynamics of macromolecular fluids". *Phys. Rev. Lett.* **2011**, *107*. [CrossRef] [PubMed]
507. Delle Site, L.; Leon, S.; Kremer, K. BPA-PC on a Ni(111) Surface: The Interplay between Adsorption Energy and Conformational Entropy for Different Chain-End Modifications. *J. Am. Chem. Soc.* **2004**, *126*, 2944–2955. [CrossRef] [PubMed]
508. Fritsch, S.; Poblete, S.; Junghans, C.; Ciccotti, G.; Delle Site, L.; Kremer, K. Adaptive resolution molecular dynamics simulation through coupling to an internal particle reservoir. *Phys. Rev. Lett.* **2012**, *108*. [CrossRef] [PubMed]
509. Delle Site, L. Some fundamental problems for an energy-conserving adaptive-resolution molecular dynamics scheme. *Phys. Rev. E* **2007**, *76*. [CrossRef] [PubMed]
510. Poma, A.B.; Delle Site, L. Classical to path-integral adaptive resolution in molecular simulation: Towards a smooth quantum-classical coupling. *Phys. Rev. Lett.* **2010**, *104*. [CrossRef] [PubMed]
511. Fritsch, S.; Junghans, C.; Kremer, K. Structure formation of toluene around C60: Implementation of the adaptive resolution scheme (AdResS) into GROMACS. *J. Chem. Theory Comput.* **2012**, *8*, 398–403. [CrossRef] [PubMed]
512. Poblete, S.; Praprotnik, M.; Kremer, K.; Delle Site, L. Coupling different levels of resolution in molecular simulations. *J. Chem. Phys.* **2010**, *132*. [CrossRef] [PubMed]
513. Mukherji, D.; van der Vegt, N.; Kremer, K. Preferential solvation of triglycine in aqueous urea: An open boundary simulation approach. *J. Chem. Theory Comput.* **2012**, *8*, 3536–3541. [CrossRef] [PubMed]
514. Lambeth, B.P., Jr.; Junghans, C.; Kremer, K.; Clementi, C.; Site, L.D. Communication: On the locality of Hydrogen bond networks at hydrophobic interfaces. *J. Chem. Phys.* **2010**, *133*, 221101. [CrossRef] [PubMed]
515. Poma, A.B.; Site, L.D. Adaptive resolution simulation of liquid para-hydrogen: Testing the robustness of the quantum-classical adaptive coupling. *Phys. Chem. Chem. Phys.* **2011**, *13*, 10510–10519. [CrossRef] [PubMed]
516. Potestio, R.; Delle Site, L. Quantum locality and equilibrium properties in low-temperature parahydrogen: A multiscale simulation study. *J. Chem. Phys.* **2012**, *136*, 54101. [CrossRef] [PubMed]
517. Mukherji, D.; van der Vegt, N.; Kremer, K.; Delle Site, L. Kirkwood-buff analysis of liquid mixtures in an open boundary simulation. *J. Chem. Theory Comput.* **2012**, *8*, 375–379. [CrossRef] [PubMed]
518. Mukherji, D.; Kremer, K. Coil-globule-coil transition of PNIPAm in aqueous methanol: Coupling all-atom simulations to semi-grand canonical coarse-grained reservoir. *Macromolecules* **2013**, *46*, 9158–9163. [CrossRef]
519. Agarwal, A.; Zhu, J.; Hartmann, C.; Wang, H.; Site, L.D. Molecular dynamics in a grand ensemble: Bergmann-Lebowitz model and adaptive resolution simulation. *New J. Phys.* **2015**, *17*. [CrossRef]
520. Wang, H.; Hartmann, C.; Schütte, C.; Site, L.D. Grand-canonical-like molecular-dynamics simulations by using an adaptive-resolution technique. *Phys. Rev. X* **2013**, *3*. [CrossRef]

521. Nielsen, S.O.; Moore, P.B.; Ensing, B. Adaptive multiscale molecular dynamics of macromolecular fluids. *Phys. Rev. Lett.* **2010**, *105*. [CrossRef] [PubMed]
522. Heyden, A.; Truhlar, D.G. Conservative algorithm for an adaptive change of resolution in mixed atomistic/coarse-grained multiscale simulations. *J. Chem. Theory Comput.* **2008**, *4*, 217–221. [CrossRef] [PubMed]
523. Park, J.H.; Heyden, A. Solving the equations of motion for mixed atomistic and coarse-grained systems. *Mol. Simul.* **2009**, *35*, 962–973. [CrossRef]
524. Potestio, R.; Fritsch, S.; Español, P.; Delgado-Buscalioni, R.; Kremer, K.; Everaers, R.; Donadio, D. Hamiltonian adaptive resolution simulation for molecular liquids. *Phys. Rev. Lett.* **2013**, *110*. [CrossRef] [PubMed]
525. Potestio, R.; Español, P.; Delgado-Buscalioni, R.; Everaers, R.; Kremer, K.; Donadio, D. Monte carlo adaptive resolution simulation of multicomponent molecular liquids. *Phys. Rev. Lett.* **2013**, *111*. [CrossRef] [PubMed]
526. Voter, A.F. A method for accelerating the molecular dynamics simulation of infrequent events. *J. Chem. Phys.* **1996**, *106*, 4665–4677. [CrossRef]
527. Voter, A.F. Hyperdynamics: Accelerated molecular dynamics of infrequent events. *Phys. Rev. Lett.* **1997**, *78*, 3908–3911. [CrossRef]
528. Voter, A.F.; Montalenti, F.; Germann, T.C. Extending the time scale in atomistic simulation of materials. *Annu. Rev. Mater. Sci.* **2002**, *32*, 321–346. [CrossRef]
529. Voter, A.F. Parallel replica method for dynamics of infrequent events. *Phys. Rev. B* **1998**, *57*, R13985–R13988. [CrossRef]
530. Sørensen, M.R.; Voter, A.F. Temperature-accelerated dynamics for simulation of infrequent events. *J. Chem. Phys.* **2000**, *112*, 9599–9606. [CrossRef]
531. Hänggi, P.; Talkner, P.; Borkovec, M. Reaction-rate theory: Fifty years after Kramers. *Rev. Mod. Phys.* **1990**, *62*, 251–341. [CrossRef]
532. Elber, R.; Karplus, M. A method for determining reaction paths in large molecules: Application to myoglobin. *Chem. Phys. Lett.* **1987**, *139*, 375–380. [CrossRef]
533. Elber, R.; Karplus, M. Multiple conformational states of proteins: A molecular dynamics analysis of myoglobin. *Science* **1987**, *235*, 318–321. [CrossRef] [PubMed]
534. Elber, R.; Ghosh, A.; Cárdenas, A. Long time dynamics of complex systems. *Acc. Chem. Res.* **2002**, *35*, 396–403. [CrossRef] [PubMed]
535. Dellago, C.; Bolhuis, P.G.; Csajka, F.S.; Chandler, D. Transition path sampling and the calculation of rate constants. *J. Chem. Phys.* **1998**, *108*, 1964–1977. [CrossRef]
536. Brooks, B.R.; Brooks, C.L., III; MacKerell, A.D., Jr.; Nilsson, L.; Petrella, R.J.; Roux, B.; Won, Y.; Archontis, G.; Bartels, C.; Boresch, S.; et al. CHARMM: The biomolecular simulation program. *J. Comput. Chem.* **2009**, *30*, 1545–1614. [CrossRef] [PubMed]
537. Christen, M.; van Gunsteren, W.F. On searching in, sampling of, and dynamically moving through conformational space of biomolecular systems: A review. *J. Comput. Chem.* **2008**, *29*, 157–166. [CrossRef] [PubMed]
538. Escobedo, F.A.; Borrero, E.E.; Araque, J.C. Transition path sampling and forward flux sampling. Applications to biological systems. *J. Phys. Condens. Matter* **2009**, *21*. [CrossRef] [PubMed]
539. Klenin, K.; Strodel, B.; Wales, D.J.; Wenzel, W. Modelling proteins: Conformational sampling and reconstruction of folding kinetics. *Biochim. Biophys. Acta Proteins Proteomics* **2011**, *1814*, 977–1000. [CrossRef] [PubMed]
540. E, W.; Ren, W.; Vanden-Eijnden, E. Finite temperature string method for the study of rare events. *J. Phys. Chem. B* **2005**, *109*, 6688–6693. [CrossRef] [PubMed]
541. Vanden-Eijnden, E.; Ren, W.; Vanden-Eijnden, E. Transition pathways in complex systems: Reaction coordinates, isocommittor surfaces, and transition tubes. *Chem. Phys. Lett.* **2005**, *413*, 242–247.
542. Weinan, E.; Vanden-Eijnden, E. Transition-path theory and path-finding algorithms for the study of rare events. *Annu. Rev. Phys. Chem.* **2010**, *61*, 391–420.
543. Ren, W.; Vanden-Eijnden, E.; Maragakis, P.; Vanden-Eijnden, E. Transition pathways in complex systems: Application of the finite-temperature string method to the alanine dipeptide. *J. Chem. Phys.* **2005**, *123*, 134109. [CrossRef] [PubMed]
544. Passerone, D.; Parrinello, M. Action-derived molecular dynamics in the study of rare events. *Phys. Rev. Lett.* **2001**, *87*, 108302. [CrossRef] [PubMed]

545. Branduardi, D.; Gervasio, F.L.; Parrinello, M. From A to B in free energy space. *J. Chem. Phys.* **2007**, *126*. [CrossRef] [PubMed]
546. Dellago, C.; Bolhuis, P.G. Transition path sampling and other advanced simulation techniques for rare events. In *Advanced Computer Simulation Approaches for Soft Matter Sciences III*; Springer: Berlin, Germany, 2009.
547. Dellago, C.; Bolhuis, P.G.; Geissler, P.L. Transition path sampling. *Annu. Rev. Phys. Chem.* **2002**, *53*, 291–318.
548. Schwetlick, H.; Zimmer, J. Calculation of long time classical trajectories: Algorithmic treatment and applications for molecular systems. *J. Chem. Phys.* **2009**, *130*. [CrossRef] [PubMed]
549. Wales, D.J. Discrete path sampling. *Mol. Phys.* **2002**, *100*, 3285–3305. [CrossRef]
550. Zaloj, V.; Elber, R. Parallel computations of molecular dynamics trajectories using the stochastic path approach. *Comput. Phys. Commun.* **2000**, *128*, 118–127. [CrossRef]
551. Laio, A.; Parrinello, M. Escaping free-energy minima. *Proc. Natl. Acad. Sci. USA* **2002**, *99*, 12562–12566. [CrossRef] [PubMed]
552. Kamerlin, S.; Vicatos, S.; Dryga, A.; Warshel, A. Coarse-grained (multiscale) simulations in studies of biophysical and chemical systems. *Annu. Rev. Phys. Chem.* **2011**, *62*, 41–64. [CrossRef] [PubMed]
553. Neri, M.; Anselmi, C.; Cascella, M.; Maritan, A.; Carloni, P. Coarse-grained model of proteins incorporating atomistic detail of the active site. *Phys. Rev. Lett.* **2005**, *95*. [CrossRef] [PubMed]
554. Van Gunsteren, W.F.; Bakowies, D.; Baron, R.; Chandrasekhar, I.; Christen, M.; Daura, X.; Gee, P.; Geerke, D.P.; Glättli, A.; Hünenberger, P.H.; et al. Biomolecular modeling: Goals, problems, perspectives. *Angew. Chem. Int. Ed.* **2006**, *45*, 4064–4092. [CrossRef] [PubMed]
555. Tuckerman, M.E.; Martyna, G.J.; Berne, B.J. Molecular dynamics algorithm for condensed systems with multiple time scales. *J. Chem. Phys.* **1990**, *93*, 1287–1291. [CrossRef]

Key Engineering Materials Vols. 651-653 (2015) pp 533-538
© (2015) Trans Tech Publications, Switzerland
doi:10.4028/www.scientific.net/KEM.651-653.533

Submitted: 2014-11-28
Accepted: 2015-01-21
Online: 2015-07-10

Multiscale Simulation of Polymer Nanocomposites in Processing: Challenges and Outlooks

Ali Gooneie[1, a *], Hannelore Mattausch[1, b], Andreas Witschnigg[1, c], Stephan Schuschnigg[1, d], Clemens Holzer[1, e]

[1]Chair of Polymer Processing, Department of Polymer Engineering and Science, Montanuniversitaet Leoben, Leoben, Austria

[a]Ali.Gooneie@unileoben.ac.at, [b]Hannelore.Mattausch@unileoben.ac.at, [c]Andreas.Witschnigg@unileoben.ac.at, [d]Stephan.Schuschnigg@unileoben.ac.at, [e]Clemens.Holzer@unileoben.ac.at

Keywords: Multiscale Simulation, Polymer Nanocomposites, Dissipative Particle Dynamics.

Abstract. This paper attempts to address current possibilities in the multiscale simulation of polymer nanocomposites (PNCs) in processing. To provide a comprehensive perspective, a number of PNCs were produced by the incorporation of nanoclays in different polymer matrices. The microstructure evolutions of the simulated counterparts of such systems were studied with and without shear flows in a dissipative particle dynamics (DPD) framework spanning from several nanometers up to a few microns. Transmission electron microscopy (TEM) was utilized to contrast the simulations against the actual nanocomposites. A satisfactory precision was achieved in the build-up of the simulated structures. A significant characteristic of anisometric particles was studied, namely the orientation of the particles due to the imposed flows. It was shown that the orientation of such particles could be well described. Finally, opportunities were addressed for the simulations to carry on to the higher scales.

Introduction

For years, the incorporation of nanoparticles in polymer matrices has been the answer for multiple requirements in polymer industries where the neat polymer cannot satisfy the needs [1]. The strong dependency of macroscale properties on the structure of the complex material followed by the instinctive hierarchy in the structure of such materials provokes the necessity to adopt a multiscale scheme in order to capture a better picture of the involved phenomena. While numerous works have been conducted on the multiscale simulation of thermal, electrical and mechanical properties [4], only a few works are aimed at the characterization of the processing behaviour of such materials [6]. The reason for that is the intricate physics involved in the processing [1]. Not only it results in difficulties in the system description, but also imposes restrictions on the numerical procedures and necessitates high computation power.

Central to the multiscale modeling protocols is the mesoscopic level where material time-space spans from nanometers to micrometers. In order to address the hydrodynamic behaviour of fluids at mesoscale, Hoogerbrugge and Koelman [2] introduced dissipative particle dynamics (DPD) model. This model benefits from a so-called coarse-graining approach which makes it more feasible to apply to the simulation of material behaviour at the mesoscale by considering fewer particles than required in an atomistic molecular dynamics simulation. DPD has been successfully applied to the polymers with a bead-spring description of the chains [4,6,7]. It has also been incorporated to predict the rheology of polymers by the use of the plane Couette flow with Lees-Edwards periodic boundary conditions [6].

In this work, we attempt to show the possibilities of DPD method to model the PNCs and link the atomistic simulations to the macroscale processing. Two important issues are discussed, i.e. prediction of the flow curves of PNCs, and orientation of clay particles under flow. It is shown that with the application of available data from molecular simulations, one can utilize DPD to simulate material behavior for a system of a few hundreds of nanometers. Then, with the benefit of scaling

rules [5], it is possible to use the outputs in an upper scale DPD simulation with a length scale of a few microns. The final results of such a multiscale scheme could serve as reasonable inputs for macroscale simulations.

Experimental

Materials and sample preparation. Polypropylene (PP) was PP BB412E, Borealis, Vienna (Austria). It was mixed with 5 wt% of modified clay in a twin screw extruder at processing conditions of 180 ˚C and 150 rpm.

Polyamide was PA 46 Stanyl TW341, DSM Engineering Plastics Europe (Netherlands). It was mixed with 5 wt% of Nanofil SE 3010 clay, Rockwood Additives (UK), in a twin screw extruder at processing conditions of 290 ˚C and 100 rpm.

Characterization tests. The flow curve of the neat PP was approximated with the application of the Cox-Merz rule to the frequency sweep tests reported before [1]. This method showed satisfactory precision for the PP. The microstructure was studied utilizing TEM according to the procedures explained in [1].

For PA sample, ultrathin sections (90 nm) were cut with a Leica Ultramicrotome UCT equipped with a Reichert FCS cryosystem. Images were taken using a FEI Tecnai G2 20 transmission electron microscope (FEI Eindhoven) with a Gatan ultrascan 1000 ccd camera. Acceleration voltage was 200kV.

Theory and simulation

In DPD method, the time evolution of each particle is dominated by the total interparticle force which is itself a sum of three pairwise, additive forces namely the conservative force (F_{ij}^{C}), the dissipative force (F_{ij}^{D}), and the random force (F_{ij}^{R}). The definitions of these forces are:

$$F_{ij}^{C} = a_{ij}\chi_{ij}\left(1-\frac{r_{ij}}{r_c}\right)\hat{\mathbf{r}}_{ij}. \quad (1)$$

$$F_{ij}^{D} = -\gamma_{ij}\omega^{D}r_{ij}\left[\left(\mathbf{v}_i-\mathbf{v}_j\right)\cdot\hat{\mathbf{r}}_{ij}\right]\hat{\mathbf{r}}_{ij}. \quad (2)$$

$$F_{ij}^{R} = \sigma_{ij}\omega^{R}r_{ij}\xi_{ij}\hat{\mathbf{r}}_{ij}. \quad (3)$$

In these equations, r_{ij} is the distance between the particles *i* and *j*, $\hat{\mathbf{r}}_{ij}$ is the unit vector pointing from the center of particle *j* to that of particle *i*, χ_{ij} equals one for particles with a distance less than the force cutoff radius r_c and equals to zero otherwise. a_{ij} is the maximum repulsion between bead *i* and bead *j*. γ_{ij} and σ_{ij} are the friction coefficient and the noise amplitude between bead *i* and bead *j*, respectively. ω^{D} and ω^{R} are r-dependent weight functions which are usually taken as

$$\omega^{D}(r) = \left[\omega^{R}(r)\right]^2 = \chi_{ij}\left(1-\frac{r_{ij}}{r_c}\right)^2. \quad (4)$$

$\mathbf{v}_i$ and $\mathbf{v}_j$ are the velocity vectors of the *i*th and *j*th beads, respectively. ξ_{ij} is a Gaussian random number with zero mean and unit variance. Excellent descriptions of the DPD method are already given in various papers [2,3]. Therefore, it is not intended to recapitulate the details any further. In this work, the rescaled values from molecular dynamics simulations were used for a_{ij} for all possible pairs, i.e. 25 for polymer-polymer, 33 polymer-clay, and 15 for clay-clay in DPD units [4]. The conventional γ_{ij} for polymer-polymer is 4.5. The flow curve of the polymer was simulated in the nanoscale to ensure that this value is in agreement with our simulations. Afterwards, this setup was rescaled to account for the magnification and further coarse-graining necessary for the microscale simulations of the PNCs. The friction coefficients of the polymer-clay and clay-clay

pairs were determined from the optimization of the flow curves of the nanocomposites at microscale. The scaled-down friction coefficients were approximated to be in good agreement with the proposed value of 5.6 for such pairs [7]. Therefore, the same value was taken to be the correct value here too. One should keep in mind that this value is of minor significance in the hydrodynamic DPD simulations as was pointed out by Chatterjee et al [7]. The systems were simulated at 200 ˚C. The time step for all simulations was set to 0.001.

The simulations were carried out at nano and micro scales. Once, a cubic system with a volume of 1000 in DPD units with a unit length of 20 nm was simulated. The flow curves for polymers with 5 and 20 beads representative of molecular weights of approximately 75,000 g/mol and 300,000 g/mol were determined. Later, a clay molecule with 3 layers was added to the system and sheared in different directions in order to study the orientation of the clay particle under different flow directions and intensities. In an upper scale of simulations, the length scale of the cube was increased to correspond to 200 nm in actual units and thus enabled us to simulate a system with an actual length of 2 microns. The effect of adding different contents of clay on the flow curve of the polymer was examined in a well-dispersed system.

Results and discussion

Flow curve determination. The viscosity of a PP-clay system was probed at different shear rates. At first, PP was modeled with 5- and 20-bead chains. The results are shown in Fig. 1a. It shows a good agreement with the experiments suggesting that with the experimental value for the zero shear rate viscosity, one can predict the full flow curve of the PP melt from DPD simulations. It is shown that a 20-bead chain is a more accurate representative for the PP under study. In Fig. 1b, the viscosity of the PNCs with different clay contents are shown. The characteristic non-Newtonian behavior of PNCs in the low shear rates is well captured. The simulated values are the same for different clay contents. One should note that the microscale DPD systems are based on the well-dispersed PNCs. Therefore, the increase in the clay content doesn't influence the viscosity significantly after the so-called rheological percolation threshold. Indeed, the flow curves of the PP or PNC could be utilized later in FEM or FVM schemes for the macroscale simulations.

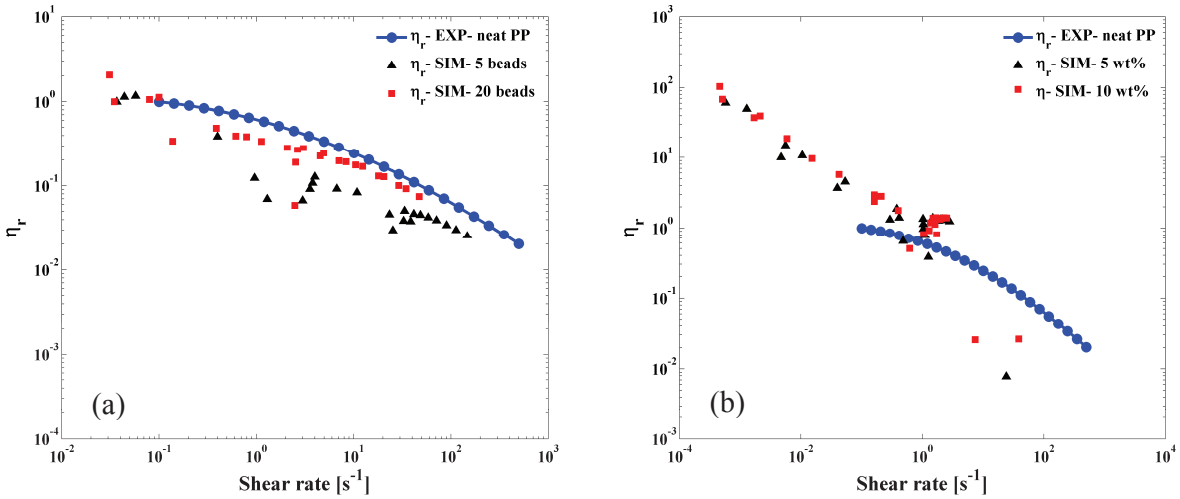

Figure 1. The ratio of the viscosity to the zero shear rate viscosity (η_r) of the PP melt (a) and the PNC with 5 and 10 wt% of clay (b).

Microstructures of PNCs. The PNCs were characterized utilizing TEM in order to depict accurate representations in DPD counterparts. As one can see in Fig. 2, the DPD systems in nano and micro scales are quite capable of describing the actual PNCs utilized in the simulations.

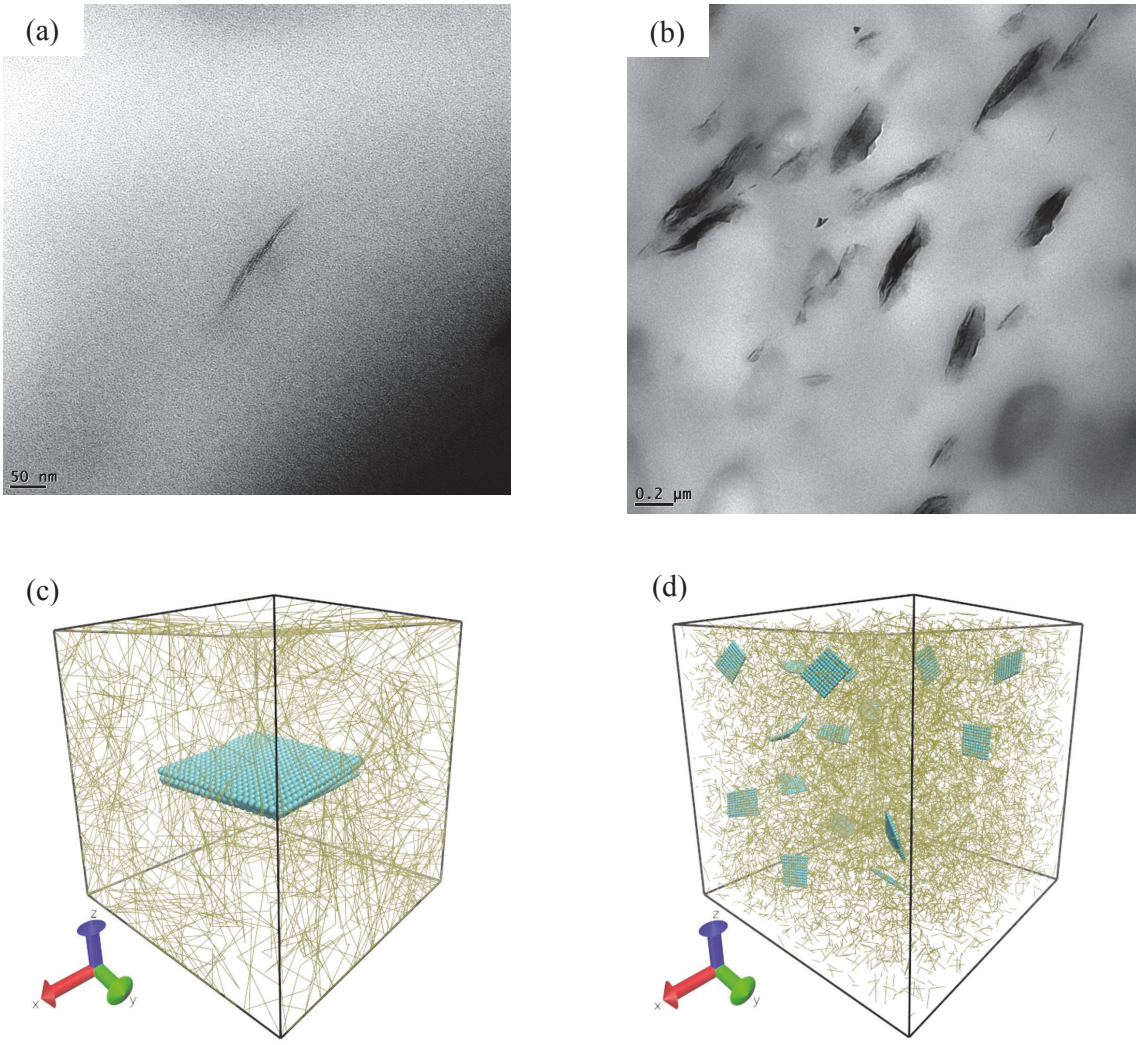

Figure 2. The TEM micrographs of the PP-clay nanocomposites in nano (a) and micro (b) scales and their DPD counterparts (c and d) at comparable length scales.

In PP-based PNCs, the response of a single 3-layered clay particle to the shear flows in different directions was probed. Fig. 3 shows the orientation of the particle in DPD time unit for different flow directions. One can see that the clay aligns according to the flow direction. However, due to the low attractive forces between the polymer chains and the clay layers, almost no increase in the gallery distance is achieved. Simulations at different shear rates showed that the higher shear rates force the clay to orient faster even though still no apparent increase in the exfoliation degree is observed (data not shown here due to space considerations). It further approves the ability of the DPD method to predict the rheology of PNCs and use it at upper simulation scales.

Future work. The incorporation of DPD method at different scales promises an excellent opportunity to pursue multiscale simulation of PNCs in processing. Some of the commercial and academic potential applications could be: (i) applying the method to other commercial polymer-nanoparticle systems such as polyamide-clay, or polyamide-carbon nanotube; (ii) incorporation of compatibilizing agents in the PNCs; (iii) evaluation of the dispersion quality with the help of statistical studies; and (iv) study of aggregates of nanoparticles in PNC systems. Fig.4 is an example for the latter case of such a structure in polyamide-clay systems.

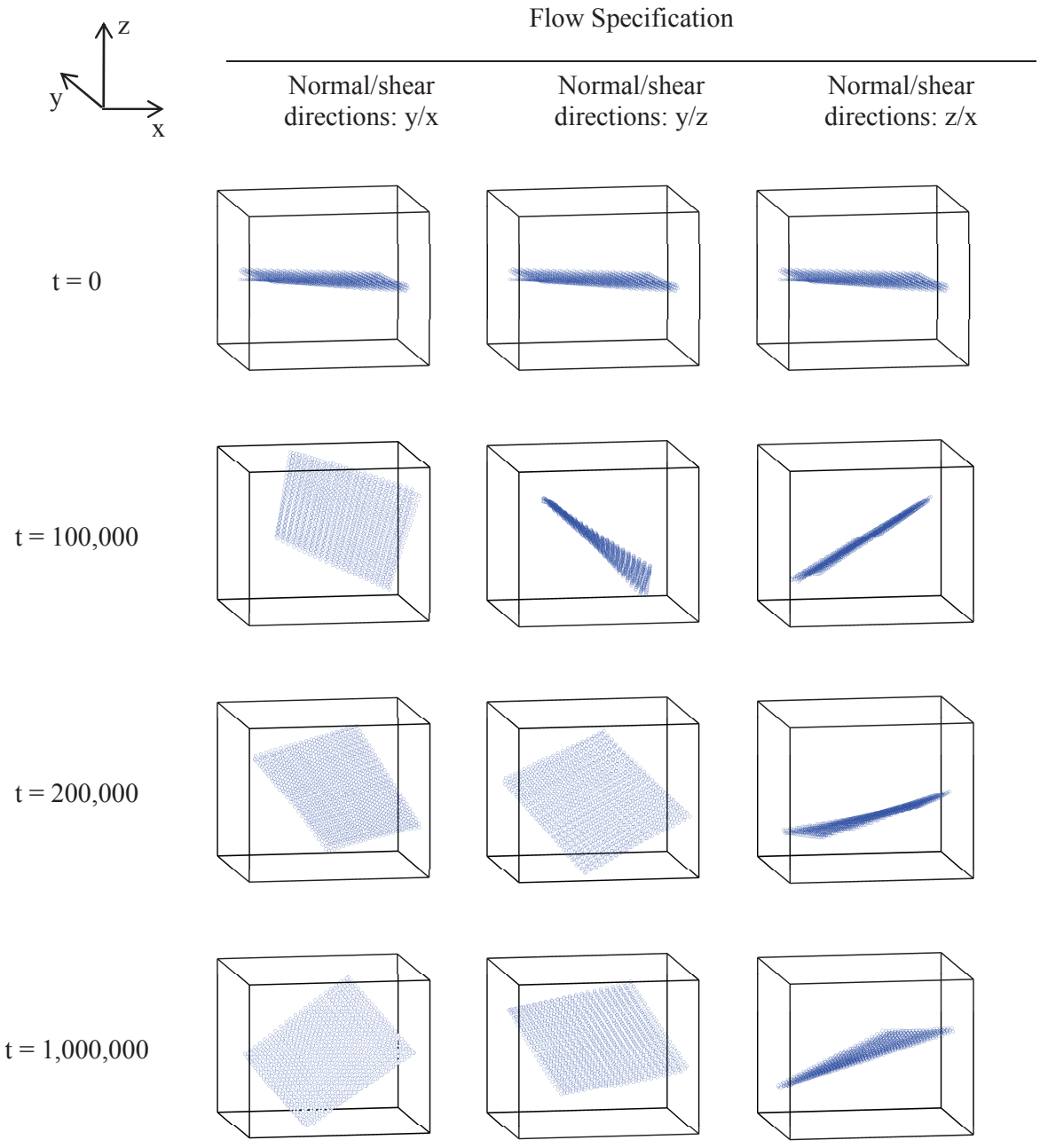

Figure 3. The orientation of a 3-layered clay particle in DPD time steps (t) subject to shear flows in different directions at nanoscale in PP-based PNCs. The shear rate was 0.0176 in DPD units.

Still, the increase in the number of beads at upper scales of simulation necessitates either higher computation power such as the advances in the graphics processing units (GPUs), or development of physical basis to setup the systems with fewer complications as well as good accuracy. Furthermore, in some cases the peculiarities in the physics of a nanoparticle itself introduces difficulties to describe the DPD system with high accuracy. Semiflexible carbon nanotubes with a minimum length of 1 micron and a minimum aspect ratio of 100, are good examples of such difficulties.

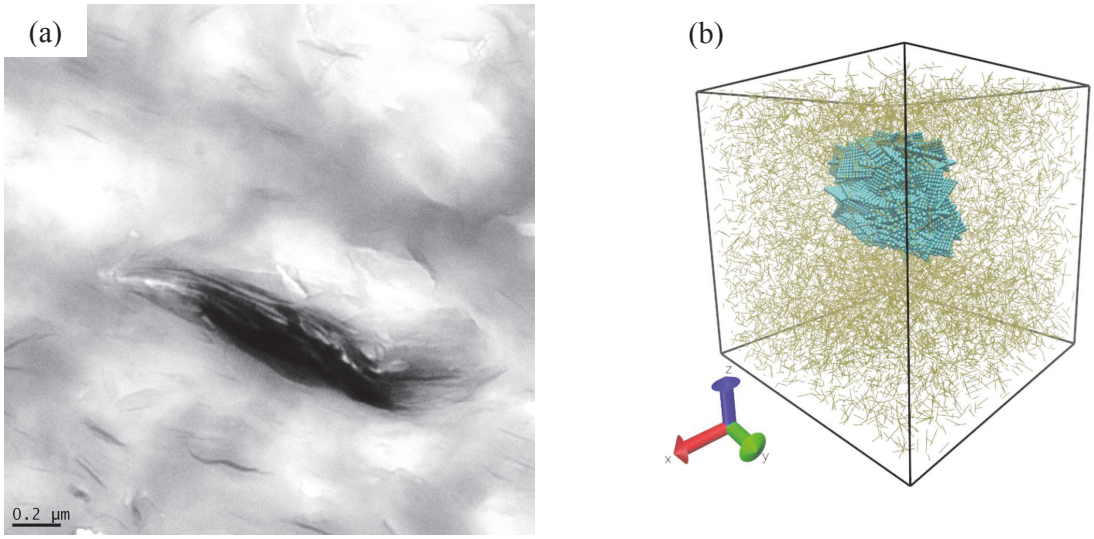

Figure 4. TEM micrograph of an aggregated structure in a polyamide-clay nanocomposite and its counterpart in DPD system.

Conclusion

It was shown that the DPD method is capable to describe PNC systems ranging from several nanometers to a few microns with good accuracy. DPD was used to predict the flow curves of the neat polymer and PNCs. The response of the individual particles to the imposed flows was also described. The application of scaling rules for different coarse-graining degrees makes it possible to use DPD at different length/time scales. The outputs of such simulations such as the viscosity function can be incorporated in FEM or FVM numerical methods at macroscale. Thus, it provides a perfect opportunity to design a multiscale simulation scheme for PNC systems in processing.

References

[1] H. Mattausch, S. Laske, I. Duretek, J. Kreith, G. Maier, C. Holzer, Investigation of the influence of processing conditions on the thermal, rheological and mechanical behavior of polypropylene nanocomposites, Polymer Engineering and Science. (2013) 1001-1010.

[2] P.J. Hoogerbrugge, J.M.V.A. Koelman, Simulating microscopic hydrodynamic phenomena with dissipative particle dynamics, Europhys. Lett. 19 (1992) 155–160.

[3] R.D. Groot, P.B. Warren, Dissipative particle dynamics: Bridging the gap between atomistic and mesoscopic simulation, J. Chem. Phys. 107 (1997) 4423-4435.

[4] G. Scocchi, P. Posocco, M. Fermeglia, S. Pricl, Polymer-clay nanocomposites: A multiscale molecular modeling approach, J. Phys. Chem. B. 111 (2007) 2143-2151.

[5] R.M. Fuechslin, H. Fellermann, A. Eriksson, H.J. Ziock, Coarse graining and scaling in dissipative particle dynamics, J. Chem. Phys. 130 (2009) 214102.

[6] D.A. Fedosov, G.E. Karniadakis, B.Caswell, Steady shear rheometry of dissipative particle dynamics models of polymer fluids in reverse Poiseuille flow, J. Chem. Phys. 132 (2010) 144103.

[7] A. Chatterjee, L.M. Wu, Predicting rheology of suspensions of spherical and non-spherical particles using dissipative particle dynamics (DPD): Methodology and experimental validation, Molecular Simulation. 34 (2008) 243-250.

Material Forming ESAFORM 2015
10.4028/www.scientific.net/KEM.651-653

Multiscale Simulation of Polymer Nanocomposites in Processing: Challenges and Outlooks
10.4028/www.scientific.net/KEM.651-653.533

DOI References
[2] P.J. Hoogerbrugge, J.M.V.A. Koelman, Simulating microscopic hydrodynamic phenomena with dissipative particle dynamics, Europhys. Lett. 19 (1992) 155-160.
http://dx.doi.org/10.1209/0295-5075/19/3/001
[5] R.M. Fuechslin, H. Fellermann, A. Eriksson, H.J. Ziock, Coarse graining and scaling in dissipative particle dynamics, J. Chem. Phys. 130 (2009) 214102.
http://dx.doi.org/10.1063/1.3143976
[6] D.A. Fedosov, G.E. Karniadakis, B. Caswell, Steady shear rheometry of dissipative particle dynamics models of polymer fluids in reverse Poiseuille flow, J. Chem. Phys. 132 (2010) 144103.
http://dx.doi.org/10.1063/1.3366658
[7] A. Chatterjee, L.M. Wu, Predicting rheology of suspensions of spherical and non-spherical particles using dissipative particle dynamics (DPD): Methodology and experimental validation, Molecular Simulation. 34 (2008) 243-250. (a) (b).
http://dx.doi.org/10.1080/08927020801957748

6. Development of Suitable Methods for Multiscale Simulation of Polymer / Layered Silicate Nanocomposites Under Shear Flow

This chapter reports the main results of the thesis. The results are given in three papers as follows:

6.1 Coupled Orientation and Stretching of Chains in Mesoscale Models of Polydisperse Linear Polymers in Startup of Steady Shear Flow Simulations

[Gooneie A., Schuschnigg S., Holzer C.: Coupled orientation and stretching of chains in mesoscale models of polydisperse linear polymers in startup of steady shear flow simulations, Macromolecular Theory and Simulations 25 (2), 2016, pp. 170–186]

In this paper, the orientation of linear polymer chains is studied under applied shear flows.

6.2 Orientation of Anisometric Layered Silicate Particles in Uncompatibilized and Compatibilized Polymer Melts Under Shear Flow: A Dissipative Particle Dynamics Study

[Gooneie A., Schuschnigg S., Holzer C.: Orientation of anisometric layered silicate particles in uncompatibilized and compatibilized polymer melts under shear flow: A dissipative particle dynamics study, Macromolecular Theory and Simulations 25 (1), 2016, pp. 85–98]

The orientation of layered silicates subject to various shear flows is simulated in this paper. The interactions between components are particularly highlighted.

6.3 Dissipative Particle Dynamics Models of Orientation of Weakly-Interacting Anisometric Silicate Particles in Polymer Melts under Shear Flow: Comparison with the Standard Orientation Models

[Gooneie A., Schuschnigg S., Holzer C.: Dissipative particle dynamics models of orientation of weakly-interacting anisometric silicate particles in polymer melts under shear flow: comparison with the standard orientation models, Macromolecular Theory and Simulations 25 (3), 2016, pp. 287–302]

The strain-dependent upscaling strategy for the orientation process in developed and tested against available standard rheological models.

Coupled Orientation and Stretching of Chains in Mesoscale Models of Polydisperse Linear Polymers in Startup of Steady Shear Flow Simulations

Ali Gooneie,* Stephan Schuschnigg, Clemens Holzer

Polydisperse linear polymers are studied in startup of steady shear flow simulations using dissipative particle dynamics. The results show that with an increase in polydispersity the stress overshoot declines while the steady-state stress increases. Various physical characteristics of the systems are studied including frequency of nonbonded interactions, gyration radius data, flow alignment angles, and average bond lengths. The patterns in the data suggest higher forces are necessary to orient and stretch long chain fractions in the flow direction. Relaxation modulus data prove the broad range of relaxation mechanisms in polydisperse systems. Linear viscoelasticity theory is used to quantify the relaxation spectrum. The results indicate an increase in the longest relaxation time in systems with higher polydispersity. The steady-state shear viscosity results show higher viscosities with an increase in polydispersity at all shear-rates. The good agreement of the characteristic behaviors of modeled polydisperse polymers with experiments is encouraging for future work.

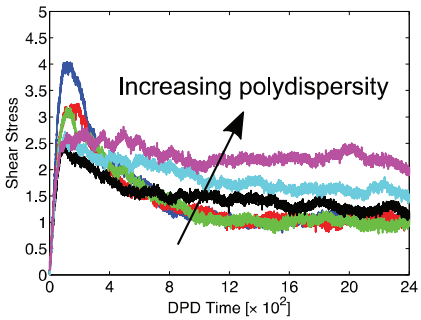

1. Introduction

It is well-established that the final properties of extruded films and spun fibers are strongly dependent on the molecular characteristics of the polymer.[1–4] The orientation and crystallization during processing are two of the most influencing phenomena. These features have complicated correlations with melt rheological properties as well as molecular variables such as molecular weight and molecular weight distribution. It has been shown that the molecular weight and its distribution change the flow behavior of the polymer melt.[5] Fujiyama et al.[6] provide a comprehensive experimental work on the rheological properties of poly(propylene)s with different molecular weight distributions. According to their results many of the rheological properties depend on the polydispersity including the end correlation coefficient in capillary flow, the die swell ratio, the critical shear-rate and shear stress for the onset of melt fracture, the zero-shear viscosity, the characteristic relaxation time, and the oscillatory storage and loss moduli. The influence of polydispersity is not only limited to these properties. It also affects the flow patterns of the melt even in the simplest geometries. Studies have shown that a highly monodisperse sample partitions into two fractions with different local shear-rates in a sliding plate rheometer.[7] The polydisperse sample possesses a smooth spatial variation of the local shear-rates in the same experimental setup. Other reports on the polydisperse

A. Gooneie, S. Schuschnigg, Prof. C. Holzer
Department of Polymer Engineering and Science
Montanuniversität Leoben
Otto Glöckel-Straße 2, 8700 Leoben, Austria
E-mail: ali.gooneie@unileoben.ac.at

Macromol. Theory Simul. **2016**, *25*, 170–186

DOI: 10.1002/mats.201500060

samples in cone-plate geometry also show a heterogeneous shear flow during startup of shear flow experiments.[8,9] As a result, modeling strategies starting from molecules and chains up to the processing scale are necessary in order to fully understand the phenomena.[10–14] Unfortunately, this is not a simple procedure and takes plenty of resources to achieve.

Direct consequences of the polydispersity on the microstructure of the processed parts have been an interesting topic due to its commercial applications. Bashir et al.[4] performed experimental investigations to study the influence of the polydispersity on the microstructural evolutions in melt extruded polyethylene fibers. Their results proved the significance of high molecular weight fractions in the formation of extended chain fibrils in row nucleated structures. Studies on the structural development and crystallization kinetics of melt spun poly(propylene) filaments have shown the strong influence of the polydispersity on such characteristics. For instance, the crystallinity is found to increase with higher polydispersity at a constant set of spinning conditions.[15] It has been suggested that polydispersity influences the structure and properties of poly(propylene) mainly by the ability of high molecular weight fractions to promote stress-induced crystallization during the processing. Moreover, the effect of these long chains on the elongational viscosity is of critical importance. Yu and Wilkes[1–3] investigated the structural features in the extruded films of two high density polyethylene resins with different molecular weight distributions. They suggested that the relaxation behavior of an oriented polymer melt is the dominating parameter. The presence of fiber nuclei in the resin with the broad molecular weight distribution was evident while it was missing in the sample with narrow distribution. These fiber nuclei were suggested to be due to the longer relaxation behavior of the broad sample. They further performed melt rheological experiments on the resins to understand the effect of the molecular weight distribution on the melt relaxation time behavior. The results showed that by adjusting the extrusion variables one can control the relaxation time behavior. It further led to the possibility of processing extruded films from each of the resins with and without the presence of fiber nuclei structure. Other authors have also tested polymers with a more complex backbone structure. Plog et al.[16] studied blends of methylhydroxyethyl cellulose with similar weight-averaged molecular weight but varying molecular weight distributions. Utilizing a combination of size exclusion chromatography, multiangle laser scattering, and differential refractometery, they determined that the relaxation times were dependent on the polydispersity. They also found that the longest relaxation time of the polymers in uniaxial elongation in capillary break extensional rheometer increases with polydispersity.

Such studies prove that a deep knowledge of the effects of polydispersity on the microstructural evolutions could result in achieving favored final properties. However, it is not always easy to study the nature of different molecular weight fractions in a polydisperse polymer in an experimental framework. For this reason, the computer simulation techniques are the best candidates to perform detailed studies. However, it is unfortunate that no comprehensive work has been devoted to the study of polydisperse polymers. There are rare instances found in the literature. For instance, Rorrer and Dorgan[17] investigate the confined polydisperse polymers in a Monte Carlo study and revealed profound influences of polydispersity on the behavior of the systems.

Over the past few years, dissipative particle dynamics (DPD) has been developed as an attractive numerical technique capable of capturing both thermodynamics and hydrodynamics of complex systems. DPD is a particle-based coarse-grained mesoscopic method proposed by Hoogerbrugge and Koelman[18] in which particles interact through soft potentials. This will enable access to longer time scales. DPD implicitly accounts for hydrodynamic interactions by employing velocity-dependent dissipative forces. With the introduction of the Lees–Edwards boundary conditions, DPD has been successfully applied to study the dynamic behavior of a variety of complex fluids such as polymer solutions,[19] entangled linear polymer melts,[20–22] surfactant solutions,[23] suspensions of spherical and nonspherical particles,[24–26] etc. The agreement between the results of DPD and experiments is promising for this broad range of systems.

The purpose of this study is to provide detailed analyses of characteristic polydisperse linear polymers with tailored chain length distributions modeled in a DPD framework. We focus on the orientation and stretching of chains of different fractions in the bulk and relate it to the transient and steady-state shear rheological properties. Furthermore, the contributions of bonded and nonbonded interactions to the overall flow characteristics are discussed. The formation of the oriented microstructure in the systems is investigated. Moreover, the relaxation behaviors of the systems are studied. Analyses of this kind are extremely hard to perform in experiments if not impossible. The results of this work will enable us to understand the underlying mechanisms of the oriented microstructure formation in extruded films, spun fiber, etc. during processing from monodisperse and polydisperse linear polymers.

2. Simulation Details

2.1. Description of the Model

In the DPD simulation method, a set of particles move according to Newton's equation of motion.[27–30]

These particles, or beads, interact through simplified force laws. The forces acting on the beads are pairwise and additive. They are the conservative force (F_{ij}^{C}), the dissipative force (F_{ij}^{D}), and the random force (F_{ij}^{R}). The conservative force is a soft repulsion given by

$$F_{ij}^{C} = a_{ij}\chi_{ij}\left(1-\frac{r_{ij}}{r_c}\right)\hat{\boldsymbol{r}}_{ij} \quad (1)$$

where r_{ij} is the distance between the beads i and j, $\hat{\boldsymbol{r}}_{ij}$ is the unit vector pointing from the center of bead j to that of bead i, χ_{ij} equals 1 for beads with a distance less than the force cutoff radius r_c and equals 0 otherwise. a_{ij} is the maximum repulsion between bead i and bead j. The other two forces are responsible for the conservation of the total momentum in the system and are given by

$$F_{ij}^{D} = -\gamma_{ij}\omega^{D}r_{ij}\left[\left(\boldsymbol{v}_i-\boldsymbol{v}_j\right)\times\hat{\boldsymbol{r}}_{ij}\right]\hat{\boldsymbol{r}}_{ij} \quad (2)$$

$$F_{ij}^{R} = \sigma_{ij}\omega^{R}r_{ij}\xi_{ij}\hat{\boldsymbol{r}}_{ij} \quad (3)$$

Here, γ_{ij} and σ_{ij} are the friction coefficient and the noise amplitude between bead i and bead j, respectively. ω^{D} and ω^{R} are r_{ij}-dependent weight functions. The system obeys the fluctuation–dissipation theorem in which one of the two weight functions fixes the other one.[31] This theory necessitates that

$$\omega^{D}\left(r_{ij}\right)=\left[\omega^{R}\left(r_{ij}\right)\right]^2 \quad (4)$$

$$\sigma_{ij}^2=2\gamma_{ij}k_BT \quad (5)$$

In our simulations, the weight functions are defined as

$$\omega^{D}\left(r_{ij}\right)=\left[\omega^{R}\left(r_{ij}\right)\right]^2=\chi_{ij}\left(1-\frac{r_{ij}}{r_c}\right)^2 \quad (6)$$

$\boldsymbol{v}_i$ and $\boldsymbol{v}_j$ are the velocity vectors of the ith and jth beads, respectively. ξ_{ij} is a Gaussian random number with zero mean and unit variance. Recently, some modifications for standard DPD formulation have been proposed. Pan et al.[24] developed a new formulation of DPD in the spirit of fluid particle model. They divided the dissipative forces explicitly into central and shear components. In this way, they could redistribute and balance these forces to obtain the correct hydrodynamics in the study of Brownian colloidal suspensions. Yamanoi et al.[20] used entanglement forces instead of conservative forces in order to capture the physics of entangled polymer melts. They were able to reproduce both static and dynamic properties of linear polymer systems.

In this work, the standard DPD formulation was incorporated in order to run the simulations. Length, mass, and energy are in units of the force cutoff radius, mass of a single DPD bead, and k_BT, respectively, where k_B is Boltzmann's constant and T is the absolute temperature. All of these variables were set to unity in our simulations. The maximum repulsion parameter between beads has been set to 25 to comply with the compressibility of water molecules.[27,28] The friction coefficients were all set to 4.5 which is a typical value for polymer systems. Each flexible polymer chain was comprised of a finite number of beads linked together using harmonic springs with spring constant of 50 and equilibrium length of 1. This setup should reduce unphysical bond crossings to some extent.[32] However, they still occur in the models and we were not able to completely remove them from the models due to the reasons explained later on.

Chains with different lengths were mixed together to study polydispersity effects in the model systems. To characterize polydisperse systems, the number- and weight-averaged lengths ($\bar{L}_n$ and $\bar{L}_w$, respectively) of a system were defined using similar formulations to the typical number- and weight-averaged molecular weights ($\bar{M}_n$ and $\bar{M}_w$, respectively). They are $\bar{L}_n=\frac{\sum n_iN_i}{\sum n_i}$ and $\bar{L}_w=\frac{\sum n_iN_i^2}{\sum n_iN_i}$ with n_i as the number of chains and N_i as the number of beads in ith fraction of chains in a system. Polydispersity index (PDI) was defined by $\mathrm{PDI}=\frac{\bar{L}_w}{\bar{L}_n}$. The length distributions were produced in a way that $\bar{L}_n$ and the total number of beads should equal to predefined values. For $\bar{L}_n$, the defined values of 20, 50, and 100 were selected. The total number of beads was set to generate a system with a bead number density of 3. At first, beta and normal probability distribution functions were incorporated to generate length polydispersity. The polydispersity was modified by tuning the parameters of the probability functions. The produced length distributions in this manner are shown in Figures 1–3. While this approach is simple and fast, it is very difficult to produce systems with high PDI values. Therefore, systems with high PDIs were designed manually. The length distributions of the resulting systems are depicted in Figure 3. The nomenclature and specific characteristics of all systems are listed in Table 1.

The computational domain was set to $20 \times 20 \times 20$ in DPD length units. The chains were allowed to equilibrate before starting the flow for 5×10^4 time steps. The shear flow was applied by the incorporation of Lees–Edwards boundary conditions. This boundary condition applies a no-slip condition on the walls normal to the velocity gradient direction. For the other walls, periodic boundary conditions are set. The stress tensor in the form of components is calculated from simulations using the virial theorem.[33] This method has been successfully utilized before in DPD simulations of steady shear properties of polymer fluids with Lees–Edwards boundary conditions.[34] The applied shear-rates were

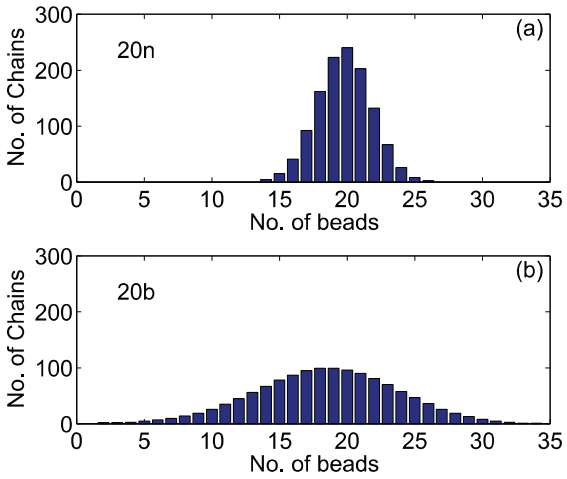

Figure 1. Length distribution in systems with $\overline{L}_n \approx 20$: a) 20n and b) 20b samples.

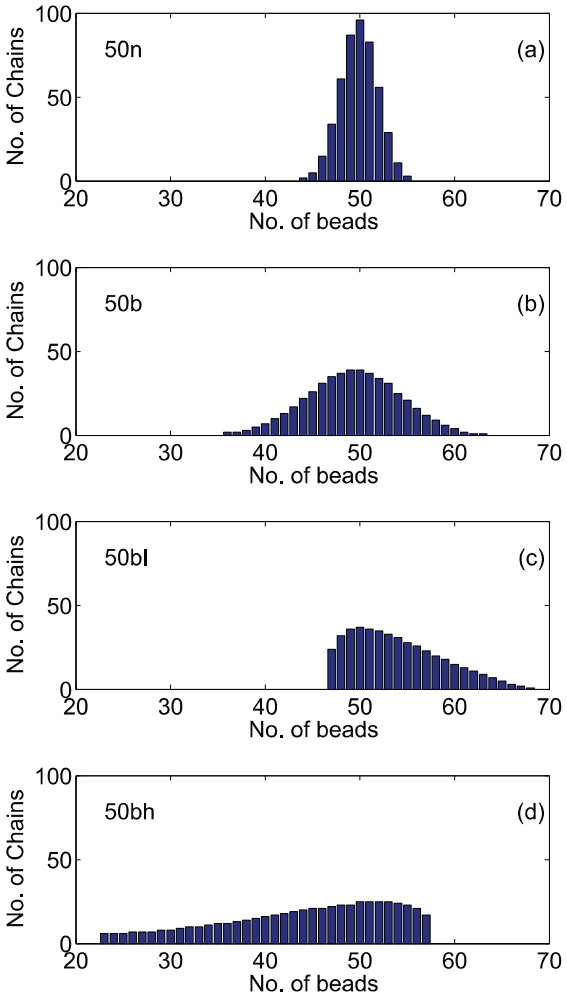

Figure 2. Length distribution in systems with $\overline{L}_n \approx 50$: a) 50n, b) 50b, c) 50bl, and d) 50bh samples.

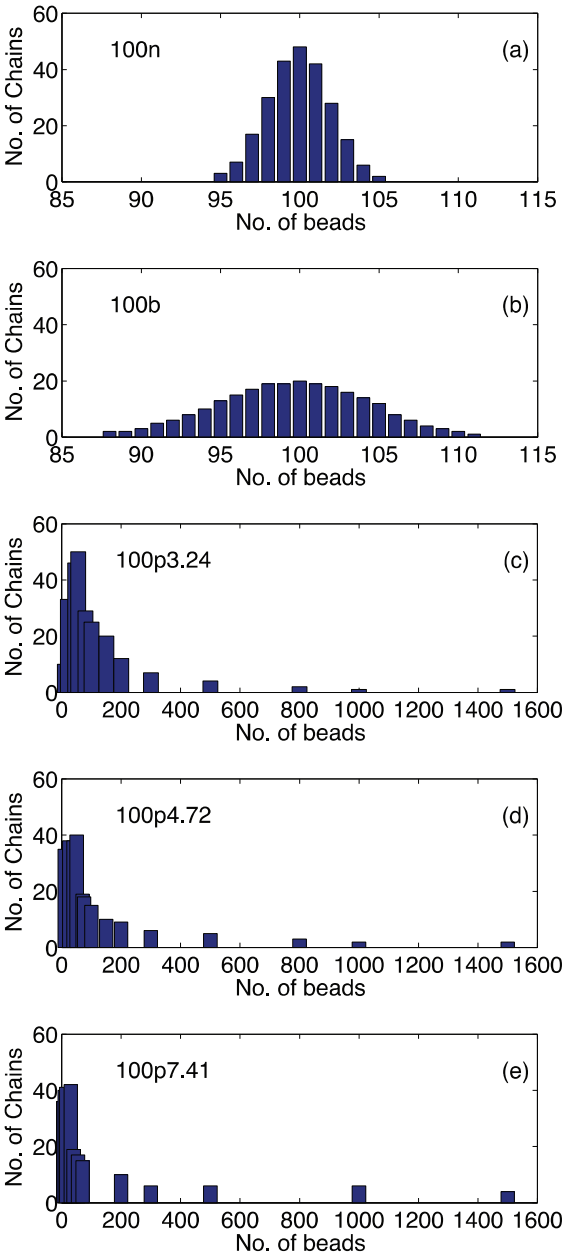

Figure 3. Length distribution in systems with $\overline{L}_n \approx 100$: a) 100n, b) 100b, c) 100p3.24, d) 100p4.72, and e) 100p7.41 samples.

chosen large enough so that the velocity profile is not significantly influenced by thermal fluctuations. Also, it was always noted that this value should not be so large to distort the thermostat and alter the temperature profile. The shear-rate of 0.08 was found to optimally satisfy these criteria and therefore was utilized in most of the simulations. Other shear-rates reported in this paper also showed satisfactory results regarding these conditions however not as well as 0.08. The maximum recorded average temperature in the systems at

Table 1. The nomenclature and specific characteristics of all simulated systems.

Name	$\bar{L}_n$	PDI	Total number of beads	Type of distribution
20	20	1.00	24 000	None
20n	20	1.01	24 017	Normal [$\sigma^{a)} = 2$]
20b	19	1.08	24 007	Normal [$\sigma = 5$]
50	50	1.00	24 000	None
50n	50	1.00	24 033	Normal [$\sigma = 2$]
50b	50	1.01	24 014	Normal [$\sigma = 5$]
50bl	54	1.01	24 001	Re-scaled[b)] beta [$a^{c)} = 1.5$, $b^{d)} = 5$]
50bh	44	1.04	24 046	Re-scaled beta [$a = 5$, $b = 1.5$]
100	100	1.00	24 000	None
100n	100	1.00	24 080	Normal [$\sigma = 2$]
100b	100	1.00	24 081	Normal [$\sigma = 5$]
100p3.24	100	3.24	24 000	Manual
100p4.72	100	4.72	24 000	Manual
100p7.41	99	7.41	24 000	Manual
300	300	1.00	24 000	None
500	500	1.00	24 000	None
1000	1000	1.00	24 000	None

[a)] σ is the standard deviation; [b)]The original beta distribution is nonzero only on the interval (0,1). Therefore, we had to rescale its values to our desired chain length interval; [c)] a is the first shape parameter of a beta distribution; and [d)] b is the second shape parameter of a beta distribution.

the highest applied shear-rate was almost 1.36 which is fairly close to the set value of 1.

The incorporation of periodic boundary conditions makes it almost impossible to access true coordinates of beads in long runs under flow. Indeed, there is always the possibility to record trajectories in every time step and modify the periodic coordinates knowing their positions and the velocity field. However, the benefit of accelerated calculations will be definitely suppressed in large systems such as the models considered here. In this study, it was necessary to calculate the size and orientation of each chain in time. Fortunately, these parameters are based on the true relative coordinates of the beads in each individual chain rather than on their actual coordinates in time and space. Consequently, the true relative coordinates of beads in each chain were first determined and then used in chain size and orientation calculations. To do that, it was assumed that the first bead in every chain possesses its true relative coordinates at every time step. This is an appropriate assumption considering that (i) it is only necessary to find the true relative coordinates and (ii) the first bead is connected to only one other adjacent bead. Based on the periodic coordinates of the first and second beads, all possible projections of the second bead were found in space. Only one of these projections results in a reasonable bond length (with the first bead) which would also satisfy the minimum bond energy requirement. This projection is set to be the true relative coordinates of the second bead. Other projections lead to a bond length in the orders of the side of the simulation box and produce unstable bonds due to very large bond potentials. In this way, the true relative coordinates of beads in each chain were determined and incorporated in mean gyration radius, nonbonded intramolecular interactions, and segmental orientation calculations.

The simulations were run for 5×10^5 time steps under flow and the beads trajectories recorded. The final 10^5 steps were used to calculate the steady-state shear rheological data. The time step was set to 0.005 in all simulations. In order to provide an estimation of the timescales in experiments and simulations according to Fedosov et al.,[34] the relaxation times of the simulated and the experimental flow curves of a commercial poly(propylene) presented elsewhere[35] were compared. The results suggest that 1 [t] in the DPD simulations approximately equals 1.2 ms where [t] is the DPD unit of time.

Relaxation modulus of the polydisperse systems was also calculated. In the calculations, the flow was stopped at the end of the flow simulations and the chains were allowed to relax for another 5×10^5 time steps. The stress

was recorded meanwhile and divided by the product of the shear-rate of the initial flow and time to yield the relaxation modulus.[36] The results were discussed in terms of the linear viscoelasticity theory.

2.2. Limitations of the Model

It was attempted to construct *efficient* models in this work to present a precise picture of the polydisperse linear polymers in a reasonable time window. However, these models deviate from a *perfect* model in a few points, which are to be explained here for full disclosure. Despite our attempts, no solution has been found so far to overcome the remaining obstacles to build a more accurate model. Although we were skeptical at first about the capability of the models to show the effects of polydispersity, satisfactory qualitative agreement was observed in various simulation aspects with several experiments from other authors. These surprising agreements motivated us to write this paper.

The softness of the potentials in DPD method allows the polymer chains to slide through each other and result in the unphysical phenomena of bond crossings. The consequence of these bond crossings is that the DPD simulations cannot describe the reptation dynamics of the entangled polymer melts.[37] Therefore, effort must be made to avoid this problem so that the dynamics of the long chain fractions in polydisperse systems are captured correctly. There are mainly three approaches so far to prevent the bond crossings in coarse-grained simulations. First approach proposed by Padding and Briels[38,39] introduces an algorithm which prevents bond crossings. In their method, a bond is considered as an elastic band and the energy minimization conditions are used to determine the possible entanglement positions. While this approach is very promising, it is computationally very intensive. A second strategy was proposed by Pan et al.[40] who could reduce the frequency of bond crossings by adding segmental repulsive forces to the force field. This approach also requires heavy calculations. Moreover, the length scale of the segmental repulsions is physically ambiguous.[41] Another method was investigated by Nikunen et al.[32] who used simple topological constraints to prevent chain crossings. This way both Rouse and reptational dynamics were captured for short and long chains, respectively.[37]

Following Nikunen et al.[32], various sets of repulsion parameters and spring constants were tested in this work in order to avoid bond crossings. Unfortunately, the simulations became unstable and the results were unrealistic when more severe constraints were incorporated. We believe that the larger number of beads in our system compared with the previous study produce strong time-dependent variations in the force field when using larger force constants. Therefore, smaller time steps could solve the problem. According to our investigations the instabilities still persist for time steps of 0.0001 (though decreased) which is already very small and increases the simulation time significantly. Furthermore, the main benefit of DPD, i.e., access to the longer time scales, would be sacrificed if very small time steps are incorporated. It is noteworthy that the simulations were run utilizing DL_MESO_2.5 code package, which has been introduced and successfully tested elsewhere.[42] This further assures the stability of the DPD code. The possibility of reducing the number of beads in the simulations was also considered. However, in the current study, where a wide range of chain lengths must be accessible to produce broad polydispersity profiles, a low bead number density is extremely limiting. Moreover, there are certain reports showing the significance of bead number density in the simulation results.[27,29] Therefore, it was decided not to decrease the bead number density.

As a consequence of the interplaying factors, it was currently the only efficient solution to somewhat reduce the possibility of the bond crossings by the method of topological constraints. To do this, the repulsion parameter was set to 25 to comply with other works while the spring coefficient of the harmonic bonds was set to 50 which is much larger than typical values for polymers according to literature.[43–45] As it will be shown, the bonds stretch due to the flow and increase their lengths which consequently lead to an increase in the frequency of the bond crossings. In order to compare the systems with the geometrical condition proposed by Nikunen et al.[32] the impenetrable radius of beads $r_{\min}$ was approximated to be 0.6 in the systems from the radial distribution function at the start of the flow. This value was compared with the corresponding maximum average bond length $l_{\max}$ in the systems during the simulations. If $\sqrt{2}r_{\min} > l_{\max}$, any two bonds cannot cross each other. The stronger this criterion is overwhelmed the higher is the possibility of bond crossings. In the start of the simulations, when the $l_{\max}$ has its minimum value of 1.02, this criterion reads $0.85 \not> 1.02$ which proves that bond crossings exist. Indeed this situation gets worse throughout the simulations, when the bonds are stretched but $r_{\min}$ remains almost constant. Therefore, one can only conclude that the bond crossings are slightly decreased due to this setup, but still dominant in the models. Consequently, it should be stated that this work presents mesoscale models of polymer chains which follow a *slightly improved* version of the Rouse model. It will be shown in the rest of the paper that these models are quite interestingly capable to qualitatively capture the effects of chain length polydispersity. However, the current model cannot provide a precise description regarding entanglement density, disentanglement time, and other significant aspects of the reptation model.

The box size has been shown to influence the response of simulated polymer systems.[46] Since the longest chains in the models are made of 1500 beads, it is necessary to build boxes much larger than 20 × 20 × 20. Also, the box size in the direction of flow is often taken larger than the other directions due to the large extensions. However, such simulations could take very long times because of the sharp increase in the number of beads upon enlarging the box. Therefore, it was attempted to compensate for this issue by the application of the periodic boundary conditions. This necessitated running heavy postprocessing calculations on the simulated periodic coordinates to find the true relative coordinates of the beads. Quantifying physical characteristics of the models was made possible only by this true relative coordinates. Such calculations were almost four times as much time-consuming as the simulation itself. Therefore, one can see that generating an efficient model was based on several important factors.

In addition to the results presented here for a 20 × 20 × 20 box, all of the monodisperse models were also simulated in a 10 × 10 × 10 box with the same conditions. The data from this box were almost the same as the larger 20 × 20 × 20 box except for the velocity profile which was slightly noisier in the smaller box. This further led to noisier stress profiles. However, the averaged stress values over several time steps in the boxes showed negligible differences. Repetition of simulations also approved the reproducibility of the results in both boxes. It should be noted that the results reported in this paper are from a single run on a 20 × 20 × 20 box, while separate runs have been performed to assure the reproducibility.

3. Results and Discussion

3.1. Startup of Shear Flow Simulations

It has been shown by birefringence measurements that the segment orientation of entangled polymers results in a stress overshoot in startup of shear flow.[47] Recent molecular dynamics simulations of bead-spring chains showed the chain stretch is the reason behind this overshoot instead of segment orientation.[48] However, further investigations in primitive path network simulations proved the chain stretch to be of limited influence on the overshoot and supported the experiments that the orientation is the dominant parameter.[49] On the contrary, other authors used the same technique and found that both orientation and stretch determine the response of entangled polymers in large step shear deformations.[50] Recently, Brownian dynamics simulations revealed heterogeneous local chain stretching, suggesting the coupling between stretching and orientation.[51]

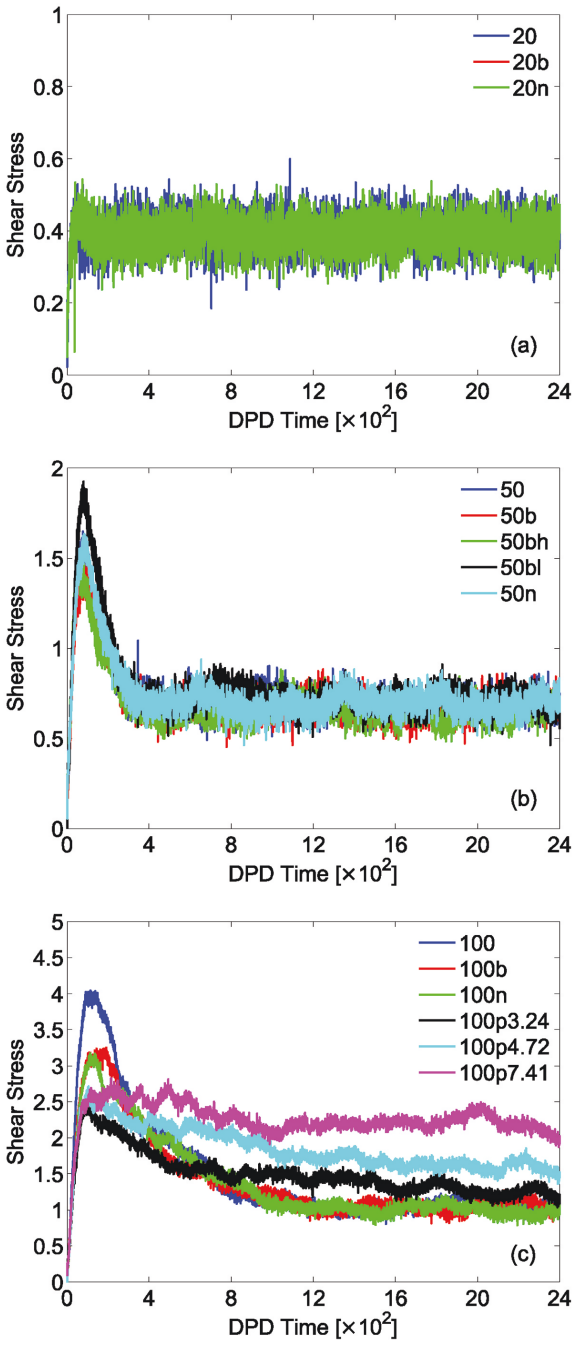

Figure 4. Shear stress of systems with a) $\overline{L}_n \approx 20$, b) $\overline{L}_n \approx 50$, and c) $\overline{L}_n \approx 100$, in startup of shear flow simulations at a constant shear-rate of 0.08 in DPD unit.

The shear stress of various systems is plotted over time in Figure 4. The data are shown for different monodisperse and polydisperse systems with various $\overline{L}_n$ values. The length distribution has almost no effect on the stress profile for systems with $\overline{L}_n$ = 20 (20, 20b, 20n samples) and $\overline{L}_n$ = 50 (50, 50b, 50n samples). However, slight changes in the stress overshoot are evident. One might

assume that this is due to the equal proportions of short and long chains in the system. To test this hypothesis, systems of $\bar{L}_n = 50$ with an uneven length distribution were also simulated utilizing rescaled beta distribution functions (50bl and 50bh, see Figure 2c,d respectively). No significant change is observed in the stress profiles of any of these systems as shown in Figure 4b. The average chain length of the systems was also altered by simulating normal distributions of systems with $\bar{L}_n = 100$ in order to check if the stress profiles would change. It is obvious from Figure 4c that there is almost no change in the steady-state stress values of such systems (100, 100b, and 100n samples). However, the change in the stress overshoot is more pronounced. The PDI was also varied in this system to study its effect on the stress profile. The PDI reflects the relative difference of chain lengths in a system. If this value increases, one could expect a more pronounced difference between the length and therefore the dynamics of different fractions in a system. Systems with $\bar{L}_n = 100$ and different PDI values were designed and tested (see Figure 4c). The steady-state stress as well as the stress overshoot changed with PDI. It should be pointed out that the design of such polydisperse systems was not an easy task. It is necessary to have access to a wide range of chain lengths in order to be able to reach a high PDI value. Moreover, the $\bar{L}_n$ should be kept constant. There is almost no limit to generate the longer chains. However, it is a challenge to satisfy all the prerequisites by designing the shorter chains since they can vary in a limited range. For systems with $\bar{L}_n = 20$ and 50, this range is the intervals from 2 to 19 and from 2 to 49, respectively. Therefore, it was rather impossible to achieve high PDI values for these systems and it was only possible to design highly polydispersed systems with $\bar{L}_n = 100$.

It is observed in the simulations that the stress overshoot is decreased with the polydispersity. In a monodisperse system, all chains possess a unique relaxation behavior due to their similar dynamics. They all move, rotate, and orient in the same time scale. Such similar chain dynamics is replaced with a broad relaxation spectrum of all possible length scales in the polydisperse systems. At short times after startup of flow, short chains move fast while only parts of long chains have moved. Long chains would take much longer times to respond to the applied flow field. As a result, the stress overshoots of short and long chains do not overlap. Instead, they produce a range of stress overshoots resulting from different fractions. Hence, the sharp stress overshoot becomes broader and reduces to some extent depending on how much the relaxation modes overlap. Such interpretation is in agreement with the coarse-grained molecular simulation results of Hoy et al.[52] which indicated that the chains contribute independently to the stress in a mixture of chains with different lengths.

Experimental data are hard to find on the polydisperse systems with molecular characteristics close to our simulated systems due to the limitations in polymerization. Most of the available works have used a blending strategy, i.e., mixing different molecular weights of the same homopolymer, to achieve mixtures with various polydispersity profiles. For instance, Boukany and Wang[7] investigated the velocity profiles of sheared polydisperse polybutadiene mixtures. They present their results for startup of shear flow experiments at a shear-rate of 0.32 s^{-1} for 2 mixtures with $\bar{M}_n = 740$ and 810 kg mol^{-1}, and PDI = 1.02 and 1.72, respectively. The system with higher polydispersity shows a broader stress profile and approaches the steady-state much slower than the other one.

The good qualitative agreement between the observed trends in stress profiles of our simulations and these experiments encourages further investigations to be carried out on the model systems to explain the effects of polydispersity. In the rest of this paper, it is intended to study different fractions, i.e., chains with different lengths, separately and compare them with each other. Such detailed analyses are extremely difficult to conduct in experiments if not impossible.

In a DPD model comprised of multiple beads, there is a certain amount of energy dissipated due to the friction each time two beads interact. By increasing the number of bonded beads to generate longer chains, the possibility of such nonbonded interactions is reduced. Therefore, the energy loss during the flow is altered when the polydispersity is changed. It should further influence the stress profile. The frequency of nonbonded interactions were monitored in the systems and plotted in Figure 5. In these calculations, an interaction was defined whenever two nonbonded beads were distanced less than the force cutoff radius. The intramolecular and intermolecular interactions were calculated separately. For the intramolecular interactions, the true relative coordinates were used in the calculations. It should be emphasized that by intramolecular interactions nonbonded bead–bead interactions are intended and not the bonded interactions such as bond stretching, bond bending, or torsion in the force field. The frequency of the intramolecular interactions reduces in early stages of the simulation and reaches a steady-state value. The intermolecular interactions on the other hand go through a maximum and reach a steady-state in samples with low PDI values. The results show that the total frequency of all nonbonded interactions decreases over time. This decrease is more pronounced in polydisperse systems. Therefore, the dissipative interactions are not the reason why the steady-state stresses in the polydisperse systems are higher than their monodisperse counterparts. The characteristic behaviors in the frequencies of intramolecular and intermolecular interactions are indeed interesting and could be explained in an orientation-stretch framework.

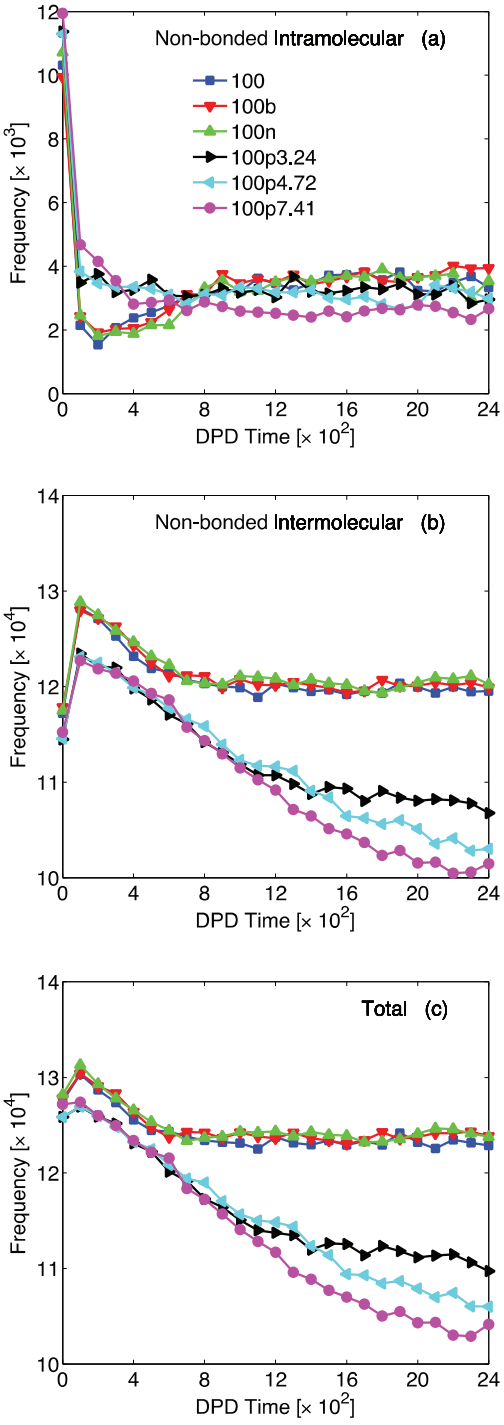

Figure 5. Frequency of a) intramolecular, b) intermolecular, and c) total nonbonded interactions in the systems with $\overline{L}_n \approx 100$ in startup of shear flow simulations at a constant shear-rates of 0.08, in DPD unit. The legends are shown in part a.

With the start of the flow, chains gradually move and align in the flow direction. The orientation of the polymers can be characterized by the order tensor $\boldsymbol{S}$[39,53]

$$\boldsymbol{S}=\frac{3}{2}\left(\langle \boldsymbol{uu}\rangle-\frac{1}{3}\boldsymbol{I}\right) \tag{7}$$

$$\langle \boldsymbol{uu}\rangle = \frac{1}{n_{\text{chain}}(N-1)}\sum_{i=1}^{n_{\text{chain}}}\sum_{j=2}^{N}\frac{\boldsymbol{R}_{i,j}-\boldsymbol{R}_{i,j-1}}{\left|\boldsymbol{R}_{i,j}-\boldsymbol{R}_{i,j-1}\right|}\times\frac{\boldsymbol{R}_{i,j}-\boldsymbol{R}_{i,j-1}}{\left|\boldsymbol{R}_{i,j}-\boldsymbol{R}_{i,j-1}\right|} \tag{8}$$

where n_{chain} is the total number of chains, N is the number of beads in the chain, and $\boldsymbol{I}$ is the unit tensor. $\boldsymbol{R}_{i,j}$ represents the position of the jth bead on the ith chain. In an anisotropic system, the eigenvector of the largest eigenvalue of the order tensor gives the preferential orientation of the bonds. The angle between this eigenvector and the flow direction is the flow alignment angle χ. It is given by

$$\tan 2\chi=\frac{2S_{xy}}{S_{xx}-S_{yy}} \tag{9}$$

The evolution of flow alignment angle with time is demonstrated in Figure 6 for the model systems. One can see that the bonds orient with time according to the flow direction. As the orientation progresses, the intramolecular interactions reduce due to the decreased probability of two nonbonded beads in the same chain to interact. In polydisperse systems with long chain fractions, the intramolecular interactions are more frequent in the start of the simulations. When the long chains align in the course of the flow, the intramolecular interactions decrease more rapidly than when short chains align. This decrease is more important in polydisperse systems since the major part of the intramolecular interactions is coming from long fractions. Therefore, they show less frequency of intramolecular interactions at the steady-state compared to the systems with low PDI values even though they

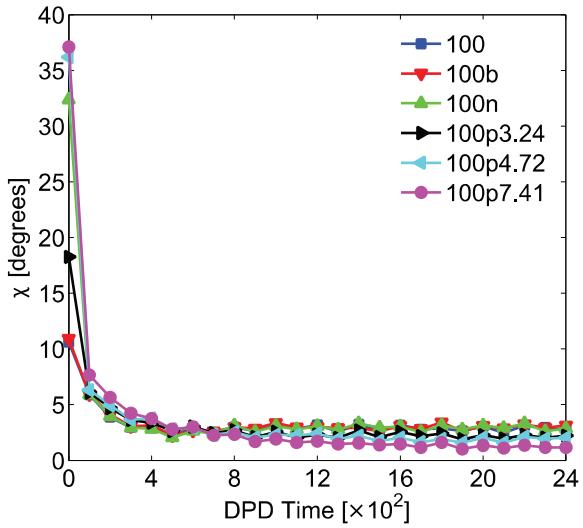

Figure 6. The evolution of flow alignment angle with time in the systems with $\overline{L}_n \approx 100$ in startup of shear flow simulations at a constant shear-rate of 0.08, in DPD unit.

have higher values in the beginning. If a chain with 1500 beads aligns, the probability of two nonbonded beads of the same chain to be distanced less than the force cutoff radius is reduced the same as for the alignment of 15 chains of 100 beads. This point states the fact that the penalty of alignment of long fractions on the frequency of intramolecular interactions is much more severe than the short fractions. Such a statistical explanation also applies to the intermolecular interactions. Keeping in mind that the bead number density is constant in the simulations, a chain of 1500 beads can form intermolecular interactions with 22500 beads. This number for a chain of 100 beads in a monodisperse system is 23900 beads. Hence, for a specific bead there is a larger number of surrounding beads to interact with in the latter system.

When systems undergo flow, the chains move, orient and stretch accordingly. This complex dynamics leads to a competition between the construction and destruction of interaction sites with different orders. In this paper, the order of an interaction site is defined as the number of the beads participating in that site. The number of sites with multiple intermolecular interactions, i.e., orders higher than 3, is plotted with time in Figure 7. In the monodisperse system, all orders reach the steady-state. The sites with orders higher than 10 show a distinct maximum in the early stages of the simulation. This is ascribed to the temporary distortions in the local rearrangements of the segments due to the applied flow. In the polydisperse system, the steady-state is not reached. This further supports the slower dynamics in polydisperse systems as a result of the long chain fractions. It is interesting to note that the number of low-ordered sites is increasing while high-ordered sites are being destroyed gradually by the flow. The flow is removing the beads one by one from the high-ordered sites. This results in 10-ordered sites to become 9-ordered and so on. Therefore, the destroyed high-ordered sites add up to the lower ordered sites thus increasing their population. This information provides insight into the evolution of an oriented microstructure in the systems.

Similar behavior is also seen in the nonbonded interaction data of monodisperse systems with various chain lengths. The data for such systems are plotted in Figure 8. The reduction in the number of interactions becomes more distinguished as the length of the chains grows. The results clearly support our earlier remarks that the length of the chains plays a critical role in the frequency of nonbonded interactions.

The overall elongation of a polymer chain can be characterized by the xx component of the mean square gyration tensor $\langle R_g^2 \rangle$[39,53]

$$\langle R_g^2 \rangle = \frac{1}{n_{chain} N} \sum_{i=1}^{n_{chain}} \sum_{j=1}^{N} (R_{i,j} - R_{i,c})(R_{i,j} - R_{i,c}) \quad (10)$$

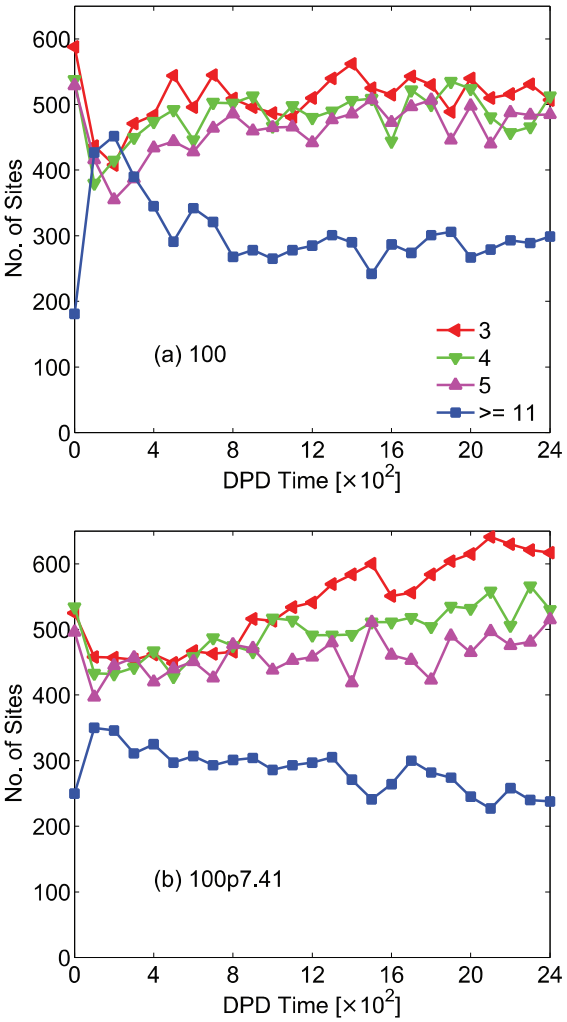

Figure 7. Number of sites with different orders over time in a) 100 and b) 100p7.41 systems at a constant shear-rate of 0.08 in DPD unit. The legends are shown in part a.

Here, $R_{i,c} = \frac{1}{N} \sum_{j=1}^{N} R_{i,j}$ is the position of the center of mass of the *i*th chain with *N* beads. Figure 9 shows the time dependence of the xx component of the mean square gyration tensor for various fractions in polydisperse systems. It is obvious that the chains stretch and increase their size during the flow. The kinetics of chain stretching is slowed down with increasing the chain length of the fraction. In the longest fractions of the polydisperse systems the steady-state is not achieved in the scope of the simulations. It is interesting to note that in the 100p3.24 system, the longest fraction with 1500 beads in each chain does not start to stretch until the very late stages of the simulation. However, in the 100p7.41 system the longest chains are more influenced by the applied flow. The same behavior was also observed in repetitions. Since the velocity profile was well-developed in all simulations,

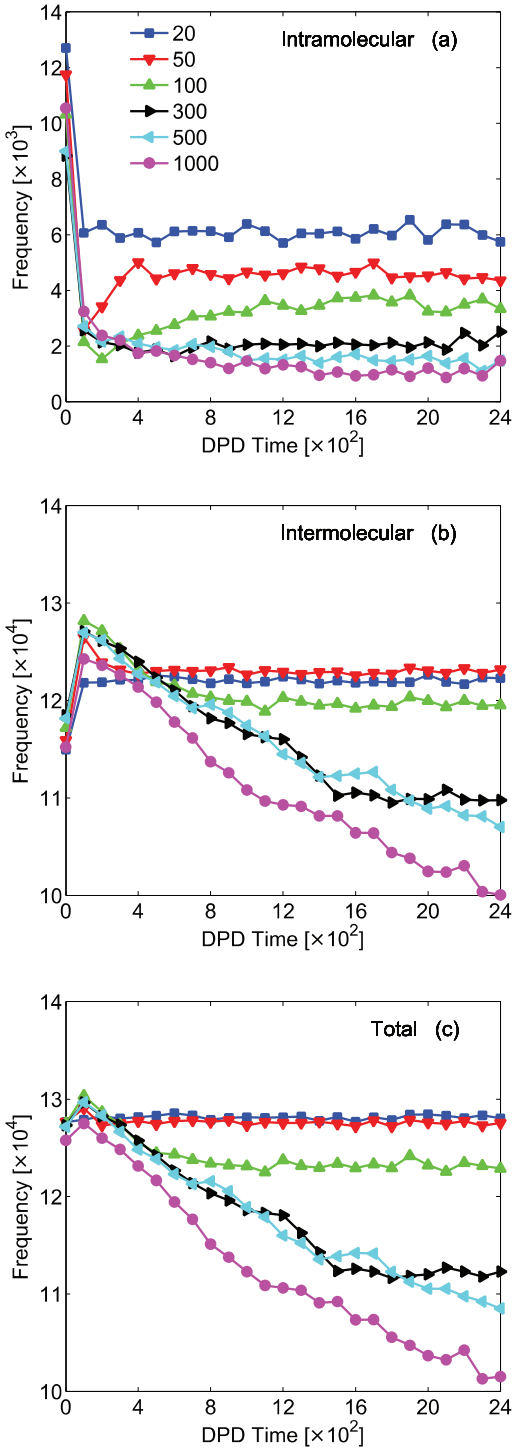

Figure 8. Frequency of a) intramolecular, b) intermolecular, and c) total nonbonded interactions in the monodisperse systems (chain lengths from 20 to 1000) in startup of shear flow simulations at a constant shear-rate of 0.08, in DPD unit. The legends are shown in part a.

we suspect that this is probably due to the fact that the share of longest chains in the total number of beads is increased in the 100p7.41 system. The longest chains are more influenced by the applied flow as a consequence of this increased share in the melt. The typical configurations of two of the longest chains of system 100p7.41 are given in Figure 10 with time. It further demonstrates that the longest fraction of the chains is only partially stretched in the flow direction. To compare the behavior of short fractions, the typical configurations of two of the short chains of system 100p7.41 are also given with time in Figure 11. It is obvious that the chains are more influenced by temporary flow heterogeneities as they can stretch and/or recoil much faster during the flow. The gyration radius data obviously show the delayed relaxation mechanism in polydisperse systems. Based on the data, the oriented microstructure is still developing very slowly in polydisperse systems which is a consequence of the long fractions.

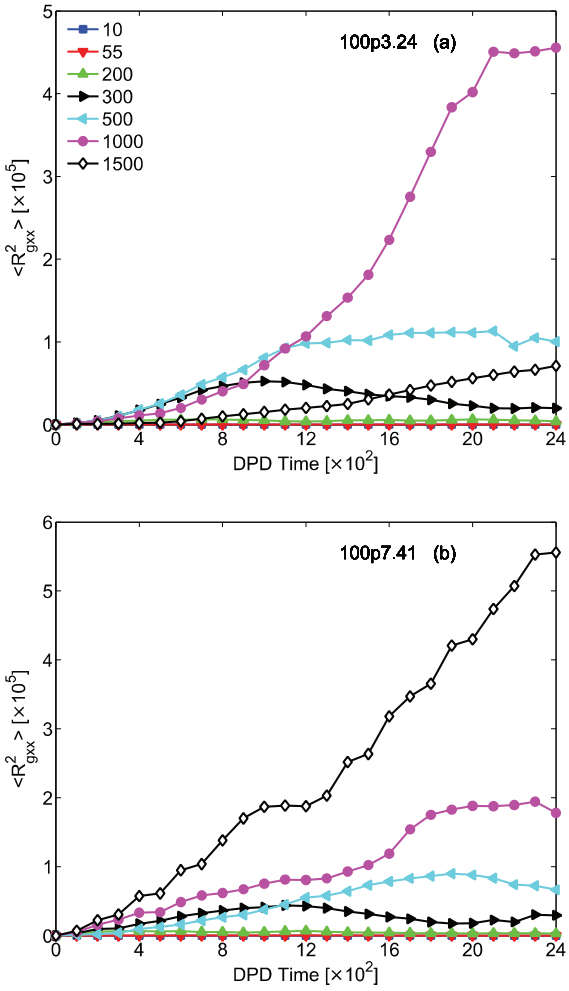

Figure 9. The evolution of the xx component of the mean square gyration tensor with time for various fractions in a) 100p3.24 and b) 100p7.41 systems at a constant shear-rates of 0.08 in DPD unit. The number of beads in each fraction is shown in the legend. The legends are shown in part a.

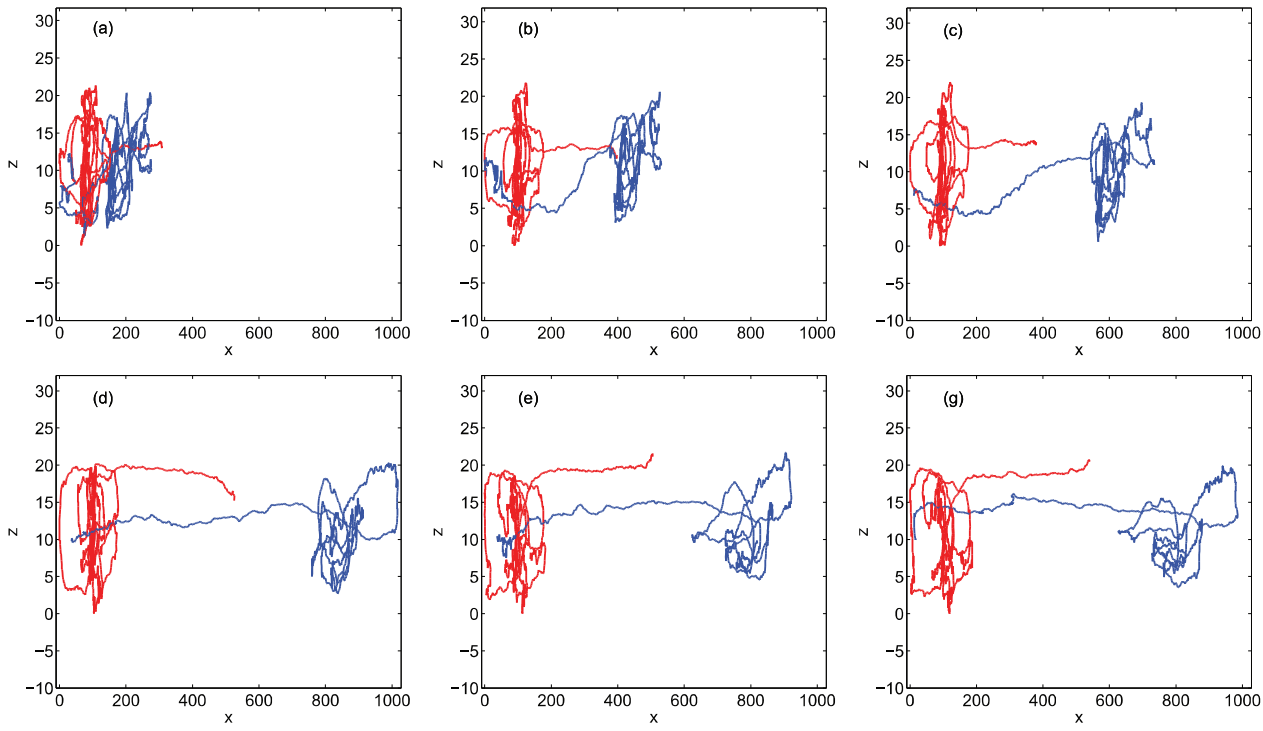

Figure 10. The stretching of two chains shown in blue and red colors with 1500 beads in system 100p7.41 at a) 100, b) 200, c) 400, d) 1100, e) 1900, and g) 2400 DPD time, at a constant shear-rate of 0.08 in DPD unit. Note that the true relative coordinates are used in the figures.

The progress in orientation and stretching of chains in flow becomes more important especially in fractions with longer chains. Moreover, the bonds would also orient and stretch according to the flow. The average bond length is plotted in Figure 12 for various systems with $\overline{L}_n = 100$ over time. According to the results, the bonds are stretched and it becomes more intensive as the PDI increases. Consequently, the contribution of the bonded energy should be also higher in such systems. Figure 13 shows the contributions from bonded and nonbonded energies to the total potential energy of the system over time. The bonded energy gradually dominates the total potential energy of the system over time (100p3.24, 100p4.72, and 100p7.41 samples). Thus, it is clear that the configurational reorganizations, i.e., orientation and stretching of the bonds and chains, determine the potential energy as well as the stress profile. High stresses are necessary in polydisperse systems due to orientation and stretching of long fractions as observed in the stress profiles. Such reorganizations are indeed more energy-consuming in polydisperse systems where long fractions are present. These results are also in agreement with recent Brownian dynamics simulations in an entangled polymer melt. Studies have shown that the coupled effects of segment orientation and chain stretch result in an emerging stress overshoot before the Rouse time.[51] In contrast, substantial chain stretching has been found to persist well beyond the Rouse time.

3.2. Relaxation Behavior

In order to provide a more accurate insight into the relaxation behavior, the shear relaxation modulus of various systems were calculated, see Figure 14. The modulus data are normalized to the average initial modulus G° which is the average modulus value of the first 4000 steps of the simulations. The data are scattered at the largest correlation times where the relaxation modulus is close to zero because of the finite measuring time. The absolute values of the negative data are represented on the logarithmic scale with filled red circles in order to assess the proximity to zero of the scattered data. The relaxation modulus approaches zero when the number of filled and unfilled circles are equal. It should be noted that the filled circles are plotted in front of the unfilled circles. This may appear as if the filled circles are dominating the unfilled circles. The results show that the data start to scatter at relatively longer times in polydisperse systems as a sign of the slower relaxation. The linear viscoelasticity theory is used in order to find the relaxation spectrum of the systems. The theory suggests that the relaxation modulus can be expresses in terms of a discrete relaxation spectrum $\{g_i, \tau_i\}$ as

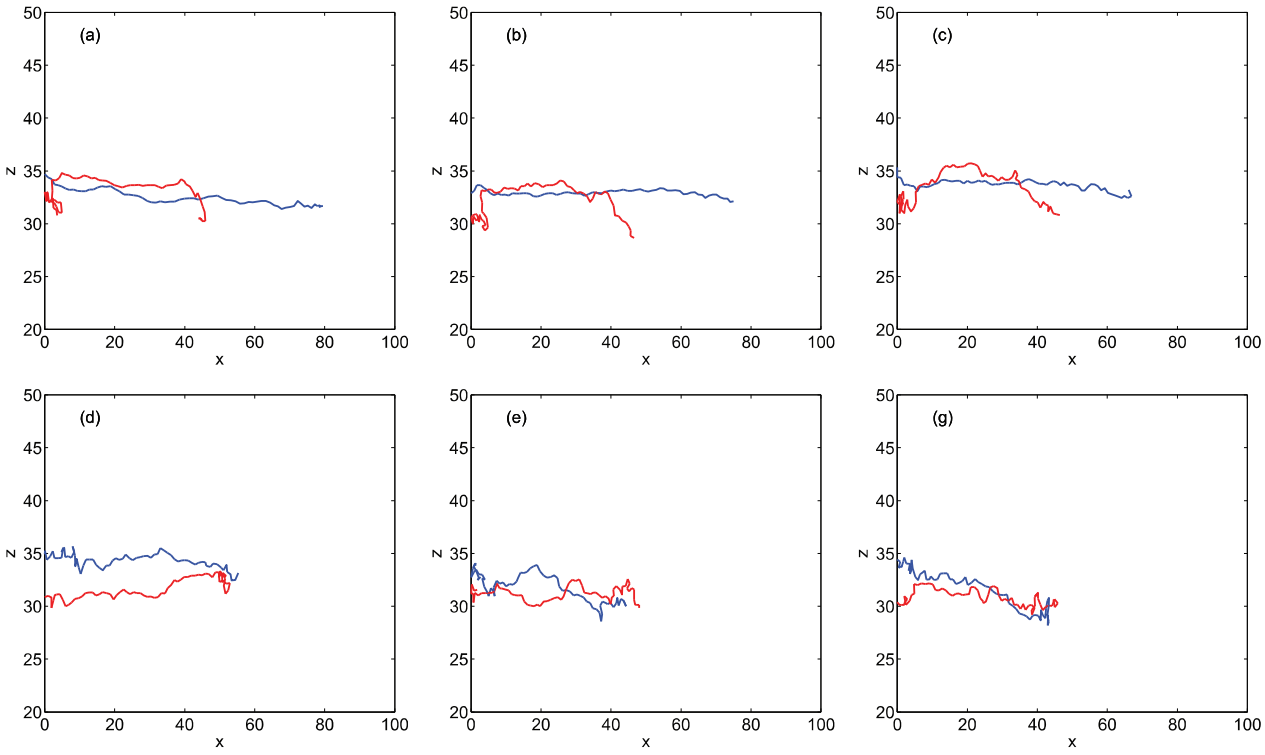

Figure 11. The stretching of two chains shown in blue and red colors with 70 beads in system 100p7.41 at a) 100, b) 200, c) 400, d) 1100, e) 1900, and g) 2400 DPD time, at a constant shear-rate of 0.08 in DPD unit. Note that the true relative coordinates are used in the figures.

$$G(t)=\sum_{i=1}^{N} g_i e^{-\frac{t}{\tau_i}} \quad (11)$$

In this equation, N is the number of relaxation modes, g_i and τ_i are the relaxation modulus and the relaxation time of the ith mode, respectively. The relaxation times were estimated for each system by fitting a relaxation spectrum with maximum 5 relaxation modes to the simulation results, see Table 2. One can see that the relaxation spectrum is broader in polydisperse systems. The longest relaxation times especially increase in polydisperse systems compared with their monodisperse counterparts. This finding is in agreement with measurements of other authors. Experimental studies on several polymers including polystyrene mixtures,[16] methylhydroxyethyl cellulose blends,[16] and poly(propylene)s [6] have shown an increased longest relaxation time with increasing polydispersity via different techniques. With the maximum relaxation time of the samples at hand, one can determine the flow strength in terms of the dimensionless Weissenberg number (W_i), $W_i=\dot{\gamma}\tau_o$ where $\dot{\gamma}$ is the applied shear-rate and τ_o is the longest relaxation time. For instance in the 100p7.41 sample, the W_i at the shear-rates of 0.023, 0.08, and 0.152 is 9.32, 32.41, and 61.58, respectively. These data show that the applied flows are strong enough to cancel out thermal fluctuations to a large extent.

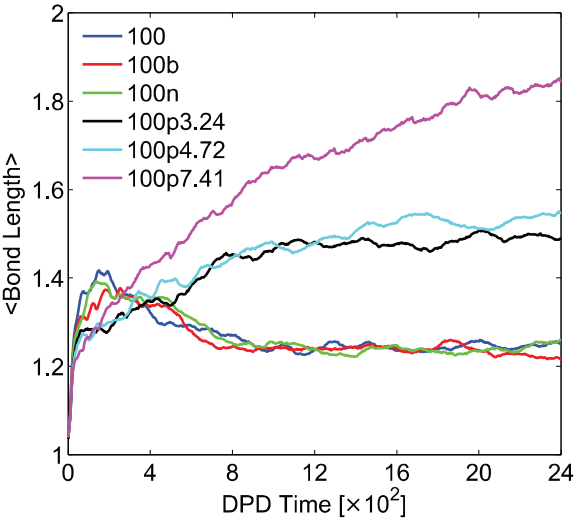

Figure 12. The evolution of the average bond length over time in systems with $\bar{L}_n \approx 100$ in startup of shear flow simulations at a constant shear-rate of 0.08 in DPD unit.

3.3. Effect of Flow Intensity

The applied shear-rate influences the stress profiles in startup of shear flow experiments. To test its effects, systems with $\bar{L}_n = 100$ were simulated at different

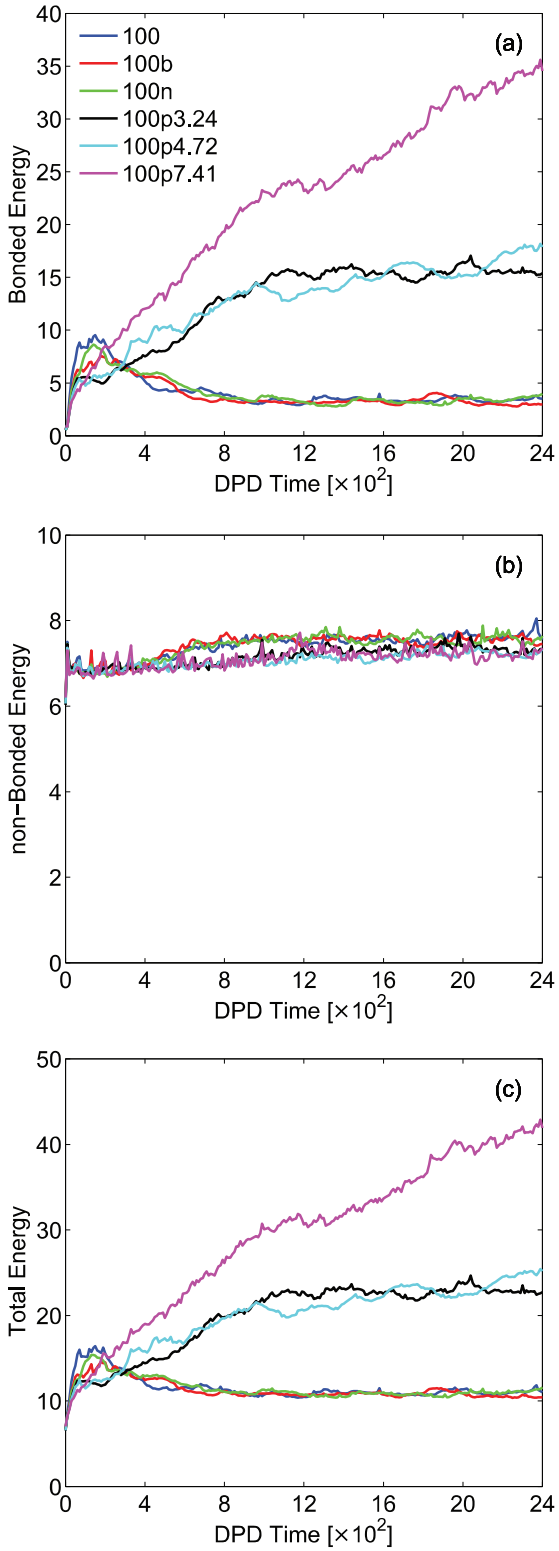

Figure 13. Evolutions of the a) averaged bonded potential energy per bond, b) averaged nonbonded potential energy per bead, and c) averaged total potential energy with time in systems with $\bar{L}_n \approx 100$ in startup of shear flow simulations at a constant shear-rate of 0.08 in DPD unit. The legends are shown in part a.

shear-rates, see Figure 15. The systems with high PDI show broad stress profiles at all shear-rates tested. Moreover, they decline faster at higher shear-rates to the steady-state. The accelerated dynamics of the long fractions in stronger flows leads to this behavior. The steady-state stress is also affected by increasing the applied shear-rate and seems to approach the limiting value of the monodisperse system.

The steady-state shear viscosities are plotted against the applied shear-rate in Figure 16. Polydisperse systems show relatively higher viscosities at all shear-rates. The difference is more important at smaller shear-rates while it becomes less significant as the shear-rate increases. This trend is a result of the overwhelming nonbonded energy in the system. It has been shown by other authors that the DPD simulations suffer from the fact that at high shear-rates the increasing dissipated energy distorts the thermostat.[34] As a result, the nonbonded energy of the system is so large that it becomes the dominating factor in the total energy of the system. Consequently, the previous conclusion on the role of bonded energy in polydisperse systems is of less significance, yet still valid. Moreover, at very low shear-rates the deviations from the applied linear velocity profile leads to local flow heterogeneities.[23,26,34] Such distortions would impose strong numerical uncertainties in the calculations. Therefore, it is important to note such effects when studying the effects of very low and very high shear-rates on the response of the systems. At the studied shear-rates, the polydispersity leads to higher steady-state shear viscosities due to the higher stresses necessary to stretch and orient the longer fractions. The results are in agreement with experimental data of Gahleitner[54] who reported the viscosity data of several poly(propylene)s against shear-rate. Among all of his samples, two have close molecular characteristics to the simulated systems in this work: polymers with (1) $\bar{M}_n$ = 139.3 kg mol^{-1} and PDI = 5.5, and (2) $\bar{M}_n$ = 129.4 kg mol^{-1} and PDI = 3.5. The first polymer showed higher viscosities at all shear-rates, with an order of magnitude larger zero-shear viscosity value than the second polymer.

4. Conclusions

Startup of steady shear flow properties of polydisperse linear polymers were studied in a DPD framework. It was shown that the stress overshoot generally decreased with the introduction of polydispersity into the models. This behavior was ascribed to the broad relaxation response of various length scales present in polydisperse systems. Steady-state stress became larger as polydispersity increased due to the higher forces necessary to orient and stretch long chain fractions in the flow direction. Detailed analyses of nonbonded interactions proved a complex microstructural evolution because of orientation and

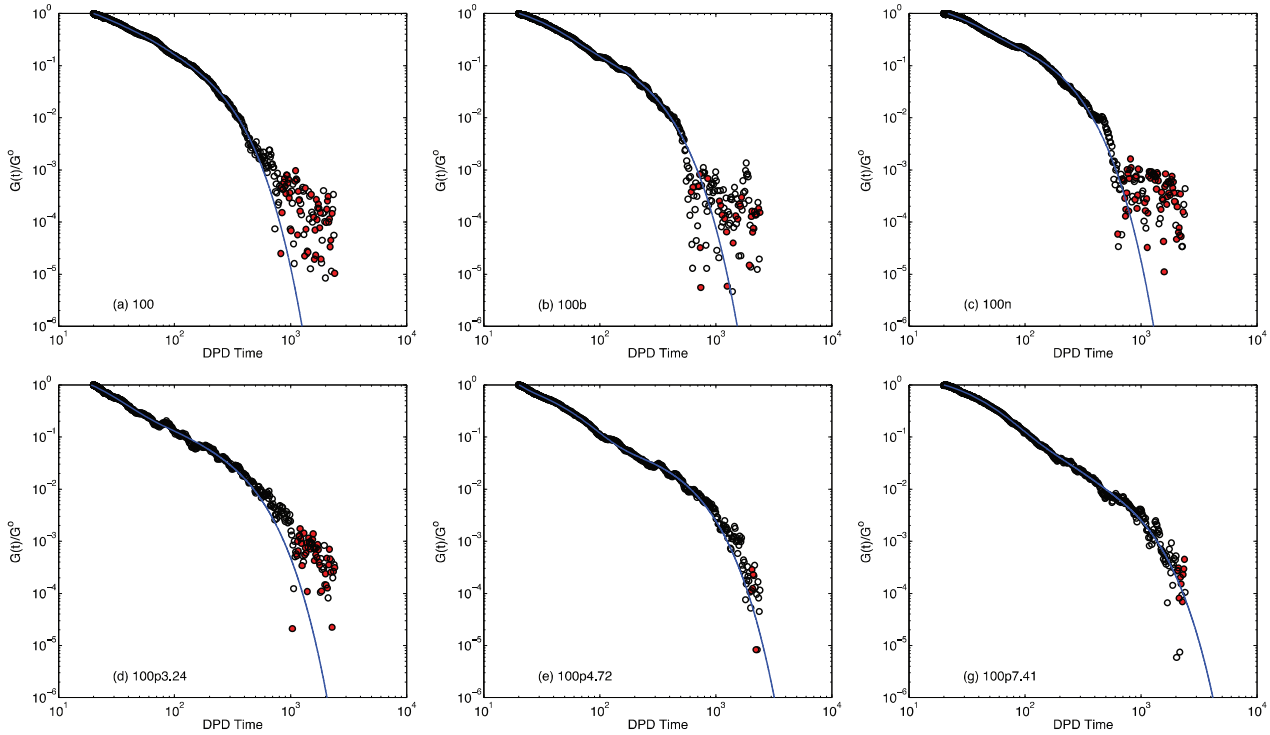

Figure 14. Shear relaxation modulus $G(t)$ normalized to the average initial modulus G° in systems with $\overline{L}_n \approx 100$ in startup of shear flow simulations at a constant shear-rate of 0.08 in DPD unit (unfiled markers). The solid lines are the fitting results from the linear viscoelasticity theory. The absolute values of the negative data are represented by filled red circles.

chain stretching during the flow. It was evident that the orientation of long chain fractions forces more severe penalties on the frequency of nonbonded interactions than the short chain fractions. The results support the coupled effect of orientation and stretching to influence the stress profile in startup of shear flow simulations. The orientations and stretching occurred in the early stages of the simulation and led to the appearance of stress overshoot in the systems. While the bond orientation became steady rather fast, the bond stretching continued in the longer times. The gyration radius data also proved the chains to increase their size during the flow. The larger size and the slowed-down elongation dynamics of long fractions were evident.

Table 2. The relaxation times of the systems with $\overline{L}_n = 100$ derived from fitting the linear viscoelastic model to the shear relaxation modulus data.

System	τ_0	τ_1	τ_2	τ_3	τ_4
100	97.98	28.37			
100b	121.74	22.58			
100n	98.06	28.30			
100p3.24	171.84	66.18	49.15	25.26	
100p4.72	281.08	173.67	61.481	42.38	24.43
100p7.41	405.14	283.77	170.36	40.95	23.17

Relaxation modulus data proved the broad range of relaxation mechanisms in polydisperse systems. The relaxation spectrum was quantified benefiting from the linear viscoelasticity theory. The results showed an increase in the longest relaxation time in systems with higher PDIs. This is in qualitative agreement with the available measurements in the literature from a variety of polymers. The startup of shear flow simulations were performed at different shear-rates. The steady-state shear viscosity results showed higher viscosities in the polydisperse systems at all shear-rates. It was noted that these observations are in qualitative agreement with the available experimental data of different poly(propylene)s.

The satisfactory qualitative agreement of the characteristic behaviors of polydisperse polymers with experiments is encouraging. The underlying physical phenomena could be studied in such simulations while it stays hardly accessible to experiments. Therefore, the results of this work enable us to understand the oriented microstructure formation in extruded films, spun fiber, etc. during processing from polydisperse polymers. Further challenges still remain for future work including the effective incorporation of physical constraints to avoid bond crossings and reproduce reptational dynamics,

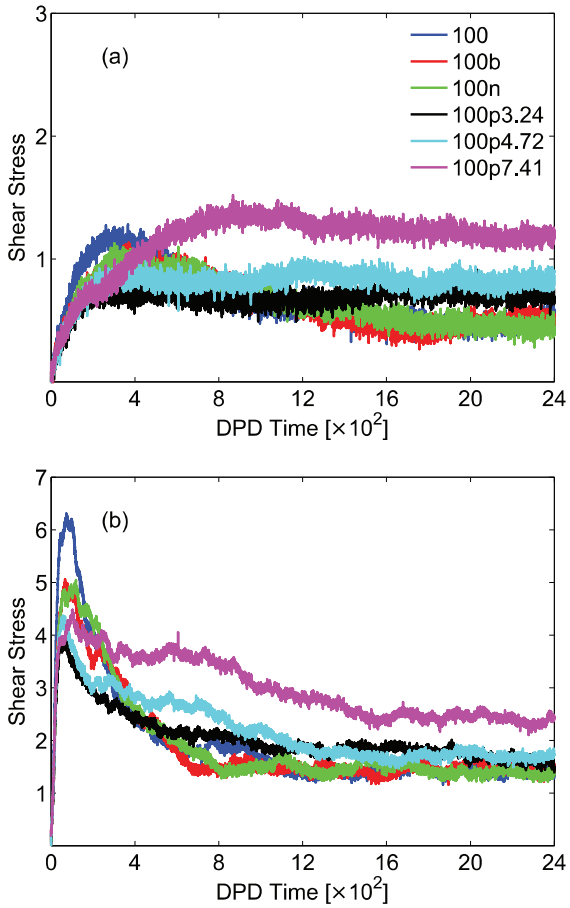

Figure 15. Shear stress of systems with $\bar{L}_n \approx 100$ in startup of shear flow simulations at constant shear-rates of a) 0.023 and b) 0.152, in DPD unit. The legends are shown in part a.

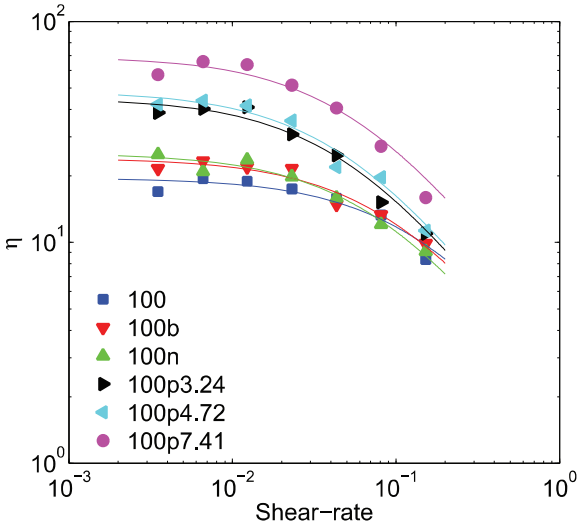

Figure 16. Steady-state shear viscosity η as a function of the applied shear-rate for systems with $\bar{L}_n \approx 100$ in DPD unit. The curves are guides to the eye.

design of systems with various polydispersity profiles, modeling real systems rather than characteristic polymers, and multiscale simulation of final products from such analyses.

Received: August 18, 2015; Revised: November 11, 2015; Published online: February 1, 2016; DOI: 10.1002/mats.201500060

Keywords: chain stretching; dissipative particle dynamics; orientation; polydispersity; shear flow

[1] T.-H. Yu, G. L. Wilkes, *J. Rheol.* **1996**, *40*, 1079.
[2] T.-H. Yu, G. L. Wilkes, *Polymer* **1996**, *37*, 4675.
[3] T.-H. Yu, G. L. Wilkes, *J. Plast. Film Sheet.* **1997**, *13*, 299.
[4] Z. Bashir, J. A. Odell, A. Keller, *J. Mater. Sci.* **1986**, *21*, 3993.
[5] J. F. Vega, S. Rastogi, G. W. M. Peters, H. E. H. Meijer, *J. Rheol.* **2004**, *48*, 663.
[6] M. Fujiyama, Y. Kitajima, H. Inata, *J. Appl. Polym. Sci.* **2002**, *84*, 2128.
[7] P. E. Boukany, S.-Q. Wang, *J. Rheol.* **2007**, *51*, 217.
[8] P. Tapadia, S. Ravindranath, S.-Q. Wang, *Phys. Rev. Lett.* **2006**, *96*, 196001.
[9] P. Tapadia, S.-Q. Wang, *Phys. Rev. Lett.* **2006**, *96*, 016001.
[10] T. Borg, E. J. Pääkkönen, *J. Non-Newton. Fluid Mech.* **2009**, *159*, 17.
[11] A. Leygue, C. Bailly, R. Keunings, *J. Non-Newton. Fluid Mech.* **2006**, *133*, 28.
[12] J.-C. Majesté, A. Allal, J.-P. Montfort, *Rheol. Acta* **2003**, *42*, 477.
[13] M. R. Nobile, F. Cocchini, *Rheol. Acta* **2000**, *39*, 152.
[14] R. Prez-Aparicio, J. Colmenero, F. Alvarez, J. T. Padding, W. J. Briels, *J. Chem. Phys.* **2010**, *132*, 024904.
[15] S. Misra, F.-M. Lu, J. E. Spruiell, G. C. Richeson, *J. Appl. Polym. Sci.* **1995**, *56*, 1761.
[16] J. P. Plog, W.-M. Kulicke, C. Clasen, *Appl. Rheol.* **2005**, *15*, 28.
[17] N. A. Rorrer, J. R. Dorgan, *J. Chem. Phys.* **2014**, *141*, 214905.
[18] P. J. Hoogerbrugge, J. M. V. A. Koelman, *Europhys. Lett.* **1992**, *19*, 155.
[19] K. Zhang, C. W. Manke, *Mol. Simul.* **2000**, *25*, 157.
[20] M. Yamanoi, O. Pozo, J. M. Maia, *J. Chem. Phys.* **2011**, *135*, 044904.
[21] V. Ortiz, S. O. Nielsen, D. E. Discher, M. L. Klein, R. Lipowsky, J. Shillcock, *J. Phys. Chem. B* **2005**, *109*, 17708.
[22] D. C. Visser, *J. Comput. Phys.* **2006**, *214*, 491.
[23] S. Meng, J. Zhang, Y. Wang, X. Li, C. Wu, T. Hou, L. Xiao, G. Lu, *Mol. Simul.* **2015**, *41*, 772.
[24] W. Pan, B. Caswell, G. E. Karniadakis, *Langmuir* **2010**, *26*, 133.
[25] A. Chatterjee, L.-M. Wu, *Mol. Simul.* **2008**, *34*, 243.
[26] A. Gooneie, S. Schuschnigg, C. Holzer, *Macromol. Theory Simul.* **2016**, *25*, 85.
[27] R. D. Groot, P. B. Warren, *J. Chem. Phys.* **1997**, *107*, 4423.
[28] J.-G. Gai, G.-H. Hu, H.-L. Li, S.-P. Zhu, S. Hoppe, *Ind. Eng. Chem. Res.* **2010**, *49*, 11369.
[29] R. M. Füchslin, H. Fellermann, A. Eriksson, H.-J. Ziock, *J. Chem. Phys.* **2009**, *130*, 214102.
[30] A. Maiti, S. McGrother, *J. Chem. Phys.* **2004**, *120*, 1594.
[31] P. Español, P. Warren, *Europhys. Lett.* **1995**, *30*, 191.
[32] P. Nikunen, I. Vattulainen, M. Karttunen, *Phys. Rev. E* **2007**, *75*, 036713.
[33] C. G. Cray, K. I. Gubbins, *Theory of Molecular Fluids*, Clarendon Press, New York **1984**.

[34] D. A. Fedosov, G. E. Karniadakis, B. Caswell, *J. Chem. Phys.* **2010**, *132*, 144103.
[35] A. Gooneie, H. Mattausch, A. Witschnigg, S. Schuschnigg, C. Holzer, *Key Eng. Mater.* **2015**, *651*, 533.
[36] R. B. Bird, R. C. Armstrong, O. Hassager, *Dynamics of Polymeric Liquids*, John Wiley & Sons Inc., New York **1987**.
[37] M. Doi, S. F. Edwards, *The Theory of Polymer Dynamics*, Clarendon Press, Oxford **1986**.
[38] J. T. Padding, W. J. Briels, *J. Chem. Phys.* **2002**, *117*, 925.
[39] J. T. Padding, W. J. Briels, *J. Chem. Phys.* **2003**, *118*, 10276.
[40] G. Pan, C. W. Manke, *Int. J. Mod. Phys. B* **2003**, *17*, 231.
[41] T. W. Sirk, Y. R. Slizoberg, J. K. Brennan, M. Lisal, J. W. Andzelm, *J. Chem. Phys.* **2012**, *136*, 134903.
[42] M. A. Seaton, R. L. Anderson, S. Metz, W. Smith, *Mol. Simul.* **2013**, *39*, 796.
[43] R. D. Groot, *J. Chem. Phys.* **2003**, *118*, 11265.
[44] H.-J. Qian, L.-J. Chen, Z.-Y. Lu, Z.-S. Li, *Phys. Rev. Lett.* **2007**, *99*.
[45] S. Kim, A. M. Palomino, C. M. Colina, *Mol. Simul.* **2012**, *38*, 723.
[46] K. Kremer, G. S. Grest, *J. Chem. Phys.* **1990**, *92*, 5057.
[47] D. S. Pearson, A. D. Kiss, L. J. Fetters, M. Doi, *J. Rheol.* **1989**, *33*, 517.
[48] Y. Lu, L. An, S.-Q. Wang, Z.-G. Wang, *ACS Macro Lett.* **2014**, *3*, 569.
[49] Y. Masubuchi, H. Watanabe, *ACS Macro Lett.* **2014**, *3*, 1183.
[50] K. Furuichi, C. Nonomura, Y. Masubuchi, H. Watanabe, G. Ianniruberto, F. Greco, G. Marrucci, *Rheol. Acta* **2008**, *47*, 591.
[51] Y. Lu, L. An, S.-Q. Wang, Z.-G. Wang, *Macromolecules* **2015**, *48*, 4164.
[52] R. S. Hoy, M. O. Robbins, *J. Chem. Phys.* **2009**, *131*, 244901.
[53] T. Aoyagi, M. Doi, *Comput. Theor. Polym. Sci.* **2000**, *10*, 317.
[54] M. Gahleitner, *Prog. Polym. Sci. (Oxford)* **2001**, *26*, 895.

Orientation of Anisometric Layered Silicate Particles in Uncompatibilized and Compatibilized Polymer Melts Under Shear Flow: A Dissipative Particle Dynamics Study[a]

Ali Gooneie,* Stephan Schuschnigg, Clemens Holzer

The orientation of a three-layered silicate particle in uncompatibilized and compatibilized polymer melts is studied under shear flows utilizing dissipative particle dynamics (DPD). Based on trajectories, pair distribution functions are calculated in orthogonal planes. Regardless of the applied flow direction, it is shown that the layers rearrange themselves so that their surfaces would be normal to the velocity gradient direction. The maximum shear stress values fall in numerical uncertainties in uncompatibilized systems while they show a characteristic overshoot in compatibilized counterparts. This overshoot is shown to be a result of (i) the large interfaces between the silicate layers and the matrix due to the exfoliation, and (ii) the increased energy dissipation due to friction at the interface.

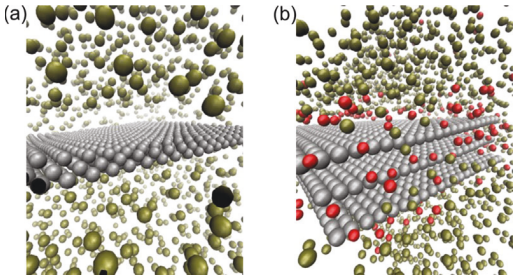

1. Introduction

The incorporation of non-spherical particles has led to the development of advanced materials with anisometric properties. Polymer-layered silicate nanocomposites (PLNs) are an excellent example of such materials.[1–4] They particularly exhibit superior improvement in mechanical properties,[5–10] gas-barrier properties,[11,12] solvent resistance,[3] and reduced flammability[6,13–15] relative to their unfilled polymer matrices. It should be noted that this is achieved at very low loadings of the nanoparticle, typically 1–10 wt%.[2,4] This allows for the light-weight PLN to be processed by conventional techniques in much the same way as unfilled polymers. However, a well-dispersed microstructure of tactoids, i.e., the exfoliated structure must be ensured in order to achieve the optimal performance of PLNs.[2] Unfortunately, it is indeed difficult to have such structures due to (i) the large aspect ratio of silicate layers, (ii) slow diffusion kinetics of polymer chains inside narrow silicate galleries, and (iii) the unfavorable mixing energy of silicate particles and polymer chains. Consequently, the fabrication of stable microstructures in PLNs has been the topic of many experimental and theoretical studies.

Melt intercalation is a widely used commercial method of PLN production which relies on the mixing ability of silicate layers with polymer melt. Many approaches have been taken in order to promote the intermixing of silicate

A. Gooneie
Chair of Polymer Processing, Department of Polymer Engineering and Science, Montanuniversität Leoben, Otto Glöckel-Straße 2, 8700-Leoben, Austria
E-mail: ali.gooneie@unileoben.ac.at
S. Schuschnigg
Chair of Polymer Processing, Department of Polymer Engineering and Science, Montanuniversität Leoben, Otto Glöckel-Straße 2, 8700-Leoben, Austria
E-mail: stephan.schuschnigg@unileoben.ac.at
Prof. C. Holzer
Chair of Polymer Processing, Department of Polymer Engineering and Science, Montanuniversität Leoben, Otto Glöckel-Straße 2, 8700-Leoben, Austria
E-mail: clemens.holzer@unileoben.ac.at

[a]**Supporting Information** is available from the Wiley Online Library or from the author.

Macromol. Theory Simul. **2016,** *25*, 85–98

DOI: 10.1002/mats.201500045

and polymers. This includes modification of the silicate surface,[9,16,17] changing the molecular structure of the polymer,[18] and incorporation of compatibilizing molecules in the matrix.[19–21] In compatibilized PLNs, the silicate layers are usually modified with surfactant molecules such as alkylammonium. This promotes the compatibility of the layers with the compatibilizing molecules. The compatibilizing molecules could be polymers such as maleic anhydride grafted polypropylene (MA-g-PP). The improved compatibility leads to the improved dispersion of silicate layers in the polymer matrix. Such a mechanism is absent in uncompatibilized PLNs, resulting in the formation of aggregated microstructures. The application of dispersive stresses of shear and/or extensional types is also found to help achieve finer dispersions.[2,22] As a result, the evolution of microstructure under flow has been an intriguing subject and many researchers have devoted years to understand it.

During the processing of PLNs, the material experiences a variety of flow deformations which could cause translation, rotation, bending, and breaking of layered silicates. These phenomena influence the properties of the final part which are highly dependent on the microstructural characteristics and particles orientation. The modeling of spherical[22,23] and non-spherical suspensions such as fibers[24,25] and sheets,[26,27] has been the subject of many publications over the past few decades. The mesoscopic standard orientation model is based on the Jeffery's equation for the motion of a single fiber in an infinite Newtonian matrix.[28] Later, it was modified by Folgar and Tucker to account for fiber–fiber interactions.[29] Afterward, Advani and Tucker improved it by the introduction of the second-order moment tensor of the probability density function for orientation.[30] More recently, various versions of this model have been developed to account for phenomena such as slow orientation kinetics,[31] semiflexibility of the fibers,[32] etc.

In recent years, the rapid development of the computer technology has made complicated numerical simulations possible.[33,34] Computer simulations have made significant contributions to our understanding of shear-induced microstructural evolutions within the limitation of the model complexity and the accessible time and length scales.[35,36] Detailed molecular simulations have shown great potential to model complex phenomena at an atomistic level.[37–41] Coarse-graining technique has been successfully applied to molecular dynamics method in order to access longer time and length scales.[42–44] Anderson et al.[45] utilized coarse-grained molecular dynamics (CGMD) to explore the intermolecular interactions that influence mesoscale morphology development in PLNs. Sinsawat et al.[46] also used CGMD to investigate aspects of the polymer matrix that promote the formation of intercalated or exfoliated structures. More recently, Kalra et al.[47] incorporated CGMD to study spherical nanoparticle dispersions in polymer melts under shear flows. Such studies have shown the capability of computer simulations to help distinguish the phenomena involved in the formation of microstructures in polymer nanocomposites.

A relatively new mesoscopic particle simulation method is dissipative particle dynamics (DPD) proposed by Hoogerbrugge and Koelman in 1992.[48] In its core, DPD is similar to molecular dynamics except that the individual DPD particles (beads) represent the collective dynamic behavior of several molecules.[49] This coarse-graining approach as well as softer interaction potentials between DPD beads allows for the simulation of dynamic phenomena over longer time scales. Benefiting from this advantage, Kim et al.[50] incorporated DPD in order to investigate the conformational behavior of a pH-responsive polymer and its effect on the permeability in clay-polymer nanocomposites. By the implementation of plane Couette flow with the Lees–Edwards periodic boundary conditions into DPD, the method has been widely used as the standard virtual rheometer in particle simulations to obtain steady-state shear properties. It has been utilized in many works to study the rheology of different systems including polymer solutions,[51] surfactant solutions,[52] entangled polymer melts,[53] and suspensions.[54–56] While the method has proved promising in many systems, it still suffers from the intrinsic instabilities at very low or very high shear-rates and needs further improvements.[52,57]

The rheology of dispersed particles in solutions or polymer melts has already been treated with DPD.[54–56,58] The presence of non-spherical solid particles with complex geometries in the matrix usually leads to more difficult and time-consuming calculations. A common method to overcome such problems, the freezing technique, has been employed in several works.[55] In the freezing technique, a large solid particle is constructed out of smaller spherical particles by aggregating them as a rigid entity. While this approach has been shown to entail significant savings in computational costs, it loses an important physical characteristic of non-spherical particles with high aspect ratios, i.e., semiflexibility and bending of the particles.

In this work, we have constructed a three-layered silicate particle out of spherical beads by defining interaction potentials for bonds, bond angles, and bond dihedrals. In this manner, the layers of silicate could show controlled semiflexibility and, therefore, represent a more realistic description of the particles. These particles were added to a polymer melt and imposed to shear flows with different directions and shear-rates. The rearrangement of the layers was followed to study the orientation of the particle under flow. Pair distribution functions were calculated in three orthogonal planes in order to provide a better perspective over the orientation process. Finally, the effects

of silicate surface modification and compatibilizing agents were explored. It was achieved by replacing some of the polymer chains with compatibilizer molecules as well as changing the interaction coefficients between the beads.

2. Simulation Details

DPD was first introduced by Hoogerbrugge and Koelman to study the colloidal suspensions.[48] In standard DPD, each particle (bead) is subject to the sum of three central, pairwise, additive forces: the conservative force (F_{ij}^{C}), the dissipative force (F_{ij}^{D}), and the random force (F_{ij}^{R}). [49] The definitions of these forces are:

$$F_{ij}^{C} = a_{ij}\chi_{ij}\left(1-\frac{r_{ij}}{r_C}\right)\hat{\mathbf{r}}_{ij} \quad (1)$$

$$F_{ij}^{D} = -\gamma_{ij}\omega^{D}r_{ij}\left[\left(\mathbf{v}_i-\mathbf{v}_j\right)\cdot\hat{\mathbf{r}}_{ij}\right]\hat{\mathbf{r}}_{ij} \quad (2)$$

$$F_{ij}^{R} = \sigma_{ij}\omega^{R}r_{ij}\xi_{ij}\hat{\mathbf{r}}_{ij} \quad (3)$$

Here, r_{ij} is the distance between the beads i and j, $\hat{\mathbf{r}}_{ij}$ is the unit vector pointing from the center of bead j to that of bead i, χ_{ij} equals one for beads with a distance less than the force cutoff radius r_c and equals 0 otherwise. a_{ij} is the maximum repulsion between bead i and bead j. γ_{ij} and σ_{ij} are the friction coefficient and the noise amplitude between bead i and bead j, respectively. $\underline{\boldsymbol{\omega}}^{D}$ and ω^{R} are r_{ij}-dependent weight functions. The system obeys the fluctuation-dissipation theorem in which one of the two weight functions fixes the other one.[59] This theory necessitates that

$$\omega^{D}\left(r_{ij}\right) = \left[\omega^{R}\left(r_{ij}\right)\right]^2 \quad (4)$$

$$\sigma_{ij}^2 = 2\gamma_{ij}k_BT \quad (5)$$

In our simulations, the weight functions are defined as

$$\omega^{D}\left(r_{ij}\right) = \left[\omega^{R}\left(r_{ij}\right)\right]^2 = \chi_{ij}\left(1-\frac{r_{ij}}{r_C}\right)^2 \quad (6)$$

$\mathbf{v}_i$ and $\mathbf{v}_j$ are the velocity vectors of the ith and jth beads, respectively. ξ_{ij} is a Gaussian random number with zero mean and unit variance. Recently, some modifications for standard DPD formulation have been proposed. Pan et al.[56] developed a new formulation of DPD in the spirit of fluid particle model in such a way that the dissipative forces were explicitly divided into central and shear components. It allowed them to redistribute and balance these forces to obtain the correct hydrodynamics in the study of Brownian colloidal suspensions. In order to capture the physics of entangled polymer melts, Yamanoi et al.[53] used entanglement forces instead of conservative forces and were able to reproduce both static and dynamic properties of linear polymer systems.

In this work, the standard DPD formulation was incorporated in order to run the simulations. Nikunen et al.[60] have shown that for short polymer chains (such as this study) the standard DPD formulation is accurate enough to capture the dynamics of the polymer chains. The short chains perfectly depict Rouse-like dynamics utilizing the standard DPD.[61] If longer chains were incorporated in the simulations, it would be necessary to modify the DPD formulation in order to capture the reptation dynamics as well.[43,44,53] However, the model in this work is based on short chains and it is not necessary to introduce any changes to the standard DPD formulation. Length, mass and energy are in units of force cutoff radius, mass of a single DPD bead, and k_BT, respectively. Here, k_B is the Boltzmann's constant and T is the absolute temperature. All of these variables are set to unity in our simulations. In the simulations, DPD thermostat is utilized to control the temperature. Table 1 gives the maximum repulsion parameters that have been used to characterize the PLN systems. It is important to note that in this paper all the values are in DPD units unless noted otherwise. For uncompatibilized systems with no silicate surface treatment, the repulsion parameters for polymer–silicate and silicate–silicate pairs were taken from the works of Scocchi et al.[62] and Pereira et al.[63] They had used a multiscale method to evaluate rescaled self and mixed DPD energies from binding and non-binding energies of molecular dynamics simulations. In this manner, they were able to reproduce the maximum repulsion parameters for DPD simulations of PA 6-Clay and PP-Clay nanocomposites. With the addition of the third species, i.e., the compatibilizer, to the PLNs and treatment of the silicate surfaces, the parameters were changed accordingly. Surface treatment is usually performed by the addition of aliphatic molecules to the surface of the layers.[2] Based on detailed DPD simulations (see Supporting Information for more details), we decided that the surface treatment could be simply incorporated in the simulations by changing the surface energy of the silicate beads without actually adding them to the simulation system. This assumption excludes the physical effects of these molecules such as steric hindrance against polymer penetration and reduction of gallery distance. Nevertheless, it is justified by the simplifying nature of the coarse-graining approach used to model silicate layers in DPD. The repulsion parameters in compatibilized systems were obtained from (i) the theoretical Flory–Huggins parameters of sample polyethylene-g-maleic anhydride mixtures,[18] and (ii) the rescaled molecular dynamics energies of alkylammonium surfactant molecules with short aliphatic tails.[62,63] Yildirim and Yurtsever [18] have reported the variations

Table 1. The maximum repulsion parameters used to characterize the PLN systems.

	Polymer	Layered silicate	Compatibilizer
Without compatibilizer and surface treatment			
Polymer	25	33	–
Layered silicate	33	15	–
Compatibilizer	–	–	–
With compatibilizer and surface treatment			
Polymer	25	30	32
Layered silicate	30	32.8	10
Compatibilizer	32	10	32

of the Flory–Huggins interaction parameter (χ) with temperature between polyethylene and polyethylene grafted maleic anhydride. According to their results, $\chi \approx 2$ at 190 °C. By incorporating the equation $\chi = (0.286 \pm 0.002)(a_{ij} - 25)$ proposed by Groot and Warren,[49] one can estimate $a_{ij} = 32$ for polymer–compatibilizer interactions Pereira et al.[63] have reported repulsion parameters between aliphatic tails of alkylammonium molecules in a variety of PLNs to vary in the range from 30.2 to 32.8. Since the polyolefin-based compatibilizer molecules closely resemble such aliphatic tails a value of a_{ij}=32 was chosen to represent the compatibilizer–compatibilizer interactions.[62] In compatibilized systems, the coarse-grained silicate beads are assumed to include surfactant molecules and therefore the interactions of such beads with other components should be similar to that of the surfactant. This is indeed a valid assumption considering that in practice the surfactant molecules are supposed to alter the interactions between silicate layers and other components.[2] Consequently, the polymer–silicate and silicate–silicate interactions were represented by a_{ij}=30 and 32.8, respectively.[62,63] Finally, the repulsion parameter of compatibilizer–silicate interactions was set to 10 which is in the orders of silicate–silicate interactions.[63] This value is based on the fact that in a compatibilized system the compatibilizer beads should exhibit weak repulsion with the silicate beads in order to promote their dispersion. A comparatively detailed system was also simulated where the silicate layers were covered with aliphatic surfactants (see Supporting Information). In these detailed simulations the repulsion parameters were taken from the work of Scocchi et al.[62] and used without any change. The results from the simulations were in good agreement with the results from the constructed system here. Therefore, it justifies utilizing coarse-grained silicate beads including surfactant aliphatic tails and correcting the repulsion parameters. Indeed, a careful modification of the repulsion parameters is crucial to achieve accurate results. The friction coefficients were set to 5.6 for interactions of all types with silicate beads and 4.5 for other pairs. These typical values have been used in many works by other authors.[49,50,55,57,64–67]

The flexible polymer and compatibilizer molecules were modeled as linear chains of 20 and 5 beads linked together using harmonic springs with spring constants of 20 and 5, respectively. A three-layered silicate molecule of 21 × 21 beads in each layer was constructed to represent the nanoparticle, see Figure 1. The beads of the layered silicate were connected with bead-spring harmonic potentials with a spring constant of 500.[50] By the introduction of harmonic potentials for bond angles and dihedrals, each layer was allowed to experience limited bending and curvature in order to provide an accurate representation of semiflexible silicate layers. The coefficients of harmonic

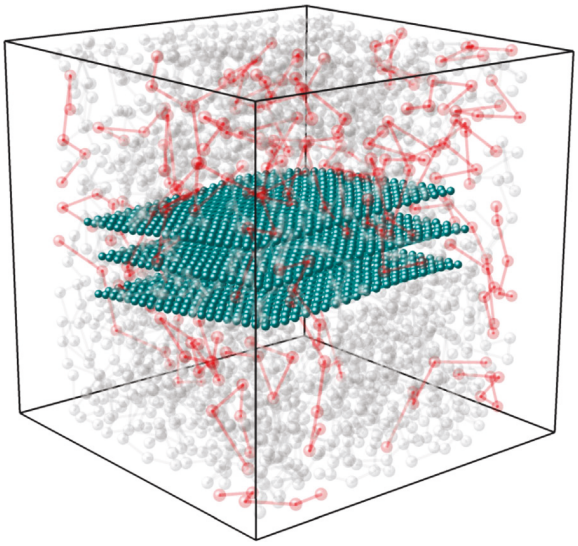

Figure 1. A snapshot of a compatibilized system, with the three-layered silicate in the center of the box. The compatibilizer molecules are shown in red and the polymer chains are transparent to preserve clarity.

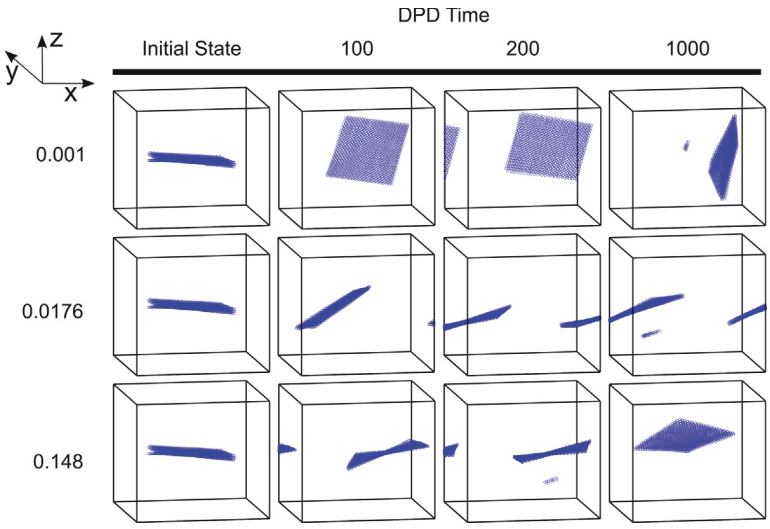

Figure 2. Trajectories of the layered silicate in DPD time at different shear-rates in uncompatibilized systems. The flow is defined by $V_x - G_z$ and the shear-rate of each row is given in the figure. The beads are allowed to go out and come back in the simulation box by the application of the periodic boundary conditions.

bond angles and dihedrals were all set to 1000. This value has been successfully incorporated before in CGMD simulations to define the stiffness of each sheet in terms of Lennard Jones energy unit.[45,46] However, it is necessary to use rather smaller time steps than conventional in order to assure structural stability of the molecules. Here, the time step for all simulations was set to 0.001.

The molecules were allowed to equilibrate before starting the flow. The computational domain was set to $10 \times 10 \times 10$ in DPD units. Each side of the simulation box represents approximately 200 nm in actual dimensions. Initially, it was filled with polymer (and compatibilizer) chains to have a bead number density of 3. Then, the layered silicate was added to the center of the box. All of the chains which were fully or partially inside the galleries were deleted. It resulted in 2742 polymer (and compatibilizer) beads and 1323 silicate beads, giving a bead number density of almost 4 for the simulations. Systems with 0 and 10 vol% of compatibilizer were studied in this work. By the incorporation of Lees–Edwards boundary condition, the system was sheared in different directions (with respect to the initial orientation of the layers). Besides, different shear-rates were applied in order to study the orientation of the particle. In this paper, the applied shear flows are defined by their velocity and velocity gradient directions. For instance, a shear flow defined by $V_x - G_y$ is representative of a flow with the velocity in x-direction and the velocity gradient in y-direction. The applied shear-rates were 0.001, 0.0176, and 0.148 in DPD units. Utilizing the method proposed by Fedosov et al.,[57] these values are approximately equal to actual shear-rates of 0.817, 14.38, and 120.92 s^{-1}, respectively, in an equivalent experimental setup. The nondimensional Peclet number (Pe) is also evaluated in the simulations. The Pe number could provide the possibility to compare our simulations with other simulations and even with experiments. The Pe number can be calculated using[68]

$$\mathrm{Pe} = 6\pi\eta\frac{\dot{\gamma}\, l_P^3}{k_B T} \tag{7}$$

In this equation, η is the viscosity of the polymer, $\dot{\gamma}$ is the applied shear-rate in the simulations, and l_p is the characteristic length of the layered silicate particles. This length equals 5 in DPD length unit in our simulations corresponding to the length of a silicate layer. Here, $k_B T$ equals 1. Since the polymer chains follow the Rouse dynamics in our simulations, the Rouse model is utilized to estimate η assuming that it does not depend on the shear-rate. This model predicts the viscosity as[69]

$$\eta = \frac{\xi\rho a^2 M N_0}{36 M_0^2} \tag{8}$$

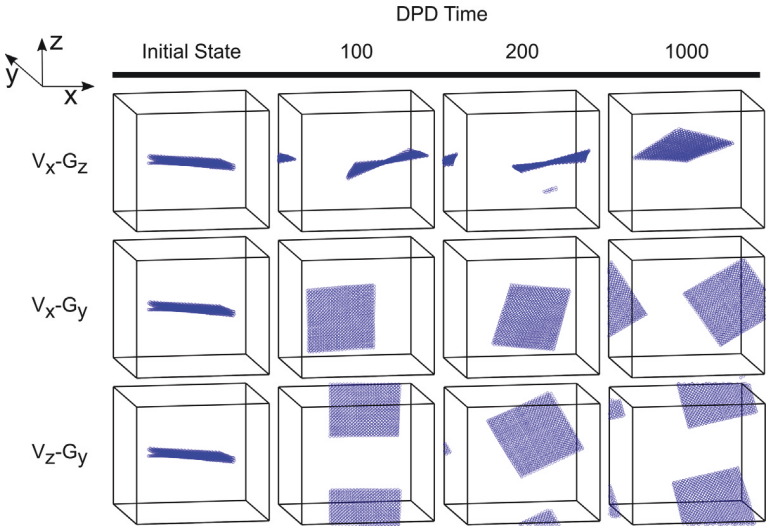

Figure 3. Trajectories of the layered silicate in DPD time under different flow directions in uncompatibilized systems. The shear-rate is 0.148 and the flow of each row is defined in the figure. The beads are allowed to go out and come back in the simulation box by the application of the periodic boundary conditions.

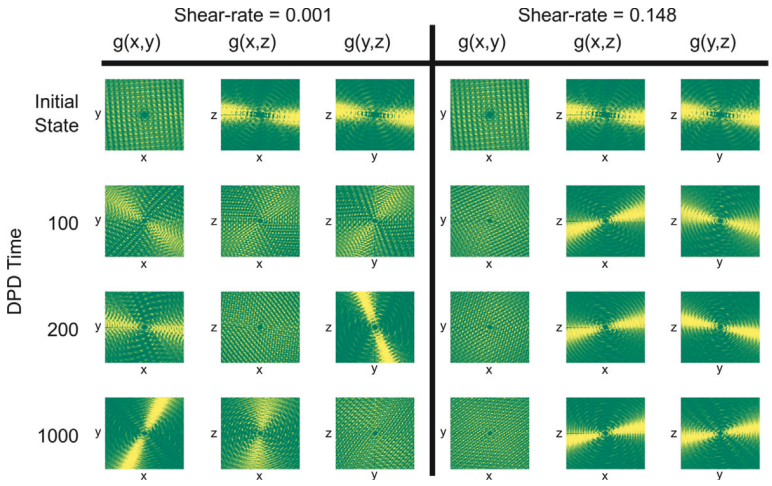

Figure 4. Pair distribution function in orthogonal planes at different time and shear-rates in uncompatibilized systems. The flow is defined by $V_x - G_z$. The shear-rates and times are given in the figure. The time of each row is shown in front of it.

where ξ is the bead–bead friction coefficient, and ρ is the bead number density which is 2.74 in our simulations. a and M_0 are the characteristic length and the molecular weight of each bead which both equal 1. M is the molecular weight of a chain which is 20 in our simulations. $\frac{\rho N_0}{M}$ is the number density of the chains in the simulation box and equals 0.137. By incorporating these equations, the Pe number is approximately 16.15, 284.27, and 2390.45 at the applied shear-rates of 0.001, 0.0176, and 0.148 in DPD units, respectively.

The simulations were run for 10^6 time steps and the beads trajectories recorded. Based on the trajectory data, the pair distribution functions of the simulated silicate beads were calculated according to Morris and Katyal[70] in three orthogonal planes, i.e., the flow plane, the shear plane, and the neutral plane. Such data help visualize the orientation of the layered silicate in space. The average normal vectors of the silicate layers were also calculated. These vectors were used to find the angle of the sheets with the flow and/or the velocity gradient directions.

3. Results and Discussion

3.1. Uncompatibilized Systems

Shear flow fields were applied to the model uncompatibilized systems to study the orientation phenomena. The evolution of the particle orientation under flow is demonstrated in Figure 2 at different shear-rates. In this figure, the applied shear flow is defined by $V_x - G_z$. The beads are allowed to travel through the walls (if not normal to the velocity gradient direction) of the simulation box by the application of the well-known periodic boundary conditions. One can see that the layers rearrange in space with time. At low shear-rates, the layers show some deviations from the complete alignment, and therefore there might be snapshots with no preferred orientation whatsoever. However, the orientation gets more prominent with an increase in shear-rate and the distorted orientation of the layers is suppressed to a great deal. The shear-rate dependency of orientation is also observed experimentally for anisometric particles such as fibers,[31,32,71,72] carbon nanotubes,[1] clays,[73–78] etc. It should be noted that the

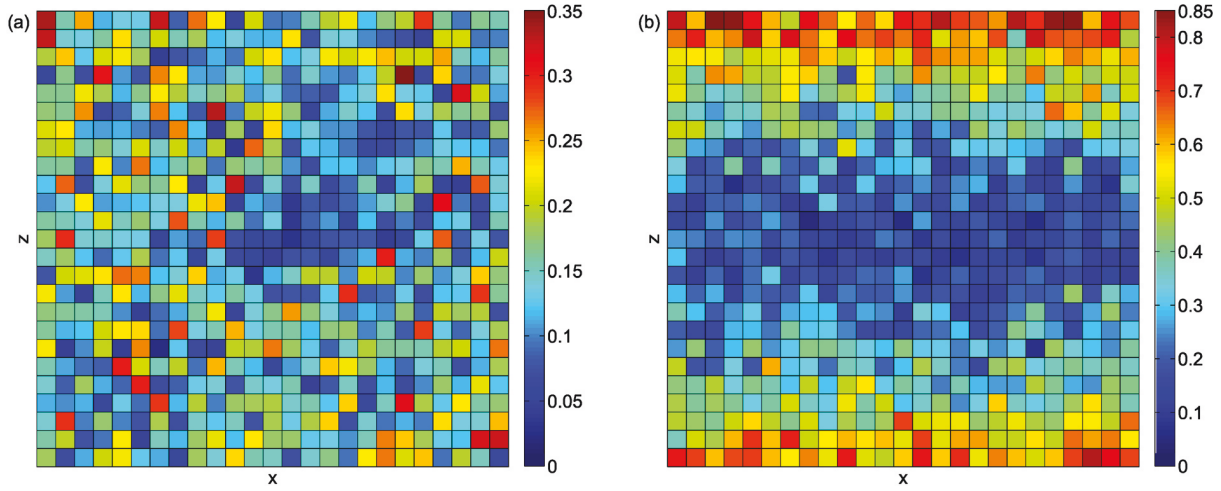

Figure 5. Time-averaged values of the velocity magnitude in the simulation box in uncompatibilized systems. The box is viewed from the xz-plane for a shear-rate of (a) 0.001 and (b) 0.148 in DPD unites. The applied flow is $V_x - G_z$.

semiflexible nature of the simulated layered silicate is reflected in the trajectory data.

It is interesting to perform the same analysis when the flow direction is changed. Figure 3 shows the trajectory of the layers in space for different flow directions at a constant shear-rate. The results explicitly indicate that the silicate layers rotate and rearrange themselves in respect to the flow direction. From these trajectories, it appears as if in the preferred orientation the layers are normal to the applied velocity gradient direction. This observation is in agreement with the small angle X-ray scattering measurements of Bihannic et al.[79] and Philippe et al.[68] They reported that natural clay particles tend to align with their surface normal to the velocity gradient direction and partly rotate around flow streamlines.

In order to provide a three-dimensional overview of the microstructure evolution in time, the pair distribution function was calculated in three orthogonal planes. The results are shown in Figure 4 for two different shear-rates. The data perfectly reflect the orientation of the layers under flow in different planes. Some deviations in alignment are present at low shear-rates as inherited from their corresponding trajectories. The origin of such deviations could be discussed based on the nature of DPD simulations. It has been shown before that the applied velocity gradient in the Lees–Edwards boundary conditions loses its linearity at very low shear-rates.[52,57] Therefore, it results in local flow heterogeneities in the simulation box. These heterogeneities would impact the local force field around the beads and temporarily alter the direction of the force field. As a consequence of such distortions, the movements of the beads would depict a more random path and contribute to the apparent oscillations in the generated trajectories.

Figure 5 shows the time-averaged velocity magnitude distribution in the simulation box for low and high shear-rates. In this simulation, the applied shear flow is defined by $V_x - G_z$. It is evident that the velocity field is quite distorted at low shear-rates (Figure 5a) while it is well-developed at high shear-rates (Figure 5b). It is noteworthy that the orientation field is known to be strongly dependent on the Pe number.[68] This number characterizes the ratio of the viscous to thermal stresses. If Pe is small (usually the case at low shear-rates), the thermal fluctuations become more important. Thus, at low shear-rates the microstructure is controlled more by Brownian motions rather than shear forces. This crucial issue not only dominates the DPD simulations, but also influences experimental measurements.[68,79] Regardless of the deviations at low shear-rates, for high Pe numbers the layers reorganize themselves to be normal to the velocity gradient direction. Figure 6 plots the pair distribution function at the end of the simulations in different planes. As expected, the orientation has completed at high shear-rates.

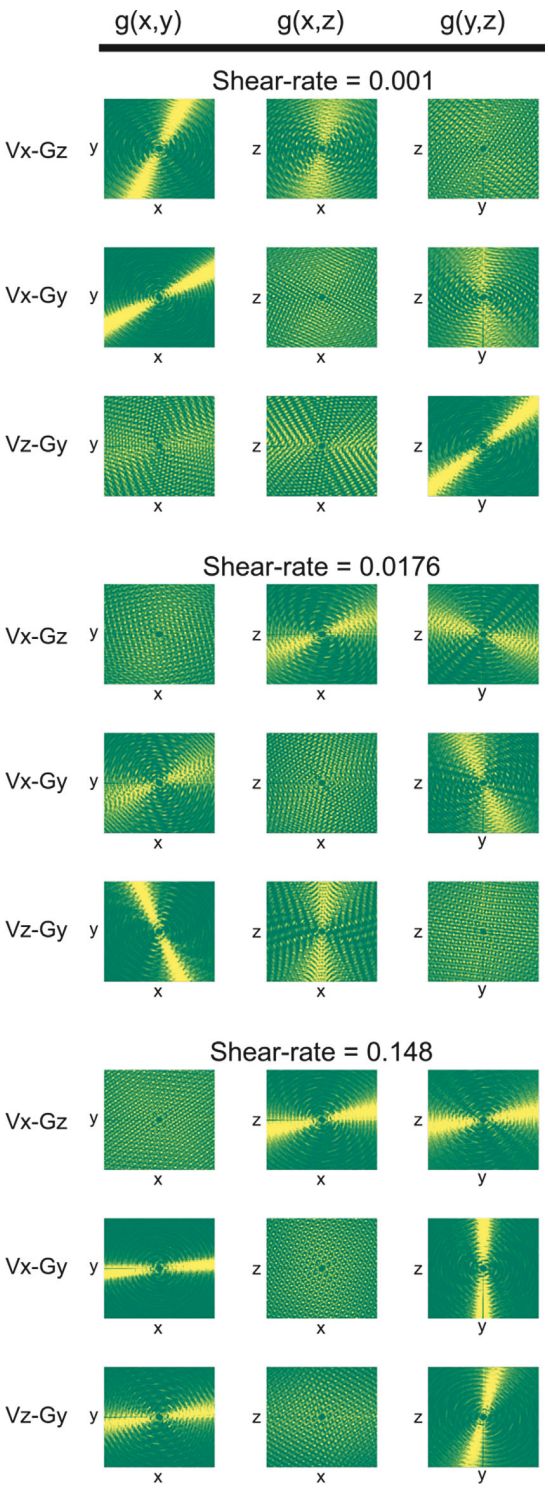

Figure 6. Pair distribution function in orthogonal planes at different shear-rates at the end of the simulations in uncompatibilized systems. The flow is defined for each row and the shear-rates are given in the figure.

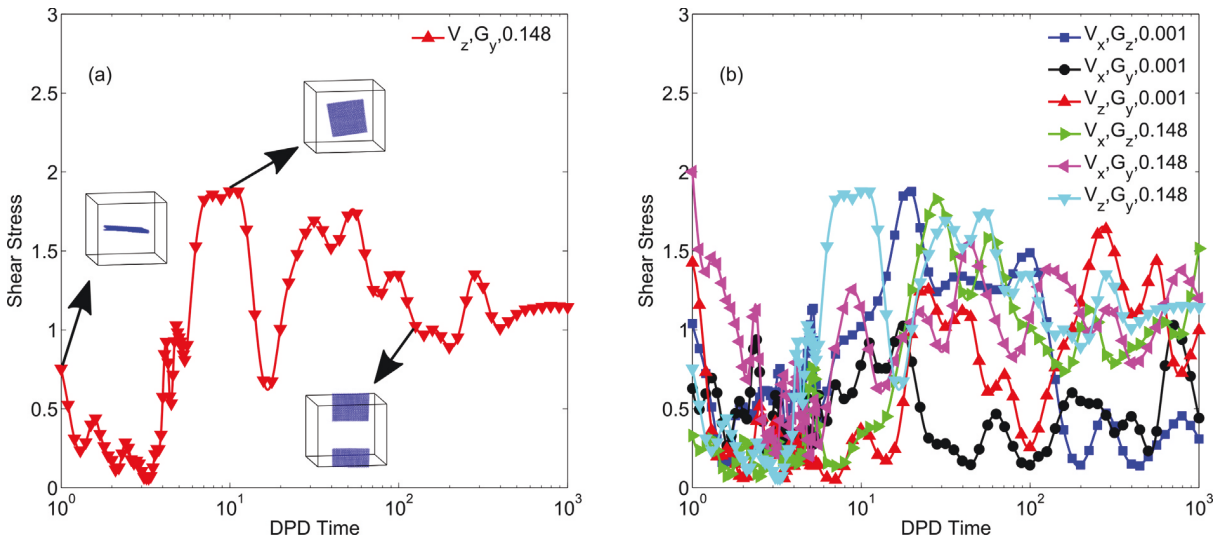

Figure 7. The evolution of the shear stress with simulation time in uncompatibilized systems; The stress plots are shown in (a) for the flow $V_z - G_y$ and shear-rate of 0.148, and in (b) for various systems. The trajectories of the layered silicate are shown on the stress plot in (a).

During the course of orientation, the imposed flow is supposed to provide the anisometric silicate layers with the necessary energy to rotate in space. This phenomenon is shown in many works to appear with an overshoot in the stress profile with time.[31,72,75,77,78] The shear stress in the simulations was recorded with time and plotted in Figure 7 for different setups. The states of the layers at different stages are also included in Figure 7a. One can see that the stress increases slightly with the progress of orientation until it completes. Then, it declines and reaches a steady value. However, the attained maximum stress values are not very distinct and are in the range of numerical uncertainties of the simulations producing the noises in the stress signal, see Figure 7b. From the stress data, it appears as if the orientation of the layers is not a very energy-consuming process. Apparently, more powerful flows only accelerate this process while balancing out thermal fluctuations and keeping the alignment of the layers intact. More discussion will be provided on this issue throughout the rest of the paper.

3.2. Compatibilized Systems

With the compatibilizer molecules present in the system and the silicate layers treated, the shear flow is expected to orient the layers and separate them from one another.[2,4,7,21] In the equilibrium run prior to the startup of the flow simulations, the galleries opened up to some extent and the interlayer distance was increased. Figure 8 demonstrates the evolutions of the microstructure under flow for compatibilized systems. In the frames, the flow is defined by $V_x - G_z$, and the beads are allowed to go out and come back inside the simulation box through the application of periodic boundary conditions. In this way, the separation of the layers could be visualized more easily. As anticipated, the layers are separated to a higher extent. At high shear-rates the layers disperse along the flow direction while all of them almost keep their surface normal to the velocity gradient

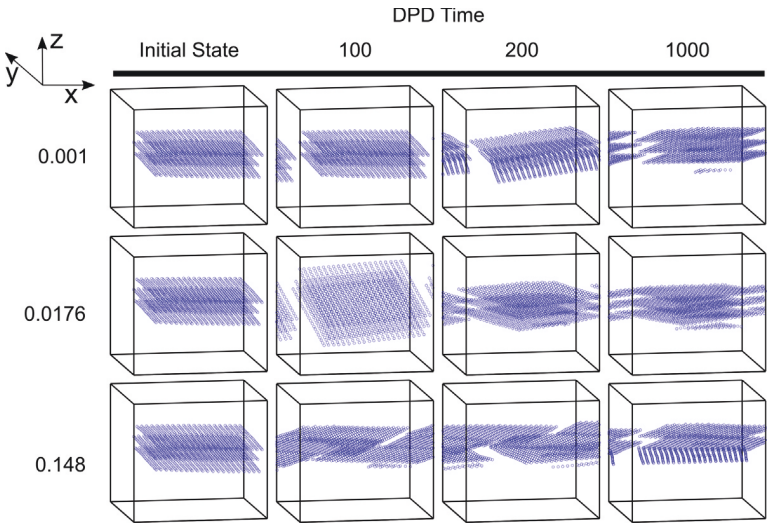

Figure 8. Trajectories of the layered silicate in DPD time at different shear-rates in compatibilized systems. The flow is defined by $V_x - G_z$ and the shear-rate of each row is given in the figure. The beads are allowed to go out and come back in the simulation box by the application of the periodic boundary conditions.

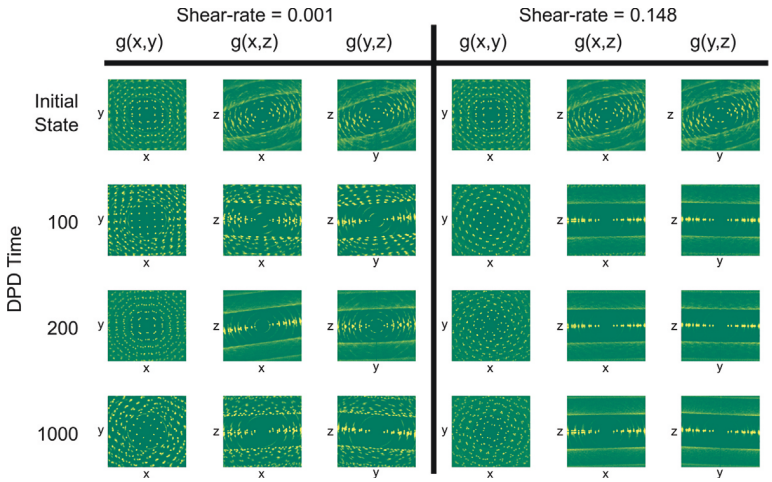

Figure 9. Pair distribution function in orthogonal planes at different time and shear-rates in compatibilized systems. The flow is defined by $V_x - G_z$. The shear-rates and times are given in the figure. The time of each row is shown in front of it.

direction. Evidently, the microstructure changes from tightly packed oriented layers to the exfoliated oriented layers under the flow by surface treatment of the silicate layers and introduction of the compatibilizer molecules. The layers are expanded to some extent in comparison with uncompatibilized systems. This suggests improved thermodynamic affinity between the components due to the lower repulsion coefficients.[62,65] It should be noted that high exfoliation degrees are only achieved at high shear-rates. The reason is that at high shear-rates, the larger velocity difference between the adjacent layers results in increased exfoliation degrees along the flow direction.

To further investigate the microstructure, pair distribution functions in different planes are plotted in Figure 9. It is clear that the layers align with their surfaces almost normal to the velocity gradient direction as in the uncompatibilized systems. The results approve this idea that the orientation process occurs more stably in compatibilized systems, even though it may not complete in the simulation time at low shear-rates. The slowed-down kinetics of orientation points to the increased resistance against translation and rotation of the silicate layers. To explain this observation, shear stress of the systems is plotted against time in Figure 10. A sudden increase in the stress is apparent when the layers start to align in respect to the applied shear flow. According to the trajectories, the stress decays gradually to complete the orientation of compatibilized systems as a sign of reaching a stable microstructure. By comparing the stress profiles in the uncompatibilized and compatibilized systems, one might ascribe the significant increase in the stress to the larger interfacial area of the silicate in the compatibilized systems. For tightly packed silicate layers, matrix molecules and silicate can interact through two effective interfaces while this number increases to six as a result of exfoliation. Therefore, more resistance against the silicate mobility is expected from the matrix molecules. In order to investigate this hypothesis, uncompatibilized and compatibilized single-layered

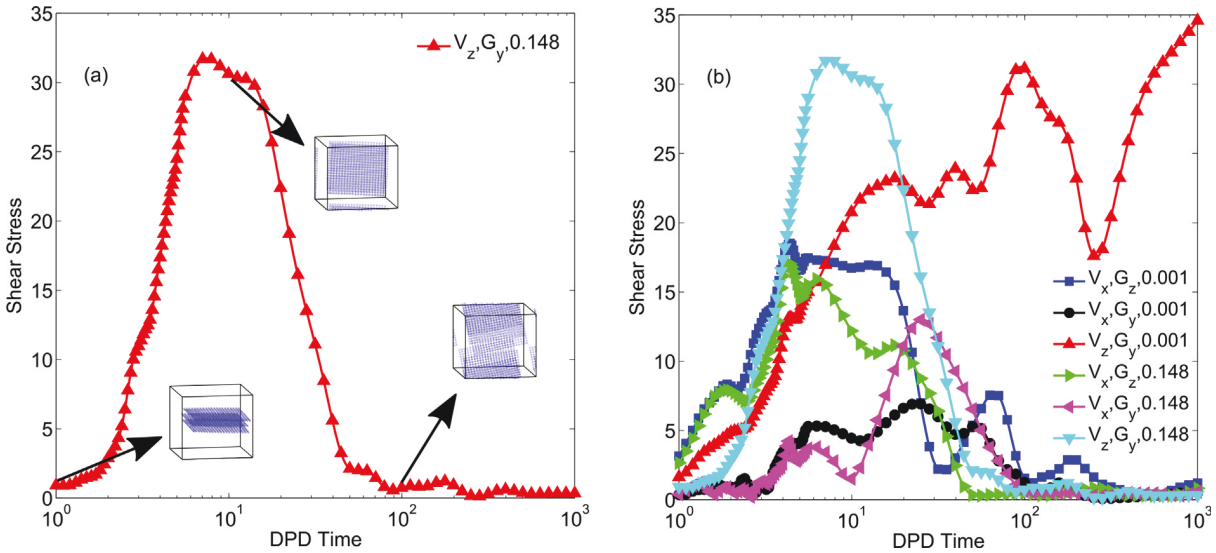

Figure 10. The evolution of the shear stress with simulation time in compatibilized systems; The stress plots are shown in (a) for the flow $V_z - G_y$ and shear-rate of 0.148, and in (b) for various systems. The trajectories of the layered silicate are shown on the stress plot in (a).

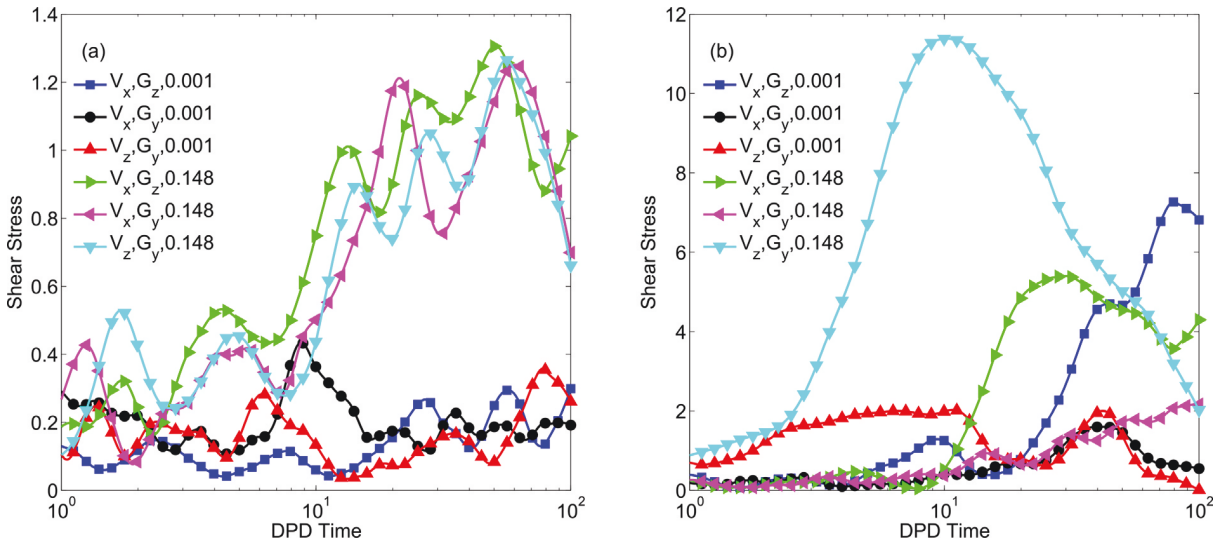

Figure 11. The evolution of the shear stress with simulation time in (a) uncompatibilized and (b) compatibilized systems for different flows. A single-layered silicate is used in these simulations.

silicate nanocomposites were simulated with the same conditions as their multilayer counterparts. In this way, one makes sure that the effective interface is the same in both systems. The stress profiles of the corresponding systems are shown in Figure 11. To compare the results for all systems, the maximum shear stress values in each setup is plotted in Figure 12. It includes results of all flow directions, applied shear-rates, single- and three-layered silicate simulations. One can see that the maximum stress values reached are reduced in the single-layered silicate samples in all systems. However, there is still a pronounced maximum in the stress values of compatibilized systems with orientation while it is not distinct in the uncompatibilized systems (see Figure 11; notice the different y-scales). Consequently, while the interacting interface of the silicate is of critical importance in the development of resisting forces against orientation, it is not for sure the only reason for such a sharp increase in stress. Otherwise, the uncompatibilized and compatibilized systems with a single-layered silicate should almost behave in the same way.

With a closer look at the interface of the simulated nanocomposites, one notices the close contacts of polymer and compatibilizer beads with the silicate beads in the compatibilized systems, see Figure 13. Such contacts are significantly reduced in the uncompatibilized

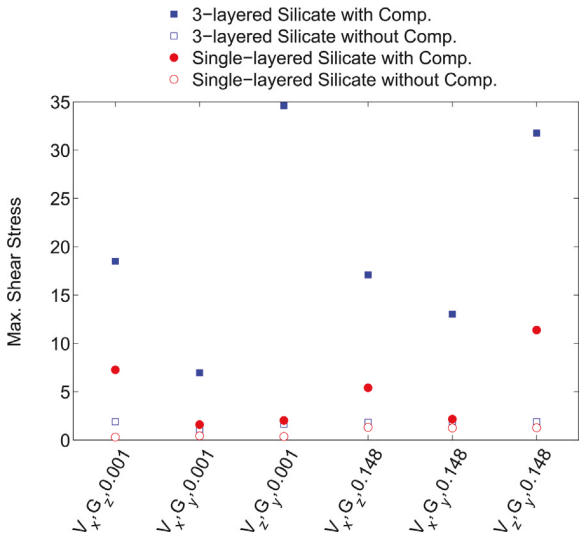

Figure 12. The maximum shear stress values for different simulation setups in uncompatibilized and compatibilized systems. Single- and three-layered silicate simulations are included for comparison. Note that some data points are overlapping.

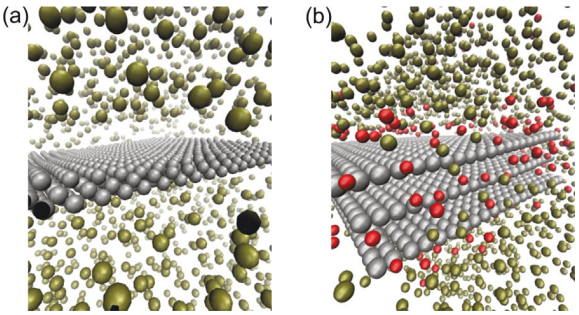

Figure 13. A snapshot of the interface of the layered silicate in (a) uncompatibilized and (b) compatibilized systems. The silicate, compatibilizer, and polymer beads are shown in gray, red, and green, respectively. The bonds are not shown for clarity.

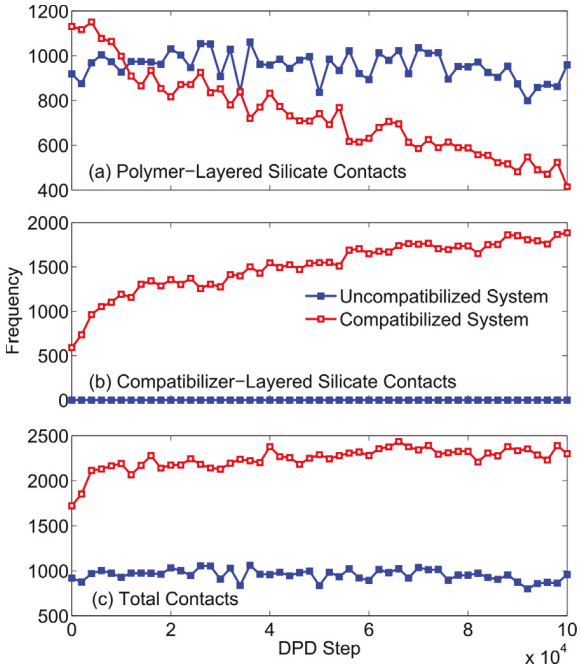

Figure 14. Number of contacts between the beads of (a) polymer-layered silicate, (b) compatibilizer-layered silicate, and (c) the total contacts in uncompatibilized (filled blue markers) and compatibilized (empty red markers) systems. A single-layered silicate is used in these calculations.

nanocomposites due to the higher repulsion parameters present.[2,62,63] The more contacts occur at the interface, the more energy is dissipated due to the friction. Such energy-consuming contacts increase the overall viscosity of the nanocomposites. Consequently, it requires higher stresses and longer times to complete the orientation as evidenced by results. In Figure 14, the number of bead–bead contacts between polymer–silicate, compatibilizer–silicate, and the sum of these contacts are plotted for the uncompatibilized and compatibilized systems of a single-layered silicate PLN. The contact between two beads is defined when their centers are distanced equal or shorter than the cutoff radius from each other. The results clearly show that the total number of contacts at the silicate interface for the compatibilized system is more than two times of the contacts in the uncompatibilized counterpart. Moreover, one can also observe that the compatibilizer beads gradually replace the polymer beads at the interface of silicate layers. This phenomenon is simply a result of the lower repulsion parameter between silicate and compatibilizer beads. These contacts contribute to more than 75% of total contacts leading to increased friction forces at the interface. Such higher dissipated energy values should be provided by the shear forces as it is seen in the shear stress data. Therefore, the significant increase in the shear stress with the orientation progress in compatibilized systems is a result of both the available interacting interface and number of contacts between the silicate and matrix beads (including the compatibilizer) through such interfaces.

In order to provide a comparative analysis of the orientation state with time for uncompatibilized and compatibilized systems, the average orientation angles of the systems were calculated. For this purpose, the orientation angle was calculated as the complement of the angle between the normal vector of the silicate layer and the flow direction. For a three-dimensional microstructure comparison, the complement of the angle between the normal vector of the silicate layer and the velocity gradient direction was also evaluated. The results are shown in Figure 15 and 16. The final microstructure of the compatibilized systems under flows with different directions show the preferred orientation of the silicate layers according to the flow direction in all setups. The oscillations in the orientation angle are obvious in

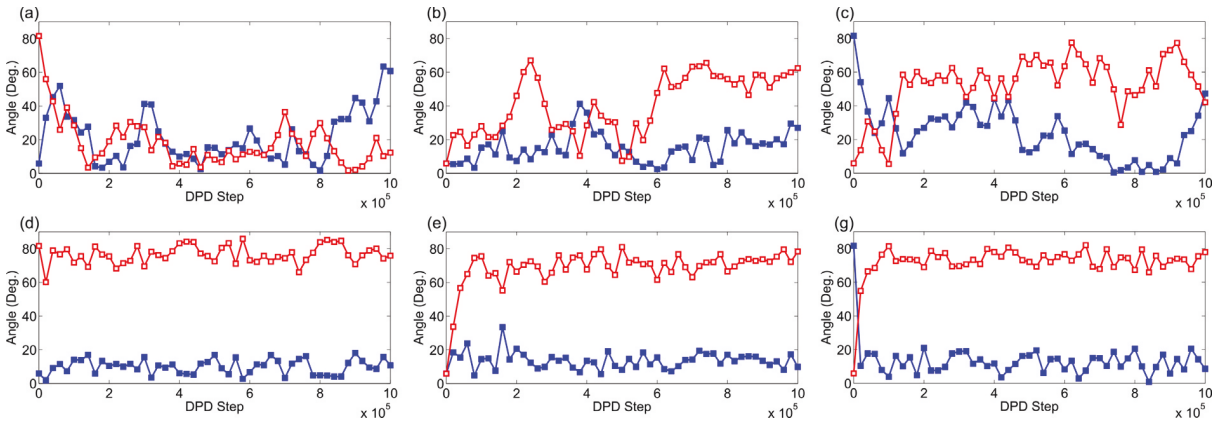

Figure 15. The evolution of the orientation angle (filled blue markers) and the angle with the velocity gradient direction (empty red markers) in uncompatibilized systems. The flow type is $V_x - G_z$ in (a, d), $V_x - G_y$ in (b, e), and $V_z - G_y$ in (c, g). The applied shear-rate is 0.001 in (a, b, c) and 0.148 in (d, e, g).

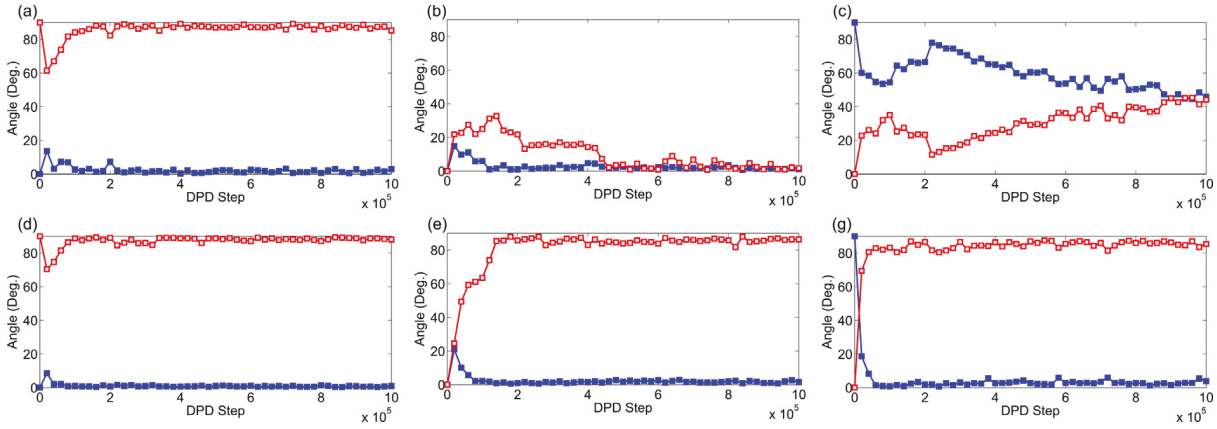

Figure 16. The evolution of the orientation angle (filled blue markers) and the angle with the velocity gradient direction (empty red markers) in compatibilized systems. The flow type is $V_x - G_z$ in (a, d), $V_x - G_y$ in (b, e), and $V_z - G_y$ in (c, g). The applied shear-rate is 0.001 in (a, b, c) and 0.148 in (d, e, g).

uncompatibilized systems, both at low and high shear-rates. However, they are significantly reduced by increasing the applied shear-rate. In compatibilized systems, the evolution of orientation angle is more stable in all shear-rates. One might explain, it as a result of the increased Pe number due to higher shear stress values.[68] This increase is also responsible for incomplete orientation in some samples at low shear-rates during the time scope of the simulation. At high shear-rates, however, the orientation process is stable and reaches the completely oriented microstructure within the simulation time. The results clearly support that the stability of the orientation process increases in compatibilized systems and higher shear-rates.

4. Conclusion

The orientation of layered silicate particles in polymer melts under different shear flows was studied utilizing DPD method. An anisometric semiflexibile three-layered silicate particle was inserted in a simulation box filled with polymer chains. The system was imposed to shear flows with different directions as well as shear-rates. The trajectories were recorded in order to follow the orientation process with time. Moreover, pair distribution functions were calculated in three orthogonal planes in order to provide a three-dimensional view over the orientation process. Regardless of the applied flow direction, it was shown that the layers rearrange themselves so that their surfaces would be normal to the velocity gradient direction. Some deviations from a completely oriented microstructure were evidenced at low shear-rates. It was ascribed to the local flow heterogeneities as well as the small Pe number at low shear-rates. The comparison of the time-averaged velocity magnitude profiles in the systems at low and high shear-rates proved the existence of such heterogeneities. Furthermore, the small Pe number at low shear-rates was found responsible for the dominating thermal fluctuations disturbing the completely oriented microstructure. These observations were in good agreement with previous publications.

The effects of silicate surface treatment and compatibilizing molecules were studied by introducing compatibilizer molecules and modifying the repulsion parameters between the beads. Higher exfoliation degrees were evidenced in such compatibilized systems at high shear-rates while none was seen in uncompatibilized counterparts. In compatibilized systems, the pair distribution functions and trajectory data showed that the silicate layers align perpendicular to the velocity gradient direction the same as the uncompatibilized systems. However, it was demonstrated that the orientation process becomes more stable in these systems even at low shear-rates. The calculations of the orientation angle as well as the angle with the velocity gradient direction also showed this behavior.

The shear stress was plotted with time for uncompatibilized and compatibilized systems. The stress profile falls in numerical uncertainties in uncompatibilized systems while it shows a characteristic overshoot in compatibilized systems. This overshoot was shown to be a result of (i) the large interfaces between the silicate layers and the matrix due to the exfoliation and (ii) the increased number of bead–bead contacts between the matrix and the layers leading to higher energy dissipations. This idea also explains why the orientation process becomes more stable in compatibilized systems even at low shear-rates. In compatibilized systems, higher energy dissipations lead to an increase in the overall viscosity (as reflected in the shear stress data) and therefore Pe number. The contribution of

thermal fluctuations to the overall response of the system becomes less significant compared with the shear stresses. Thus, the orientation process is less controlled by such distortions.

Received: June 25, 2015; Revised: September 15, 2015; Published online: September 29, 2015; DOI: 10.1002/mats.201500045

Keywords: compatibilizer; dissipative particle dynamics; layered silicate; orientation; shear flow

[1] S. Abbasi, P. J. Carreau, A. Derdouri, *Polymer* **2010**, *51*, 922.
[2] C.-W. Chiu, T.-K. Huang, Y.-C. Wang, B. G. Alamani, J.-J. Lin, *Prog. Polym. Sci.* **2014**, *39*, 443.
[3] S. Pavlidou, C. D. Papaspyrides, *Prog. Polym. Sci.* **2008**, *33*, 1119.
[4] S. Sinha Ray, M. Okamoto, *Prog. Polym. Sci.* **2003**, *28*, 1539.
[5] D. J. Lowe, A. V. Chapman, S. Cook, J. J. C. Busfield, *J. Polym. Sci. Part B Polym. Phys.* **2011**, *49*, 1621.
[6] D. Gao, R. Li, B. Lv, J. Ma, F. Tian, J. Zhang, *Compos. Part B* **2015**, *77*, 329.
[7] I. González, J. I. Eguiazábal, J. Nazábal, *J. Polym. Sci. Part B Polym. Phys.* **2005**, *43*, 3611.
[8] H. Mattausch, S. Laske, I. Duretek, J. Kreith, G. Maier, C. Holzer, *Polym. Eng. Sci.* **2013**, *53*, 1001.
[9] T. Wu, K. O'Kelly, B. Chen, *J. Polym. Sci. Part B Polym. Phys.* **2014**, *52*, 55.
[10] Z.-Z. Yu, G.-H. Hu, J. Varlet, A. Dasari, Y.-W. Mai, *J. Polym. Sci. Part B Polym. Phys.* **2005**, *43*, 1100.
[11] E.-H. Song, B.-H. Kang, T.-Y. Kim, H.-J. Lee, Y.-W. Park, Y.-C. Kim, B.-K. Ju, *ACS Appl. Mater. Interfaces* **2015**, *7*, 4778.
[12] J. J. Decker, K. P. Meyers, D. R. Paul, D. A. Schiraldi, A. Hiltner, S. Nazarenko, *Polymer* **2015**, *61*, 42.
[13] S. Yoshimoto, F. Ohashi, T. Kameyama, *J. Polym. Sci. Part B Polym. Phys.* **2005**, *43*, 2705.
[14] H. Qin, S. Zhang, C. Zhao, M. Yang, *J. Polym. Sci. Part B Polym. Phys.* **2005**, *43*, 3713.
[15] Q. T. Nguyen, T. D. Ngo, P. Tran, P. Mendis, D. Bhattacharyya, *Compos. Part A* **2015**, *74*, 26.
[16] K. Dal Pont, J.-F. Gérard, E. Espuche, *J. Polym. Sci. Part B Polym. Phys.* **2013**, *51*, 1051.
[17] H. Mauroy, T. S. Plivelic, J.-P. Suuronen, F. S. Hage, J. O. Fossum, K. D. Knudsen, *Appl. Clay Sci.* **2015**, *108*, 19.
[18] E. Yildirim, M. Yurtsever, *J. Polym. Res.* **2012**, *19*, 9771.
[19] K. Chrissopoulou, I. Altintzi, I. Andrianaki, R. Shemesh, H. Retsos, E. P. Giannelis, S. H. Anastasiadis, *J. Polym. Sci. Part B Polym. Phys.* **2008**, *46*, 2683.
[20] V. Bershtein, A. Fainleib, L. Egorova, K. Gusakova, O. Grigoryeva, D. Kirilenko, S. Konnikov, V. Ryzhov, P. Yakushev, N. Lavrenyuk, *Nanoscale Res. Lett.* **2015**, *10*, 165.
[21] Q. Li, Q. Yang, Y. Huang, G. Chen, Y. Lv, *J. Macromol. Sci. Part B Phys.* **2012**, *51*, 1776.
[22] P. S. Stephanou, *J. Chem. Phys* **2015**, *142*, 064901.
[23] P. S. Stephanou, V. G. Mavrantzas, G. C. Georgiou, *Macromolecules* **2014**, *47*, 4493.
[24] M. Rajabian, C. Dubois, M. Grmela, *Rheol. Acta* **2005**, *44*, 521.
[25] M. Rajabian, C. Dubois, M. Grmela, P. J. Carreau, *Rheol. Acta* **2008**, *47*, 701.
[26] H. Eslami, M. Grmela, M. Bousmina, *J. Rheol.* **2007**, *51*, 1189.
[27] H. Eslami, M. Grmela, M. Bousmina, *Rheol. Acta* **2009**, *48*, 317.
[28] G. B. Jeffery, *Proc. R. Soc. London Ser. A* **1922**, *102*, 161.
[29] F. Folgar, C. L. Tucker, *J. Reinf. Plast. Compos.* **1984**, *3*, 98.
[30] S. G. Advani, C. L. Tucker, *J. Rheol.* **1987**, *31*, 751.
[31] C. L. Tucker II, J. Wang, *J. F. O'Gara, J. Rheol.* **2008**, *52*, 1179.
[32] H. Niskanen, H. Eloranta, J. Tuomela, J. Hämäläinen, *Int. J. Multiphase Flow* **2011**, *37*, 336.
[33] A. Mesbah, F. Zaïri, S. Boutaleb, J. M. Gloaguen, M. Naït-Abdelaziz, S. Xie, T. Boukharouba, J. M. Lefebvre, *J. Appl. Polym. Sci.* **2009**, *114*, 3274.
[34] N. Sheng, M. C. Boyce, D. M. Parks, G. C. Rutledge, J. I. Abes, R. E. Cohen, *Polymer* **2004**, *45*, 487.
[35] A. Montazeri, M. Sadeghi, R. Naghdabadi, H. Rafii-Tabar, *Phys. Lett. A* **2011**, *375*, 1588.
[36] F. W. Starr, J. F. Douglas, S. C. Glotzer, *J. Chem. Phys.* **2003**, *119*, 1777.
[37] G. G. Vogiatzis, D. N. Theodorou, *Macromolecules* **2014**, *47*, 387.
[38] K. Johnston, V. Harmandaris, *Macromolecules* **2013**, *46*, 5741.
[39] E. N. Skountzos, A. Anastassiou, V. G. Mavrantzas, D. N. Theodorou, *Macromolecules* **2014**, *47*, 8072.
[40] A. N. Rissanou, A. J. Power, V. Harmandaris, *Polymer* **2015**, *7*, 390.
[41] B. D. Todd, P. J. Daivis, *Phys. Rev. Lett.* **1998**, *81*, 1118.
[42] C. Baig, V. A. Harmandaris, *Macromolecules* **2010**, *43*, 3156.
[43] J. T. Padding, W. J. Briels, *J. Chem. Phys.* **2002**, *117*, 925.
[44] J. T. Padding, W. J. Briels, *J. Chem. Phys.* **2003**, *118*, 10276.
[45] K. L. Anderson, A. Sinsawat, R. A. Vaia, B. L. Farmer, *J. Polym. Sci. Part B Polym. Phys.* **2005**, *43*, 1014.
[46] A. Sinsawat, K. L. Anderson, R. A. Vaia, B. L. Farmer, *J. Polym. Sci. Part B Polym. Phys.* **2003**, *41*, 3272.
[47] V. Kalra, F. Escobedo, Y. L. Joo, *J. Chem. Phys.* **2010**, *132*, 024901.
[48] P. J. Hoogerbrugge, J. M. V. A. Koelman, *Europhys. Lett.* **1992**, *19*, 155.
[49] R. D. Groot, P. B. Warren, *J. Chem. Phys.* **1997**, *107*, 4423.
[50] S. Kim, A. M. Palomino, C. M. Colina, *Mol. Simul.* **2012**, *38*, 723.
[51] K. Zhang, C. W. Manke, *Mol. Simul.* **2000**, *25*, 157.
[52] S. Meng, J. Zhang, Y. Wang, X. Li, C. Wu, T. Hou, L. Xiao, G. Lu, *Mol. Simul.* **2015**, *41*, 772.
[53] M. Yamanoi, O. Pozo, J. M. Maia, *J. Chem. Phys.* **2011**, *135*, 044904.
[54] E. S. Boek, P. V. Coveney, H. N. W. Lekkerkerker, P. Van Der Schoot, *Phys. Rev. E Stat. Nonlinear Soft Matter Phys.* **1997**, *55*, 3124.
[55] A. Chatterjee, L.-M. Wu, *Mol. Simul.* **2008**, *34*, 243.
[56] W. Pan, B. Caswell, G. E. Karniadakis, *Langmuir* **2010**, *26*, 133.
[57] D. A. Fedosov, G. E. Karniadakis, B. Caswell, *J. Chem. Phys.* **2010**, *132*, 144103.
[58] D. C. Visser, *J. Comput. Phys.* **2006**, *214*, 491.
[59] P. Español, P. Warren, *Europhys. Lett.* **1995**, *30*, 191.
[60] P. Nikunen, I. Vattulainen, M. Karttunen, *Phys. Rev. E Stat. Nonlinear Soft Matter Phys.* **2007**, *75*, 036713.
[61] M. Doi, S. F. Edwards, *The Theory of Polymer Dynamics*, Clarendon Press, Oxford **1986**.
[62] G. Scocchi, P. Posocco, M. Fermeglia, S. Pricl, *J. Phys. Chem. B* **2007**, *111*, 2143.
[63] S. P. Pereira, G. Scocchi, R. Toth, P. Posocco, D. R. Nieto, S. Pricl, M. Fermeglia, *J. Multiscale Model.* **2011**, *03*, 151.
[64] V. Ortiz, S. O. Nielsen, D. E. Discher, M. L. Klein, R. Lipowsky, J. Shillcock, *J. Phys. Chem. B* **2005**, *109*, 17708.
[65] A. Maiti, S. McGrother, *J. Chem. Phys.* **2004**, *120*, 1594.
[66] J.-G. Gai, G.-H. Hu, H.-L. Li, S.-P. Zhu, S. Hoppe, *Ind. Eng. Chem. Res.* **2010**, *49*, 11369.
[67] R. M. Füchslin, H. Fellermann, A. Eriksson, H.-J. Ziock, *J. Chem. Phys.* **2009**, *130*, 214102.
[68] A. M. Philippe, C. Baravian, V. Bezuglyy, J. R. Angilella, F. Meneau, I. Bihannic, L. J. Michot, *Langmuir* **2013**, *29*, 5315.

[69] J. D. Ferry, *Viscoelastic Properties of Polymers*, 3rd ed. Wiley, New York **1980**.
[70] J. F. Morris, B. Katyal, *Phys. Fluids* **2002**, *14*, 1920.
[71] J. H. Phelps, C. L. Tucker III, *J. Non Newton. Fluid Mech.* **2009**, *156*, 165.
[72] N. U. Qadir, D. A. Jack, *Compos. Part A* **2009**, *40*, 1524.
[73] D. Z. Gunes, R. Scirocco, J. Mewis, J. Vermant, *J. Non Newton. Fluid Mech.* **2008**, *155*, 39.
[74] S. T. Knauert, J. F. Douglas, F. W. Starr, *J. Polym. Sci. Part B Polym. Phys.* **2007**, *45*, 1882.
[75] M. M. Malwitz, P. D. Butler, L. Porcar, D. P. Angelette, G. Schmidt, *J. Polym. Sci. Part B Polym. Phys.* **2004**, *42*, 3102.
[76] B.-U. Nam, K.-D. Min, Y. Son, *Mater. Lett.* **2015**, *150*, 118.
[77] P. Nawani, C. Burger, L. Rong, B. Chu, B. S. Hsiao, A. H. Tsou, W. Weng, *Polymer* **2010**, *51*, 5255.
[78] M. Rajabian, G. Naderi, P. J. Carreau, C. Dubois, *J. Polym. Sci. Part B Polym. Phys.* **2010**, *48*, 2003.
[79] I. Bihannic, C. Baravian, J. F. L. Duval, E. Paineau, F. Meneau, P. Levitz, J. P. De Silva, P. Davidson, L. J. Michot, *J. Phys. Chem. B* **2010**, *114*, 16347.

Supporting Information

Orientation of Anisometric Layered Silicate Particles in Uncompatibilized and Compatibilized Polymer Melts under Shear Flow: A Dissipative Particle Dynamics Study

Ali Gooneie*, Stephan Schuschnigg, Clemens Holzer

Chair of Polymer Processing, Department of Polymer Engineering and Science,
Montanuniversität Leoben, Leoben, Austria
E-mail: ali.gooneie@unileoben.ac.at

A detailed system was constructed and simulated in order to verify the coarse-graining approach of the silicate layers in the compatibilized systems. Aliphatic surfactant tails were attached to one in every five silicate beads on both sides of the layers. Each surfactant molecule was composed of 2 beads connected with harmonic springs of with a spring constant of 50, see Figure 1. The system was allowed to equilibrate before the flow starts.

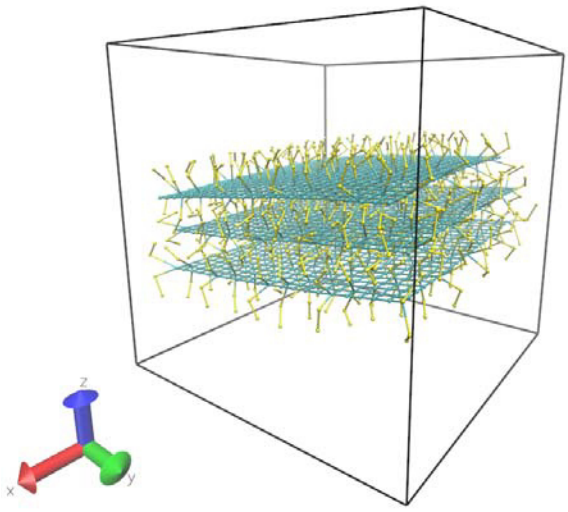

Figure 1. A snapshot of a compatibilized system, with the 3-layered silicate in the center of the box. The polymer and compatibilizer molecules are not shown to preserve clarity. The aliphatic surfactants are shown in yellow.

The repulsion parameters between the pairs are all taken from the works of Pereira et al.[1] and Scocchi et al.[2] to make sure that the simulation results are in tally with previous works. Table 1 summarizes the repulsion parameters used. A shear-rate of 0.148 was applied in the simulations. The shear flows were defined by their velocity and velocity gradient directions. For instance, a shear flow defined by V_x-G_y is representative of a flow with the velocity in x-direction and the velocity gradient in y-direction. All other simulation parameters were the same as the original paper.

Table 1. The Maximum Repulsion Parameters Used to Characterize the Compatibilized PLN Systems

	Polymer	**Layered Silicate**	**Compatibilizer**	**Surfactant**
Polymer	25	33	32	32.5
Layered Silicate	33	15	30.7	30.7
Compatibilizer	32	30.7	32	32
Surfactant	32.5	30.7	32	32

The orientation process was monitored by calculating the average orientation angle as well as the average angle with the velocity gradient direction. The results are shown in Figure 2. The simulation results from our proposed coarse-graining approach used in the paper are also included for comparison. One can see that there is a good agreement between the evolutions of orientation in both setups. The results encourage the coarse-graining approach utilized in this study. The possibility to design both uncompatibilized and compatibilized systems with the same bead number density is a critical advantage of the proposed coarse-grained system. This fact makes it much easier to compare the stress levels in these two types of systems. Consequently, we have decided to perform the simulations on the coarse-grained systems.

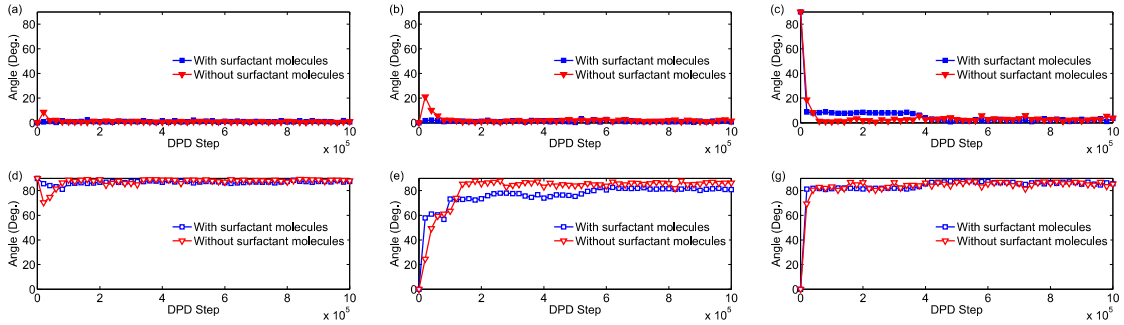

Figure 2. The evolution of the orientation angle (a,b,c) and the angle with the velocity gradient direction (d,e,g) in compatibilized systems. The flow type is V_x-G_z in (a,d), V_x-G_y in (b,e), and V_z-G_y in (c,g). The applied shear-rate is 0.148.

References

[1] S. P. Pereira, G. Scocchi, R. Toth, P. Posocco, D. R. Nieto, S. Pricl, M. Fermeglia, *J. Multiscale Modell.* **2011,** *03,* 151.

[2] G. Scocchi, P. Posocco, M. Fermeglia, S. Pricl, *J. Phys. Chem. B* **2007,** *111,* 2143.

Dissipative Particle Dynamics Models of Orientation of Weakly-Interacting Anisometric Silicate Particles in Polymer Melts under Shear Flow: Comparison with the Standard Orientation Models

Ali Gooneie,* Stephan Schuschnigg, Clemens Holzer

Dissipative particle dynamics (DPD) models of orientation of weakly-interacting silicate particles in a polymer matrix are presented. To examine the DPD models, the evolution of orientation under shear flow is compared with the predictions of the standard orientation models, namely, the Folgar–Tucker (FT) and the strain reduction factor (SRF) models. While the orientation patterns are the same in all models, the slow orientation kinetics observed in previous experiments is only predicted in the DPD and SRF models. Since the coefficients of the SRF model are in good agreement with the experiments, the good tally between the DPD and SRF models supports the capability of DPD to successfully simulate the orientation process. The orientation in a large cell constructed from unit cells with various averaged initial orientation angles is evaluated from evolutions in the unit cells based on the affine deformation assumption. The good agreement between such calculations and SRF model predictions supports that the affine deformation assumption in the large cell is reasonable. It is argued that the nonaffine deformation originated from the particle-based nature of DPD models at the lower scale could be combined with the affine deformation at the upper scale to yield appropriate estimations of the orientation state.

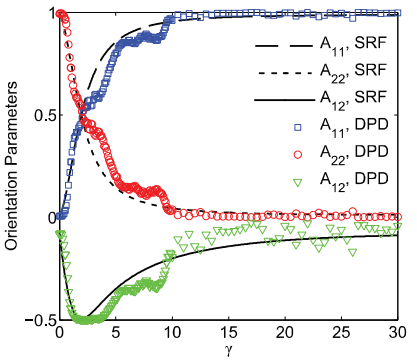

1. Introduction

It is a well-known fact that the local orientation of anisometric particles determines the local mechanical and physical properties in a reinforced composite material.[1–4] Thus, any useful prediction of the structural performance or dimensional accuracy of the final part necessitates a precise prediction of the flow-induced particle orientation. Consequently, it is of great significance to be able to predict the orientation patterns that arise during processing of such complex materials. For this reason, several particle orientation models have been developed and combined with traditional continuum calculations to simulate injection molding,[5–8] compression molding,[9–11] and extrusion processes.[12]

The standard orientation model is based on Jeffery's equation for the motion of an ellipsoid in an infinite

A. Gooneie, S. Schuschnigg, Prof. C. Holzer
Chair of Polymer Processing
Department of Polymer Engineering and Science
Montanuniversität Leoben
Otto Glöckel-Straße 2, 8700 Leoben, Austria
E-mail: ali.gooneie@unileoben.ac.at

Macromol. Theory Simul. **2016**, *25*, 287–302

DOI: 10.1002/mats.201500086

Newtonian matrix.[13] Folgar and Tucker[14] incorporated this model to represent flow effects and added an isotropic rotary diffusion term to represent fiber–fiber interactions. The rotary diffusion term results in deviations from a perfect alignment at steady state which is consistent with experimental results. A widely used method to represent the average orientation state is with the second- and fourth-order orientation tensors developed by Advani and Tucker.[15] These tensors are defined as the second and fourth moments of the orientation distribution function. The resulting model has been utilized to predict the flow-induced orientation of various anisometric particles including short fibers,[5,16] layered silicates,[17–19] and carbon nanotubes.[20] Other authors have also investigated different approaches such as nonequilibrium thermodynamics in order to derive constitutive equations that could describe polymer nanocomposites with nanofibers and nanosheets.[21–24]

The Folgar–Tucker (FT) model has been later modified by Huynh[25] to account for the reduced strain in concentrated suspensions by the introduction of a strain reduction factor (SRF). The slower orientation kinetics was also manifested by Sepehr et al.[26] who introduced a slip coefficient to slow down the rate of particle orientation. In order to objectively account for the reduced strain during orientation in any coordinates system, Wang et al.[27] developed the so-called reduced-strain closure (RSC) model based on the idea of reducing the growth rates of the eigenvalues of the orientation tensor while using the same expressions for eigenvector rotation. They show that their model successfully predicts the transient shear stress data in a shear-reversal experiment for a polybutylene terephthalate resin filled with 30 wt% glass fibers.

Although these models have proven to be efficient in the prediction of particle orientation, they cannot provide a detailed description of the system microstructure but only an average evaluation. Detailed computer simulations have shown great potential to model complex phenomena at an atomistic level. Benefiting from the vast capabilities of such methods, Rissanou et al.[28] performed detailed atomistic molecular dynamics (MD) simulations of graphene-based polyethylene nanocomposites. They found that chain segmental dynamics slowed down at the polyethylene/graphene interface by a factor of at least five compared with the bulk. Indeed, there are many instances like this in the literature. Various systems have been studied before by these approaches including unentangled and entangled polymer melts,[29–36] polymer solutions,[37] suspensions,[38–43] etc. Anderson et al.[44] and Sinsawat et al.[45] utilized coarse-grained molecular dynamics (CGMD) to study the microstructure formation in polymer-layered silicate nanocomposites. Moreover, shear-induced microstructure evolutions have been treated before in such frameworks including CGMD and dissipative particle dynamics (DPD) methods. For instance, Kalra et al.[46] utilized CGMD to study how shear flow affects the kinetics of particle aggregation at the initial stages in systems with polymers of different chain lengths. Meng et al.[47] incorporated DPD to investigate the rheology of surfactant solutions. They found that under shear flow the worm-like micelles formed by surfactant molecules are first oriented along the flow direction and then are broken up into small spherical micelles. Also, the rheological properties of colloidal suspensions of spheres, rods, and disks were investigated by Boek et al.[39] utilizing DPD. These works all approve that the detailed simulation techniques are able to provide fresh insights into complex systems.

Since it was proposed, DPD has received tremendous attention from the research community due to its coarse-grained nature and the fact that it incorporates soft dissipative potentials.[48,49] Attempts have been made to improve DPD to represent a more accurate physical model of polymer chains, forces of the DPD particles, and even the applied shear flow. Some reports are briefly noted here. Yamanoi et al.[50] introduced entanglement forces instead of conservative forces and were able to reproduce both static and dynamic properties of linear polymer systems. Pan et al.[40] divided the dissipative forces into central and shear components which allowed them to obtain the correct hydrodynamics in the study of Brownian colloidal suspensions. Fedosov et al.[51] used the reverse Poiseuille flow in order to investigate the steady shear rheology of polymer chains. It was shown that the reverse Poiseuille flow yields more complete rheograms than those computed from conventional Lees–Edwards Couette flow particularly near the zero-shear-rate plateaus. In spite of these attempts, DPD still suffers from the intrinsic instabilities at very low or very high shear-rates and needs further improvements.[51,52] In order to capture reptational dynamics of long polymer chains[53] in DPD, Nikunen et al.[32] used simple topological constraints to prevent bond crossings. This way scalings of the longest relaxation time and the diffusion coefficient with the chain length were predicted correctly. In a similar study, Sirk et al.[54] introduced the modified segmental repulsive potential to prevent unphysical bond crossings in DPD polymer models. Their method was shown to be able to capture entanglements in the mechanical behavior of polymers.

Various aspects of DPD simulations have been addressed in the literature. A few instances are reviewed here. For simulating flows at extreme dissipation rates, Chatterjee[55] showed that Lees–Edwards boundary condition in conjunction with the velocity-dependent DPD thermostat could result in nonphysical jumps in the

velocity profiles. Consequently, a modified version of this boundary condition was introduced to correct this error unconditionally. Thermodynamic, hydrodynamic, and rheological responses of model DPD fluids under extreme shears were simulated utilizing the modified Lees–Edwards boundary condition.[56,57] The results suggest that this modification facilitates momentum flow from shear boundaries to the system bulk. However, there exist upper thresholds for imposing shear on the system beyond which temperature cannot be controlled properly and nonphysical jumps reappear. A number of studies are devoted to evaluate different thermostats in nonequilibrium DPD simulations. For instance, Pastorino et al.[58] characterized the Langevin and DPD thermostats in a broad range of nonequilibrium DPD simulations of polymeric systems. Khani et al.[59] tested the Lowe–Andersen thermostat[60,61] as an alternative to the DPD thermostat in the mesoscopic simulation of entangled polymers. These studies conclude that great care is needed in nonequilibrium DPD simulations of soft matter systems in order to ensure that the simulations are free of artifacts due to an inappropriate choice of the thermostat. The systematic coarse-graining procedure in DPD models has also been treated in the works of Fu et al.[62,63] who evaluate the limits and conditions of coarse-graining based on thermodynamic and transport properties.

In a recent study, we incorporated DPD models to predict the orientation of semiflexible-layered silicate particles in uncompatibilized and compatibilized polymer melts under various shear flows.[52] The model could successfully capture the orientation of such anisometric particles. It was shown that regardless of the applied flow direction, the layered silicates would rearrange themselves so that their surfaces would be normal to the velocity gradient direction. This was noted to be in agreement with certain experimental results.[64,65] Here, we aim to test the creditability of such models by comparison with the widely-used FT and SRF models. To do this, the development of orientation is modeled using both methods. Two cases are considered: (i) a unit cell including four silicate particles embedded in a polymer matrix and (ii) an accumulation of such unit cells in a large cell with various initial orientation states. The details are explained in Section 2. It will be shown that the FT and SRF models with coefficients either derived from or close to previous experimental results are in tally with the DPD simulations thus confirming their capability. The large cell is then modeled with the affine deformation assumption which is again validated by the FT and SRF models. It is argued that this assumption could provide the opportunity of a multiscale data transfer in materials with such weakly-interacting particles.

2. Theory

2.1. The Standard Orientation Model

The standard orientation model is based on Jeffery's equation for the motion of an ellipsoid.[13] This model is applicable to dilute suspensions and has been used in most orientation models to account for the hydrodynamic contributions in orientation. If the unit vector directed along the fiber axis, $\mathbf{p}$, is used to denote the fiber orientation, the time derivative of this vector, $\dot{\mathbf{p}}$, following the particle can be written as

$$\dot{\mathbf{p}} = \mathbf{W}\cdot\mathbf{p} + \lambda\left(\mathbf{D}\cdot\mathbf{p} - \mathbf{D}:\mathbf{ppp}\right) \tag{1}$$

where $\mathbf{W} = \frac{1}{2}(\mathbf{L} - \mathbf{L}^{\mathrm{T}})$ is the vorticity tensor and $\mathbf{D} = \frac{1}{2}(\mathbf{L} + \mathbf{L}^{\mathrm{T}})$ is the rate-of-deformation tensor. $\mathbf{L}$ represents the velocity gradient tensor with components $L_{ij} = \frac{\partial v_i}{\partial x_j}$ where v_i is the component of velocity in the x_j direction. $\lambda = (r^2 - 1)/(r^2 + 1)$ is a constant that depends on the particle aspect ratio, r. For prolate and oblate spheroids of large aspect ratio λ is 1 and −1, respectively. In Jeffery's model, the first term corresponds to the fiber rotation due to the vorticity of the flow. The second term represents a rotation of the fiber axis toward the direction of maximum elongation rate.

Orientation calculations often use the second- and fourth-order orientation tensors, $\mathbf{A}_2$ and $\mathbf{A}_4$, respectively, introduced by Advani and Tucker.[15] These tensors are given by

$$\mathbf{A}_2 = \oint \mathbf{pp}\,\psi(\mathbf{p})\,\mathrm{d}\mathbf{p} \tag{2}$$

$$\mathbf{A}_4 = \oint \mathbf{pppp}\,\psi(\mathbf{p})\,\mathrm{d}\mathbf{p} \tag{3}$$

Here, $\psi(\mathrm{p})$ is the probability density function for fiber orientation and the integral is performed over all orientation states. In order to model concentrated suspensions of non-Brownian particles, Folgar and Tucker[14] added the diffusion term to the Jeffery's equation. The FT model for the orientation change in terms of the orientation tensors can be written as

$$\dot{\mathbf{A}}_2 = \mathbf{W}\cdot\mathbf{A} - \mathbf{A}\cdot\mathbf{W} + \lambda(\mathbf{D}\cdot\mathbf{A} + \mathbf{A}\cdot\mathbf{D} - 2\mathbf{A}_4:\mathbf{D}) + 2C_I\dot{\gamma}(\mathbf{I} - 3\mathbf{A}) \tag{4}$$

In this equation, $\dot{\mathbf{A}}_2$ is the material derivative of the second-order orientation tensor. C_I is a phenomenological coefficient called the interaction coefficient which models the randomization effect of interactions between particles. $\dot{\gamma} = (2\mathbf{D}:\mathbf{D})^{\frac{1}{2}}$ is the scalar magnitude of $\mathbf{D}$ typically known as the shear-rate in simple shear flows. The last term in this equation represents an isotropic rotary diffusion which models the effect of particle–particle

interactions on the orientation. A consequence of adding this term to the orientation model is that the steady orientation state for large strains does not necessarily depict a perfect alignment.

It has been shown that the kinetics of orientation in materials with anisometric particles such as fibers or layered silicates is significantly slower than FT model predicts.[26] To overcome this problem and provide a better prediction for the experimental results, a simple strategy is to modify the right-hand side of Equation (4) by some factor $k < 1$[25]

$$\dot{\mathbf{A}}_2 = k[\mathbf{W}\cdot\mathbf{A} - \mathbf{A}\cdot\mathbf{W} + \lambda(\mathbf{D}\cdot\mathbf{A} + \mathbf{A}\cdot\mathbf{D} - 2\mathbf{A}_4 : \mathbf{D}) + 2C_I\dot{\gamma}(\mathbf{I} - 3\mathbf{A})] \quad (5)$$

In this model, the $1/k$ is often referred to as the "strain reduction factor." The idea behind this model, known as the SRF model, was also proved by the work of Sepehr et al.[26] who proposed the slip coefficient k to empirically modify the FT model. They suggest that the shear strain applied on the fibers γ_s after time t is

$$\gamma_s = k\dot{\gamma}t \quad (6)$$

For short fibers in a polypropylene matrix, they report slip coefficient values in the range of 0.33–0.38. It has been suggested that the SRF model can be safely used for the prediction of orientation in simple flows like in this study.

On a mesoscopic level, Rajabian et al.[23,24,66] developed a rheological model for ellipsoid particles in viscoelastic polymeric fluids by adding a dissipation function to the Jeffery's model. They described such dissipations as a function of the overall free energy with respect to the conformation tensors $\mathbf{\Phi}_{\mathbf{A}_2}$ and $\mathbf{\Phi}_{\mathbf{C}}$. The conformation tensors are further formulated utilizing two second-order symmetric structure tensors $\mathbf{A}_2$ and $\mathbf{C}$, i.e., the orientation tensor of the particles (same as Equation (2) by Advani and Tucker[15]) and the tensor describing the extension of polymer molecules, respectively. The evolutions of the components of these structure tensors with time are then given by

$$\dot{A}_{ij} = A_{ik}W_{kj} - W_{ik}A_{kj} + \lambda(A_{ik}D_{kj} + D_{ik}A_{kj} - 2D_{kl}A_{ijkl}) - \frac{2}{3}(D_{lm}D_{ml})^{\frac{1}{2}}\Lambda_p(A_{il}\Phi_{A_{lj}} + A_{lj}\Phi_{A_{il}}) + \frac{4}{9}(D_{lm}D_{ml})^{\frac{1}{2}}\Lambda_p A_{ij}\Phi_{A_{kk}} \quad (7)$$

$$\dot{C}_{ij} = -C_{jk}W_{ik} - W_{jk}C_{ik} + C_{jk}D_{ik} + D_{jk}C_{ik} - \Lambda_m(C_{kj}\Phi_{C_{ik}} + C_{ik}\Phi_{C_{kj}}) \quad (8)$$

The components of the conformation tensors are

$$\Phi_{C_{ij}} = -\frac{k_B T}{2}\left[n_m C_{ij}^{-1} - \frac{n_m b}{1 - trC}\delta_{ij} - B_{pm}(n_p n_m)^{\frac{1}{2}}(\delta_{ij} - A_{ij})\right] \quad (9)$$

and

$$\Phi_{A_{ij}} = -\frac{k_B T}{2}\left[n_p A_{ij}^{-1} - B_{pm}(n_p n_m)^{\frac{1}{2}}(trC\,\delta_{ij} - C_{ij}) - 2B_{pp}n_p(\delta_{ij} - A_{ij})\right] \quad (10)$$

In these equations, $n_p = \frac{4\phi}{d^2 l}$ and $n_m = (1-\phi)\frac{\rho N_o}{M_w}$ where ϕ, l, and d are the volume fraction, length, and diameter of the particles, respectively. M_w and ρ are the molecular weight and density of the polymer and N_o is the Avogadro's number. B_{pm} and B_{pp} are phenomenological parameters determined by experiments which denote the interactions between particle–macromolecule and particle–particle pairs, respectively. Λ_p and Λ_m are the mobility parameters for the particles and macromolecules. The parameter b is defined by $b = \frac{2HR_o^2}{k_B T}$ where H is the spring constant and R_o is the maximum spring length for the modeled polymer chains utilizing the finitely extensible nonlinear elastic springs. Here, k_B is the Boltzmann's constant and T is the absolute temperature. In the evolution equations, the initial conditions are the equilibrium solutions obtained by solving $\Phi_{C_{ij}} = 0$ and $\Phi_{A_{ij}} = 0$. The governing equations of this mesoscopic model (MM) can be readily solved in the case of an imposed flow. Moreover, the model is adaptable to nano-sized particles considering the fact that the model addresses the particle–macromolecule interactions in both the free energy and mobility coefficients.

In order to solve the evolution equations of $\mathbf{A}_2$ according to any of these models, a closure approximation is necessary to calculate $\mathbf{A}_4$. Kagarise et al.[18] have compared various closure approximations, i.e., quadratic, hybrid, and linear closure approximations, for nanorod (carbon nanofibers) and nanoplatelet (nanoclays) polymer nanocomposites in a range of 0.01–10 s^{-1} of shear-rates. Their results proved that the quadratic closure approximation predicts the steady-state viscosity with the least error. Therefore, the quadratic closure approximation was also used in this work.[15]

2.2. Simulation Details

DPD was introduced to simulate the hydrodynamic behavior of fluids and colloidal suspensions.[48,49] In DPD, each elementary unit called "bead" represents several atoms or molecules. The dynamics of these beads is governed by Newton's law supplemented by friction and random forces to provide the thermostat of the system. Two beads at positions $\mathbf{r}_i$ and $\mathbf{r}_j$ in space with a separation vector of $\mathbf{r}_{ij} = \mathbf{r}_i - \mathbf{r}_j$ and a unit vector of $\hat{\mathbf{r}}_{ij} = \mathbf{r}_{ij}/|\mathbf{r}_{ij}|$ experience three central, additive forces: the conservative force

$$F_{ij}^C = a_{ij}\chi_{ij}\left(1 - \frac{r_{ij}}{r_c}\right)\hat{\mathbf{r}}_{ij}, \quad (11)$$

the dissipative force

$$F_{ij}^{D} = -\gamma_{ij}\omega^{D}r_{ij}[(\mathbf{v}_i - \mathbf{v}_j)\cdot\hat{\mathbf{r}}_{ij}]\hat{\mathbf{r}}_{ij}, \quad (12)$$

and the random force

$$F_{ij}^{R} = \sigma_{ij}\omega^{R}r_{ij}\xi_{ij}\hat{\mathbf{r}}_{ij} \quad (13)$$

in which r_{ij} is the distance between the beads i and j. χ_{ij} equals 1 for beads distanced less than the force cutoff radius r_c and equals 0 otherwise. $\mathbf{v}_i$ and $\mathbf{v}_j$ are the velocity vectors of the ith and jth beads, respectively. ζ_{ij} is a Gaussian random number with zero mean and unit variance. a_{ij}, γ_{ij}, and σ_{ij} are the maximum repulsion, the friction coefficient, and the noise amplitude between bead i and bead j, respectively. ω^{D} and ω^{R} are the r_{ij}-dependent weight functions. Utilizing the fluctuation–dissipation theorem,[67] one can write

$$\omega^{D}(r_{ij}) = \left[\omega^{R}(r_{ij})\right]^2 = \chi_{ij}\left(1 - \frac{r_{ij}}{r_c}\right)^2 \quad (14)$$

$$\sigma_{ij}^2 = 2\gamma_{ij}k_B T \quad (15)$$

Mass, length, and energy are in units of mass of a single bead, r_c, and $k_B T$, respectively. All of these variables are set to unity in our simulations. The volume fraction of the layered silicates in the simulations is defined as $\phi = \frac{n_{ls}}{n_{ls} + n_p}$ where n_{ls} and n_p are the number of layered silicate and polymer beads, respectively. In the simulations, DPD thermostat is utilized to control the temperature. It should be emphasized that in this paper all of the values are in DPD units unless noted otherwise. We simulate a system consisting of polymer chains and silicate layers. The maximum repulsion parameter between polymer–polymer was set to 25.[49] For polymer–silicate and silicate–silicate pairs, the maximum repulsions were taken from the works of Scocchi et al.[68] and Pereira et al.[69] who used the rescaled binding and non-binding molecular dynamics energies to determine the self and mixed DPD energies in a multiscale strategy. In this way, they were able to predict the structure of a number of polymer–clay nanocomposites which were in excellent agreement with previous experimental and atomistic simulation results. These values were 33 and 15 for polymer–silicate and silicate–silicate, respectively. We showed before that these values can provide an accurate representation of the orientation in such systems.[52] The friction coefficients were 5.6 for interactions between polymer–silicate and silicate–silicate pairs, and 4.5 for polymer–polymer pairs.[38,51,70–72]

The polymer molecules were modeled as linear flexible chains of 50 beads connected together by harmonic springs with a spring constant of 50. It has been shown before by Nikunen et al.[32] that for short polymer chains like here the standard DPD formulation is accurate enough to perfectly capture the dynamics of the polymer chains, i.e., the Rouse-like dynamics.[73] Therefore, the standard DPD model is used to model the polymers. It is noteworthy that the dynamics of the comparatively larger silicate particles deviate from the Rouse behavior and therefore underline the role of hydrodynamic interactions. This issue will be dealt with later in the paper. A silicate particle is modeled with a 21 × 21 bead connected together by harmonic springs with a spring constant of 500[70] and an equilibrium length of 0.25 which yields layers with an equilibrium length of 5. The changes in the length are limited between 5 and 6 under the flow conditions considering the strong spring constant used to describe the bonds of the layered silicates. Moreover, harmonic potentials are used to describe the bond angles which allow for the precise representation of the semi-flexibility of silicate layers. The coefficient of harmonic bond angles was set to 1000 with respect to certain CGMD simulations.[44,45]

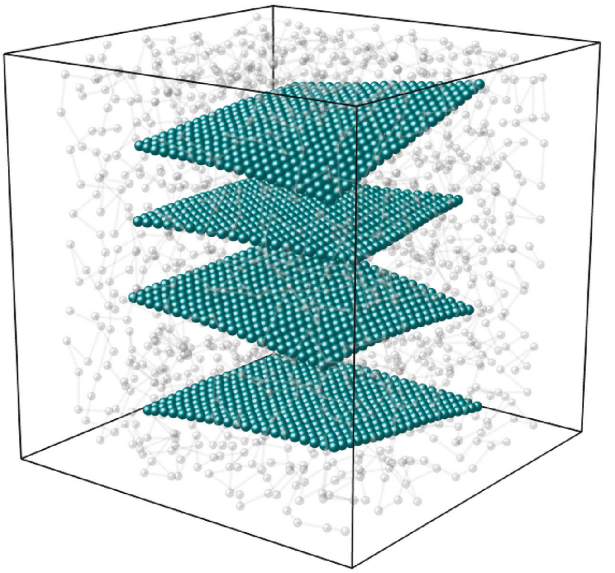

Figure 1. Snapshot of the system with four semiflexible silicate particles in the box. The polymer chains are transparent to preserve clarity.

Four silicate layers were inserted inside a cube filled with equilibrated polymer chains. The chains that were completely or partially crossing with the silicate layers were all removed from the system to avoid unphysical initial configurations. This led to a system with 25 polymer chains surrounding the silicate layers. The bead number density of the resulting system was 3. The silicate layers were all parallel to each other in the initial configuration setups. Figure 1 shows the simulated system. This system will be referred to as the "unit cell" in the rest of the paper. The system was equilibrated for 2×10^5 steps

before running the simulations. A time step of 0.001 was used in the simulations. This time step is rather small compared to what is often expected in DPD simulations. There are two main reasons for this choice: (i) This small time step allows us to export trajectory data of the particles at short intervals during the simulations. In this way, we were able to compare the simulation results with the standard orientation models more carefully, especially at the small strains where the orientation kinetics shows a pronounced transition. (ii) The incorporation of semiflexibility in the layered silicates necessitates smaller time steps to be taken in order to preserve the stability of the numerical procedure. It should be noted that such small time steps can be found in other DPD simulations too. For instance, Pan et al.[40] used a time step between 0.0002 and 0.0005 in their simulations. Another example is the work of Fedosov et al.[51] who used a time step of 0.005. The total number of steps was 10^6 to ensure reaching the steady state.

The computational domain was set to $10 \times 10 \times 10$ in DPD units. Recently, Moreira et al.[74] have shown that the box-size effects can be safely ignored for polymer systems if the gyration radius of the chains is smaller than or equal to the box size. In a recent paper,[75] the gyration radius of polymer chains with 50 beads in each chain was simulated. According to the results, the gyration radius increases to values larger than 10 only at applied shear strains, γ, larger than 32. Therefore, it is safe to assume that the box-size effects are negligible for polymers in the strains below 30 used in this study. However, due to the presence of relatively larger silicate layers in the current system, simulations were also carried out in larger boxes of $20 \times 20 \times 20$ and $30 \times 30 \times 30$ size to study the box-size effects. The Less–Edwards boundary condition was incorporated to shear the system in different directions. The system was sheared either parallel or normal to the initial orientation of the silicate layers. The shear-rate was set to 0.1 (in DPD units) in all simulations. This value was selected to avoid thermal fluctuations that could distort the velocity profile at very low shear-rates, and the overwhelming of the thermostat at very high shear-rates due to the energy dissipations.[51,52]

The orientation state of a silicate layer at a time step was modeled utilizing the average normal unit vector $\mathbf{p}$ to the layer. Knowing $\mathbf{p}$, one can find the average angle of the layer with the flow direction, i.e., the orientation angle θ. The orientation state in the shear plane was used for the evaluation of orientation state in different models in this work. Previous simulations as well as experiments have shown that the orientation state of such particles can be well described in the shear plane and only minor oscillations are observed along the third dimension.[52,64,65] Therefore, the unit vector $\mathbf{p}$ in the shear plane with components p_i and p_j was used to model the orientation state. The orientation tensor was defined in 2D after Fan and Advani[76] as $p_1=\sin\left(\frac{\pi}{2}+\theta\right)$ and $p_2=\cos\left(\frac{\pi}{2}+\theta\right)$. The components of the second-order orientation tensor for a system composed of N particles are

$$\mathbf{A}_2 \Leftrightarrow A_{ij} = \frac{1}{N}\sum_{k=1}^{N} p_i^k p_j^k \tag{16}$$

One should note that $\mathbf{A}_2$ is symmetric ($A_{ij} = A_{ji}$) and the main diagonal components are normalized ($A_{11} + A_{22} = 1$). In order to provide a graphical representation of the orientation state, the orientation ellipse was drawn. The axes of the ellipse are the eigenvalues of $\mathbf{A}_2$ and the major axis of the ellipse is rotated anticlockwise equal to θ from the horizontal x-axis.[76] The major axis of the orientation ellipse represents the preferred orientation of layered silicates. An elongated ellipse shows higher degree of alignment in the direction of the major axis, whereas a circle shows no particular preference of orientation.

In order to estimate the interaction coefficient C_I in FT and SRF models, the relationship proposed by Phan-Thien et al.[77] was used. Assuming isotropic particle diffusion, one can write

$$D_r = C_I \dot{\gamma} \tag{17}$$

where D_r is the rotational diffusivity coefficient. For 2D anisometric particles, D_r is given by[65]

$$D_r = \frac{3k_BT}{32\eta_o l_p^3} \tag{18}$$

Here, k_BT is 1 and l_p is the characteristic length of the particles. This length equals 5 in DPD length unit in our simulations corresponding to the length of a silicate layer under flow. η_o is the viscosity of the suspending fluid. Since the polymer chains follow the Rouse dynamics in this work, the Rouse model was used to estimate η_o. This model predicts the viscosity as[73]

$$\eta_o = \frac{\xi\rho a^2 M N_o}{36 M_o^2} \tag{19}$$

where ξ is the bead–bead friction coefficient and ρ is the bead number density of polymer chains which is 1.25 in our simulations. This value is calculated only for polymer chains in the simulated nanocomposite models by hypothetically removing all silicate beads from the system. a and M_0 are the characteristic length (equals r_c in the present model systems) and the molecular weight of each bead which both equal 1. M is the molecular weight of a chain which is 50 here. $\frac{\rho N_o}{M}$ is the number density of the chains in the simulation box and equals 0.025. Utilizing these data one finds $C_I = 9.6 \times 10^{-4}$. This value is in good agreement with the FT model predictions of experimental

results for polypropylene/layered silicate nanocomposites at a shear-rate of 0.1 s^{-1} with $C_I \approx 8.3 \times 10^{-4}$.[17] The good correspondence with experiments ensures that the DPD results are in fact compared with solid experimental studies rather than only phenomenological models with unresolved coefficients. Therefore, by comparing DPD simulations with FT and SRF models the orientation patterns of DPD results are tested not only against accepted models but also against experimental data since the coefficients used in these models are very close to the experimental results. It should be noted that such a small particle–particle interaction coefficient depicts a system with weakly-interacting particles in which the steady orientation state is expected to be very close to the perfect alignment of the particles.[14,15] It will be shown that the DPD simulations as well as the FT and SRF models predict such a behavior.

Following our previous paper, the nondimensional Peclet number (Pe) is also evaluated.[52] The corresponding Pe number to the applied shear-rate is 1840.8. This rather large value ensures that thermal fluctuations are of minor significance in the simulations. Moreover, it shows that the simulated system is experiencing shear-thinning effects mainly due to the orientation of its components, i.e., polymer chains and silicate layers. Recently, the orientation and stretching of polymer chains was addressed in a paper.[75] Here, we attempt to focus more on the orientation of layered silicates. Lastly, it is noteworthy that the error bars of the simulated data were not added to the figures. The error bars were not noticeable since they were comparatively small with regard to the scales of the figures. Therefore, they only resulted in losing the clarity of the figures considering that various data points collapse on each other in most of the figures. As a judgment call, we decided not to include them in the figures.

3. Results and Discussion

Center of mass mean square displacements (MSD) of the silicate layers have been measured according to the relation $MSD = \langle [\mathbf{R}_i(t) - \mathbf{R}_i(0)]^2 \rangle$ during the simulations in the $20 \times 20 \times 20$ box. In this equation, $\mathbf{R}_i(t)$ and $\mathbf{R}_i(0)$ are the position vectors of the center of mass of the ith silicate layer at the start of the simulation and at time t, respectively. The results are plotted in Figure 2. The dynamics of the silicate layers deviate from the Rouse-like dynamics with a relationship of $MSD \propto t^{0.5}$.[33,78] This observation proves the significance of surrounding constraints limiting the movements of the particles. Therefore, the hydrodynamic interactions play an important role in the dynamics of the silicate particles in the system. This justifies utilizing a DPD model to simulate the current system instead of faster approaches such as the Langevin dynamics.

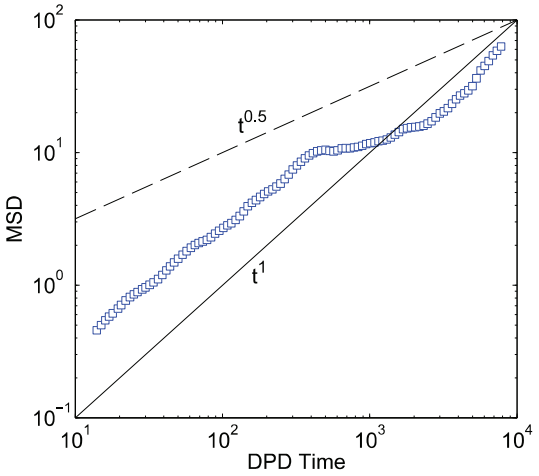

Figure 2. Center of mass mean square displacements (MSD) of the silicate layers measured during the simulations in the $20 \times 20 \times 20$ box. The solid and dashed lines represent $MSD \propto t^{1}$ and $MSD \propto t^{0.5}$ scaling relations with time t, respectively.

In order to ensure that box-size effects are negligible in the orientation results, the simulations were run in orthogonal cubic boxes with sides of 10, 20, and 30. The evolutions of the orientation parameters are plotted in Figure 3 as a function of the applied shear strain, γ, given by $\gamma = t\dot{\gamma}$ where t and $\dot{\gamma}$ are the time and the applied shear-rate, respectively. The influence of the box size on the orientation parameters is within the range of numerical uncertainties. Consequently, one can utilize the smallest box which provides an optimum condition in both the accuracy of the data and the computation costs. In the rest of the paper, the simulation data of the smallest box are reported. The results are presented in two parts. In the first part, the orientation process in the unit cell described in Section 2 is followed as a function of the applied shear strain. The results are compared with the FT and SRF models. Thereafter, a simple approach is developed by which one can transfer the orientation data from the unit cell to a large cell composed of several unit cells. This multiscale approach is tested against the orientation models to ensure its capability.

3.1. Orientation Process in the Unit Cell

In a simple shear flow, the particles with an initial random alignment rotate and gradually align to reach a steady orientation state in which they are aligned close to the flow direction. Figure 4 shows the evolution of orientation parameters from DPD simulations and compares them with the FT model predictions for the normal initial orientation of the particles with respect to the flow direction. The results of both methods depict the same pattern for the orientation of silicate particles. The steady orientation state shows an almost perfect orientation

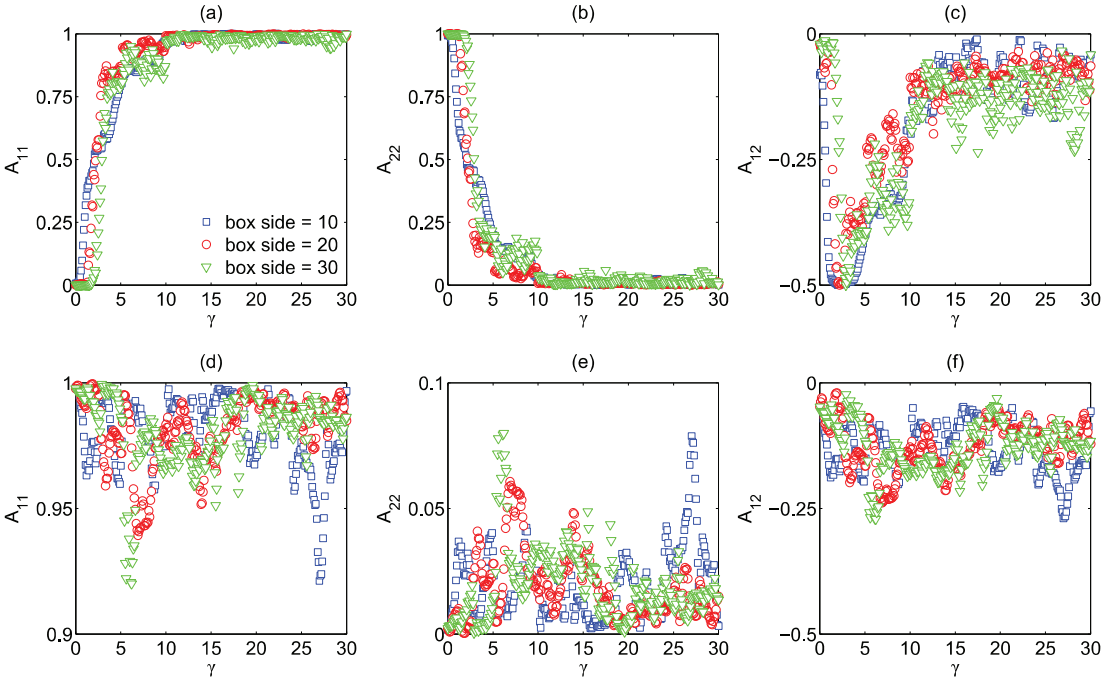

Figure 3. The evolution of orientation parameters in orthogonal cubic boxes with sides of 10, 20, and 30 as a function of the applied shear strain, γ. Parts (a)–(c) and (d)–(f) are simulations results for the normal and parallel initial orientation of the particles with respect to the flow direction, respectively. The legends are shown in part (a). Note that the *y*-scales are not the same in different parts.

state where all particles are parallel to the flow direction. This characteristic behavior is ascribed to the suspensions of weakly-interacting particles also reflected in the estimated C_I value. In the initial stages of the orientation process ($0<\gamma<10$), the FT model depicts faster kinetics than the simulations. This issue has been discussed by other authors to be a disadvantage of the FT model since experiments have shown slower orientation kinetics in shear flows.[25,27,79] In this regard, DPD models might be appropriate candidates to predict such slow kinetics as it will be discussed in further details. The orientation ellipse is drawn at several strains in Figure 5 in order to provide a graphical representation of the orientation states. From the data it is obvious that the DPD model predicts a more perfectly aligned steady orientation state. One should note that the ellipse based on DPD simulations closely resembles a straight line since all of the particles possess almost the same orientation state at all strains. Since the particles are the same, such a uniform orientation evolution in the simulations proves that the velocity profile is highly linear which is critical to the validity of the simulations.[52]

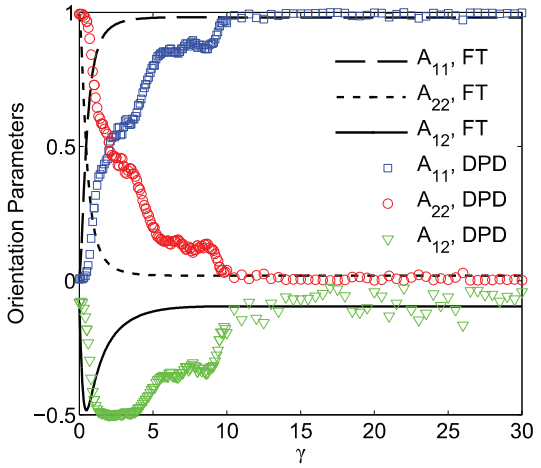

Figure 4. The evolution of orientation parameters against the applied shear strain, γ, from DPD simulations and FT model for the normal initial orientation of the particles with respect to the flow direction. Note that the number of plotted simulated data points is decreased for $\gamma>10$ to preserve clarity.

It is obvious from the data presented in Figures 4 and 5 that the DPD model shows a slower kinetics for the orientation than the FT model does. It has also been shown in experiments that the kinetics of orientation is somewhat slower than the FT model predicts and therefore several approaches have been proposed to modify it. Here, the SRF model is used to account for the slow orientation kinetics. It should be noted that this model can be used in simple flow fields. In general flow fields however one needs to utilize an objective model such as the RSC model developed by Wang et al.[27] The SRF model incorporates a factor of *k* to reduce the strain which is transferred to the particles from the bulk.

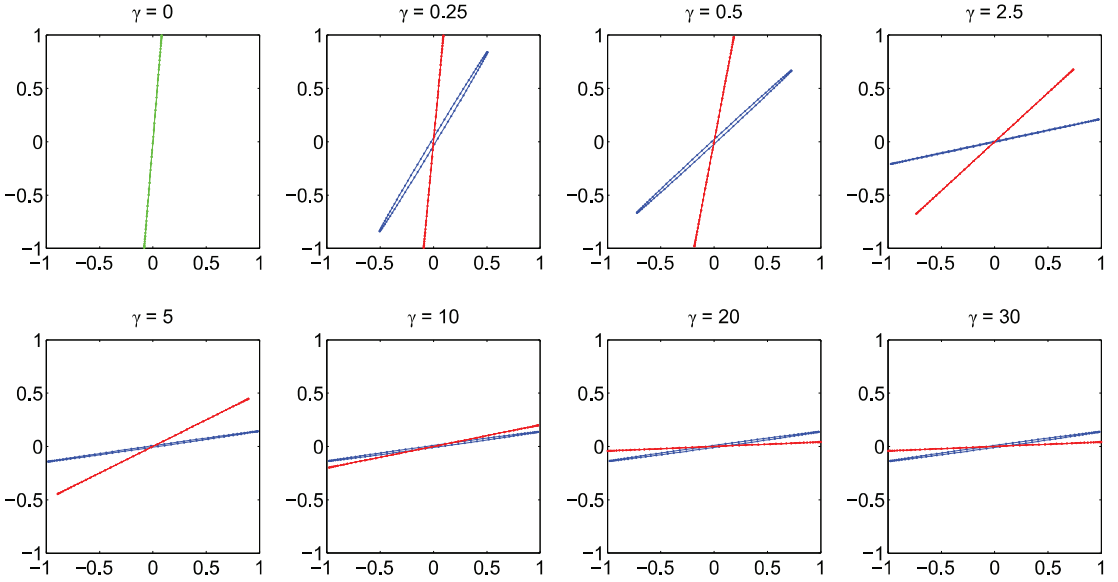

Figure 5. The orientation ellipse at absolute shear strains, γ, according to DPD simulations (red) and FT model (blue) for the normal initial orientation of the particles (green) with respect to the flow direction. The velocity and velocity gradient directions are along the horizontal and vertical axes, respectively. The horizontal and vertical axes of the plots are transformed eigenvalues of $\mathbf{A}_2$ with respect to the average orientation angle of the layered silicates.

Certain studies on polypropylene/organoclay nanocomposites have shown that the onset of the stress overshoot in startup of steady shear flow experiments depends on the applied shear strain rather than the time after the flow has been imposed.[17,19,80,81] These experiments have proven that the stress overshoot occurs at approximately the same absolute strain range of $\gamma \approx 1$ to 3 regardless of the applied shear-rate indicating that the shear stress scales with strain. Such a characteristic behavior has also been observed in non-Brownian suspensions and liquid crystalline polymers.[82] The stress profiles in these experiments have been quantitatively corresponded to the hydrodynamic stresses caused by the rotation and alignment of ellipsoidal particles.[83] The hydrodynamic stresses are calculated based on the rotational movements of the particles which can be estimated from Jeffery's equation or its modified versions such as FT and SRF models. A constitutive equation for suspensions of ellipsoidal particles was proposed by Lipscomb et al.[83] and has been used to predict the hydrodynamic stresses and orientation tensors in experiments ever since.[17,26] For very thin disk-like particles this equations is

$$\boldsymbol{\sigma} = \phi\left[-P_o\mathbf{I} + 2\mu_o\mathbf{D} + \mu_2\mathbf{D}:\mathbf{A}_4 + 2\mu_3\left(\mathbf{D}\cdot\mathbf{A}_2 + \mathbf{A}_2\cdot\mathbf{D}\right)\right] \quad (20)$$

Here, $\mu_o = -\mu_3 = 8\eta_o/(3\pi r)$ and $\mu_2 = 20\eta_o/(3\pi r)$ where η_o is the matrix viscosity which can be taken from Equation (19), ϕ is the particle volume fraction, and r is the aspect ratio of the particles which we estimate from the number of beads in each silicate to be 0.04762. By coupling the SRF model with Equation (20), the only unknown parameter is k. We adjust k so that the stress overshoot appears at $\gamma \approx 3$. The initial values of the A_2 components in SRF model were set to correspond to a random orientation state to conform to experimental measurements. In this way k is approximated to be 0.35. The simulation results are compared with SRF model in Figure 6. The agreement between DPD and SRF models is significantly improved compared with FT model after the introduction of the strain reduction factor in the calculations.

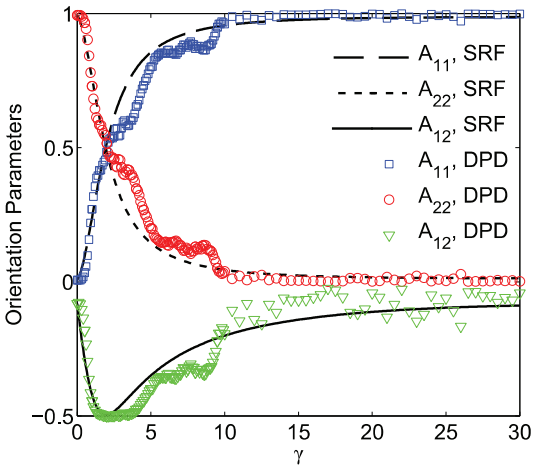

Figure 6. The evolution of orientation parameters against the applied shear strain, γ, from DPD simulations and SRF model for the normal initial orientation of the particles with respect to the flow direction. Note that the number of plotted simulated data points is decreased for $\gamma > 10$ to preserve clarity.

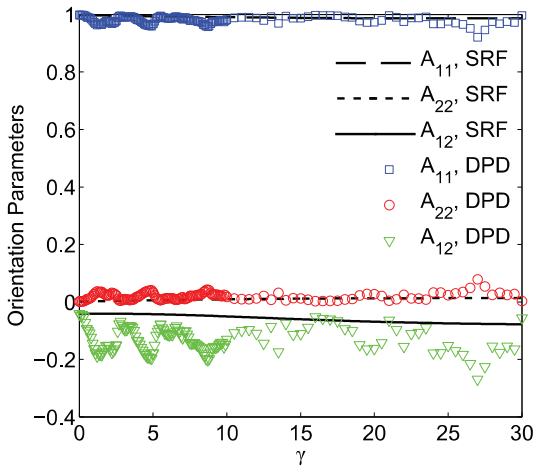

Figure 7. The evolution of orientation parameters against the applied shear strain, γ, from DPD simulations and SRF model for the parallel initial orientation of the particles with respect to the flow direction. Note that the number of plotted simulated data points is decreased for $\gamma > 10$ to preserve clarity.

The orientation kinetics in the system with a parallel initial orientation of silicate particles is plotted in Figure 7. As expected, the particles preserve their alignment. One should note that the agreement between the DPD results and the SRF model is rather poor for A_{12} component in comparison with the other orientation parameters. This behavior is simply due to the fact that according to Equation (16) in the vicinity of small and large orientation angles the changes in the A_{12} component are abrupt for small changes in the orientation angle. Therefore, the mathematical formulation of A_{12} results in more pronounced oscillations for a parallel initial orientation state with very small orientation angles. The fact that the almost perfectly oriented silicates oscillate under the flow is not limited only to the DPD simulation here. Small angle X-ray scattering measurements of a colloidal dispersion consisting of anisometric natural clay particles have shown that the particles tend to align along the flow direction with their surface normal to the velocity gradient direction, and partly rotate around flow streamlines.[64] Consequently, the oscillations observed could be possibly an advantage of DPD models in comparison with the SRF model. However, further studies must be conducted in order to prove or disprove this hypothesis.

The system simulated in this work represents an uncompatibilized polymer nanocomposite. In such systems the frequency of bead–bead contacts between polymer chains and silicate layers is relatively limited in comparison with compatibilized systems.[52] The orientation process could be slightly slowed down if the compatibility of the polymer molecules and silicate layers increases. With the improved compatibility, the number of dissipative bead–bead interactions at the interfaces between the polymer chains and silicate layers increases. Therefore, in more compatible systems the slower kinetics may be ascribed to the increased resistance against the movements and rotations of the layered silicates. Further information can be found elsewhere.[52]

As a result of the analyses provided so far, it can be stated that the DPD models depict the same orientation patterns as the FT and especially SRF models. Since the coefficients of these models are in good agreement with the experimental measurements, the good tally between them supports the creditability of DPD models. This ensures the conclusion that DPD models are capable to predict the orientation of weakly-interacting silicate particles in a polymer matrix with a good accuracy. Considering this encouraging capability, further studies could be conducted to investigate various aspects of molecular architecture on the orientation kinetics of layered silicates. These aspects can include (but not limited to) variations in the length of polymer chains, polydispersity in the length of polymer chains, altering the polymer type and shape, flexibility and aspect ratio of silicate layers, surface functionalization of layered silicates, etc. Such characteristics are directly accessible to DPD models while are merely indirectly controlled in standard orientation models. Flow conditions may also be varied in DPD simulations by changing the simulation temperature, the applied shear-rate, and the type of flow. These parameters can also be controlled in standard orientation models in a rather more straightforward fashion than in DPD simulations. Furthermore, the effects of the concentration of the layered silicate particles on the orientation kinetics could be explored. However, it could be necessary to adopt larger simulation boxes in this case which obliges more computation power and time. In sum, the capability of DPD models opens up many routes for future work on this academically and commercially interesting class of materials.

3.2. Scaleup of Orientation Evolution

The simulations discussed so far are presenting the orientation behavior of four silicate particles in a unit cell with an initial orientation state of either parallel or normal to the flow direction. One way to change the initial orientation state of the system without risking instability in the simulations and preserving the highly anisometric nature of the silicate particles is to build a large cell which each side of it could be several times the size of the unit cell. However, it is too time-consuming to simulate this large system. Therefore, a simple strategy to model such a large cell based on the unit cell is developed here.

A large cell is set up from $5 \times 5 \times 5$ unit cells. By mixing unit cells with different initial orientation states, i.e., parallel and normal to the flow, in the large cell, one can

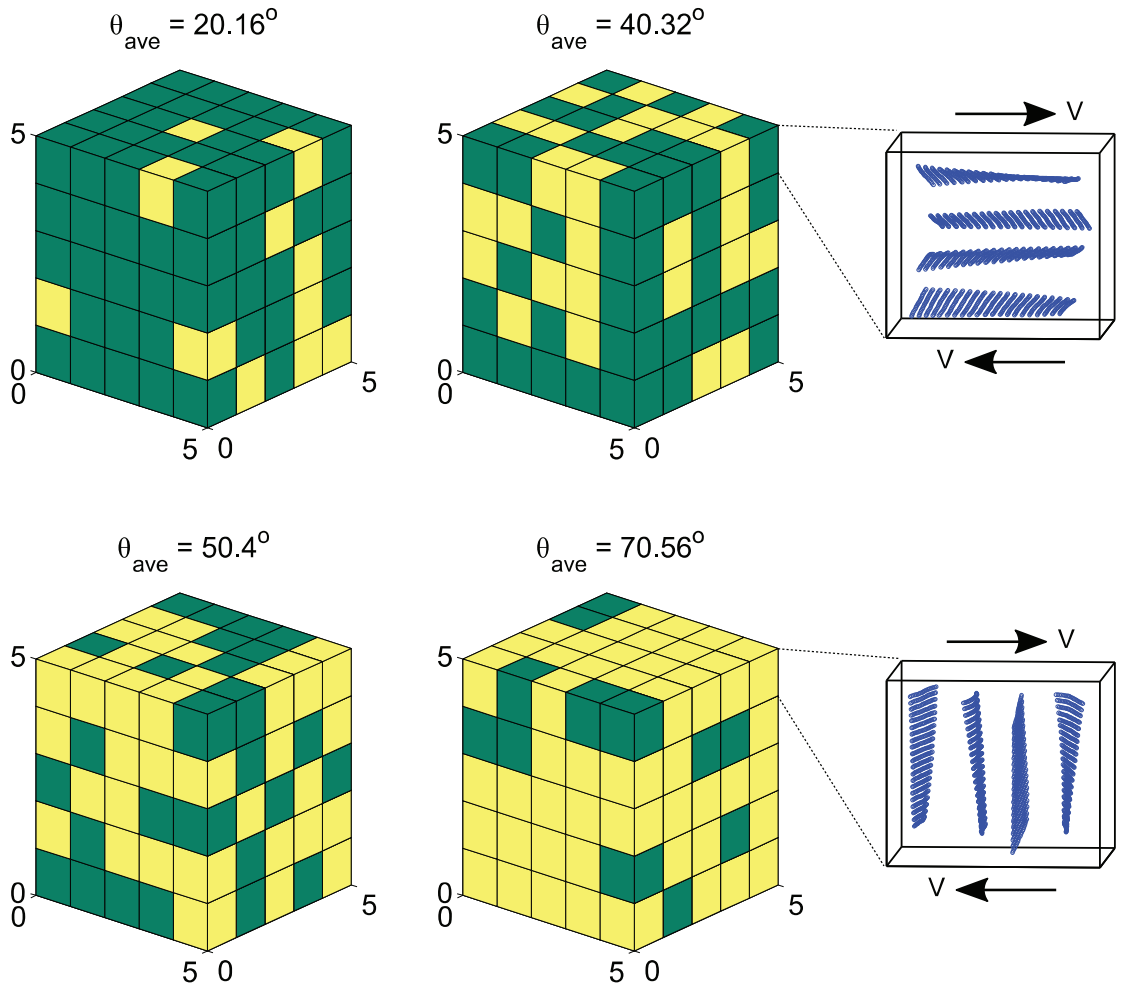

Figure 8. Examples of random mixing of unit cells in the large cell to produce different averaged initial orientation angles, θ_{ave}. The initial orientation of each constructing unit cell prior to the flow is manifested.

achieve a variety of averaged initial orientation angles in the large cell as shown in Figure 8. The idea of using only two types of fundamental unit cells to construct different systems provides the opportunity to significantly reduce the amount of simulations. We assume an affine deformation in the large cell. Consequently, if the strain imposed on the large cell is γ, the strain imposed on each unit cell is also γ. It is noteworthy to emphasize that the deformation in each unit cell is nonaffine due to the particle-based nature of DPD models. If each side of the unit cell is equivalent to 200 nm in tally with the previous report,[52] then the large cell has a side of 1 μm. Consequently, one can see that at a length scale where the polymer chains and particles sizes become important, the nonaffine deformations are dominant in the calculations. In order to calculate the average orientation angles in the large cell versus the applied strain, the orientation angles of the layered silicates in the constructing unit cells were taken at the corresponding applied strain from the DPD simulations of the unit cells. These values were then utilized to find the averaged second-order orientation tensor of the large cell. The average was performed over the total number of the layered silicate particles in the large cell based on its number of constructing unit cells of each type, i.e., parallel or normal to the flow.

The assumption of affine deformation in the large cell is promising since all of the unit cells are identical in every aspect except for their initial orientation. It has been shown before in biological systems that for fibrous tissues the underlying fiber orientation influences the macroscale to microscale strain transfer.[84] Moreover, it has been reported that local structural heterogeneities in polymer hydrogels could lead to nonaffine deformations.[85,86] However, it has also been stated that the importance of nonaffine deformations is strongly dependent on the scale of the deformation. Hatami-Marbini and Picu[87] studied the mechanics of random fiber networks above the rigidity percolation threshold and observed that they

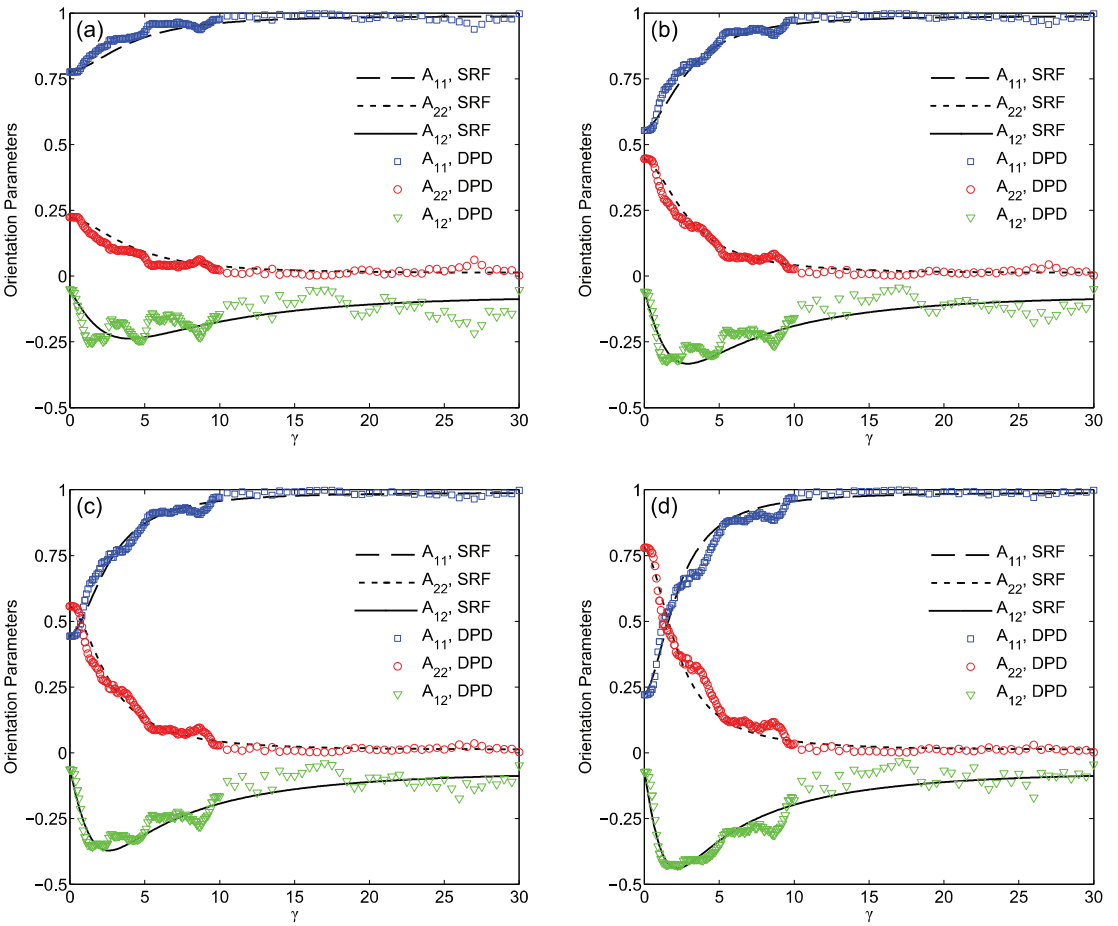

Figure 9. The evolution of orientation parameters against the applied shear strain, γ, from DPD simulations and SRF model for the systems with averaged initial orientation angles of a) 20.16°, b) 40.32°, c) 50.40°, and d) 70.56°. Note that the number of plotted simulated data points is decreased for $\gamma > 10$ to preserve clarity.

deform nonaffinely at all scales. They also found that as the scale of observation decreased, the nonaffinity increased following a power law scaling with exponent of ≈1.6. This simply means that if the length scale of the simulation is increased to five times its initial value, the nonaffinity of deformations decreases by a factor of 13. These experimental observations suggest that the coupling of nonaffine deformations at the DPD unit cell with the affine deformation at the large cell could provide results with reasonable precision. In order to test this assumption, the orientation parameters of such large cells were evaluated with strain based on the affine deformation in the large cell and compared with the predictions of SRF model.

The orientation parameters of large cells with various averaged initial orientation angles are plotted versus the applied strain in Figure 9. The good agreement between the SRF model and the DPD results coupled with the affine deformation assumption in the large cells supports the earlier hypothesis that the combination of affine and nonaffine deformations at different scales can give reasonable predictions of a system. One should note that the coefficients used in the SRF model are the same as those derived in the previous section. It is interesting to observe that in the systems with a more random averaged initial orientation state (see Figure 9b,c) the agreement between the SRF model and the simulations is much better than the systems with a more pronounced preferred initial orientation state (see Figure 9a,d). This is ascribed to the fact that the strain reduction factor in SRF model was determined based on the $\mathbf{A}_2$ corresponding to a random initial orientation tensor. It should be emphasized again that the calculation of A_{12} component is trickier than the other orientation parameters due to the strong instabilities at very small or large orientation angles inherited from its mathematical expression. Experiments suggest that some oscillations are also present in actual systems which could be possibly an advantage of DPD models.[64] Further simulations need to be done in order to prove or disprove this hypothesis. The orientation ellipse is shown

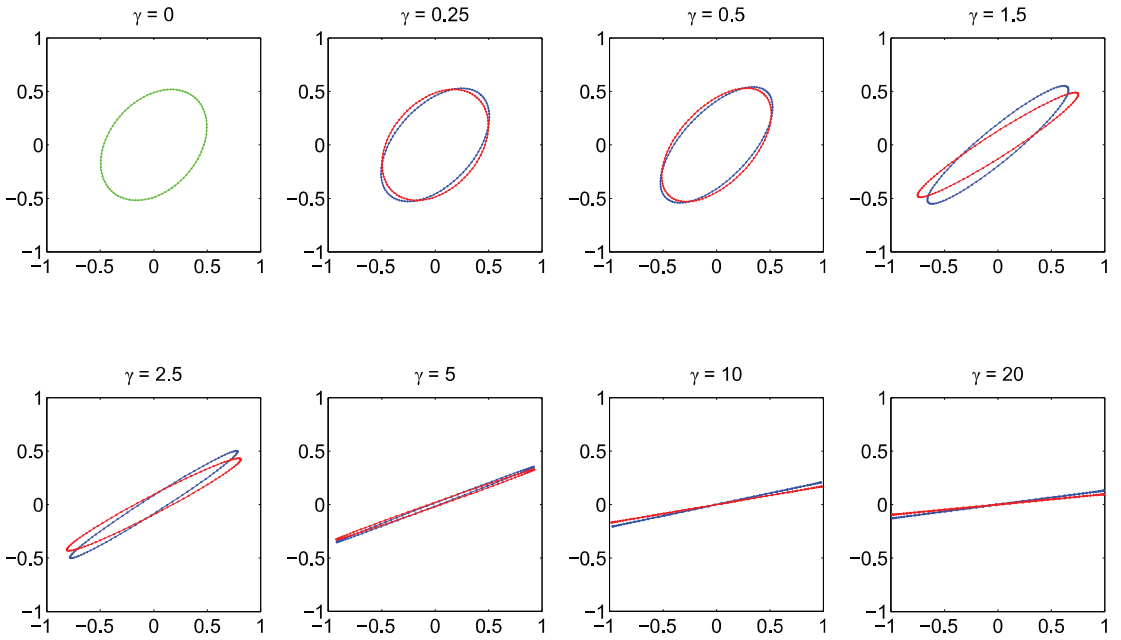

Figure 10. The orientation ellipse at absolute shear strains, γ, according to DPD simulations (red) and SRF model (blue) for the averaged initial orientation angle of 50.40° (green) with respect to the flow direction. The velocity and velocity gradient directions are along the horizontal and vertical axes, respectively. The horizontal and vertical axes of the plots are transformed eigenvalues of $\mathbf{A}_2$ with respect to the average orientation angle of the layered silicates.

in Figure 10 for the large cell with the averaged initial orientation angle of 50.4°. Both methods predict the preferred orientation of the silicate layers in the flow direction typical of weakly-interacting particles.

It can be simply shown that for any initial orientation state in the large cell, the second-order orientation tensor $\mathbf{A}_2^{lc}$ at any specific strain of γ follows the mixture law of the constructing unit cells, i.e., $\mathbf{A}_2^{lc} = \alpha \mathbf{A}_2^{p,uc} + (1-\alpha)\mathbf{A}_2^{n,uc}$. In this equation, $\mathbf{A}_2^{p,uc}$ and $\mathbf{A}_2^{n,uc}$ are the second-order orientation tensors of the constructing unit cells with parallel and normal initial orientation states, respectively, at the strain of γ. α is the fraction of the unit cells with parallel initial orientation state which must be included in the large cell to produce the desired initial orientation state. This simple formula is a result of detailed simulations presented here and is capable to reproduce the experimental predictions of SRF model based on published literature. Considering that the deformation can be often assumed affine unless the characteristic length of heterogeneity is comparable to the simulation length scale, this formula can produce reasonable results in the orientation calculations.

The possibility to transfer the orientation data from the unit cells to the large cell incorporating the applied strain as the linking parameter encourages a multiscale strategy to simulate the orientation process. The incorporation of the dimensionless strain parameter makes it possible to simplify the scaleup rules due to the coarse-graining nature of the DPD method when transferring the orientation data to the upper scale.[88] Furthermore, it has been shown experimentally that such non-Brownian systems exhibit strain-dependent microstructural reorganizations rather than time-dependent evolutions.[19,80] Moreover, as stated by Wang et al.[27] for non-Brownian particles the overall evolution of orientation process depends on the accumulated strain independent of the deformation rate. For fiber suspensions, they emphasize that "in the orientation modeling, kinetics means the rate of change of orientation with respect to strain, rather than the rate with respect to time."[27] As a result of all these arguments, it seems reasonable to use the applied strain to transfer the orientation data between different scales.

Attention must be paid that in systems with interacting particles such a scaleup strategy could not be applied unless the fundamental unit cell of DPD model is large enough to correctly account for particle–particle interactions. In order to highlight this issue, the MM model is incorporated to evaluate accurate estimations of the evolutions of orientation parameters with time in Cloisite/polypropylene nanocomposites. Rajabian et al.[24] performed startup of simple shear flow experiments on such nanocomposites containing 3–7 vol% of nanoparticles. They proposed the following set of parameters to best fit the experimental data: $l = 1$ nm, $d = 100$ nm, $\Lambda_p = 0.5 \times 10^{-5}$, $\Lambda_m = 5.9 \times 10^{-5}$, $b = 1$, $B_{pm} = -1.5$, $B_{pp} = -5$, $M_w = 8 \times 10^5 \frac{g}{mol}$, $\rho = 760 \frac{kg}{m^3}$, and $T = 473.2$ K. Utilizing these values and benefiting from the proposed mixing strategy, one can compare the large cell orientation data

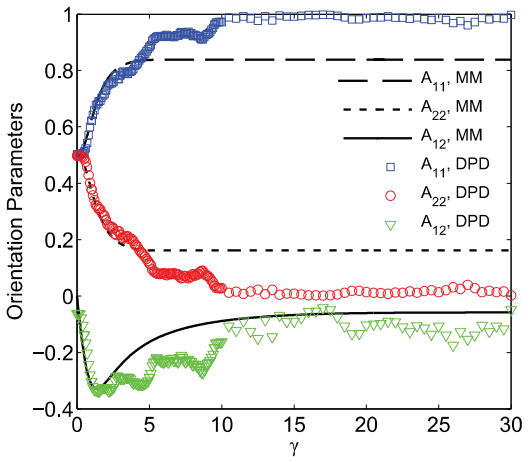

Figure 11. The evolution of orientation parameters against the applied shear strain, γ, from DPD simulations and mesoscopic model (MM) for the averaged initial orientation angle of 45° of the particles with respect to the flow direction. Note that the number of plotted simulated data points is decreased for $\gamma > 10$ to preserve clarity.

with the MM model predictions of Cloisite/polypropylene nanocomposites (see Figure 11). It is clear from the data that even though the kinetics of orientation in both methods manifests a reasonable agreement, the steady orientation state in the MM model is less perfect than the DPD simulations. This imperfect steady orientation state denotes strong interactions between the particles in the Cloisite/polypropylene systems. Consequently, one has to build a unit cell for DPD simulations which can include particle–particle interactions in order to correct for such effects in real nanocomposite materials.

4. Conclusions

This study focused on DPD models of weakly-interacting anisometric silicate particles embedded in a polymer matrix. The orientation process of silicate particles was investigated after the application of either parallel or normal shear flows. It was observed that the particles would reorganize themselves so that their surfaces would be normal to the velocity gradient direction. The steady orientation state showed an almost complete alignment along the flow typical of suspensions of weakly-interacting particles. In order to test the DPD models, the evolution of orientation under the shear flow was also modeled utilizing the widely used FT model. The particle–particle interaction coefficient in FT model was estimated from the simulated DPD system and was found to be very close to experimental measurements of polypropylene/organoclay nanocomposites. This coefficient was very small in value which approved the weak interactions among the silicate particles. The overall agreement between DPD results and FT model was good and both could predict the steady perfect alignment of the particles. However, the orientation kinetics was slower in DPD simulations rather than FT predictions. This was noted to be in agreement with experiments which propose slower orientation kinetics than FT predictions due to the reduced strains transferred to the particles from the bulk. To compensate for this problem, SRF model was incorporated. The strain reduction factor in this model was estimated based on experimental measurements, which suggest that the stress overshoot in such non-Brownian materials should occur at almost the same strain regardless of the applied shear-rate. The predictions from the SRF model were in good agreement with the DPD results. It was noted that both coefficients in the SRF model, i.e., the particle–particle interaction coefficient and the strain reduction factor, were determined either from solid experimental measurements or found to be very close to them. This encourages that the DPD models are not only compared with a valid model but also with actual measurements from the literature. Therefore, the good tally between the DPD and SRF models supports the capability of DPD to successfully simulate the orientation process of silicate particles in a polymer matrix.

A large cell was then constructed from unit cells with various averaged initial orientation angles. The evolution of orientation in the large cell was evaluated from evolutions in the unit cells based on the affine deformation assumption. The good agreement between such calculations and SRF model predictions supports that the affine deformation assumption in the large cell is reasonable. It was argued that the nonaffine deformation originated from the particle-based nature of DPD models at the lower scale, i.e., unit cells, could be combined with the affine deformation at the upper scale, i.e., the large cell, to yield appropriate estimations of the orientation state. The idea of using the dimensionless strain parameter to transfer orientation data to the upper scale was based on (i) the experiments which propose strain-dependent rather than time-dependent structural evolutions in such non-Brownian materials, (ii) the feasibility of scaling in these coarse-grained models, and (iii) that the orientation kinetics is simply the rate of change with respect to strain rather than time. It was noted that this strategy could be used to perform multiscale simulations of orientation process provided that the unit cell represents a precise description of the interactions between the components.

Received: November 19, 2015; Revised: March 11, 2016; Published online: April 14, 2016; DOI: 10.1002/mats.201500086

Keywords: dissipative particle dynamics; orientation; shear flow; silicate particles; standard orientation models

[1] S. Cheng, R. A. Cairncross, Y. G. Hsuan, C. Y. Li, *Polymer* **2013**, *54*, 5016.
[2] D. A. Brune, J. Bicerano, *Polymer* **2002**, *43*, 369.
[3] J. S. Shelley, P. T. Mather, K. L. DeVries, *Polymer* **2001**, *42*, 5849.
[4] S. Abbasi, P. J. Carreau, A. Derdouri, *Polymer* **2010**, *51*, 922.
[5] R. S. Bay, C. L. Tucker, *Polym. Compos.* **1992**, *13*, 317.
[6] R. S. Bay, C. L. Tucker, *Polym. Compos.* **1992**, *13*, 332.
[7] S. T. Chung, T. H. Kwon, *Polym. Compos.* **1996**, *17*, 859.
[8] K. Ortman, D. Baird, P. Wapperom, A. Aning, *Polym. Compos.* **2012**, *33*, 1360.
[9] S. G. Advani, C. L. Tucker, *Polym. Compos.* **1990**, *11*, 164.
[10] X. L. Xie, T. Q. Yang, C. Y. Tang, *Polym. Int.* **2003**, *52*, 310.
[11] L. G. Reifschneider, H. U. Akay, *Polym. Compos.* **1994**, *15*, 261.
[12] G. Ausias, J. F. Agassant, M. Vincent, *Int. Polym. Process.* **1994**, *9*, 51.
[13] G. B. Jeffery, *Proc. R. Soc. London, Ser. A* **1922**, *102*, 161.
[14] F. Folgar, C. L. Tucker, *J. Reinf. Plast. Compos.* **1984**, *3*, 98.
[15] S. G. Advani, C. L. Tucker, *J. Rheol.* **1987**, *31*, 751.
[16] A. P. R. Eberle, G. M. Vélez-García, D. G. Baird, P. Wapperom, *J. Non-Newton. Fluid Mech.* **2010**, *165*, 110.
[17] E. Nazockdast, H. Nazockdast, *Appl. Rheol.* **2011**, *21*, 25434.
[18] C. Kagarise, K. W. Koelling, Y. Wang, S. E. Bechtel, *Rheol. Acta* **2008**, *47*, 1061.
[19] W. Letwimolnun, B. Vergnes, G. Ausias, P. J. Carreau, *J. Non-Newton. Fluid Mech.* **2007**, *141*, 167.
[20] E. Cueto, R. Monge, F. Chinesta, A. Poitou, I. Alfaro, M. R. Mackley, *Int. J. Mater. Form.* **2010**, *3*, 1327.
[21] H. Eslami, M. Grmela, M. Bousmina, *J. Rheol.* **2007**, *51*, 1189.
[22] H. Eslami, M. Grmela, M. Bousmina, *Rheol. Acta* **2009**, *48*, 317.
[23] M. Rajabian, C. Dubois, M. Grmela, P. J. Carreau, *Rheol. Acta* **2008**, *47*, 701.
[24] M. Rajabian, G. Naderi, P. J. Carreau, C. Dubois, *J. Polym. Sci., Part B: Polym. Phys.* **2010**, *48*, 2003.
[25] H. M. Huynh, *Master's Thesis*, University of Illinois at Urbana-Champaign, USA **2001**.
[26] M. Sepehr, G. Ausias, P. J. Carreau, *J. Non-Newton. Fluid Mech.* **2004**, *123*, 19.
[27] J. Wang, J. F. O'Gara, C. L. Tucker, *J. Rheol.* **2008**, *52*, 1179.
[28] A. N. Rissanou, A. J. Power, V. Harmandaris, *Polym.* **2015**, *7*, 390.
[29] C. Baig, V. A. Harmandaris, *Macromolecules* **2010**, *43*, 3156.
[30] C. Baig, B. J. Edwards, D. J. Keffer, *Rheol. Acta* **2007**, *46*, 1171.
[31] J. D. Moore, S. T. Cui, H. D. Cochran, P. T. Cummings, *J. Non-Newton. Fluid Mech.* **2000**, *93*, 101.
[32] P. Nikunen, I. Vattulainen, M. Karttunen, *Phys. Rev. E: Stat. Nonlinear Soft Matter Phys.* **2007**, *75*, 36713.
[33] J. T. Padding, W. J. Briels, *J. Chem. Phys.* **2002**, *117*, 925.
[34] J. T. Padding, W. J. Briels, *J. Chem. Phys.* **2003**, *118*, 10276.
[35] G. Pan, C. W. Manke, *Int. J. Mod. Phys. B* **2003**, *17*, 231.
[36] J. D. Moore, S. T. Cui, H. D. Cochran, P. T. Cummings, *J. Non-Newton. Fluid Mech.* **2000**, *93*, 83.
[37] K. Zhang, C. W. Manke, *Mol. Simul.* **2000**, *25*, 157.
[38] A. Chatterjee, L.-M. Wu, *Mol. Simul.* **2008**, *34*, 243.
[39] E. S. Boek, P. V. Coveney, H. N. W. Lekkerkerker, P. Van Der Schoot, *Phys. Rev. E: Stat. Nonlinear Soft Matter Phys.* **1997**, *55*, 3124.
[40] W. Pan, B. Caswell, G. E. Karniadakis, *Langmuir* **2010**, *26*, 133.
[41] J. F. Morris, B. Katyal, *Phys. Fluids* **2002**, *14*, 1920.
[42] E. N. Skountzos, A. Anastassiou, V. G. Mavrantzas, D. N. Theodorou, *Macromolecules* **2014**, *47*, 8072.
[43] K. D. Papadimitriou, E. N. Skountzos, S. S. Gkermpoura, I. Polyzos, V. G. Mavrantzas, C. Galiotis, C. Tsitsilianis, *ACS Macro Lett.* **2016**, *5*, 24.
[44] K. L. Anderson, A. Sinsawat, R. A. Vaia, B. L. Farmer, *J. Polym. Sci., Part B: Polym. Phys.* **2005**, *43*, 1014.
[45] A. Sinsawat, K. L. Anderson, R. A. Vaia, B. L. Farmer, *J. Polym. Sci., Part B: Polym. Phys.* **2003**, *41*, 3272.
[46] V. Kalra, F. Escobedo, Y. L. Joo, *J. Chem. Phys.* **2010**, *132*, 24901.
[47] S. Meng, J. Zhang, Y. Wang, X. Li, C. Wu, T. Hou, L. Xiao, G. Lu, *Mol. Simul.* **2015**, *41*, 772.
[48] P. J. Hoogerbrugge, J. M. V. A. Koelman, *Europhys. Lett.* **1992**, *19*, 155.
[49] R. D. Groot, P. B. Warren, *J. Chem. Phys.* **1997**, *107*, 4423.
[50] M. Yamanoi, O. Pozo, J. M. Maia, *J. Chem. Phys.* **2011**, *135*, 44904.
[51] D. A. Fedosov, G. E. Karniadakis, B. Caswell, *J. Chem. Phys.* **2010**, *132*, 144103.
[52] A. Gooneie, S. Schuschnigg, C. Holzer, *Macromol. Theory Simul.* **2016**, *25*, 85.
[53] M. Doi, S. F. Edwards, *The Theory of Polymer Dynamics*, Clarendon Press, Oxford **1986**.
[54] T. W. Sirk, Y. R. Slizoberg, J. K. Brennan, M. Lisal, J. W. Andzelm, *J. Chem. Phys.* **2012**, *136*, 134903.
[55] A. Chatterjee, *Mol. Simul.* **2007**, *33*, 1233.
[56] A. Moshfegh, G. Ahmadi, A. Jabbarzadeh, *Eur. Phys. J. E* **2015**, *38*, 1.
[57] A. Moshfegh, A. Jabbarzadeh, *Mol. Simul.* **2015**, *41*, 1264.
[58] C. Pastorino, T. Kreer, M. Müller, K. Binder, *Phys. Rev. E: Stat. Nonlinear Soft Matter Phys.* **2007**, *76*, 026706.
[59] S. Khani, M. Yamanoi, J. Maia, *J. Chem. Phys.* **2013**, *138*, 174903.
[60] C. P. Lowe, *Europhys. Lett.* **1999**, *47*, 145.
[61] H. C. Andersen, *J. Chem. Phys.* **1980**, *72*, 2384.
[62] C.-C. Fu, P. M. Kulkarni, M. Scott Shell, L. Gary Leal, *J. Chem. Phys.* **2012**, *137*, 164106.
[63] C.-C. Fu, P. M. Kulkarni, M. S. Shell, L. G. Leal, *J. Chem. Phys.* **2013**, *139*, 94107.
[64] I. Bihannic, C. Baravian, J. F. L. Duval, E. Paineau, F. Meneau, P. Levitz, J. P. De Silva, P. Davidson, L. J. Michot, *J. Phys. Chem. B* **2010**, *114*, 16347.
[65] A. M. Philippe, C. Baravian, V. Bezuglyy, J. R. Angilella, F. Meneau, I. Bihannic, L. J. Michot, *Langmuir* **2013**, *29*, 5315.
[66] M. Rajabian, C. Dubois, M. Grmela, *Rheol. Acta* **2005**, *44*, 521.
[67] P. Español, P. Warren, *Europhys. Lett.* **1995**, *30*, 191.
[68] G. Scocchi, P. Posocco, M. Fermeglia, S. Pricl, *J. Phys. Chem. B* **2007**, *111*, 2143.
[69] S. P. Pereira, G. Scocchi, R. Toth, P. Posocco, D. R. Nieto, S. Pricl, M. Fermeglia, *J. Multiscale Modell.* **2011**, *3*, 151.
[70] S. Kim, A. M. Palomino, C. M. Colina, *Mol. Simul.* **2012**, *38*, 723.
[71] V. Ortiz, S. O. Nielsen, D. E. Discher, M. L. Klein, R. Lipowsky, J. Shillcock, *J. Phys. Chem. B* **2005**, *109*, 17708.
[72] A. Maiti, S. McGrother, *J. Chem. Phys.* **2004**, *120*, 1594.
[73] J. D. Ferry, *Viscoelastic Properties of Polymers*, 3rd ed., Wiley, New York 1980.
[74] L. A. Moreira, G. Zhang, F. Müller, T. Stuehn, K. Kremer, *Macromol. Theory Simul.* **2015**, *24*, 419.
[75] A. Gooneie, S. Schuschnigg, C. Holzer, *Macromol. Theory Simul.* **2016**, *25*, 170.
[76] Z. Fan, S. G. Advani, *Polymer* **2005**, *46*, 5232.
[77] N. Phan-Thien, X.-J. Fan, R. I. Tanner, R. Zheng, *J. Non-Newton. Fluid Mech.* **2002**, *103*, 251.
[78] R. Ṕrez-Aparicio, J. Colmenero, F. Alvarez, J. T. Padding, W. J. Briels, *J. Chem. Phys.* **2010**, *132*, 24904.

[79] J. H. Phelps, C. L. Tucker III, *J. Non-Newton. Fluid Mech.* **2009**, *156*, 165.
[80] M. J. Solomon, A. S. Almusallam, K. F. Seefeldt, A. Somwangthanaroj, P. Varadan, *Macromolecules* **2001**, *34*, 1864.
[81] E. Nazockdast, H. Nazockdast, F. Goharpey, *Polym. Eng. Sci.* **2008**, *48*, 1240.
[82] R. G. Larson *The Structure and Rheology of Complex Fluids*, Oxford University Press, New York 1999.
[83] G. G. Lipscomb, M. M. Denn, D. U. Hur, D. V. Boger, *J. Non-Newton. Fluid Mech.* **1988**, *26*, 297.
[84] W. M. Han, S.-J. Heo, T. P. Driscoll, L. J. Smith, R. L. Mauck, D. M. Elliott, *Biophys. J.* **2013**, *105*, 807.
[85] A. Basu, Q. Wen, X. Mao, T. C. Lubensky, P. A. Janmey, A. G. Yodh, *Macromolecules* **2011**, *44*, 1671.
[86] Q. Wen, A. Basu, P. A. Janmey, A. G. Yodh, *Soft Matter* **2012**, *8*, 8039.
[87] H. Hatami-Marbini, R. C. Picu, *Acta Mech.* **2009**, *205*, 77.
[88] R. M. Füchslin, H. Fellermann, A. Eriksson, H.-J. Ziock, *J. Chem. Phys.* **2009**, *130*, 214102.

7. Conclusions and Research Outlooks

In this final chapter, I review the main conclusions of this thesis briefly. Also, major research directions are discussed for future endeavors.

In their molten state, polymer nanocomposites (PNCs) are often categorized as non-Brownian suspensions. This is a consequence of the high viscosity of the matrix polymer as well as the physical characteristics of the suspended nanoparticles [73, 109]. It is well-known that the strong van der Waals interactions between nanoparticles lead to the formation of aggregated microstructures in PNCs, which significantly influences thermal, electrical, rheological, and mechanical properties of these materials [103, 184]. Therefore, a multitude of studies has been devoted to address these issues from both experimental and theoretical viewpoints [30, 37, 67, 73 - 75, 103, 119, 122, 136, 229]. It is generally accepted that the microstructure developments are controlled significantly by the applied flow fields on the PNCs [184]. This notion has led to numerous rheological investigations, which provide an indirect yet online knowledge about the microstructural evolutions due to different flow fields [112, 133, 189, 205].

In order to predict the microstructure, rheology offers a number of (mostly) mesoscopic models which can be coupled with macroscopic models once their coefficients are evaluated in measurements [76]. Such models often fail to provide detailed molecular information of the PNCs and are limited to averaged descriptions of the overall microstructure. Furthermore, a new set of measurements is necessary every time either the material or the flow change.

Consequently, the multiscale modelling approaches were incorporated which enabled the passing of information between the hierarchy of length/time scales inherent in PNCs [229]. These methods can provide an ab initio approach which rules out (or at least minimizes) any necessity for experimentation. Various aspects of PNCs have been treated before with different types of multiscale methods [6, 75, 229].

Despite all efforts, a framework for dynamic bridging of microstructure evolutions to macroscopic models has been hindered so far since it often necessitates millions of steps of simulation at the mesoscopic scale to account for a small portion of a macroscopic flow [66]. Therefore, a single-step sequential message-passing approach is often used in the multiscale simulation of PNCs rather than a dynamic microstructure development [22, 23, 183, 188, 203, 207, 232]. In this PhD research, a theoretical framework was developed based on well-credited mesoscopic dissipative particle dynamics (DPD) models in order to propose a solution to this problem.

Firstly, startup of steady shear flow properties of polydisperse linear polymers were studied using DPD. It was shown that the stress overshoot generally decreased with the introduction of polydispersity into the models due to the broad relaxation response of various length scales present in polydisperse systems. Steady-state stress became larger as polydispersity increased due to the higher forces necessary to orient and stretch long chain fractions in the flow direction. Detailed analyses of nonbonded interactions proved a complex microstructural evolution because of orientation and chain stretching during the flow. It was evident that the orientation of long chain fractions forces more severe penalties on the frequency of

nonbonded interactions than the short chain fractions. The results support the coupled effect of orientation and stretching to influence the stress profile in startup of shear flow simulations. The gyration radius data also proved that the chains increase their size during the flow. The larger size and the slowed-down elongation dynamics of long fractions were evident. Moreover, the startup of shear flow simulations were performed at different shear-rates. The steady-state shear viscosity results showed higher viscosities in the polydisperse systems at all shear-rates. It was noted that these observations are in qualitative agreement with the available experimental data of different PP samples.

Secondly, the orientation of layered silicate particles in polymer melts under different shear flows was studied utilizing DPD method. An anisometric semiflexible three-layered silicate particle was embedded in uncompatibilized and/or compatibilized polymer matrices. The system was imposed to shear flows with different directions as well as shear-rates. Pair distribution functions in three orthogonal planes proved that regardless of the applied flow direction, the layers rearrange themselves so that their surfaces would be normal to the velocity gradient direction. Some deviations from a completely oriented microstructure were evidenced at low shear-rates due to the dominating thermal fluctuations at small Peclet numbers. These observations were in good agreement with previous publications. Furthermore, the effects of silicate surface treatment and compatibilizing molecules were studied by introducing compatibilizer molecules and modifying the repulsion parameters between the beads. Higher exfoliation degrees were evidenced in such compatibilized systems at high shear-rates while none was seen in uncompatibilized counterparts. In compatibilized systems, the pair distribution functions and trajectory data showed that the silicate layers align perpendicular to the velocity gradient direction the same as the uncompatibilized systems. However, it was demonstrated that the orientation process becomes more stable in these systems even at low shear-rates. The calculations of the orientation angle as well as the angle with the velocity gradient direction also showed this behavior. The shear stress was plotted with time for uncompatibilized and compatibilized systems. The stress profile falls in numerical uncertainties in uncompatibilized systems while it shows a characteristic overshoot in compatibilized systems. This overshoot was shown to be a result of (i) the large interfaces between the silicate layers and the matrix due to the exfoliation and (ii) the increased number of bead–bead contacts between the matrix and the layers leading to higher energy dissipations. This idea also explains why the orientation process becomes more stable in compatibilized systems even at low shear-rates. In compatibilized systems, higher energy dissipations lead to an increase in the overall viscosity (as reflected in the shear stress data) and therefore results in larger Peclet numbers. The contribution of thermal fluctuations to the overall response of the system becomes less significant compared with the shear stresses. Thus, the orientation process is less controlled by such distortions.

Finally, the orientation process of weakly-interacting silicate particles was compared with the predictions of the frequently-used orientation models, i.e. the Folgar-Tucker model (FT), the strain reduction factor model (SRF), and the more elaborate model of Rajabian et al. [168, 169]. It was shown that DPD model could successfully predict the slowed-down orientation kinetics (due to the reduced strains transferred to the particles from the bulk) in agreement with experiments while FT fails to predict such effects. On the other hand, the predictions of

the SRF model and DPD simulations were in good agreement. It was noted that both coefficients in the SRF model, i.e., the nanoparticle–nanoparticle interaction coefficient and the strain reduction factor, were determined either from solid experimental measurements or found to be very close to them. This encourages that the DPD models are not only compared with a valid model but also with actual measurements from the literature. Therefore, the good tally between the DPD and SRF models further supports the capability of DPD to successfully simulate the orientation process of silicate particles in a polymer matrix.

The conclusions presented so far prove the main hypothesis of this research to be true: DPD is capable to capture the orientation process in PNCs correctly during an applied flow field. In order to construct the multiscale strategy, a large cell was constructed from unit cells with various averaged initial orientation angles. The evolution of orientation in the large cell was evaluated from evolutions in the unit cells based on the affine deformation assumption. The good agreement between such calculations and SRF model predictions supports that the affine deformation assumption in the large cell is reasonable. It was argued that the nonaffine deformation originated from the particle-based nature of DPD models at the lower scale, i.e., unit cells, could be combined with the affine deformation at the upper scale, i.e., the large cell, to yield appropriate estimations of the orientation state. The idea of using the dimensionless strain parameter to transfer orientation data to the upper scale was based on (i) the experiments which propose strain-dependent rather than time-dependent structural evolutions in such non-Brownian materials, (ii) the feasibility of scaling in these coarse-grained models, and (iii) that the orientation kinetics is simply the rate of change with respect to strain rather than time. It was noted that this strategy could be used to perform multiscale simulations of orientation process provided that the unit cell represents a precise description of the interactions between the components. Therefore, the other main hypothesis of this research, i.e. the orientation process in non-Brownian PNCs are strain-dependent rather than time-dependent, was verified successfully for layered silicate nanoparticles.

My efforts in this field have resulted in a strain-bridging algorithm which allows for an accelerated passing of the microstructure information to the macroscopic models [76]. Indeed, a determining outlook would be to investigate the physical foundation of the strain-dependent microstructure evolutions under flow and to further develop the strain-bridging algorithm. While the strain-dependent microstructure evolution is experimentally observed for non-Brownian suspensions under flow [109, 112, 133, 189], it has not received much theoretical investigation yet. Therefore, it should be addressed in more details in order to build the multiscale theory upon it.

Moreover, one can consider the strain-bridging algorithm in its current form incomplete since it has been only used to develop the orientation patterns of weakly-interacting layered silicate particles in a generic polymer under shear flows [76]. In addition to polymer/layered silicate nanocomposites, the strain-bridging algorithm must also be tested for other non-Brownian PNCs with spherical, disk-like, and rod-like nanoparticles of both weakly- and strongly-interacting types. It is a fascinating outlook to extend this methodology to materials other than PNCs as well provided that their microstructural evolution under flow is proved to be strain-dependent rather than time-dependent. For instance, the flow of biological fluids in body could be envisioned in the strain-dependent multiscale scheme [57]. The formation and

destruction of instantaneous structures due to various inclusions such as drugs are suitable targets for further investigations utilizing the new methodology. It is a remaining challenge for future research to improve, extend, and generalize this algorithm.

It is a significant topic for further investigation to not only focus on the formation of anisotropic (preferentially oriented) structures of nanoparticles within the polymer matrix, but also to consider the interplay of the flow-induced large- and small-scale dispersion mechanisms of nanoparticles (e.g. the intercalation and exfoliation processes in the case of layered silicates, respectively) with the orientation process. Only after such a generalization, the strain-bridging algorithm can truly serve to predict the microstructure evolutions of advanced materials under flow using a hierarchy of scales.

The upscaling methodology developed in this study should be linked to atomistic models (e.g. molecular dynamics) on the lower hand, and to appropriate macroscopic models (e.g. smoothed particle hydrodynamics) on the upper hand, to result in a complete multiscale model. The results of this PhD work are expected to be at the heart of this multiscale model where an accelerated, dynamic passing of microstructure/flow information is most needed between the meso and macro scales.

The outcome of these efforts will be eventually a theoretical framework for multiscale modelling of (at least) non-Brownian PNCs experiencing shear flows. This framework should allow for a detailed atomistic modelling of PNCs, followed by a dynamic passing of microstructure information to macroscopic models. This dynamic self-developing multiscale strategy will certainly push the rheological theories forward.

8. Acronyms and Nomenclature

The present list of acronyms and nomenclature is reproduced from our review paper (Gooneie A., Schuschnigg S., Holzer C.: A Review of Multiscale Computational Methods in Polymeric Materials, Polymers 9 (1), 2017, pp. 16). If any abbreviation or parameter is different from the definitions in this table, it is clearly pointed in the text.

Acronyms	
Acronym	Full phrase
AA	All-Atomistic
AC	Amorphous Cell method
AdResS	Adaptive Resolution Scheme
AIMD	Ab Initio Molecular Dynamics
AtC	Atomistic/Continuum method
BD	Brownian Dynamics
BDM	Bridging Domain Method
BGK-LB	Bhatnagar, Gross, And Krook LB method
BSM	Bridging Scale Method
CACM	Composite Grid Atomistic/Continuum Method
CADD	Coupled Atomistic and Discrete Dislocation method
CFD	Computational Fluid Dynamics
CG	Coarse-Grained
CGMD	Coarse-Grained Molecular Dynamics
CLS	Coupling of Length Scales method
CRW	Conditional Reversible Work
D2Q9	2-dimensional lattice with 9 allowed velocities used in LB simulations
D3Q19	3-dimensional lattice with 19 allowed velocities used in LB simulations
DDFT	Dynamic Density Functional Theory
DFT	Density Functional Theory
DPD	Dissipative Particle Dynamics
EFCG	Effective Force CG
EM	Energy Minimization
FDM	Finite Difference Method
FE	Finite Element

FEAt	Finite-Element/Atomistic method
FEM	Finite Element Method
FVM	Finite Volume Method
GDM	Generalized Differences Methods
GFEM	Galerkin Finite Element Method
GPU	Graphics Processing Unit
H-AdResS	Hamiltonian Adaptive Resolution Scheme
HSM	Hybrid Simulation Method
IBI	Iterative Boltzmann Inversion
IMC	Inverse Monte Carlo
LB	Lattice Boltzmann
LGCA	Lattice Gas Cellular Automata
LSM	Lattice Spring Model
MC	Monte Carlo
MD	Molecular Dynamics
Na-MMT	Sodium Montmorillonite
NEMS	Nano-Electro-Mechanical Systems
OpenFOAM	Open Source Field Operation And Manipulation
PA	Polyamide
PAC	Pseudo Amorphous Cell method
Pe	Peclet number
PE	Polyethylene
PNC	Polymer Nanocomposite
PP	Polypropylene
pPMF	Pair Potential of Mean Force
PS	Polystyrene
PTT	Poly(Trimethylene Terephthalate)
QC	Quasicontinuum method
QM	Quantum Mechanics
QUICK	Quadratic Upstream Interpolation for Convective Kinematics
Re	Reynolds number
RVE	Representative Volume Element

SDPD	Smoothed Dissipative Particle Dynamics
SPH	Smoothed Particle Hydrodynamics
SRF	Strain Reduction Factor model
SUPG	Streamline-Upwind/Petrov-Galerkin
TB	Tight Binding
TDGL	Time-Dependent Ginzburg-Landau
VMS	Variational Multiscale methods
We	Weissenberg number
XRD	X-Ray Diffraction

Nomenclature	
Symbol	Meaning
A	$A = 6\xi k_B T$ in BD method
$\mathbb{A}_{ij}$	maximum repulsion between bead i and bead j in DPD method
$\mathbf{a}_i$	acceleration of ith particle
B^A	atomistic domain in concurrent simulations
B^C	continuum domain in concurrent simulations
B^H	handshake region in concurrent simulations
B^I	interfacial region in concurrent simulations
B^P	padding region in concurrent simulations
b_i	fitting parameter
c_i	fitting parameter
$\mathbf{D}^{\mathfrak{d}}$	the diffusion term of $\mathfrak{d}$
D_{cm}	center-of-mass self-diffusion coefficient
e	element
$\mathfrak{e}$	absolute unit charge of an electron
E_f	Young's modulus
E_i	energy of atom, particle, or node i
$\overline{E}_i$	energy of the ith representative atom in QC method
E_k	eigenstate of energy
$E_{k_{el}}$	eigenstate energy of an electron

E_{k_n}	eigenstate energy of a nucleon
E^{tot}	total energy
$\Delta\mathrm{F}(\psi_\alpha)$	free energy difference in H-AdResS method
$\mathrm{F}_{ij}^{\mathrm{C}}$	conservative force between bead i and its neighboring bead j within the force cutoff radius r_{cut}
$\mathrm{F}_{ij}^{\mathrm{D}}$	dissipative force between bead i and its neighboring bead j within the force cutoff radius r_{cut}
$\mathrm{F}_{ij}^{\mathrm{R}}$	random forces between bead i and its neighboring bead j within the force cutoff radius r_{cut}
$\mathrm{F}_{\alpha}^{drift}$	drift force of molecule α
$\bar{\mathbf{f}}$	vector of applied forces in the FE region of a concurrent simulation
$\mathbf{f}_i$	force acting on the ith atom, particle, or node
$\mathbf{f}_{\alpha\beta}$	force acting between molecules α and β
$\mathbf{f}^{th}$	thermodynamic force
$\mathbf{f}_i^{\mathrm{B}}$	Brownian random force acting on the ith particle
$\mathbf{f}_{\alpha\beta}^{\mathrm{AA}}$	atomistic forces acting on molecule α due to the interaction with molecule β
$\mathbf{f}_{\alpha\beta}^{\mathrm{CG}}$	CG forces acting on molecule α due to the interaction with molecule β
G'	storage modulus
G''	loss modulus
$\mathrm{H}(\mathbf{\Gamma}_i)$	Hamiltonian of the system at system state $\mathbf{\Gamma}_i$
$\widehat{\mathrm{H}}$	modified Hamiltonian of the H-AdResS method
$\Delta\mathrm{H}(\mathbf{\Gamma}_{i\rightarrow j})$	change in the system Hamiltonian for going from system state $\mathbf{\Gamma}_i$ to $\mathbf{\Gamma}_j$
$\Delta\mathrm{H}(\psi_\alpha)$	compensation term in the Hamiltonian of the H-AdResS method
$\mathrm{H}_{FE}(\mathbf{u}_\alpha,\dot{\mathbf{u}}_\alpha)$	Hamiltonian of the FE region as a function of the nodal displacements $\mathbf{u}_\alpha$, and time rate of nodal displacements $\dot{\mathbf{u}}_\alpha$
$\mathrm{H}_{FE/MD}(\mathbf{r}_j,\mathbf{v}_j,\mathbf{u}_\alpha,\dot{\mathbf{u}}_\alpha)$	Hamiltonian of the FE/MD handshake region as a function of the atomic positions $\mathbf{r}_j$, atomic velocities $\mathbf{v}_j$, nodal displacements $\mathbf{u}_\alpha$, and time rate of nodal displacements $\dot{\mathbf{u}}_\alpha$
$\mathrm{H}_{MD}(\mathbf{r}_j,\mathbf{v}_j)$	Hamiltonian of the MD region as a function of the atomic positions $\mathbf{r}_j$, and atomic velocities $\mathbf{v}_j$
$\mathrm{H}_{MD/TB}(\mathbf{r}_j,\mathbf{v}_j)$	Hamiltonian of the MD/TB handshake region as a function of the atomic positions $\mathbf{r}_j$, and atomic velocities $\mathbf{v}_j$

$\mathrm{H}_{TB}(\mathbf{r}_j,\mathbf{v}_j)$	Hamiltonian of the TB region as a function of the atomic positions $\mathbf{r}_j$, and atomic velocities $\mathbf{v}_j$
H_{tot}	total Hamiltonian
h	Planck's constant
$\mathbf{J}^{\vartheta,\mathrm{C}}$	convection flux term in FVM formulation
$\mathbf{J}^{\vartheta,\mathrm{D}}$	diffusion flux term in FVM formulation
K	the all-atom kinetic energy of the molecules
k_B	Boltzmann's constant
k_T	isothermal compressibility
l	bond length
M, M_w	molecular weight
m	mass of an atom or particle
m_{el}	mass of an electron
m_n	mass of a nucleon
N	number of atoms, particles, or nodes
N_c	number of monomers per chain
N_e	number of elements
N_q	number of quadrature points in the numerical integration
N_r	number of representative atoms in QC method
$\mathbf{P}$	the projection matrix
$\Delta\mathrm{p}(\psi_\alpha)$	pressure difference along the interface in H-AdResS method
$\mathrm{p}_{i\to j}$	probability of accepting a new configuration for going from system state $\mathbf{\Gamma}_i$ to $\mathbf{\Gamma}_j$
p^{R}	probability distribution function
$\mathrm{p}^{\mathrm{R}}_{target}$	the target probability distribution function of AA simulations
Q^{ϑ}	the generation/destruction of ϑ within the control volume per unit volume
$\mathrm{R}(\mathrm{u})$	residual form of a partial differential equation in terms of the unknown function u in FEM scheme
R_g	radius of gyration
$\mathbf{R}_i$	center of mass coordinates of the ith molecule
$\mathbf{r}$	coordinates vector of an atom, or particle, or node

r	distance
r_{cut}	force cutoff radius
$\mathbf{r}_{el_i}$	spatial coordinates of an electron
$\hat{\mathbf{r}}_{ij}$	unit vector pointing from the center of bead j to that of bead i
$\mathbf{r}_{n_j}$	spatial coordinates of a nucleon
$\mathbf{r}_e^{cent}$	coordinates of the Gauss point in element e taken at the centroid of the triangular elements
$\mathbf{r}_e^q$	position of quadrature point q of element e in the reference configuration
$\delta\mathbf{r}_i^{\mathrm{B}}(\mathrm{t}+\Delta\mathrm{t})$	random displacement of the ith particle due to the random forces during time step $\Delta\mathrm{t}$
$\mathbf{S}$	surface vector
S_i	ith subregion
$\{\mathrm{S}_\mathrm{Q}\}$	set of weighting functions in FEM
$\mathrm{s}_{entropy}$	rescaling factor for the entropy change
$\mathrm{s}_{friction}$	rescaling factor for the friction change
T	temperature
t	time
$\Delta\mathrm{t}$	time step
$\mathrm{U}(\mathbf{r})$	potential energy
U^A	potential energies of the atomistic region
U^{atom}	energy functional of a systems assuming it is entirely modelled using atoms
U^C	potential energies of the continuum region
$\mathrm{U}^{\mathrm{CG}}(\mathrm{r},l,\theta,\mho)$	general form of the CG potential function in IBI method
U^{FE}	energy functional of a systems assuming it is entirely modelled using FEM
U^H	potential energies of the handshake region
U^{int}	energy of internal interactions
U^{tot}	total potential energy of the entire system
$\mathrm{U}_{angle}^{\mathrm{CG}}(\theta)$	bond angle potential in the blob model
$\mathrm{U}_{bond}^{\mathrm{CG}}(l)$	bond potential in the blob model

$U^{CG}_{nonbonded}(\mathbf{r})$	potential of nonbonded interactions in the blob model
U^{AA}_{α}	potential energy of molecule α in the AA representation
U^{CG}_{α}	potential energy of molecule α in the CG representation
$\mathbf{u}$	vector of nodal displacements in the FE region of a concurrent simulation
$u(\mathbf{r})$	the unknown function in FEM which one needs to find
$u_h(\mathbf{r})$	approximation of the function $u(\mathbf{r})$ under consideration in FEM
$\mathbf{u}_{\alpha}$	displacements of atom, particle, or node α
$\dot{\mathbf{u}}_{\alpha}$	rate of displacements of atom, particle, or node α
u^n	values of the function u_h at node n of the mesh
V_e	volume of element e
dV	volume element of the simulation domain in FEM
∂V_e	surfaces surrounding the volume V_e of element e
v	macroscopic velocity magnitude
$\mathbb{v}$	$\mathbb{v} = \sqrt{3}\,\mathbb{v}_s$ in LB method
$\mathbf{v}(\mathbf{r},t)$	macroscopic local velocity at node $\mathbf{r}$ at time t in LB
$\tilde{\mathbf{v}}_i(t+\Delta t)$	estimated velocity in the next time step using a predictor method in DPD velocity-Verlet algorithm
$\delta\mathbf{v}^B_i(t+\Delta t)$	Random velocity change of the ith particle due to the random forces during time step Δt
$\mathbf{v}_i$	velocity of ith atom, particle, or node
$\lvert\mathbb{v}_i\rvert$	velocity magnitude in i-direction in LB method
$\{\mathbb{v}_k\}$	set of prescribed velocity vectors connecting the neighboring nodes in LB method
$\mathbb{v}_s$	speed of sound
W	a function of deformation gradient $\boldsymbol{\Delta}$
w_i	weighting constants used in LB method
$z_n e$	positive unit charge of a nucleon
$\boldsymbol{\Gamma}_i$	system state in a phase space at position i
γ	exact solution in the projection method
$\dot{\gamma}$	shear-rate
$\bar{\gamma}(\mathbf{r}_{\alpha})$	coarse scale solution of a problem in the projection method
γ'	fine scale solution of a problem in the projection method

$\boldsymbol{\Delta}$	deformation gradient
δ	delta function
$\Delta\mu(\psi_\alpha)$	chemical potential gradient in H-AdResS method
ε	neighboring cells of a specific element in FVM
ζ	random number between 0 and 1 which is to determine the acceptance or rejection of a new configuration
ζ_{ij}	a Gaussian random number with zero mean and unit variance used in the definition of the random forces between beads i and j in DPD method
η	viscosity
Θ	a weighting function to link FE and atomistic models in concurrent simulations
θ	bond angle
θ_{ave}	averaged initial orientation angle
$\boldsymbol{\Lambda}_{ik}$	collision matrix used in LB method
λ	multiplication parameter in in DPD velocity-Verlet algorithm
μ	fitting parameter
ν	fitting parameter
ϑ	a general conserved scalar variable in FVM scheme
ξ	friction coefficient between atoms or particles
ξ_{ij}	friction coefficient between bead i and bead j in DPD method
ξ_m	friction coefficient between particles of freely-rotating chains
ϖ	wave function of electrons
ϱ	fluid density in CFD
$\varrho(\mathbf{r},\mathrm{t})$	macroscopic local density at node $\mathbf{r}$ at time t in LB method
$\varrho_i(\mathrm{r})$	molecular density profile in the ith iteration step as a function of the position in the direction perpendicular to the interface, in AdResS method
ϱ^*	reference molecular density
ϱ_i	ith weighting function in FEM
σ_{ij}	noise amplitude between bead i and bead j in DPD method
ς_i^α	shape function of node i evaluated at the point with coordinates $\mathbf{r}_\alpha$
τ	characteristic collision time in LB method

$\Phi(\mathrm{u})$	integral form of the weighted residuals in FEM
$\varphi(\mathbf{r})_k$	wave function in Schrödinger's equation
ϕ	wave function of the nuclei
χ_{ij}	a parameter in DPD formulation which equals 1 for beads with a distance less than r_{cut} and equals 0 otherwise
$\Psi_i(\mathbf{r},\mathrm{t})$	particle distribution function used in LB at node $\mathbf{r}$ at time t moving with velocity $\mathbb{v}_i$ In the i-direction
$\Psi_i^{\mathrm{eq}}(\mathbf{r},\mathrm{t})$	equilibrium particle distribution function used in LB at node $\mathbf{r}$ at time t moving with velocity $\mathbb{v}_i$ In the i-direction
ψ	spatial interpolation function in AdResS method
$\psi_n(\mathbf{r})$	interpolation functions in FEM for node n
$\psi_n^e(\mathbf{r})$	interpolation functions in FEM for node n in element e
Ω	simulation domain in FEM
$\partial\Omega$	boundaries of the simulation domain in FEM
$\mho$	dihedral angle
ω	frequency
ω_i	quadrature weight signifying how many atoms a given representative atom stands for in the description of the total energy, in QC method
$\omega^{\mathrm{D}}(\mathrm{r}_{ij})$	dissipative weight function in DPD method
ω^q	associated Gauss quadrature weights of quadrature point q of element e
$\omega^{\mathrm{R}}(\mathrm{r}_{ij})$	random weight function in DPD method

9. References

[1] Abbasi S., Carreau P.J., Derdouri A.: Flow induced orientation of multiwalled carbon nanotubes in polycarbonate nanocomposites: Rheology, conductivity and mechanical properties, Polymer 51 (4), 2010, pp. 922–935

[2] Abraham F.F., Broughton J.Q., Bernstein N., Kaxiras E.: Spanning the continuum to quantum length scales in a dynamic simulation of brittle fracture, Europhysics Letters 44 (6), 1998, pp. 783–787

[3] Abraham F.F., Broughton J.Q., Bernstein N., Kaxiras E.: Spanning the length scales in dynamic simulation, Computers in Physics 12 (6), 1998, pp. 538–546

[4] Advani S.G., Tucker C.L.: A numerical simulation of short fiber orientation in compression molding, Polymer Composites 11 (3), 1990, pp. 164–173

[5] Advani S.G., Tucker C.L.: The Use of Tensors to Describe and Predict Fiber Orientation in Short Fiber Composites, Journal of Rheology 31 (8), 1987, pp. 751–784

[6] Allegra G., Raos G., Vacatello M.: Theories and simulations of polymer-based nanocomposites: From chain statistics to reinforcement, Progress in Polymer Science (Oxford) 33 (7), 2008, pp. 683–731

[7] Anderson K.L., Sinsawat A., Vaia R.A., Farmer B.L.: Control of silicate nanocomposite morphology in binary fluids: Coarse-grained molecular dynamics simulations, Journal of Polymer Science, Part B: Polymer Physics 43 (8), 2005, pp. 1014–1024

[8] Ausias G., Agassant, J. F., Vincent M.: Flow and Fiber Orientation Calculations in Reinforced Thermoplastic Extruded Tubes, International Polymer Processing 9 (1), 1994, pp. 51–59

[9] Ayton G.S., Noid W.G., Voth G.A.: Multiscale modeling of biomolecular systems: in serial and in parallel, Current Opinion in Structural Biology 17 (2), 2007, pp. 192–198

[10] Badia S., Parks M., Bochev P., Gunzburger M., Lehouc Q.: On atomistic-to-continuum coupling by blending, Multiscale Modeling and Simulation 7 (1), 2008, pp. 381–406

[11] Baig C., Harmandaris V.A.: Quantitative analysis on the validity of a coarse-grained model for nonequilibrium polymeric liquids under flow, Macromolecules 43 (7), 2010, pp. 3156–3160

[12] Bay R.S., Tucker C.L.: Fiber orientation in simple injection moldings. Part I: Theory and numerical methods, Polymer Composites 13 (4), 1992, pp. 317–331

[13] Bershtein V., Fainleib A., Egorova L., Gusakova K., Grigoryeva O., Kirilenko D., Konnikov S., Ryzhov V., Yakushev P., Lavrenyuk N.: The impact of ultra-low amounts of amino-modified MMT on dynamics and properties of densely cross-linked cyanate ester resins, Nanoscale Research Letters 10 (1), 2015, pp. 165

[14] Bleha T., Gajdos J., Karasz F.E.: Energetics of strain-induced conformational transitions in polymethylene chains, Macromolecules 23 (18), 1990, pp. 4076–4082

[15] Boek E.S., Coveney P.V., Lekkerkerker, H. N. W., Van Der Schoot, P.: Simulating the rheology of dense colloidal suspensions using dissipative particle dynamics, Physical Review E: Statistical, Nonlinear, and Soft Matter Physics 55 (3 SUPPL. B), 1997, pp. 3124–3133

[16] Born M., Oppenheimer R.: Zur Quantentheorie der Molekeln, Annalen der Physik 389 (20), 1927, pp. 457–484

[17] Branduardi D., Gervasio F.L., Parrinello M.: From A to B in free energy space, Journal of Chemical Physics 126 (5), 2007

[18] Brooks B.R., Brooks Iii C.L., MacKerell Jr. A.D., Nilsson L., Petrella R.J., Roux B., Won Y., Archontis G., Bartels C., Boresch S., Caflisch A., Caves L., Cui Q., Dinner A.R., Feig M., Fischer S., Gao J., Hodoscek M., Im W., Kuczera K., Lazaridis T., Ma J., Ovchinnikov V., Paci E., Pastor R.W., Post C.B., Pu J.Z., Schaefer M., Tidor B., Venable R.M., Woodcock H.L., Wu X., Yang W., York D.M., Karplus M.: CHARMM: The biomolecular simulation program, Journal of Computational Chemistry 30 (10), 2009, pp. 1545–1614

[19] Broughton J.Q., Abraham F.F., Bernstein N., Kaxiras E.: Concurrent coupling of length scales: Methodology and application, Physical Review B: Condensed Matter and Materials Physics 60 (4), 1999, pp. 2391–2403

[20] Brown J.R., Seo Y., Maula T., Hall L.M.: Fluids density functional theory and initializing molecular dynamics simulations of block copolymers, Journal of Chemical Physics 144 (12), 2016

[21] Brune D.A., Bicerano J.: Micromechanics of nanocomposites: comparison of tensile and compressive elastic moduli, and prediction of effects of incomplete exfoliation and imperfect alignment on modulus, Polymer 43 (2), 2002, pp. 369–387

[22] Buxton G.A., Balazs A.C.: Predicting the mechanical and electrical properties of nanocomposites formed from polymer blends and nanorods, Molecular Simulation 30 (4), 2004, pp. 249–257

[23] Buxton G.A., Balazs A.C.: Simulating the morphology and mechanical properties of filled diblock copolymers, Physical Review E: Statistical, Nonlinear, and Soft Matter Physics 67 (3 1), 2003, pp. 31802

[24] Büyüköztürk O., Buehler M.J., Lau D., Tuakta C.: Structural solution using molecular dynamics: Fundamentals and a case study of epoxy-silica interface, International Journal of Solids and Structures 48 (14-15), 2011, pp. 2131–2140

[25] Carbone P., Ali Karimi-Varzaneh H., Müller-Plathe F.: Fine-graining without coarse-graining: An easy and fast way to equilibrate dense polymer melts, Faraday Discussions 144, 2009, pp. 25–42

[26] Castillo E., Codina R.: Stabilized stress-velocity-pressure finite element formulations of the Navier-Stokes problem for fluids with non-linear viscosity, Computer Methods in Applied Mechanics and Engineering 279, 2014, pp. 554–578

[27] Castillo E., Codina R.: Variational multi-scale stabilized formulations for the stationary three-field incompressible viscoelastic flow problem, Computer Methods in Applied Mechanics and Engineering 279, 2014, pp. 579–605

[28] Chatterjee A., Wu L.-M.: Predicting rheology of suspensions of spherical and non-spherical particles using dissipative particle dynamics (DPD): Methodology and experimental validation, Molecular Simulation 34 (3), 2008, pp. 243–250

[29] Chen X., Carbone P., Santangelo G., Di Matteo A., Milano G., Müller-Plathe F.: Backmapping coarse-grained polymer models under sheared nonequilibrium conditions, Physical Chemistry Chemical Physics 11 (12), 2009, pp. 1977–1988

[30] Chiu C.-W., Huang T.-K., Wang Y.-C., Alamani B.G., Lin J.-J.: Intercalation strategies in clay/polymer hybrids, Progress in Polymer Science 39 (3), 2014, pp. 443–485

[31] Chrissopoulou K., Altintzi I., Andrianaki I., Shemesh R., Retsos H., Giannelis E.P., Anastasiadis S.H.: Understanding and controlling the structure of polypropylene/layered silicate nanocomposites, Journal of Polymer Science, Part B: Polymer Physics 46 (24), 2008, pp. 2683–2695

[32] Christen M., van Gunsteren W.F.: On searching in, sampling of, and dynamically moving through conformational space of biomolecular systems: A review, Journal of Computational Chemistry 29 (2), 2008, pp. 157–166

[33] Codina R.: Stabilization of incompressibility and convection through orthogonal sub-scales in finite element methods, Computer Methods in Applied Mechanics and Engineering 190 (13-14), 2000, pp. 1579–1599

[34] Curtin W.A., Miller R.E.: Atomistic/continuum coupling in computational materials science, Modelling and Simulation in Materials Science and Engineering 11 (3), 2003, pp. R33-R68

[35] Dal Pont K., Gérard J.-F., Espuche E.: Microstructure and properties of styrene-butadiene rubber based nanocomposites prepared from an aminosilane modified synthetic lamellar nanofiller, Journal of Polymer Science, Part B: Polymer Physics 51 (13), 2013, pp. 1051–1059

[36] De S., Fish J., Shephard M.S., Keblinski P., Kumar S.K.: Multiscale modeling of polymer rheology, Physical Review E: Statistical, Nonlinear, and Soft Matter Physics 74 (3), 2006, pp. 30801

[37] Decker J.J., Meyers K.P., Paul D.R., Schiraldi D.A., Hiltner A., Nazarenko S.: Polyethylene-based nanocomposites containing organoclay: A new approach to enhance gas barrier via multilayer coextrusion and interdiffusion, Polymer 61, 2015, pp. 42–54

[38] Dellago C., Bolhuis P.G., Csajka F.S., Chandler D.: Transition path sampling and the calculation of rate constants, Journal of Chemical Physics 108 (5), 1998, pp. 1964–1977

[39] Dellago C., Bolhuis P.G., Geissler P.L.: Transition path sampling, Advances in Chemical Physics, Bd. 123, 2002

[40] Dellago C., Bolhuis P.G.: Transition path sampling and other advanced simulation techniques for rare events, Advances in Polymer Science, Bd. 221, Springer Verlag, 2009

[41] Delle Site L., Leon S., Kremer K.: BPA-PC on a Ni(111) Surface: The Interplay between Adsorption Energy and Conformational Entropy for Different Chain-End Modifications, Journal of the American Chemical Society 126 (9), 2004, pp. 2944–2955

[42] Delle Site L.: Some fundamental problems for an energy-conserving adaptive-resolution molecular dynamics scheme, Physical Review E: Statistical, Nonlinear, and Soft Matter Physics 76 (4), 2007

[43] Den Otter W.K., Clarke J.: The temperature in dissipative particle dynamics, International Journal of Modern Physics C 11 (6), 2000, pp. 1179–1193

[44] Dennis H.R., Hunter D.L., Chang D., Kim S., White J.L., Cho J.W., Paul D.R.: Effect of melt processing conditions on the extent of exfoliation in organoclay-based nanocomposites, Polymer 42 (23), 2001, pp. 9513–9522

[45] E W., Lu J., Yang J.Z.: Uniform accuracy of the quasicontinuum method, Physical Review B: Condensed Matter and Materials Physics 74 (21), 2006

[46] E W., Ren W., Vanden-Eijnden E.: Finite temperature string method for the study of rare events, Journal of Physical Chemistry B 109 (14), 2005, pp. 6688–6693
[47] E W., Ren W., Vanden-Eijnden E.: Transition pathways in complex systems: Reaction coordinates, isocommittor surfaces, and transition tubes, Chemical Physics Letters 413 (1-3), 2005, pp. 242–247
[48] E W., Vanden-Eijnden E.: Transition-path theory and path-finding algorithms for the study of rare events, Annual Review of Physical Chemistry, Bd. 61, Annual Reviews Inc, 2010
[49] Elber R., Ghosh A., Cárdenas A.: Long time dynamics of complex systems, Accounts of Chemical Research 35 (6), 2002, pp. 396–403
[50] Elber R., Karplus M.: A method for determining reaction paths in large molecules: Application to myoglobin, Chemical Physics Letters 139 (5), 1987, pp. 375–380
[51] Elber R., Karplus M.: Multiple conformational states of proteins: A molecular dynamics analysis of myoglobin, Science 235 (4786), 1987, pp. 318–321
[52] Elliott J.A.: Novel approaches to multiscale modelling in materials science, International Materials Reviews 56 (4), 2011, pp. 207–225
[53] Escobedo F.A., Borrero E.E., Araque J.C.: Transition path sampling and forward flux sampling. Applications to biological systems, Journal of Physics: Condensed Matter 21 (33), 2009
[54] Eslami H., Grmela M., Bousmina M.: A mesoscopic rheological model of polymer/layered silicate nanocomposites, Journal of Rheology 51 (6), 2007, pp. 1189–1222
[55] Eslami H., Grmela M., Bousmina M.: A mesoscopic tube model of polymer/layered silicate nanocomposites, Rheologica Acta 48 (3), 2009, pp. 317–331
[56] Fedosov D.A., Karniadakis G.E., Caswell B.: Steady shear rheometry of dissipative particle dynamics models of polymer fluids in reverse Poiseuille flow, Journal of Chemical Physics 132 (14), 2010, pp. 144103
[57] Fedosov D.A., Noguchi H., Gompper G.: Multiscale modeling of blood flow: From single cells to blood rheology, Biomechanics and Modeling in Mechanobiology 13 (2), 2014, pp. 239–258
[58] Fermeglia M., Posocco P., Pricl S.: Nano tools for macro problems: Multiscale molecular modeling of nanostructured polymer systems, Composite Interfaces 20 (6), 2013, pp. 379–394
[59] Folgar F., Tucker C.L.: Orientation behavior of fibers in concentrated suspensions, Journal of Reinforced Plastics and Composites 3 (2), 1984, pp. 98–119
[60] Folgar F., Tucker C.L.: Orientation behavior of fibers in concentrated suspensions, Journal of Reinforced Plastics and Composites 3 (2), 1984, pp. 98–119
[61] Fornes T., Yoon P., Hunter D., Keskkula H., Paul D.: Effect of organoclay structure on nylon 6 nanocomposite morphology and properties, Polymer 43 (22), 2002, pp. 5915–5933
[62] Fornes T.D., Yoon P.J., Keskkula H., Paul D.R.: Nylon 6 nanocomposites: The effect of matrix molecular weight, Polymer 42 (25), 2001, pp. 9929–9940
[63] Fritsch S., Junghans C., Kremer K.: Structure formation of toluene around C60: Implementation of the adaptive resolution scheme (AdResS) into GROMACS, Journal of Chemical Theory and Computation 8 (2), 2012, pp. 398–403

[64] Fritsch S., Poblete S., Junghans C., Ciccotti G., Delle Site L., Kremer K.: Adaptive resolution molecular dynamics simulation through coupling to an internal particle reservoir, Physical Review Letters 108 (17), 2012

[65] Gai J.-G., Hu G.-H., Li H.-L., Zhu S.-P., Hoppe S.: Dissipative particle dynamics and flory-huggins theories for predicting the rheological behavior of ultrahigh molecular weight polyethylene blends, Industrial and Engineering Chemistry Research 49 (22), 2010, pp. 11369–11379

[66] Ganesan V., Jayaraman A.: Theory and simulation studies of effective interactions, phase behavior and morphology in polymer nanocomposites, Soft Matter 10 (1), 2014, pp. 13–38

[67] Gao D., Li R., Lv B., Ma J., Tian F., Zhang J.: Flammability, thermal and physical-mechanical properties of cationic polymer/montmorillonite composite on cotton fabric, Composites Part B: Engineering 77, 2015, pp. 329–337

[68] Gao L., Shillcock J., Lipowsky R.: Improved dissipative particle dynamics simulations of lipid bilayers, Journal of Chemical Physics 126 (1), 2007

[69] Ghanbari A., Böhm M.C., Müller-Plathe F.: A simple reverse mapping procedure for coarse-grained polymer models with rigid side groups, Macromolecules 44 (13), 2011, pp. 5520–5526

[70] Goicochea A.G.: Adsorption and disjoining pressure isotherms of confined polymers using dissipative particle dynamics, Langmuir 23 (23), 2007, pp. 11656–11663

[71] González I., Eguiazábal J.I., Nazábal J.: Compatibilization level effects on the structure and mechanical properties of rubber-modified polyamide-6/clay nanocomposites, Journal of Polymer Science, Part B: Polymer Physics 43 (24), 2005, pp. 3611–3620

[72] Gooneie A., Mattausch H., Witschnigg A., Schuschnigg S., Holzer C.: Multiscale simulation of polymer nanocomposites in processing: Challenges and outlooks, Key Engineering Materials 651, 2015, pp. 533–538

[73] Gooneie A., Nazockdast H., Shahsavan F.: Effect of selective localization of carbon nanotubes in PA6 dispersed phase of PP/PA6 blends on the morphology evolution with time, part 1: Droplet deformation under simple shear flows, Polymer Engineering & Science 55 (7), 2015, pp. 1504–1519

[74] Gooneie A., Nazockdast H., Shahsavan F.: Effect of selective localization of carbon nanotubes in pa6 dispersed phase of PP/PA6 blends on the morphology evolution with time, part 2: Relaxation of deformed droplets after cessation of flow, Polymer Engineering & Science 56 (1), 2016, pp. 51–60

[75] Gooneie A., Schuschnigg S., Holzer C.: A Review of Multiscale Computational Methods in Polymeric Materials, Polymers 9 (1), 2017, pp. 16

[76] Gooneie A., Schuschnigg S., Holzer C.: Dissipative particle dynamics models of orientation of weakly-interacting anisometric silicate particles in polymer melts under shear flow: comparison with the standard orientation models, Macromolecular Theory and Simulations 25 (3), 2016, pp. 287–302

[77] Gooneie A., Schuschnigg S., Holzer C.: Orientation of anisometric layered silicate particles in uncompatibilized and compatibilized polymer melts under shear flow: A dissipative particle dynamics study, Macromolecular Theory and Simulations 25 (1), 2016, pp. 85–98

[78] Groot R.D., Madden T.J.: Dynamic simulation of diblock copolymer microphase separation, Journal of Chemical Physics 108 (20), 1998, pp. 8713–8724
[79] Groot R.D., Warren P.B.: Dissipative particle dynamics: Bridging the gap between atomistic and mesoscopic simulation, Journal of Chemical Physics 107 (11), 1997, pp. 4423–4435
[80] Groot R.D.: Applications of Dissipative Particle Dynamics, In: Karttunen M., Vattulainen I., Lukkarinen A. (Hrsg.): Novel Methods in Soft Matter Simulations, Springer Verlag, Berlin, Germany, 2004, pp. 5–38
[81] Guenza M.G.: Advancements in multi scale modeling: Adaptive resolution simulations and related issues, European Physical Journal: Special Topics 224 (12), 2015, pp. 2491–2495
[82] Handgraaf J.-W., Serral Gracia R., Nath S.K., Chen Z., Chou S.-H., Ross R.B., Schultz N.E., Fraaije J.: A multiscale modeling protocol to generate realistic polymer surfaces, Macromolecules 44 (4), 2011, pp. 1053–1061
[83] Hänggi P., Talkner P., Borkovec M.: Reaction-rate theory: Fifty years after Kramers, Reviews of Modern Physics 62 (2), 1990, pp. 251–341
[84] Harmandaris V.A., Mavrantzas V.G., Theodorou D.N.: Atomistic molecular dynamics simulation of stress relaxation upon cessation of steady-state uniaxial elongational flow, Macromolecules 33 (21), 2000, pp. 8062–8076
[85] Hess B., León S., van der Vegt N., Kremer K.: Long time atomistic polymer trajectories from coarse grained simulations: Bisphenol-A polycarbonate, Soft Matter 2 (5), 2006, pp. 409–414
[86] Hughes T., Feijóo G.R., Mazzei L., Quincy J.-B.: The variational multiscale method - A paradigm for computational mechanics, Computer Methods in Applied Mechanics and Engineering 166 (1-2), 1998, pp. 3–24
[87] Huynh H.M.: Improved fiber orientation predictions for injection-molded composites, Master's thesis at the University of Illinois at Urbana-Champaign, USA, 2001
[88] Jeffery, G. B.: The Motion of Ellipsoidal Particles Immersed in a Viscous Fluid, Proceedings of the Royal Society of London A: Mathematical, Physical and Engineering Sciences 102 (715), 1922, pp. 161–179
[89] Jo W.H., Yang J.S.: Molecular simulation approaches for multiphase polymer systems, Advances in Polymer Science, Bd. 156, 2002
[90] Johnston K., Harmandaris V.: Hierarchical multiscale modeling of polymer-solid interfaces: Atomistic to coarse-grained description and structural and conformational properties of polystyrene-gold systems, Macromolecules 46 (14), 2013, pp. 5741–5750
[91] Kacar G., Peters E., With G. de: Mesoscopic simulations for the molecular and network structure of a thermoset polymer, Soft Matter 9 (24), 2013, pp. 5785–5793
[92] Kacar G., Peters E., With G. de: Structure of a thermoset polymer near an alumina substrate as studied by dissipative particle dynamics, Journal of Physical Chemistry C 117 (37), 2013, pp. 19038–19047
[93] Kairn T., Daivis P.J., Ivanov I., Bhattacharya S.N.: Molecular-dynamics simulation of model polymer nanocomposite rheology and comparison with experiment, Journal of Chemical Physics, Journal of Chemical Physics 123 (19), 2005

[94] Kalra V., Escobedo F., Joo Y.L.: Effect of shear on nanoparticle dispersion in polymer melts: A coarse-grained molecular dynamics study, The Journal of chemical physics 132 (2), 2010, pp. 24901
[95] Kamerlin S., Vicatos S., Dryga A., Warshel A.: Coarse-grained (multiscale) simulations in studies of biophysical and chemical systems, Annual Review of Physical Chemistry, Bd. 62, 2011
[96] Karimi-Varzaneh H.A., Carbone P., Müller-Plathe F.: Fast dynamics in coarse-grained polymer models: The effect of the hydrogen bonds, Journal of Chemical Physics 129 (15), 2008
[97] Kauzlari D., Meier J.T., Español P., Succi S., Greiner A., Korvink J.G.: Bottom-up coarse-graining of a simple graphene model: The blob picture, Journal of Chemical Physics 134 (6), 2011
[98] Khalatur P.G.: Molecular Dynamics Simulations in Polymer Science: Methods and Main Results, In: Polymer Science: A Comprehensive Reference, 10 Volume Set, Elsevier, Spain, 2012, pp. 417–460
[99] Kim S., Palomino A.M., Colina C.M.: Responsive polymer conformation and resulting permeability of clay-polymer nanocomposites, Molecular Simulation 38 (8-9), 2012, pp. 723–734
[100] Klein P.A., Zimmerman J.A.: Coupled atomistic-continuum simulations using arbitrary overlapping domains, Journal of Computational Physics 213 (1), 2006, pp. 86–116
[101] Klenin K., Strodel B., Wales D.J., Wenzel W.: Modelling proteins: Conformational sampling and reconstruction of folding kinetics, Biochimica et Biophysica Acta, Proteins and Proteomics 1814 (8), 2011, pp. 977–1000
[102] Koo B., Subramanian N., Chattopadhyay A.: Molecular dynamics study of brittle fracture in epoxy-based thermoset polymer, Composites Part B: Engineering 95, 2016, pp. 433–439
[103] Kotal M., Bhowmick A.K.: Polymer nanocomposites from modified clays: Recent advances and challenges, Progress in Polymer Science 51, 2015, pp. 127–187
[104] Kotelyanskii M., Wagner N.J., Paulaitis M.E.: Building large amorphous polymer structures: Atomistic simulation of glassy polystyrene, Macromolecules 29 (26), 1996, pp. 8497–8506
[105] Kreis K., Fogarty A.C., Kremer K., Potestio R.: Advantages and challenges in coupling an ideal gas to atomistic models in adaptive resolution simulations, European Physical Journal: Special Topics 224 (12), 2015, pp. 2289–2304
[106] Kremer K., Müller-Plathe F.: Multiscale problems in polymer science: Simulation approaches, MRS Bulletin 26 (3), 2001, pp. 205–210
[107] Laio A., Parrinello M.: Escaping free-energy minima, Proceedings of the National Academy of Sciences of the United States of America 99 (20), 2002, pp. 12562–12566
[108] Lambeth Jr. B.P., Junghans C., Kremer K., Clementi C., Site L.D.: Communication: On the locality of Hydrogen bond networks at hydrophobic interfaces, Journal of Chemical Physics 133 (22), 2010, pp. 221101
[109] Larson R. G.: The Structure and Rheology of Complex Fluids, Oxford University Press, New York, 1999

[110] Lecouvet B., Gutierrez J.G., Sclavons M., Bailly C.: Structure-property relationships in polyamide 12/halloysite nanotube nanocomposites, Polymer Degradation and Stability 96 (2), 2011, pp. 226–235

[111] Lee M.-T., Mao R., Vishnyakov A., Neimark A.V.: Parametrization of Chain Molecules in Dissipative Particle Dynamics, Journal of Physical Chemistry B, 2016

[112] Letwimolnun W., Vergnes B., Ausias G., Carreau P.J.: Stress overshoots of organoclay nanocomposites in transient shear flow, Journal of Non-Newtonian Fluid Mechanics 141 (2-3), 2007, pp. 167–179

[113] Li C., Chou T.-W.: Elastic moduli of multi-walled carbon nanotubes and the effect of van der Waals forces, Composites Science and Technology 63 (11), 2003, pp. 1517–1524

[114] Li C., Chou T.-W.: Multiscale modeling of compressive behavior of carbon nanotube/polymer composites, Composites Science and Technology 66 (14), 2006, pp. 2409–2414

[115] Li Q., Yang Q., Huang Y., Chen G., Lv Y.: Effect of compatibilizer content on the shear and extensional rheology of polypropylene/clay nanocomposites, Journal of Macromolecular Science, Part B: Physics 51 (9), 2012, pp. 1776–1793

[116] Li X., Ming P.: On the effect of ghost force in the quasicontinuum method: Dynamic problems in one dimension, Communications in Computational Physics 15 (3), 2014, pp. 647–676

[117] Li Y., Abberton B.C., Kröger M., Liu W.K.: Challenges in multiscale modeling of polymer dynamics, Polymers 5 (2), 2013, pp. 751–832

[118] Liu M.B., Liu G.R., Zhou L.W., Chang J.Z.: Dissipative Particle Dynamics (DPD): An Overview and Recent Developments, Archives of Computational Methods in Engineering 22 (4), 2015, pp. 529–556

[119] Lowe D.J., Chapman A.V., Cook S., Busfield, J. J. C.: Micromechanical models of young's modulus of NR/organoclay nanocomposites, Journal of Polymer Science, Part B: Polymer Physics 49 (22), 2011, pp. 1621–1627

[120] Makki H., Adema, K. N. S., Peters, E. A. J. F., Laven J., Van Der Ven, L. G. J., Van Benthem, R. A. T. M., With G. de: A simulation approach to study photo-degradation processes of polymeric coatings, Polymer Degradation and Stability 105 (1), 2014, pp. 68–79

[121] Maly M., Posocco P., Pricl S., Fermeglia M.: Self-assembly of nanoparticle mixtures in diblock copolymers: Multiscale molecular modeling, Industrial and Engineering Chemistry Research 47 (15), 2008, pp. 5023–5038

[122] Mattausch H., Laske S., Duretek I., Kreith J., Maier G., Holzer C.: Investigation of the influence of processing conditions on the thermal, rheological and mechanical behavior of polypropylene nanocomposites, Polymer Engineering & Science 53 (5), 2013, pp. 1001–1010

[123] Mauroy H., Plivelic T.S., Suuronen J.-P., Hage F.S., Fossum J.O., Knudsen K.D.: Anisotropic clay-polystyrene nanocomposites: Synthesis, characterization and mechanical properties, Applied Clay Science 108, 2015, pp. 19–27

[124] Meng S., Zhang J., Wang Y., Li X., Wu C., Hou T., Xiao L., Lu G.: Simulating the rheology of surfactant solution using dissipative particle dynamics, Molecular Simulation 41 (9), 2015, pp. 772–778

[125] Mesbah A., Zaïri F., Boutaleb S., Gloaguen J.M., Naït-Abdelaziz M., Xie S., Boukharouba T., Lefebvre J.M.: Experimental characterization and modeling stiffness of polymer/clay nanocomposites within a hierarchical multiscale framework, Journal of Applied Polymer Science 114 (5), 2009, pp. 3274–3291

[126] Miller R.E., Tadmor E.B.: A unified framework and performance benchmark of fourteen multiscale atomistic/continuum coupling methods, Modelling and Simulation in Materials Science and Engineering 17 (5), 2009, pp. 53001

[127] Moniruzzaman M., Winey K.I.: Polymer nanocomposites containing carbon nanotubes, Macromolecules 39 (16), 2006, pp. 5194–5205

[128] Montazeri A., Naghdabadi R.: Study the effect of viscoelastic matrix model on the stability of CNT/polymer composites by multiscale modeling, Polymer Composites 30 (11), 2009, pp. 1545–1551

[129] Montazeri A., Sadeghi M., Naghdabadi R., Rafii-Tabar H.: Multiscale modeling of the effect of carbon nanotube orientation on the shear deformation properties of reinforced polymer-based composites, Physics Letters A 375 (14), 2011, pp. 1588–1597

[130] Mukherji D., van der Vegt N., Kremer K., Delle Site L.: Kirkwood-buff analysis of liquid mixtures in an open boundary simulation, Journal of Chemical Theory and Computation 8 (2), 2012, pp. 375–379

[131] Mukherji D., van der Vegt N., Kremer K.: Preferential solvation of triglycine in aqueous urea: An open boundary simulation approach, Journal of Chemical Theory and Computation 8 (10), 2012, pp. 3536–3541

[132] Nakano A., Bachlechner M.E., Kalia R.K., Lidorikis E., Vashishta P., Voyiadjis G.Z., Campbell T.J., Ogata S., Shimojo F.: Multiscale simulation of nanosystems, Computing in Science and Engineering 3 (4), 2001, pp. 56–66

[133] Nazockdast E., Nazockdast H., Goharpey F.: Linear and nonlinear melt-state viscoelastic properties of polypropylene/organoclay nanocomposites, Polymer Engineering and Science 48 (7), 2008, pp. 1240–1249

[134] Nazockdast E., Nazockdast H.: Rheological Modeling of Polymer/layered silicate Nanocomposites, Appl. Rheol. 21 (2), 2011, pp. 25434

[135] Neri M., Anselmi C., Cascella M., Maritan A., Carloni P.: Coarse-grained model of proteins incorporating atomistic detail of the active site, Physical Review Letters 95 (21), 2005

[136] Nguyen Q.T., Ngo T.D., Tran P., Mendis P., Bhattacharyya D.: Influences of clay and manufacturing on fire resistance of organoclay/thermoset nanocomposites, Composites Part A: Applied Science and Manufacturing 74, 2015, pp. 26–37

[137] Nielsen S.O., Srinivas G., Klein M.L.: Incorporating a hydrophobic solid into a coarse grain liquid framework: graphite in an aqueous amphiphilic environment, Journal of Chemical Physics 123 (12), 2005, pp. 124907

[138] Niskanen H., Eloranta H., Tuomela J., Hämäläinen J.: On the orientation probability distribution of flexible fibres in a contracting channel flow, International Journal of Multiphase Flow 37 (4), 2011, pp. 336–345

[139] Ortman K., Baird D., Wapperom P., Aning A.: Prediction of fiber orientation in the injection molding of long fiber suspensions, Polymer Composites 33 (8), 2012, pp. 1360–1367

[140] Ortner C., Zhang L.: Atomistic/continuum blending with ghost force correction, SIAM Journal on Scientific Computing 38 (1), 2016, pp. A346-A375
[141] P. Español, P. Warren: Statistical Mechanics of Dissipative Particle Dynamics, Europhysics Letters 30 (4), 1995, pp. 191
[142] P. J. Hoogerbrugge, J. M. V. A. Koelman: Simulating Microscopic Hydrodynamic Phenomena with Dissipative Particle Dynamics, Europhysics Letters 19 (3), 1992, pp. 155
[143] Padding J.T., Briels W.J.: Coarse-grained molecular dynamics simulations of polymer melts in transient and steady shear flow, Journal of Chemical Physics 118 (22), 2003, pp. 10276–10286
[144] Padding J.T., Briels W.J.: Time and length scales of polymer melts studied by coarse-grained molecular dynamics simulations, Journal of Chemical Physics 117 (2), 2002, pp. 925–943
[145] Padding J.T., Briels W.J.: Uncrossability constraints in mesoscopic polymer melt simulations: Non-rouse behavior of C120H242, Journal of Chemical Physics 115 (6), 2001, pp. 2846–2859
[146] Pan W., Caswell B., Karniadakis G.E.: Rheology, microstructure and migration in brownian colloidal suspensions, Langmuir 26 (1), 2010, pp. 133–142
[147] Parker A.J., Rottler J.: Using soft potentials for the simulation of block copolymer morphologies, Macromolecular Theory and Simulations 23 (6), 2014, pp. 401–409
[148] Passerone D., Parrinello M.: Action-derived molecular dynamics in the study of rare events, Physical Review Letters 87 (10), 2001, pp. 108302
[149] Pavlidou S., Papaspyrides C.D.: A review on polymer-layered silicate nanocomposites, Progress in Polymer Science 33 (12), 2008, pp. 1119–1198
[150] Pereira S.P., Scocchi G., Toth R., Posocco P., Nieto D.R., Pricl S., Fermeglia M.: Multiscale Modeling of Polymer/Clay Nanocomposites, Journal of Multiscale Modelling 3 (3), 2011, pp. 151–176
[151] Poblete S., Praprotnik M., Kremer K., Delle Site L.: Coupling different levels of resolution in molecular simulations, Journal of Chemical Physics 132 (11), 2010
[152] Poma A.B., Delle Site L.: Classical to path-integral adaptive resolution in molecular simulation: Towards a smooth quantum-classical coupling, Physical Review Letters 104 (25), 2010
[153] Poma A.B., Site L.D.: Adaptive resolution simulation of liquid para-hydrogen: Testing the robustness of the quantum-classical adaptive coupling, Physical Chemistry Chemical Physics 13 (22), 2011, pp. 10510–10519
[154] Posocco P., Posel Z., Fermeglia M., Lísal M., Pricl S.: A molecular simulation approach to the prediction of the morphology of self-assembled nanoparticles in diblock copolymers, Journal of Materials Chemistry 20 (46), 2010, pp. 10511–10520
[155] Potestio R., Delle Site L.: Quantum locality and equilibrium properties in low-temperature parahydrogen: A multiscale simulation study, Journal of Chemical Physics 136 (5), 2012, pp. 54101
[156] Potestio R., Peter C., Kremer K.: Computer simulations of soft matter: Linking the scales, Entropy 16 (8), 2014, pp. 4199–4245

[157] Praprotnik M., Delle Site L., Kremer K.: A macromolecule in a solvent: Adaptive resolution molecular dynamics simulation, Journal of Chemical Physics 126 (13), 2007, pp. 134902
[158] Praprotnik M., Delle Site L., Kremer K.: Adaptive resolution molecular-dynamics simulation: Changing the degrees of freedom on the fly, Journal of Chemical Physics 123 (22), 2005
[159] Praprotnik M., Delle Site L., Kremer K.: Adaptive resolution scheme for efficient hybrid atomistic-mesoscale molecular dynamics simulations of dense liquids, Physical Review E: Statistical, Nonlinear, and Soft Matter Physics 73 (6), 2006
[160] Praprotnik M., Matysiak S., Site L.D., Kremer K., Clementi C.: Adaptive resolution simulation of liquid water, Journal of Physics: Condensed Matter 19 (29), 2007
[161] Praprotnik M., Poblete S., Delle Site L., Kremer K.: Comment on "adaptive multiscale molecular dynamics of macromolecular fluids", Physical Review Letters 107 (9), 2011
[162] Praprotnik M., Site L.D., Kremer K.: Multiscale simulation of soft matter: From scale bridging to adaptive resolution, Annual Review of Physical Chemistry, Bd. 59, 2008
[163] Pryamitsyn V., Ganesan V.: Origins of Linear Viscoelastic Behavior of Polymer−Nanoparticle Composites, Macromolecules 39 (2), 2006, pp. 844–856
[164] Qin H., Zhang S., Zhao C., Yang M.: Zero-order kinetics of the thermal degradation of polypropylene/clay nanocomposites, Journal of Polymer Science, Part B: Polymer Physics 43 (24), 2005, pp. 3713–3719
[165] Queyroy S., Neyertz S., Brown D., Müller-Plathe F.: Preparing relaxed systems of amorphous polymers by multiscale simulation: Application to cellulose, Macromolecules 37 (19), 2004, pp. 7338–7350
[166] Raabe D.: Challenges in computational materials science, Advanced Materials 14 (9), 2002, pp. 639–650
[167] Rahatekar S.S., Hamm M., Shaffer M., Elliott J.A.: Mesoscale modeling of electrical percolation in fiber-filled systems, Journal of Chemical Physics 123 (13), 2005
[168] Rajabian M., Dubois C., Grmela M., Carreau P.J.: Effects of polymer-fiber interactions on rheology and flow behavior of suspensions of semi-flexible fibers in polymeric liquids, Rheologica Acta 47 (7), 2008, pp. 701–717
[169] Rajabian M., Dubois C., Grmela M.: Suspensions of semiflexible fibers in polymeric fluids: Rheology and thermodynamics, Rheologica Acta 44 (5), 2005, pp. 521–535
[170] Rajabian M., Naderi G., Carreau P.J., Dubois C.: Flow-induced particle orientation and rheological properties of suspensions of organoclays in thermoplastic resins, Journal of Polymer Science, Part B: Polymer Physics 48 (18), 2010, pp. 2003–2010
[171] Ren W., Vanden-Eijnden E., Maragakis P., E W.: Transition pathways in complex systems: Application of the finite-temperature string method to the alanine dipeptide, Journal of Chemical Physics 123 (13), 2005, pp. 134109
[172] Rissanou A.N., Power A.J., Harmandaris V.: Structural and dynamical properties of polyethylene/graphene nanocomposites through molecular dynamics simulations, Polymers 7 (3), 2015, pp. 390–417
[173] Rudd R.E., Broughton J.Q.: Concurrent coupling of length scales in solid state systems, Physica Status Solidi B: Basic Solid State Physics 217 (1), 2000, pp. 251–291

[174] Santangelo G., Di Matteo A., Müller-Plathe F., Milano G.: From mesoscale back to atomistic models: A fast reverse-mapping procedure for vinyl polymer chains, Journal of Physical Chemistry B 111 (11), 2007, pp. 2765–2773

[175] Schwetlick H., Zimmer J.: Calculation of long time classical trajectories: Algorithmic treatment and applications for molecular systems, Journal of Chemical Physics 130 (12), 2009

[176] Scocchi G., Posocco P., Fermeglia M., Pricl S.: Polymer - Clay nanocomposites: A multiscale molecular modeling approach, Journal of Physical Chemistry B 111 (9), 2007, pp. 2143–2151

[177] Scocchi G., Posocco P., Handgraaf J.-W., Fraaije, J. G. E. M., Fermeglia M., Pricl S.: A complete multiscale modelling approach for polymer-clay nanocomposites, Chemistry - A European Journal 15 (31), 2009, pp. 7586–7592

[178] Sepahvand R., Adeli M., Astinchap B., Kabiri R.: New nanocomposites containing metal nanoparticles, carbon nanotube and polymer, Journal of Nanoparticle Research 10 (8), 2008, pp. 1309–1318

[179] Sepehr M., Ausias G., Carreau P.J.: Rheological properties of short fiber filled polypropylene in transient shear flow, Journal of Non-Newtonian Fluid Mechanics 123 (1), 2004, pp. 19–32

[180] Sheng N., Boyce M.C., Parks D.M., Rutledge G.C., Abes J.I., Cohen R.E.: Multiscale micromechanical modeling of polymer/clay nanocomposites and the effective clay particle, Polymer 45 (2), 2004, pp. 487–506

[181] Shenoy V.B., Miller R., Tadmor E.B., Rodney D., Phillips R., Ortiz M.: An adaptive finite element approach to atomic-scale mechanics - The quasicontinuum method, Journal of the Mechanics and Physics of Solids 47 (3), 1999, pp. 611–642

[182] Shimokawa T., Mortensen J.J., Schiøtz J., Jacobsen K.W.: Matching conditions in the quasicontinuum method: Removal of the error introduced at the interface between the coarse-grained and fully atomistic region, Physical Review B: Condensed Matter and Materials Physics 69 (21), 2004, 214104-1-214104-10

[183] Shou Z., Buxton G.A., Balazs A.C.: Predicting the self-assembled morphology and mechanical properties of mixtures of diblocks and rod-like nanoparticles, Composite Interfaces 10 (4-5), 2003, pp. 343–368

[184] Sinha Ray S., Okamoto M.: Polymer/layered silicate nanocomposites: A review from preparation to processing, Progress in Polymer Science 28 (11), 2003, pp. 1539–1641

[185] Sinsawat A., Anderson K.L., Vaia R.A., Farmer B.L.: Influence of polymer matrix composition and architecture on polymer nanocomposite formation: Coarse-grained molecular dynamics simulation, Journal of Polymer Science, Part B: Polymer Physics 41 (24), 2003, pp. 3272–3284

[186] Skountzos E.N., Anastassiou A., Mavrantzas V.G., Theodorou D.N.: Determination of the mechanical properties of a poly(methyl methacrylate) nanocomposite with functionalized graphene sheets through detailed atomistic simulations, Macromolecules 47 (22), 2014, pp. 8072–8088

[187] Sliozberg Y.R., Kröger M., Chantawansri T.L.: Fast equilibration protocol for million atom systems of highly entangled linear polyethylene chains, Journal of Chemical Physics 144 (15), 2016

[188] Smith K.A., Tyagi S., Balazs A.C.: Healing surface defects with nanoparticle-filled polymer coatings: Effect of particle geometry, Macromolecules 38 (24), 2005, pp. 10138–10147

[189] Solomon M.J., Almusallam A.S., Seefeldt K.F., Somwangthanaroj A., Varadan P.: Rheology of polypropylene/clay hybrid materials, Macromolecules 34 (6), 2001, pp. 1864–1872

[190] Song E.-H., Kang B.-H., Kim T.-Y., Lee H.-J., Park Y.-W., Kim Y.-C., Ju B.-K.: Highly oriented gold/nanoclay-polymer nanocomposites for flexible gas barrier films, ACS Applied Materials and Interfaces 7 (8), 2015, pp. 4778–4783

[191] Sørensen M.R., Voter A.F.: Temperature-accelerated dynamics for simulation of infrequent events, Journal of Chemical Physics 112 (21), 2000, pp. 9599–9606

[192] Spyriouni T., Tzoumanekas C., Theodorou D., Müller-Plathe F., Milano G.: Coarse-grained and reverse-mapped united-atom simulations of long-chain atactic polystyrene melts: Structure, thermodynamic properties, chain conformation, and entanglements, Macromolecules 40 (10), 2007, pp. 3876–3885

[193] Starr F.W., Douglas J.F., Glotzer S.C.: Origin of particle clustering in a simulated polymer nanocomposite and its impact on rheology, The Journal of Chemical Physics 119 (3), 2003, pp. 1777

[194] Stephanou P.S., Mavrantzas V.G., Georgiou G.C.: Continuum model for the phase behavior, microstructure, and rheology of unentangled polymer nanocomposite melts, Macromolecules 47 (13), 2014, pp. 4493–4513

[195] Stephanou P.S.: How the flow affects the phase behaviour and microstructure of polymer nanocomposites, Journal of Chemical Physics 142 (6), 2015, pp. 64901

[196] Stillinger F.H., Weber T.A.: Computer simulation of local order in condensed phases of silicon, Physical Review B: Condensed Matter and Materials Physics 31 (8), 1985, pp. 5262–5271

[197] Su Z.C., Tay T.-E., Chen Y., Tan V.: Multiscale modeling for amorphous materials - Mapping atomistic displacements to macroscopic deformation, International Journal of Applied Mechanics 4 (4), 2012

[198] Suter J.L., Groen D., Coveney P.V.: Chemically specifi C multiscale modeling of clay-polymer nanocomposites reveals intercalation dynamics, tactoid self-assembly and emergent materials properties, Advanced Materials 27 (6), 2015, pp. 966–984

[199] Tan V., Zeng X.S., Deng M., Lim K.M., Tay T.E.: Multiscale modeling of polymers - The Pseudo Amorphous Cell, Computer Methods in Applied Mechanics and Engineering 197 (6-8), 2008, pp. 536–554

[200] Theodorou D.N., Suter U.W.: Detailed molecular structure of a vinyl polymer glass, Macromolecules 18 (7), 1985, pp. 1467–1478

[201] Theodorou D.N., Suter U.W.: Geometrical considerations in model systems with periodic boundaries, Journal of Chemical Physics 82 (2), 1985, pp. 955–966

[202] Todd B.D., Daivis P.J.: Nonequilibrium molecular dynamics simulations of planar elongational flow with spatially and temporally periodic boundary conditions, Physical Review Letters 81 (5), 1998, pp. 1118–1121

[203] Travasso R., Buxton G.A., Kuksenok O., Good K., Balazs A.C.: Modeling the morphology and mechanical properties of sheared ternary mixtures, Journal of Chemical Physics 122 (19), 2005, pp. 194906

[204] Tschöp W., Kremer K., Halm O., Batoulis J., Bürger T.: Simulation of polymer melts. II. from coarse-grained models back to atomistic description, Acta Polymerica 49 (2-3), 1998, pp. 75–79
[205] Tucker II, C. L., Wang J., O'Gara J.F.: An objective model for slow orientation kinetics in concentrated fiber suspensions: Theory and rheological evidence, Journal of Rheology 52 (5), 2008, pp. 1179–1200
[206] Tuckerman M.E., Martyna G.J., Berne B.J.: Molecular dynamics algorithm for condensed systems with multiple time scales, Journal of Chemical Physics 93 (2), 1990, pp. 1287–1291
[207] Tyagi S., Lee J.Y., Buxton G.A., Balazs A.C.: Using nanocomposite coatings to heal surface defects, Macromolecules 37 (24), 2004, pp. 9160–9168
[208] van Gunsteren W.F., Bakowies D., Baron R., Chandrasekhar I., Christen M., Daura X., Gee P., Geerke D.P., Glättli A., Hünenberger P.H., Kastenholz M.A., Oostenbrink C., Schenk M., Trzesniak D., van der Vegt N., Yu H.B.: Biomolecular modeling: Goals, problems, perspectives, Angewandte Chemie - International Edition 45 (25), 2006, pp. 4064–4092
[209] Verlet L.: Computer "experiments" on classical fluids. I. Thermodynamical properties of Lennard-Jones molecules, Physical Review 159 (1), 1967, pp. 98–103
[210] Verlet L.: Computer "experiments" on classical fluids. II. Equilibrium correlation functions, Physical Review 165 (1), 1968, pp. 201–214
[211] Visser D.C.: Modelling multi-viscosity systems with dissipative particle dynamics, Journal of Computational Physics 214 (2), 2006, pp. 491–504
[212] Vogiatzis G.G., Theodorou D.N.: Local segmental dynamics and stresses in polystyrene-C60 mixtures, Macromolecules 47 (1), 2014, pp. 387–404
[213] Voter A.F., Montalenti F., Germann T.C.: Extending the time scale in atomistic simulation of materials, Annual Review of Materials Science 32, 2002, pp. 321–346
[214] Voter A.F.: A method for accelerating the molecular dynamics simulation of infrequent events, Journal of Chemical Physics 106 (11), 1996, pp. 4665–4677
[215] Voter A.F.: Hyperdynamics: Accelerated molecular dynamics of infrequent events, Physical Review Letters 78 (20), 1997, pp. 3908–3911
[216] Voter A.F.: Parallel replica method for dynamics of infrequent events, Physical Review B: Condensed Matter and Materials Physics 57 (22), 1998, pp. R13985-R13988
[217] Wales D.J.: Discrete path sampling, Molecular Physics 100 (20), 2002, pp. 3285–3305
[218] Wang H., Agarwal A.: Adaptive resolution simulation in equilibrium and beyond, European Physical Journal: Special Topics 224 (12), 2015, pp. 2269–2287
[219] Wu C.: Multiscale simulations of the structure and dynamics of stereoregular poly(methyl methacrylate)s, Journal of Molecular Modeling 20 (8), 2014
[220] Wu T., O'Kelly K., Chen B.: Biomimetic chitosan-treated clay-elastomer composites with water-responsive mechanically dynamic properties, Journal of Polymer Science, Part B: Polymer Physics 52 (1), 2014, pp. 55–62
[221] Xie X.L., Yang T.Q., Tang C.Y.: Random orientation of in situ composites based on liquid-crystalline polymers by compression moulding, Polymer International 52 (2), 2003, pp. 310–315

[222] Yamanoi M., Pozo O., Maia J.M.: Linear and non-linear dynamics of entangled linear polymer melts by modified tunable coarse-grained level Dissipative Particle Dynamics, Journal of Chemical Physics 135 (4), 2011, pp. 44904

[223] Yildirim E., Yurtsever M.: A comparative study on the efficiencies of polyethylene compatibilizers by using theoretical methods, Journal of Polymer Research 19 (2), 2012, pp. 9771

[224] Yoshimoto S., Ohashi F., Kameyama T.: Characterization and thermal degradation studies on polyaniline- intercalated montmorillonite nanocomposites prepared by a solvent-free mechanochemical route, Journal of Polymer Science, Part B: Polymer Physics 43 (19), 2005, pp. 2705–2714

[225] Youn Park J., Park C.-H., Shin Park J., Kong K.-J., Chang H., Im S.: Multiscale computations for carbon nanotubes based on a hybrid QM/QC (quantum mechanical and quasicontinuum) approach, Journal of the Mechanics and Physics of Solids 58 (2), 2010, pp. 86–102

[226] Yu Z.-Z., Hu G.-H., Varlet J., Dasari A., Mai Y.-W.: Water-assisted melt compounding of nylon-6/pristine montmorillonite nanocomposites, Journal of Polymer Science, Part B: Polymer Physics 43 (9), 2005, pp. 1100–1112

[227] Zaloj V., Elber R.: Parallel computations of molecular dynamics trajectories using the stochastic path approach, Computer Physics Communications 128 (1), 2000, pp. 118–127

[228] Zavadlav J., Podgornik R., Praprotnik M.: Adaptive Resolution Simulation of a DNA Molecule in Salt Solution, Journal of Chemical Theory and Computation 11 (10), 2015, pp. 5035–5044

[229] Zeng Q.H., Yu A.B., Lu G.Q.: Multiscale modeling and simulation of polymer nanocomposites, Progress in Polymer Science (Oxford) 33 (2), 2008, pp. 191–269

[230] Zhang K., Manke C.W.: Simulation of polymer solutions by dissipative particle dynamics, Molecular Simulation 25 (3-4), 2000, pp. 157–166

[231] Zhang P., Zhang N., Deng Y., Bluestein D.: A multiple time stepping algorithm for efficient multiscale modeling of platelets flowing in blood plasma, Journal of Computational Physics 284, 2015, pp. 668–686

[232] Zhao X., Deng S., Huang Y., Liu H., Hu Y.: Simulation of morphologies and mechanical properties of A/B polymer blend film, Chinese Journal of Chemical Engineering 19 (4), 2011, pp. 549–557